The effect of evolving micro-structural length scale on the macroscopic constitutive behaviour of granular media

Nicholas Anton Collins-Craft

A thesis submitted in partial fulfilment of the requirements for the degree of Doctor of Philosophy

The Faculty of Engineering
The University of Sydney
&
Laboratoire Navier
Université Paris-Est

2019

This is to certify that to the best of my knowledge, the content of this thesis is my own work. This thesis has not been submitted for any degree or other purposes.

I certify that the intellectual content of this thesis is the product of my own work and that all the assistance received in preparing this thesis and sources have been acknowledged.

Nicholas Anton Collins-Craft

Abstract

Granular media are ubiquitous throughout the world and developing a comprehensive understanding of their behaviour is a pressing challenge. Of particular importance is accounting for the localisation of deformation into thin bands that feature intense grain crushing. This thesis develops a framework that predicts the formation of these bands and the grain size evolution, using experimental, theoretical and numerical approaches.

Our experimental approach uses spatio-temporal plotting and Fourier analysis to extract information from photographs, allowing a sub-grain resolution of the velocity field. We investigate the effect of grain size polydispersity on the width of shear bands.

Our theoretical approach develops a novel constitutive model that combines two existing formulations. We enrich Breakage Mechanics (Einav, 2007a,b) with the Cosserat continuum (Cosserat and Cosserat, 1909) by an elastic upscaling that includes Cosserat state variables. This regularises Breakage Mechanics, allowing it to predict strain localisation phenomena such as shear bands, and adds physical fidelity to Cosserat models.

Our numerical approach uses linear stability analysis and the finite element method to determine the conditions that result in strain localisation. The linear stability analysis gives the expected initial thickness and the initial post-localisation tendencies of the system. This information informs the finite element analysis, which is used to perform a rigorous post-localisation analysis.

This thesis provides a framework which can be used to explore and further model the evolution of systems that experience strain localisation accompanied by intense grain crushing, ranging from standard laboratory tests to seismogenic faults.

Résumé

Les matériaux granulaire sont omniprésent dans la nature, et le développement d'une compréhension complète de leur comportement est un défi pressant. L'explication de la localisation de la déformation en bandes minces, qui présentent un écrasement important des grains, est d'une importance particulière. Cette thèse contribue à développer un modèle prévoyant la formation des bandes et l'évolution des tailles des grains, expérimentalement, théoriquement et numériquement.

Notre approche expérimental utilise les graphiques spatio-temporels et l'analyse de Fourier pour extraire les informations des photos, ce qui permettent une résolution des champs de meilleure que le diamètre des grains individuels. Cela permet l'étude de l'effet du polydispersité sur le largeur des bandes de cisaillement.

Notre approche théorique développe une nouveau modèle constitutif qui combine deux formulations existant. Nous enrichissons Breakage Mechanics (Einav, 2007a,b) avec le continuum de Cosserat (Cosserat and Cosserat, 1909) par un upscaling élastique qui inclut les variables d'état de Cosserat. Cette approche régularise Breakage Mechanics, permettant de prédire les phénomènes de localisation de déformation comme les bandes de cisaillement, et ajoute une fidélité physique aux modèles Cosserat.

Notre approche numérique utilise l'analyse de stabilité linéaire et la méthode des éléments fini pour déterminer les conditions conduisant à la localisation des déformations. L'analyse de stabilité linéaire donne l'épaisseur initiale attendue et les tendances post-localisation initiale du système. Cette information façonne l'analyse des éléments finis, qui est utilisée pour réaliser une analyse post-localisation rigoureuse.

Cette thèse fourni un cadre pour le développement de modèles plus raffinés qui permettront l'étude des systèmes présentant de forte localisation des déformations accompagnées d'une fragmentation intense des grains. Ce modèle permet ainsi une meilleur compréhension de nombreux phénomènes, des tests de laboratoire aux séismes.

Contents

Abstract ii

Résumé iii

Contents iv

List of Figures vii

List of Tables xiii

1 Introduction 1

2 A review of localisation phenomena in granular geomaterials 4
- 2.1 Summary . . . 4
- 2.2 Observations of localisation in geomaterials . . . 4
  - 2.2.1 Field-scale observations . . . 5
  - 2.2.2 Laboratory-scale observations . . . 9
- 2.3 Modelling localisations . . . 15
  - 2.3.1 Bifurcation theory and its application to geomechanics . . . 15
  - 2.3.2 Constitutive models . . . 16
  - 2.3.3 Numerical implementations . . . 22
- 2.4 Conclusion . . . 23

3 Continuous annular shear experiments with two-dimensional rod particles 24
- 3.1 Summary . . . 24
- 3.2 Introduction . . . 24
- 3.3 Experimental method . . . 25
- 3.4 Data analysis . . . 28
  - 3.4.1 Image treatment . . . 28
  - 3.4.2 Fourier analysis . . . 30
  - 3.4.3 Velocity analysis . . . 31
  - 3.4.4 Determining the velocity distribution in space . . . 33
- 3.5 Results . . . 33
- 3.6 Discussion . . . 35
  - 3.6.1 Smoothing . . . 35
  - 3.6.2 Differentiation . . . 37
  - 3.6.3 Further discussion . . . 39
- 3.7 Conclusion . . . 40

4 Formulating Breakage Mechanics in the Cosserat continuum **42**
4.1 Summary . . . 42
4.2 Introduction . . . 42
4.3 Definitions . . . 42
4.3.1 Strain and curvature rates . . . 42
4.3.2 Plasticity framework . . . 44
4.3.3 Stresses and couple-stresses . . . 44
4.3.4 Breakage state variable . . . 45
4.4 Upscaling procedures . . . 46
4.4.1 Elastic upscaling . . . 46
4.4.2 Inertial upscaling . . . 48
4.4.3 Limit values . . . 49
4.5 Constitutive model . . . 50
4.5.1 Thermodynamic considerations . . . 50
4.5.2 Dissipation . . . 51
4.5.3 Elasticity . . . 52
4.5.4 Plastic multiplier . . . 53
4.5.5 Incremental constitutive response . . . 54
4.5.6 Invariants . . . 54
4.6 Model calibration . . . 57
4.6.1 Cosserat stiffness relationships . . . 57
4.6.2 Experimental methods . . . 58
4.7 Conclusion . . . 59

5 Numerical applications **60**
5.1 Summary . . . 60
5.2 Introduction . . . 60
5.3 Methods . . . 60
5.3.1 Linear stability analysis . . . 61
5.3.2 Finite element method . . . 63
5.4 Parameter values . . . 64
5.4.1 Calibrated values . . . 64
5.4.2 Sensitivity analyses . . . 64
5.5 Load conditions . . . 64
5.5.1 Constant volume shearing . . . 65
5.6 Discussion . . . 77
5.6.1 Constant volume shearing . . . 78
5.6.2 Constant confining stress shearing . . . 80
5.6.3 Œdometric compression . . . 80
5.6.4 Biaxial compression . . . 81
5.7 Conclusion . . . 81

6 Conclusions and Perspectives **83**
6.1 Conclusions . . . 83
6.2 Perspectives . . . 84

Bibliography **87**

Acknowledgements **103**

Financing **104**

Appendix A Fast Fourier transform algorithm **106**

Appendix B Orthogonal distance regression algorithm **107**

Appendix C Image moment algorithm **108**

Appendix D Data robustness **109**

Appendix E Savitzky-Golay smoothing algorithm **110**

Appendix F Numerical differentiation **111**

Appendix G Convergence analysis **112**

Appendix H Constant confining stress shearing **114**
H.1 Linear stability analysis 114

Appendix I Œdometric compression **120**
I.1 Linear stability analysis 120

Appendix J Biaxial compression **123**
J.1 Linear stability analysis 124

List of Figures

1.1 A figure illustrating the conceptual approach we take to this thesis. The central illustration highlights the phenomenon we will explore, namely the formation of band structures in crushable granular media, seen here in an image modified from Sulem and Ouffroukh (2006). Our exploratory methods are experiments, theory and numerical computations, each of which informs the next method in a cycle of scientific discovery. We embed this representation within a schematic of the *Appareil Cisaillement Simple Annulaire*, an experimental device we will make substantial use of in this thesis. 2

2.1 The three fundamental types of localisation bands (Du Bernard et al., 2002). 4
2.2 Pure (PCB) and shear-enhanced compaction (SCB) in the Aztec sandstone, from Eichhubl et al. (2010). The relatively planar nature of the shear enhanced bands can be clearly contrasted with the wavy formation of the purely compactive bands. 6
2.3 Dilation band visible in darker blue, with host rock in lighter blue surrounding it (Du Bernard et al., 2002). 7
2.4 A photo of the fault core of the Punchbowl fault (Chester and Chester, 1998). 8
2.5 Cataclastic shear band with thin sections impregnated with epoxy resin (Rotevatn et al., 2008). The dramatic reduction in grain size is clearly visible. 9
2.6 Principal slip zone (PSZ) with hanging wall (HW) and foot wall (FW) of a fault in carbonate rock (Collettini et al., 2014). 9
2.7 A series of compaction bands formed in Bentheim sandstone subjected to triaxial compression at a confinement of 300 MPa (Baud et al., 2004). Clearly visible is the formation of bands initially at the top and bottom of the specimen, propagating towards the centre in the form of multiple thin bands. . 10
2.8 A close-up image of an individual compaction band (Wong and Baud, 2012). The relatively dark band exhibits clear evidence of extensive grain crushing and porosity reduction. 11
2.9 The macroscopic effect of compaction bands, with oscillations in the stress-strain curve of a Bentheim sandstone strongly correlated with peaks in the acoustic emissions data (Baud et al., 2004). 11
2.10 Shear bands in Fontainebleau sandstone (El Bied et al., 2002). On the left the sample was confined at 7 MPa then sheared, on the right the sample was saturated and confined at 28 MPa then sheared. Respective magnifications are 38 and 30×. 12
2.11 A drainage channel formed in a shear band during an undrained test on Fontainebleau sandstone confined at 50 MPa (Sulem and Ouffroukh, 2006). 13
2.12 The grain rotations observed using X-ray μCT (Hall et al., 2010). The rotations are much more intense in the shear band compared to the rest of the sample. 13
2.13 A sketch of the ACSA apparatus (Chambon and Schmittbuhl, 2002). RC indicates the roughened inner cylinder that rotates, GS the granular sample, NJ the encasing neoprene jacket pressurised by the water cell CC. A glass window W allows visual inspection of ≈80% of the sample, including the interface layer IL. 14
2.14 A view of the sample mounted in ACSA (Chambon and Schmittbuhl, 2002). RC is the cylinder, IL the interface layer (i.e. the cataclastic shear band) and BU the bulk of the sample. 15
2.15 The Cosserat continuum concept (Cosserat and Cosserat, 1909). 17

2.16 The Glarus thrust showing the sharp boundary at kilometre scale, the metre wide fault core and the centimetre wide principal slip zone (Poulet et al., 2014a). This level of displacement can be explained by coupled multiphysical models. 18
2.17 The effect of introducing thermo-hydro-mechanical couplings allows a rate-independent elastic-perfectly plastic model to reproduce rate-dependent effects at seismic slip rate without introducing spurious viscosity at low strain rates (Rattez et al., 2018c). 18
2.18 The definition of the Breakage internal variable as the ratio of the dark grey area to the striped area. The current and ultimate grain size distributions are indicated on the figure, while the initial distribution is indicated by the vertical line at the far right of the figure. This initial distribution indicates that all the particles were initially of size d_{Max}. The figure is taken from Buscarnera and Einav (2012), after a concept first discussed in Einav (2007a). 20
2.19 A yield surface in $p - q - B$ space, from Einav (2007d). 20

3.1 A photo of the ACSA in open-face mode, without any sample mounted, and the various parts annotated. 25
3.2 An example of rods (in this picture exclusively 10 mm rods) placed in a mould. 26
3.3 A schematic of the ACSA and the appropriate boundary conditions. The inner solid black line indicates the inner boundary, while the dotted black line indicates the outer edge of the teeth. We apply an initial confining pressure p uniformly to the outer boundary, and then commence shearing at a rate v at the inner wall. 27
3.4 Three images showing the different materials. (a) is the material used in Set 1, (b) the material used in Set 2 and (c) the material used in Set 3. 27
3.5 The original image in colour. 28
3.6 The image transformed to greyscale with redundant information cropped. 29
3.7 An illustration of the selected pixels lying along the arc. In (a) the entire region is visible. We highlight two points, A and B for later reference. In (b) we show a close-up, demonstrating that the arcs are sufficiently finely spaced to allow sub-grain resolution. 29
3.8 A spatio-temporal plot showing the continuity of the behaviour over time. Each column of pixels represents a five second time increment. Each row of pixels represents the same point in space, covering a region of 0.021 mm width. We label A and B the rows of pixels corresponding to the points A and B in Figure 3.7. 30
3.9 An image of the two dimensional fast Fourier transform after being appropriately phase-shifted and re-scaled for visualisation. The phase shifting (by half the image size) moves the low-frequency signal content to the centre of the image, while the re-scaling increases the contrast level. The horizontal axis is the frequency component of the pattern lying along the horizontal axis of the spatio-temporal plot, and the vertical axis is the frequency component of the pattern lying along the vertical axis of the spatio-temporal plot. 31
3.10 An illustration of the conceptual difference between classical linear and orthogonal distance regressions, for some arbitrary data. The classical linear regression is illustrated in (a), where we try to minimise the residuals (dotted blue lines) between the data points (black dots) and the regression line (black line) based on vertical distance. The orthogonal distance regression is illustrated in (b), where we try to minimise the residuals between the data points and regression line based on the orthogonal distance between the points and the line. 32
3.11 An illustration of the image moment concept, for some arbitrary data. The blue ellipse has the same set of image moments as the set of data points in black. In this particular instance the ellipse's major axis captures a region larger than the full extent of the data, while the minor axis excludes some data points. For the purposes of our velocity measurement, we are concerned only with the orientation of the ellipse relative to the signal we observe in the FFTs. 32

3.12 Un-normalised velocity in terms of pixels, with inset highlighting the region that we examine to pick the point at which the velocity begins to consistently decline rather than fluctuate about a relatively constant value. The inset is zoomed in on the region of interest in which we select the normalisation point, which we highlight in black. For the sake of clarity, we show only the velocity determined using the method of image moments. The data we show is taken from the first test of Set 1. 33
3.13 Normalised velocities for each experiment. The (a) column shows the experiments in Set 1, the (b) column the experiments in Set 2 and the (c) column the experiments in Set 3. $(.1, .2, .3)$ indicate the first, second and third experiments in the set respectively. The normalisation point for each experiment is picked separately, and only the normalised radial distance containing interesting information is presented (for each experiment there is a large section of the apparatus with no velocity, which we exclude). Each column represents a set of experiments with the same material, with the mass percentage for each material shown in the fourth figure of the column. The envelopes in rows 1-3 are the minimum and maximum velocities over each of the 20 FFTs we perform on a given spatio-temporal plot. 34
3.14 (a) The means of all three velocity distributions of each set of experiments, calculated using the method of image moments. (b) The means calculated using orthogonal distance regression. The envelopes are the minimum and maximum values from each of the three experiments done with the same material. . 35
3.15 The results of the Savitzky-Golay smoothing algorithm after being applied to the normalised velocity distributions. The velocities have been renormalised so that the mean velocities once more pass through (1,1). The envelopes included are the smoothed envelopes of the minima and maxima in Figure 3.13, renormalised by the mean velocity. The average particle size (which is also the width of the smoothing window) is included on plot (a.1) for reference. 36
3.16 The results of the Savitzky-Golay smoothing algorithm after being applied to the mean normalised velocity distributions after the measurements inside the teeth have been discarded and renormalised. (a) are calculated using the method of image moments, and (b) are calculated with the orthogonal distance regression. 37
3.17 The absolute values of the (normalised) Cauchy shear strain rate $\dot{\varepsilon}_{r\theta}$. (a-c) are for the experiments with $x_r = 6$ mm,(d-f) are for those with $x_r = 8$ mm and (g-i) are for those with $x_r = 10$ mm. 38
3.18 The strain rates calculated from the mean normalised velocity distribution. (a) The strain rates from the velocities calculated using the method of image moments, and (b) The strain rates from the velocities calculated using the ODR method. 39

4.1 A plot showing the definition of the breakage variable B as the ratio of two grading areas. $F_0(x), F_u(x)$ and $F(x)$ are the initial, ultimate and current cumulative GSDs respectively. d_{min} and d_{Max} are the minimum and maximum grain sizes present in the GSDs. 45
4.2 The three plots of (a) θ_γ, (b) θ_κ and (c) θ_I all present qualitatively the same behaviour as a function of d_{min}/d_{Max} and α. The insets are the respective plots holding $d_{min}/d_{Max} = 10^{-3}$ and varying α between 2 and 3. 50

5.1 A typical example of the behaviour of the Lyapunov exponent s versus the perturbation wavelength Λ: (a) before a bifurcation has occurred, and (b) after a bifurcation has occurred, with the points defining Λ_{min} and Λ_{max} highlighted. 62
5.2 A schematic of the system that we consider. We apply a total displacement of Δu_1 in the x_1 direction that acts as a pre-confinement, marked in blue. We then start our test at $t = 0$ and apply a displacement Δu_2 in the x_2 direction to induce shearing, marked in red. During shearing we maintain constant volume (no further Δu_1 is applied). The system is invariant in the x_3 direction. 65
5.3 The regions of the yield surface that can in principle support localisation parallel to the shear direction when sheared under constant volume conditions, using the calibrated values of the material parameters. The analysis is performed for $B = 0, 0.1, \ldots, 0.9$, with the corresponding yield surfaces above. 66

5.4 The system behaviour at constant volume with increasing shear strain. (a) The shear stress τ_{21}, and (b) the minimum wavelength for perturbation growth Λ_{min} and the fastest growing wavelength Λ_{max}. Both wavelengths have been normalised by the largest grain size d_{Max}. We place a marker on the minimum value of Λ_{max} for clarity. We will later use this value in sizing our FEM system. 67
5.5 A comparison of the $p-q$ points that lie on the initial yield surface for $B = 0$, and for $B = 0.217$ (corresponding to $\gamma_{21} = 0.2$), with the load path of the curve in Figure 5.4. 67
5.6 The system behaviour at constant volume with increasing shear strain, for six different values of maximum grain size d_{Max}. (a) The shear stress τ_{21}, and (b) the fastest growing wavelength Λ_{max}. The wavelengths have been normalised by the internal length scale of the respective material. Each of these curves were confined to the same initial γ^e_{11} before shearing commenced. A marker is placed on the minimum values of Λ_{max} for clarity. 68
5.7 The system behaviour at constant volume with increasing shear strain, for four different initial values of B. (a) The shear stress τ_{21}, (b) the fastest growing wavelength Λ_{max} normalised by d_{Max}, (c) Λ_{max} normalised by the respective initial values of d_{50}, (d) Λ_{max} normalised by the respective values of d_{50} as they evolve, (e) Λ_{max} normalised by the respective initial values of ℓ^e, and (f) Λ_{max} normalised by the respective values of ℓ^e as they evolve. Each of these curves were confined to the same initial γ^e_{11} before shearing commenced. A marker is placed on the minimum values of Λ_{max} for clarity. 69
5.8 The regions of the yield surface that can in principle support localisation parallel to the shear direction when sheared under constant volume conditions, for (a) $\omega = 0°$, (b) $\omega = 45°$, and (c) $\omega = 90°$. The analysis is once again performed for $B = 0, 0.1, \ldots, 0.9$, with the corresponding yield surfaces shown above. 70
5.9 The system behaviour at constant volume with increasing shear strain, for four different values of ω. (a) The shear stress τ_{21}, and (b) the fastest growing wavelength Λ_{max}. The wavelengths have been normalised by the largest grain size d_{Max}. 70
5.10 The total value of B, plotted over the spatial coordinate normalised by the reference grain size x_r, for the calibrated parameter values. The increment between each curve is kept constant ($\Delta\gamma_{21} = 0.035$). . 72
5.11 The macroscopic response of the finite element system relative to the response of a single element submitted to the same strains for the calibrated parameter values. We plot the average values over the entire FEM system of (a) $\bar{q}$, (b) $\bar{p}$, (c) $\bar{\tau}_{21}$, and (d) $\bar{y}_{mix}$, against the value of $\bar{\gamma}_{21}$, once again averaged over the entire system. 72
5.12 The evolution of B for (a) initial $B = 0.3$, with increments of homogeneous strain between the lines being $\Delta\gamma^h_{21} = 0.02$, and (b) initial $B = 0.6$, with increments of homogeneous strain between the lines being $\Delta\gamma^h_{21} = 0.02$. 73
5.13 The macroscopic average stress response $\bar{\tau}_{21}$ of the finite element system relative to the response of a single element submitted to the same strains for (a) $B_0 = 0$, (b) $B_0 = 0.3$, (c) $B_0 = 0.6$ and (d) $B_0 = 0.7$. 74
5.14 The evolution of B for: (a) $\omega = 0°$, with increments of homogeneous strain between the blue lines being $\Delta\gamma^h_{21} = 0.0076$, between the black lines $\Delta\gamma^h_{21} = 0.0036$, and between the red lines $\Delta\gamma^h_{21} = 0.1888$, (b) $\omega = 20°$, with increments of homogeneous strain between the blue lines being $\Delta\gamma^h_{21} = 0.006$, between the black lines $\Delta\gamma^h_{21} = 0.0005$, and between the red lines $\Delta\gamma^h_{21} = 0.1935$, (c) $\omega = 45°$, with increments of homogeneous strain between the blue lines being $\Delta\gamma^h_{21} = 0.0077$, between the black lines $\Delta\gamma^h_{21} = 0.0022$, and between the red lines $\Delta\gamma^h_{21} = 0.1901$. (d) The evolution of γ^p_{21} for $\omega = 90°$, with increments of homogeneous strain between the blue lines being $\Delta\gamma^h_{21} = 0.0329$. 75

5.15 The evolution of $\dot{B}$ for (a) $\omega = 0°$, with the blue curve at a homogeneous strain level of $\gamma_{21}^h = 0.0620$, the black curve at a homogeneous strain level of $\gamma_{21}^h = 0.0792$, and the red curve at a homogeneous strain level of $\gamma_{21}^h = 0.8669$, (b) $\omega = 20°$, with the blue curve at a homogeneous strain level of $\gamma_{21}^h = 0.05298$, the black curve at a homogeneous strain level of $\gamma_{21}^h = 0.0615$, and the red curve at a homogeneous strain level of $\gamma_{21}^h = 0.2570$, (c) $\omega = 45°$, with the blue curve at a homogeneous strain level of $\gamma_{21}^h = 0.0486$, the black curve at a homogeneous strain level of $\gamma_{21}^h = 0.0946$, and the red curve at a homogeneous strain level of $\gamma_{21}^h = 0.2307$, (d) $\omega = 90°$, with the blue curve at a homogeneous strain level of $\gamma_{21}^h = 0.0657$. . 76
5.16 The macroscopic average stress response $\bar{\tau}_{21}$ of the finite element system relative to the response of a single element submitted to the same strains for (a) $\omega = 0°$, (b) $\omega = 20°$, (c) $\omega = 45°$ and (d) $\omega = 90°$. 77
5.17 An image of two ultra-cataclastic zones sandwiching a cataclastic zone, from Nicchio et al. (2018). The zone boundaries are highlighted in yellow. 79

G.1 We plot the value of the shearing stress τ_{21} at the boundary against the homogeneous strain γ_{21}^h for a variety of total system heights. 112
G.2 We plot the value of the shearing stress τ_{21} at the boundary against the homogeneous strain γ_{21}^h for two different numbers of elements. 113

H.1 A schematic of the system that we consider. We apply a constant confining stress τ_{11} in the x_1 direction that acts as a pre-confinement, marked in blue. We then start our test at $t = 0$ and apply a displacement Δu_2 in the x_2 direction to induce shearing, marked in red. During shearing we maintain a constant value of τ_{11}. The system is invariant in the x_3 direction. 114
H.2 The regions of the yield surface that can in principle support localisation when sheared under constant confining stress, using the calibrated values of the material parameters. The analysis is performed for $B = 0, 0.1, \ldots, 0.9$, with the corresponding yield surfaces above. 115
H.3 (a) The shear stress τ_{21} against the total shear strain γ_{21} under constant confining stress $\tau_{11} = 208.3$ MPa. (b) The minimum wavelength for perturbation growth Λ_{min}, and the fastest growing wavelength Λ_{max} against the total shear strain γ_{21}. Both wavelengths have been normalised by the maximum grain size d_{Max}. (c) The system evolution in $p - q$ space. The initial value of q is non-zero because $\tau_{11} \neq \tau_{22/33}$. (d) The evolution of the angle β of the band relative to the shear plane. 115
H.4 Illustration of the band geometry with the definition of β. 116
H.5 (a) The shear stress τ_{21} against the total shear strain γ_{21} under constant confining stress $\tau_{11} = 208.3$ MPa, for three different initial values of B. (b) The fastest growing wavelength Λ_{max} against the total shear strain γ_{21} for three different initial values of B. The wavelengths have all been normalised by the largest grain size d_{Max}. (c) The deviatoric stress invariant q against the mean stress p. (d) The angle β of the fastest growing wavelength against the total shear strain γ_{21}. 117
H.6 The regions of the yield surface that can in principle support localisation when sheared under constant confining stress, for (a) $\omega = 0°$, (b) $\omega = 45°$, and (c) $\omega = 90°$. The analysis is once again performed for $B = 0, 0.1, \ldots, 0.9$. 118
H.7 (a) The shear stress τ_{21} against the total shear strain γ_{21} under constant confining stress $\tau_{11} = 208.3$ MPa, for three different values of ω. (b) The fastest growing wavelength Λ_{max} against the total shear strain γ_{21} for three different initial values of B. The wavelengths have all been normalised by the largest grain size d_{Max}. (c) The deviatoric stress invariant q against the mean stress p. (d) The angle β of the fastest growing wavelength against the total shear strain γ_{21}. 118

I.1 A schematic of the system that we consider. We first apply an isotropic pre-confinement $p = \tau_{11} = \tau_{22}$, and then start our test by applying a displacement Δu_1 in the x_1 direction, while disallowing displacements in the other two directions. The conditions imposed in the x_3 direction are identical to those imposed in the x_2 directions. 120

I.2 The regions of the yield surface that can in principle support localisation perpendicular to the compaction direction when compacted under œdometric conditions, using the calibrated values of the material parameters. The analysis is performed for $B = 0, 0.1, \ldots, 0.9$, with the corresponding yield surfaces above. 121
I.3 The regions of the yield surface that can in principle support localisation normal to the compression direction when compacted under œdometric conditions, for (a) $\omega = 0°$, (b) $\omega = 45°$, and (c) $\omega = 90°$. The analysis is once again performed for $B = 0, 0.1, \ldots, 0.9$, with the corresponding yield surfaces above. 122
I.4 The regions of the yield surface that can in principle support localisation normal to the compression direction when compacted under œdometric conditions, for (a) $x_r = 0.01$ mm, (b) $x_r = 0.1$ mm, and (c) $x_r = 1$ mm. The analysis is performed for $B = 0, 0.1, \ldots, 0.6$, with the corresponding yield surfaces above. 122

J.1 A schematic of the system that we consider. We apply a pre-confinement of τ_{11} in the x_1 direction and τ_{22} in the x_2 direction, marked in blue, with $\tau_{11} = \tau_{22}$. We then start our test at $t = 0$ by applying a displacement Δu_1 in the x_1 direction, marked in red. We hold the value of τ_{22} constant during the test. The system is invariant in the x_3 direction. 123
J.2 (a) The deviatoric stress invariant q against the total compressive strain γ_{11} under biaxial conditions. (b) The minimum wavelength for perturbation growth Λ_{min}, and the fastest growing wavelength Λ_{max} against the total compressive strain γ_{11}. Both wavelengths have been normalised by the largest grain size d_{Max}. We place a marker on the minimum value of Λ_{max} for clarity. (c) The system evolution in $p - q$ space. (d) The evolution of the angle of the band relative to the $x_2 - x_3$ plane. 124
J.3 Illustration of the band geometry with the definition of β. 124
J.4 (a) The deviatoric stress invariant q against the total compressive strain γ_{11} under biaxial conditions. (b) The fastest growing wavelength Λ_{max} against the total compressive strain γ_{11}, normalised by the largest grain size d_{Max}. We place a marker on the minimum value of each curve for clarity. (c) The system evolution in $p - q$ space. (d) The evolution of the angle of the band relative to the $x_2 - x_3$ plane. 125
J.5 (a) The deviatoric stress invariant q against the total compressive strain γ_{11} under biaxial conditions. (b) The fastest growing wavelength Λ_{max} against the total compressive strain γ_{11}, normalised by the largest grain size d_{Max}. We place a marker on the minimum value of the curve for clarity. (c) The system evolution in $p - q$ space. (d) The evolution of the angle of the band relative to the $x_2 - x_3$ plane. 126

List of Tables

3.1 The weights for the different size fractions in each of the three sets of experiments. All three experiments have the same mean grain size by weight (4.2 mm), but different largest grain sizes. 27

4.1 Values of the coefficients for stress and plastic strain rate invariants in a Cosserat continuum made consistent with Breakage Mechanics 56

5.1 List of material constants. 64

Chapter 1

Introduction

Granular media are pervasive throughout nature, and something that everyone interacts with in some way, every single day. From a morning bowl of cereal, to the asphalt underfoot when crossing the road, granular media are absolutely impossible to ignore. Perhaps surprisingly, for something so widely-spread, the behaviour of these media are relatively poorly understood, and there is a large global scientific community including (but certainly not limited to) engineers, physicists, mathematicians, geologists, computer scientists and biologists working to progress our understanding of how they behave. Such a wide and diverse community expressing their interest in this topic is indicative that understanding granular media is not merely an abstract academic exercise, but something that has real-world implications. Indeed, if we restrict ourselves to consider *only* the intersection of civil engineering and granular media, we are still left with some of the most pressing challenges in the world. Many sedimentary rocks are composed of collections of distinct grains that have been gradually cemented together over time, making them a classic example of a granular material. Sydney itself is underlain by a strong sandstone formed in the Triassic period, meaning that every building in the city relies on engineers being able to able to model the deformation of a granular medium under external loads to at least tolerable accuracy. Even in the event that we find ourselves in a city lying on rock that would not be considered a granular material, for example Paris, which is underlain by limestone, we still cannot escape the influence of granular media. Concrete, the world's most popular construction material is yet another example of a granular medium, being composed of both grains of sand and aggregate, joined together into an artificial rock by cement.

Simply by improving our understanding of granular media, we could design more efficient structures that better utilise one of the world's most carbon-intensive materials, and thus make a not-insignificant contribution to climate change mitigation efforts. Improving our understanding of granular media does not just have an impact on designed structures. Inevitably, society must interact with geological phenomena that for the time being, are well beyond our control. Some of the most prominent examples of these are immensely destructive phenomena such as earthquakes and landslides, which we cannot yet accurately model or predict. At a less destructive, but nonetheless societally consequential level, the formation and internal structure of subsurface reservoirs for both water and hydrocarbons, has important implications for where, how, and how much of a resource can be extracted.

An interesting and important feature of each of the aforementioned examples is that we may observe the formation of narrow bands where the grains have undergone extensive crushing. Using a wide variety of evidence gathered from field observations, experiments, numerical simulations, and theoretical models, workers in granular media, particularly those concerned with geological band structures, have come to the conclusion that these structures exercise an important effect in controlling the overall behaviour of the systems of which they form a part.

It is a a consistent feature of physical systems that the behaviours at larger scales are controlled by the smallest elements, in what is labelled emergent behaviour. Indeed, the large-scale structure of the universe has been attributed by physicists to the properties of the smallest sub-atomic particles in the first moments after the Big Bang. This general pattern of emergent behaviour is as applicable to geomaterials as to any other system studied by scientists. While

in principle we could derive laws for the behaviour of granular media from Quantum Electro-Dynamics, this would be a rather tedious exercise for no conceivable benefit. The typical approach when we develop models for materials is to rely on "scale separation". The essence of scale separation is that provided the system that we are modelling is sufficiently larger (i.e. by several orders of magnitude) than its constitutive elements, the elements themselves need not be modelled and their emergent behaviours can be taken as properties of the system. As an example of this principle, if we were to model a steel beam, we would use attributes like stiffness or strength which arise directly as emergent phenomena from the atomic lattice and crystal structure, remaining tranquil in the knowledge that the behaviour of the beam will be precisely captured without needing to concern ourselves with exactly how the atomic spacing changes or whether carbon is more intensely concentrated at crystal boundaries.

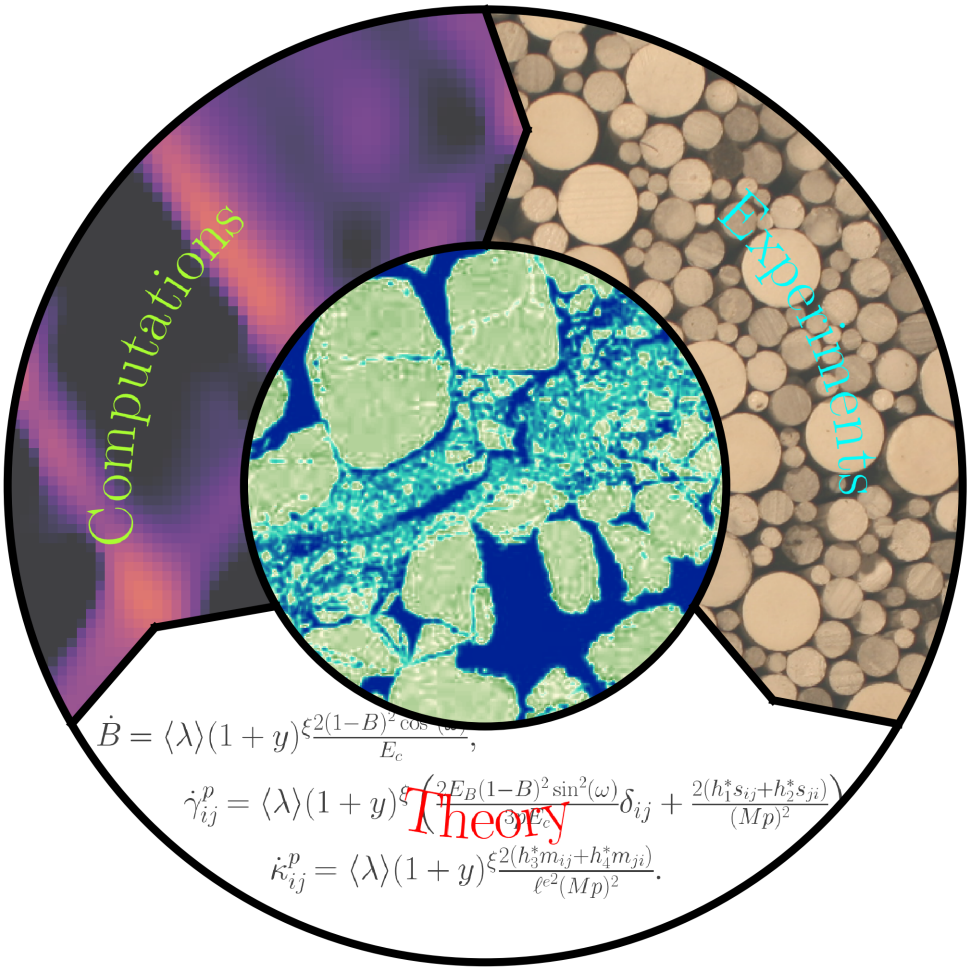

Figure 1.1: A figure illustrating the conceptual approach we take to this thesis. The central illustration highlights the phenomenon we will explore, namely the formation of band structures in crushable granular media, seen here in an image modified from Sulem and Ouffroukh (2006). Our exploratory methods are experiments, theory and numerical computations, each of which informs the next method in a cycle of scientific discovery. We embed this representation within a schematic of the *Appareil Cisaillement Simple Annulaire*, an experimental device we will make substantial use of in this thesis.

However, unlike many other systems, the modelling of granular media suffers from intractable problems of *lack of* scale-separation. Properties of constituent grains such as size, chemical composition or surface roughness all matter for the behaviour of the system. This reliance on the nature of the grains would not necessarily present a problem, if the underlying grains were not being changed by the physical processes that we wish to explore. In particular, the crushing of grains has dramatic effects on a range of physical properties of the system, such as its stiffness, the ease with which

fluids flow through it or the rate at which chemical reactions can happen. In particular, all of these properties have important roles to play when attempting to model the bands in geological structures that we previously mentioned. As these bands are typically only on the order of ten to one hundred times bigger than their constituent grains, there is a very intense feedback loop from changes in the grains, which causes changes in their emergent properties, in turn causing changes in the overall system which induce further changes in the grains. This breakdown of the scale-separation principle poses difficult problems for us in attempting to model granular media, which is part of what leads to it being such a rich and interesting field of study.

Since the 1970s, a variety of sophisticated and powerful techniques have been developed that allow the modelling of granular media as a system, while attempting to account for the underlying grains themselves in some systematic way. Broadly speaking, these developments fall within the field of "higher-order continua", where by adding additional complexity to the *mathematical structure* of our models, we may account for additional complexity in the *physical reality* that we are trying to understand. A pioneer in extending these techniques to geomechanics, i.e. the intersection of granular media, civil engineering and geology, is Ioannis Vardoulakis. This thesis lies squarely within the tradition developed by Vardoulakis and his coworkers. In particular, he exploited and refined a conceptual framework known as the Cosserat continuum that adds complexity by including particle rotations within the model, and we will make extensive use of this continuum in this thesis.

While the application of the Cosserat continuum in geomechanics has been steadily refined over time, the models arising out of this tradition have taken the size of the grains and their corresponding emergent properties as fixed-in-time system parameters. This approach has been sufficient to develop models that can quite accurately predict band formation in certain systems, but in systems where grains can extensively crush, the limitations of this approach become evident. Hence, the core aim of this thesis is to develop a Cosserat model of a granular system that takes into account the size of the underlying grains, *as well as how the size of those grains evolve over time.* In order to build this model we use the theory of Breakage Mechanics, that accounts for and predicts grain crushing, and we expand the theory to account for Cosserat effects. There is much that we still do not understand about the interaction of the grains with the band, for example whether the presence of a wide range of grain sizes (i.e. the polydispersity) matters for the overall behaviour. As such the development of experimental techniques that we can use to begin to answer questions such as this is another important part of the thesis. It is also important to understand how grain size evolution and band formation interact with a variety of different conditions that may represent standard laboratory tests from which engineers infer information for design, or conditions that are encountered in geological structures. As such, applying our model to these conditions can give us insight into what we do understand about the underlying physics, and what we do not understand and need to include in future models. We illustrate this coupled experimental-theoretical-numerical approach to the research in Figure 1.1.

By conducting this research, we hope that we will make at least a small contribution towards solving some of the difficult and important problems that we have mentioned above.

This thesis is laid out as follows: In Chapter 2 we outline the current state of the art in terms of field and laboratory observations of band structures that we categorise as shear, compaction or dilation bands, higher order continuum theories that can be used to predict band formation, and material models that describe the evolution of crushable granular media. In Chapter 3 we present a set of experiments in an annular shear apparatus, in order to explore the effect of polydispersity of the grain size distribution on the thickness of shear bands. In Chapter 4, we outline an energetic upscaling procedure and develop a Cosserat Breakage Mechanics constitutive model that can predict band formation and thickness in crushable granular media. In Chapter 5, we implement the model numerically and analyse its performance in a variety of load conditions relevant to geomechanics. Finally, in Chapter 6 we present our conclusions and perspectives for future work.

Chapter 2

A review of localisation phenomena in granular geomaterials

2.1 Summary

In this chapter we present a review of the literature concerning localisation, in particular in brittle granular media such as sands and sandstones. The observations of localisation phenomena in the field and in a variety of laboratory tests give context to the study, provide insight into the underlying physical mechanisms and shape the development of modelling approaches. The mathematical theory of bifurcation is addressed in the context of geomechanics to provide a general framework that allows the prediction of localisations and the identification of key characteristics in models developed for this purpose. We review a range of constitutive models and their extensions and refinements, with a particular study of the Breakage Mechanics family of models. Finally we briefly outline some numerical techniques that will be exploited in the implementation of the model developed in this thesis.

2.2 Observations of localisation in geomaterials

Localisations in geomaterials occur as the formation of bands where deformation is concentrated. These bands have three underlying types: compaction, shear and dilation, illustrated in Figure 2.1. Combinations are possible (i.e. compaction and shear, or dilation and shear), and whether and what sort of band occurs is determined by the stress conditions and material state.

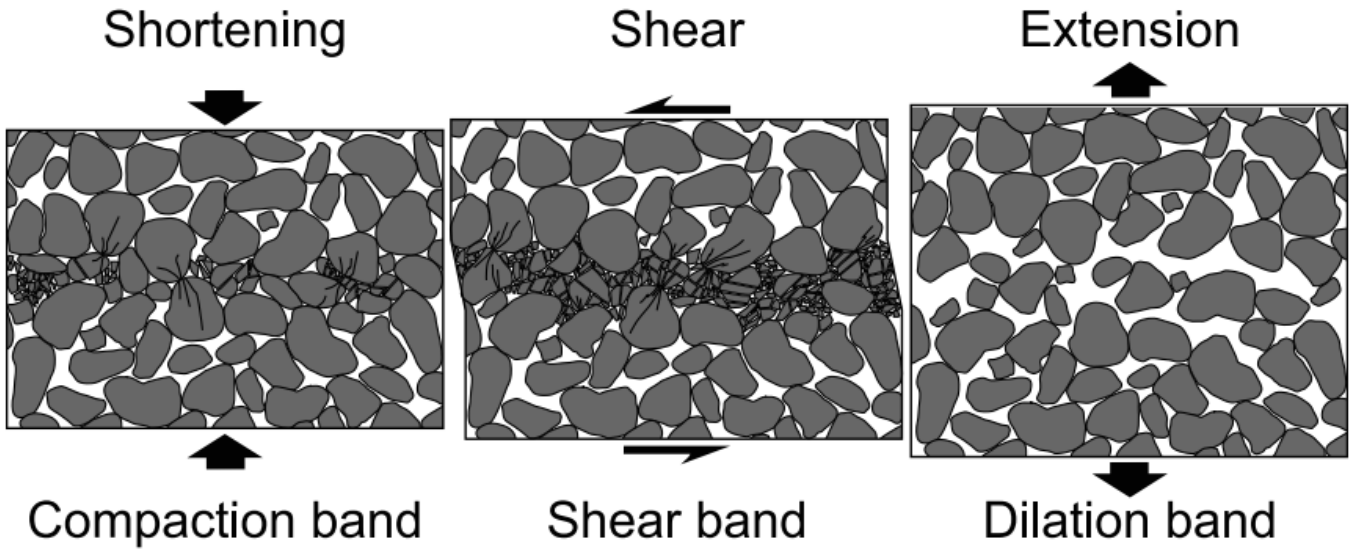

Figure 2.1: The three fundamental types of localisation bands (Du Bernard et al., 2002).

2.2.1 Field-scale observations

Compaction bands

The formation of pure compaction bands (that is to say, bands where there is no or negligible shear present) appears to be quite rare in nature, until recently being attested in the literature only in two major areas in the south-western United States, Buckskin Gulch and the Valley of Fire State Park. Both of these sites consist of Jurassic æolian sandstones, denoted the Navajo and Aztec sandstones, respectively.

The presence of deformation bands in the Navajo sandstone was first reported by Aydin and Johnson (1978). They reported the presence of three classes of structures that they labelled "deformation bands" (single bands), "zones of deformation bands" (clusters of bands) and "slip surfaces" (surfaces of discontinuous displacement), by which deformation in the rock was preferentially accommodated. Importantly, they noted that the average grain size in the deformation bands was reduced by approximately an order of magnitude relative to the parent rock. The same authors later introduced the techniques of constitutive modelling to account for the development of deformation bands, and also distinguished between the *discontinuous* deformation of a "slip surface" and the continuous deformation in other deformation bands (Aydin and Johnson, 1983). The authors however do not distinguish between the different types of bands (namely compaction and shear in this context). Mollema and Antonellini (1996) provided a closer study of the compaction bands, which are characterised by an absence of in-plane shearing, reduction in volume, some fracturing of the constituent grains but very little crushing and comminution. The compaction bands they identified occurred in rock with grain sizes of 0.3-0.8 mm and porosities of 20-25%. They also identified "deformation band faults" which occurred in layers with grain sizes 0.05-0.25 mm and porosity of less than 20%. We recognise these structures as being shear bands (or shear-enhanced compaction bands), so we will adopt this terminology from hereon. They noted that compaction bands developed in the compressive quadrant at the tips of the shear bands, from which they inferred that the compaction bands form perpendicular to the largest compressive stresses, resulting in this case in bands at a high angle to the bedding planes. They also offered a simple crack-closing model to explain the presence of the compaction bands on a qualitative level. Review papers (Fossen et al., 2007) highlighted the different mechanisms of band formation (namely disaggregation, phyllosilicate, cataclastic and dissolution-cementation) and noted that the accumulation of clay within the compaction bands reduced porosity to 10% or less and preferentially cemented them relative to the surrounding sandstone, explaining the higher resistance of the compaction bands to erosion (Holcomb et al., 2007). It has been argued that disaggregation bands formed by grain rearrangement occur at low confining pressures while cataclastic bands formed at greater depths (Beke et al., 2019; Fossen, 2010).

Parallel to the study of the Navajo sandstone, Hill (1990) extended the study of deformation banding in sandstones to the Aztec sandstone. The bands studied range from 0.5-2 cm thick, and some of them show sinuous but angular structures that result in a chevron pattern. These chevron-type formations appear significantly more frequently than the more conventional band-type structures. The deformation banding appeared in well-bedded sandstone, but not in structureless sandstone, from which we can infer that anisotropy may play a role in band formation, a conclusion later supported by other authors (Deng and Aydin, 2012). Aydin and Ahmadov (2009) confirmed that the porosities in the bands in the Aztec sandstone could be less than half that of the surrounding rock mass and the corresponding reduction in permeability could be of one order of magnitude. Their study was focused on compaction bands that are parallel-to-moderately-inclined (20°) to the bedding plane. Higher angle bands showed increasing indications of grain fracture and shearing behaviour. Eichhubl et al. (2010) reported the existence of shear-enhanced compaction bands in the Aztec sandstone (illustrated in Figure 2.2). They distinguished between shear-enhanced compaction bands, forming at $38 - 53°$ to the maximum compressive stress, and compactive shear bands that form at lower angles, and which accommodated much larger shear deformations. They noted that bedding-parallel compaction bands may be difficult to distinguish from the bedding planes themselves. Fossen et al. (2015) also found wiggley pure compaction bands, shear enhanced compaction bands in planes and cataclastic compactive shear bands that formed after the compaction bands based on their cross-cutting behaviour. A comparison of the structure of the compaction bands in the Aztec sandstone noted that the compaction bands are thinner near to their tips and the tip areas generally feature

a less homogeneous compaction (Torabi et al., 2015).

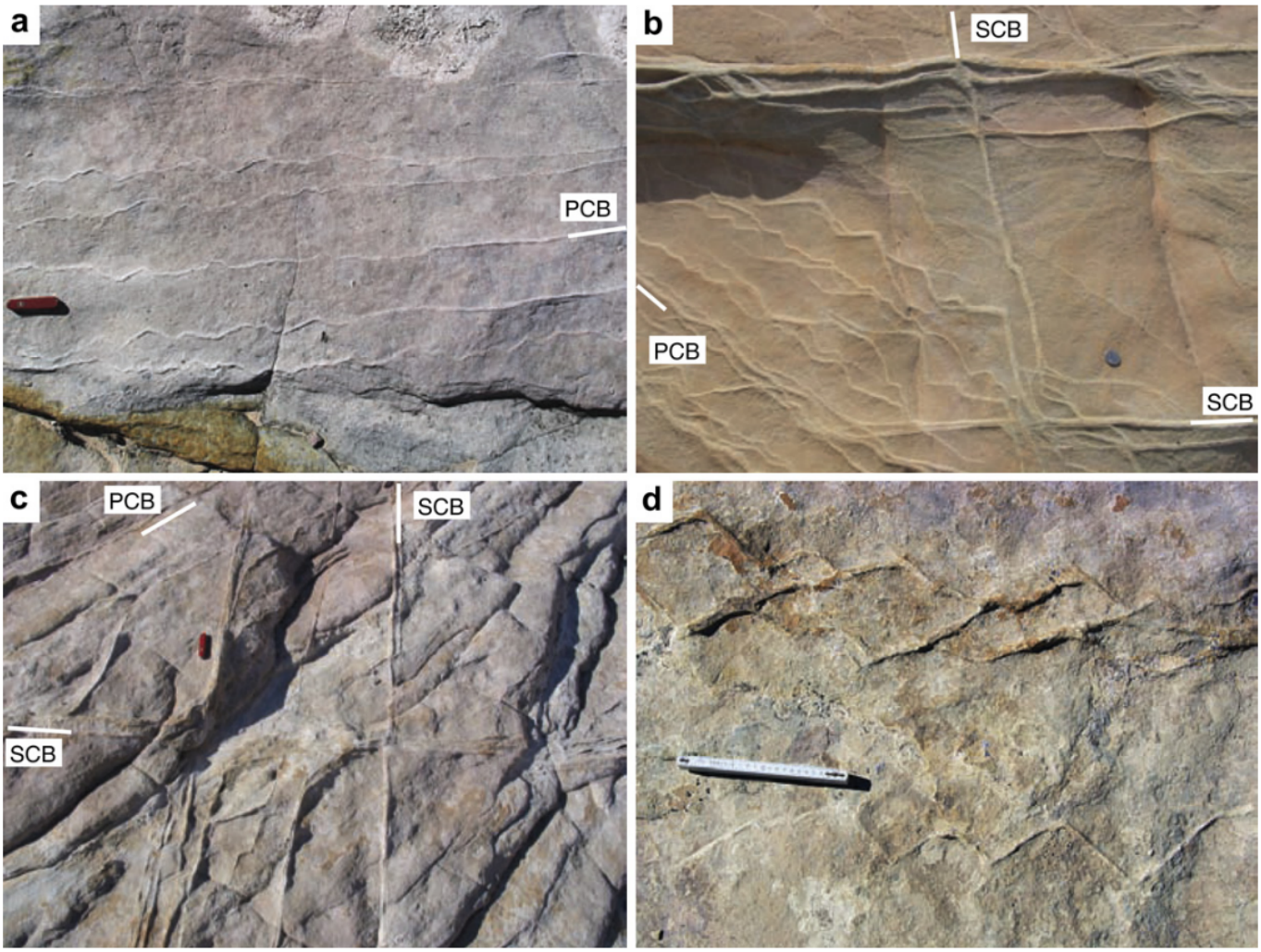

Figure 2.2: Pure (PCB) and shear-enhanced compaction (SCB) in the Aztec sandstone, from Eichhubl et al. (2010). The relatively planar nature of the shear enhanced bands can be clearly contrasted with the wavy formation of the purely compactive bands.

Geologists have also made use of models to try and infer the conditions of band formation. An anti-crack model (Schultz, 2009) has been used to predict band-normal compression stresses of 24-30 MPa for the Navajo sandstone and 31-62 MPa for the Aztec sandstone, and to infer that band formation was likely facilitated by a thrust faulting environment. Similar results have been derived using a form of Modified Cam-Clay constitutive law (Fossen et al., 2011; Schultz et al., 2010). Field geologists have argued that the bands formed in laboratory conditions formed at unrepresentative stress levels for field conditions, suggesting a different mechanism of formation (Fossen et al., 2011).

In recent years, compaction bands have been observed in Orange, France (Ballas et al., 2013), Ras il-Bajjada, Malta (Rotevatn et al., 2016), Cotiella and Tremp-Graus, Spain (Robert et al., 2018; Tavani et al., 2018), Makhtesh Katan, Israel (Gajst et al., 2018) and Shihtiping, Taiwan (Cavailhes and Rotevatn, 2018), all demonstrating dramatic porosity reduction in the band relative to the very porous host rock, and a substantial reduction in grain size.

Finally, we may conclude that in the field, pure compaction bands are rare structures that form at low levels of stress associated with shallow burials. Shear-enhanced compaction bands are comparatively more common and seem to form in similar conditions. Both band types consistently have reduced porosity relative to the surrounding rock mass, and may demonstrate moderate levels of cataclasis. The formation of these bands appears to rely on rock with high porosity and relatively large grain sizes.

Dilation bands

The formation of pure dilation bands in field conditions appears to be exceedingly rare. Du Bernard et al. (2002) described dilation bands in poorly consolidated sand near McKleyville in northern California, USA, and formed due to the action of a fault. The bands demonstrate no grain cataclasis and while the band's current porosity is 22%, the authors' upper limit on the porosity at formation is 38%. Dilation bands of approximately 1 mm thickness have subsequently been found in the Costa Rica décollement that were filled with a calcite cement (Vannucchi and Leoni, 2007). Dilation bands have also been found in core samples from the Vienna Basin in Austria. The bands demonstrate evidence of cataclasis during their formation, followed by the precipitation of a chemical cement that acts to reduce the porosity of the rock relative to the host rock (Exner et al., 2013; Lommatzsch et al., 2015).

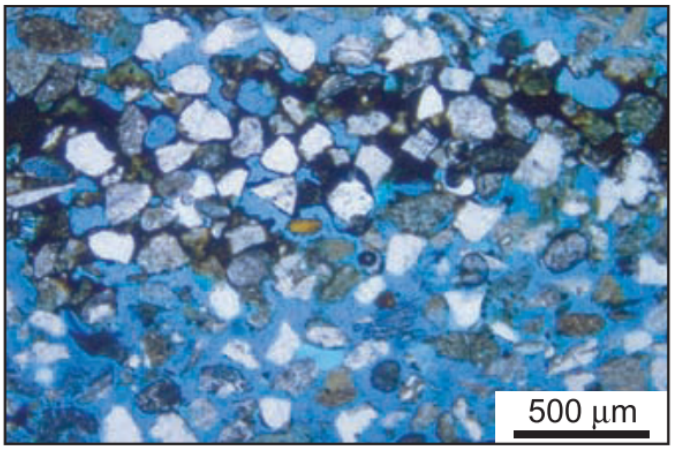

Figure 2.3: Dilation band visible in darker blue, with host rock in lighter blue surrounding it (Du Bernard et al., 2002).

Given the very limited observations of dilation bands all feature substantial cementation (as shown in Figure 2.3) that has acted to preserve the band structure, it is possible to imagine that dilation band formation, enhanced by shearing, may occur more frequently than their observation suggests, but they are subsequently "overwritten" by compaction before sufficient cementation has occurred to preserve them.

Shear bands

The most prominent example of shear band formation in the field is that which occurs during the faulting process. Geologists have examined faults both by observing the outcrops of exhumed faults, and also by drilling into active seismogenic faults and obtaining core samples.

Amongst the faults that geologists have drilled into are the San Andreas (Zoback et al., 2011, 1988), Nojima (Ando, 2001), Chelungpu (Heermance et al., 2003), Aigion (Cornet et al., 2004), Nankai Trough (Sakaguchi et al., 2011) and Longmenshan (Hou et al., 2012) fault systems. Geologists consistently find that faults act as flow barriers due to their dramatically reduced permeability (Cornet et al., 2004; Fisher and Knipe, 2001; Losh et al., 1999), and using a range of techniques are typically able to infer that the local maximum compressive strength is near perpendicular to the fault (Ando, 2001; Sulem, 2007; Zoback et al., 2011). Depending on the age of the fault and at what scale it is examined, they also find several different zones present, ranging from a damage zone on the scale of 10s of metres (Ando, 2001; Cornet et al., 2004; Vannucchi and Leoni, 2007; Zoback et al., 2011) to a core on the order of centimetres (Cornet et al., 2004; Heermance et al., 2003; Janssen et al., 2016; Vannucchi and Leoni, 2007) and a principal slip zone on the order of millimetres or less (Hou et al., 2012; Sulem, 2007; Vannucchi and Leoni, 2007) that features very fine particle sizes with evidence of grain fragmentation (Fisher and Knipe, 2001). Available evidence such as vitrinite reflectance suggests that the peak temperature due to shear heating was relatively low ($390 \pm 50°$) (Sakaguchi et al., 2011), a conclusion that is supported by the systematic absence of pseudotachylites in fault gouges (Einav et al., 2018).

While drilling into fault cores is a very useful scientific exercise and can elucidate a number of questions about the in-situ material state, it is also expensive and subject to the difficulties of removing the core intact without disturbing it. On the other hand, by examining faults and shear bands where they have been exhumed on the surface, a wider variety of conditions and formation mechanisms can be traced.

Consistently when exhumed fault gouges are examined by geologists in the field, they observe the formation of zones of cataclasis and ultra-cataclasis that accommodate a very large fraction of the displacement in the fault. A particularly important development was that advanced by Sammis et al. (1987), that observed a self-similar grain size distribution in the Lopez fault, with a fractal dimension of 2.6. They argued for a confined comminution model where the failure of the particles was dependent on the size of the neighbouring particles and the underlying failure mechanism of the grains was tensile fracture. The presence of a wide array of grain sizes in the fault core has been subsequently supported by analysis of a range of faults, including the Punchbowl (Chester and Chester, 1998) and McKinleyville (Cashman and Cashman, 2000) faults in California and the Median Tectonic Line (Wibberley and Shimamoto, 2002) in Japan. Both the Punchbowl fault and Median Tectonic Line occur where two different rock masses meet (illustrated in Figure 2.4), suggesting that the discontinuity surface between the two may generate favourable conditions for faulting. Faults exposed by intersection with mine shafts have shown that a few centimetres of ultra-cataclasite gouge can accommodate over 1 km of slip, and microstructural studies confirm that slip can further localise to the scale of millimetres (Sibson, 2003), although in general as the length of the fault increases the thickness of the principal slip zone, fault core and damage zone all increase (Shipton et al., 2006).

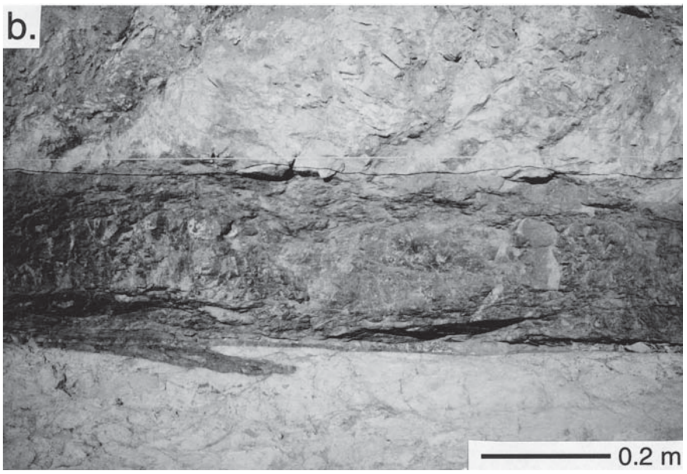

Figure 2.4: A photo of the fault core of the Punchbowl fault (Chester and Chester, 1998).

It should be noted that not all observed faults follow the grain size distribution that would be inferred from the confined comminution model. In instances where the favoured grain breakage mode is flaking and spalling, a higher proportion of relict grains is present (Exner and Tschegg, 2012; Rawling and Goodwin, 2003).

The formation of bands with significant grain cataclasis has been observed to dramatically decrease the permeability in layers of millimetric size with significantly reduced porosity (Exner and Tschegg, 2012; Griffiths et al., 2018; Lommatzsch et al., 2015; Rotevatn et al., 2016; Soliva et al., 2016; Zuluaga et al., 2014), particularly if there is additional cementation involved (Del Sole and Antonellini, 2019), but it is also possible that discrete slip surfaces form within the band (Rotevatn et al., 2008), as shown in Figure 2.5, which can have the effect of forming flow conduits (Torabi, 2014).

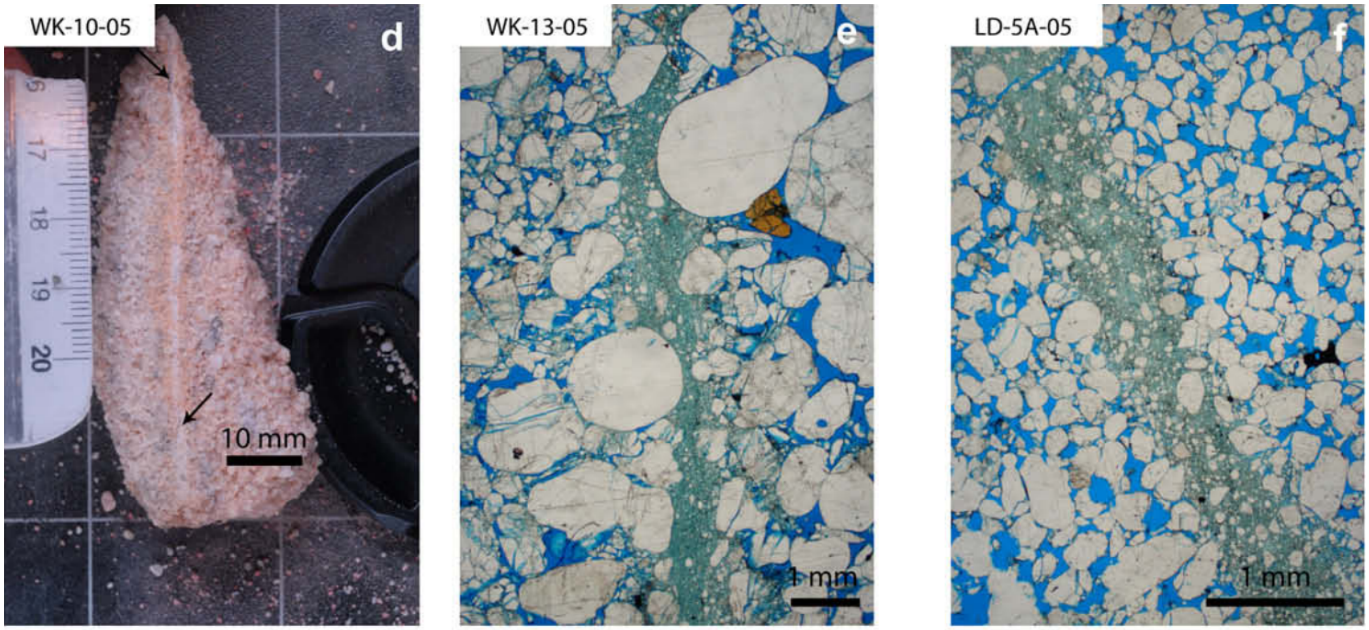

Figure 2.5: Cataclastic shear band with thin sections impregnated with epoxy resin (Rotevatn et al., 2008). The dramatic reduction in grain size is clearly visible.

As well as siliclastic rocks, faults with localised shear zones of intense cataclasis have been observed in calcium (De Paola et al., 2008) and carbonate (Collettini et al., 2014; Delle Piane et al., 2017; Ferraro et al., 2018, 2019) rich rocks. Carbonate rocks in particular are more prone to reactions at low burial depths, feature more fluid/rock interaction and favour a more ductile deformation mode. Nevertheless, cataclastic bands of between 300 μm and 2 cm have been observed in limestones (Collettini et al., 2014) (see Figure 2.6), and cataclastic behaviour has been observed in siliclastic rocks at shallow depth (Torabi, 2014).

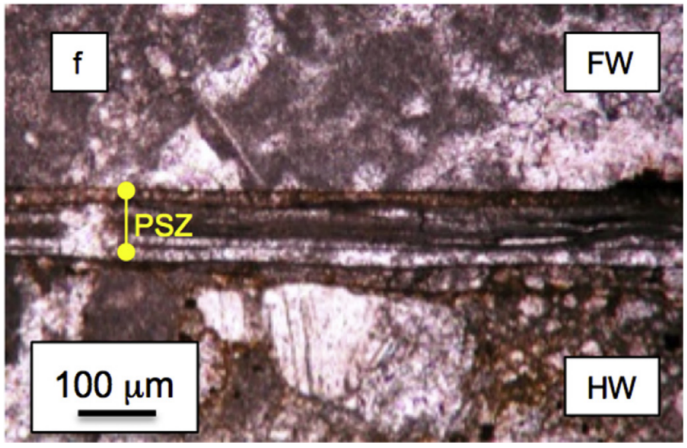

Figure 2.6: Principal slip zone (PSZ) with hanging wall (HW) and foot wall (FW) of a fault in carbonate rock (Collettini et al., 2014).

From a review of the literature, we can conclude that shear bands consistently exhibit grain cataclasis and a substantial reduction in porosity which reduces the permeability by orders of magnitude. Depending on burial conditions, fluid flow and chemical changes dependant on mineralogy, there may be substantial cementation post formation of the shear band.

2.2.2 Laboratory-scale observations

While the formation of localisation bands in the field is important to study, providing context to *why* it is desirable to model the formation of bands, as well as providing a history of the full evolution of the band, the sometimes

complex geological history can obscure the underlying mechanisms of band formation. In addition, there is significant evidence presented above indicating the coupled nature of the physical processes involved, in particular shear heating which affects fluid pressurisation and triggers chemical processes. In order to disentangle these effects and more closely control the mechanical values, experimental studies in the laboratory are extremely useful to understand the underlying physics, particularly when studying the initiation of the band formation.

Compaction bands

When studying the deformation of granular rocks, experimentalists typically make use of the triaxial apparatus in order to control the confining pressure. A number of studies conducted under pure isotropic confinement observed plasticity related to grain sliding, rotating and crushing without forming any localisation bands in Berea, Boise (Zhang et al., 1990a,b) and Bentheim (Schutjens et al., 1995) sandstones. In this context high confinement is a confining stress near to the value that initiates plasticity for a given sandstone.

In order to produce compaction bands, experimentalists consistently have to apply a high confining pressure before initiating triaxial shearing to generate compaction bands. This behaviour is observed in Castlegate (Dewers et al., 2017; Olsson, 1999; Olsson and Holcomb, 2000), Bentheim (Klein et al., 2001; Vajdova and Wong, 2003), Berea (Baud et al., 2004, 2006) and Bleurswiller (Heap et al., 2015; Tembe et al., 2008) sandstones. The exact pressure range in which compaction band formation is favoured and how wide the bands are is very dependent on the material tests (see Baud et al. (2004) for a comprehensive treatment).

Using acoustic emission (AE) techniques, the location of compaction band formation can be determined. The bands preferentially form either near the top or bottom of the sample (Olsson and Holcomb, 2000), a behaviour illustrated in Figure 2.7, or near notches (Stanchits et al., 2009; Vajdova and Wong, 2003) that have the effect of concentrating the stresses. Multiple bands can form (Klein et al., 2001) that are near to perpendicular to the maximum compressive stress.

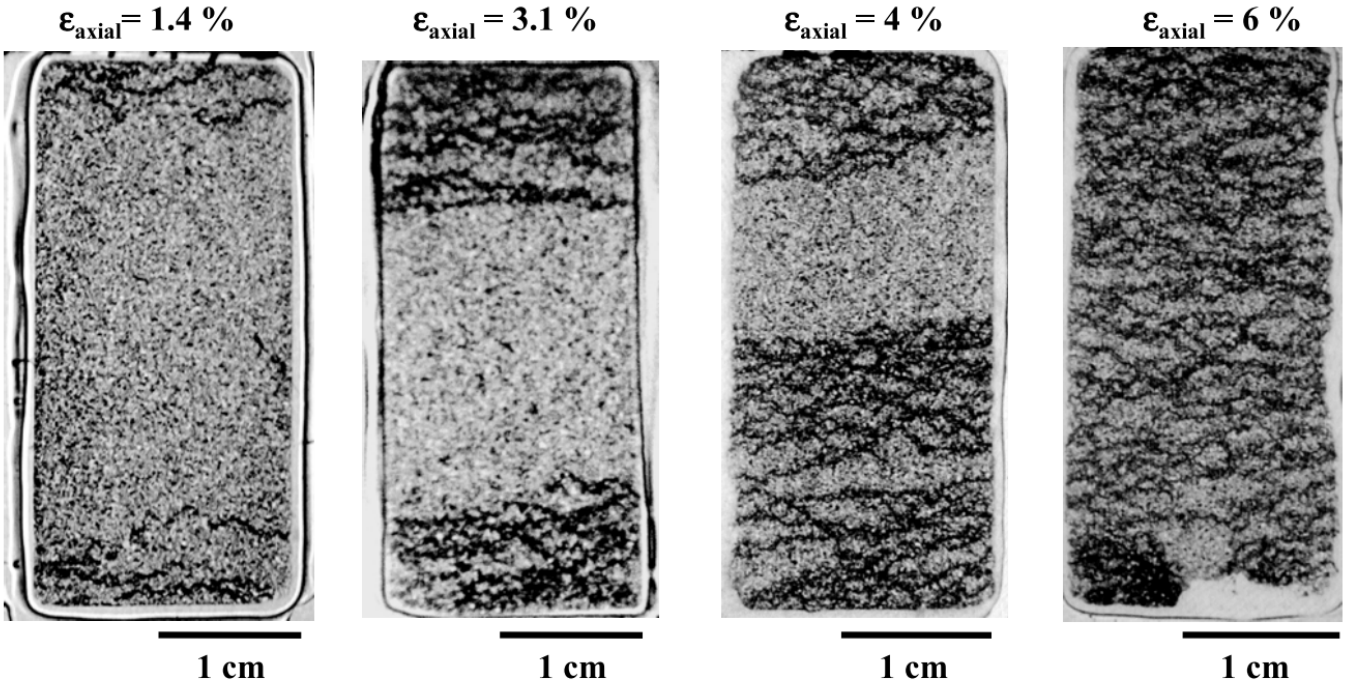

Figure 2.7: A series of compaction bands formed in Bentheim sandstone subjected to triaxial compression at a confinement of 300 MPa (Baud et al., 2004). Clearly visible is the formation of bands initially at the top and bottom of the specimen, propagating towards the centre in the form of multiple thin bands.

The compaction bands are highly localised and feature a significant reduction in porosity and grain cataclasis (Heap et al., 2015; Klein et al., 2001; Skurtveit et al., 2013; Stanchits et al., 2009; Vajdova and Wong, 2003), visible in

Figure 2.8. Much like in the field, highly porous rocks favour the formation of compaction bands (Castellanza et al., 2009; Papazoglou et al., 2017; Wong and Baud, 2012; Wong et al., 2001), although their formation in the laboratory occurs at much higher confining pressures than that inferred from field observations.

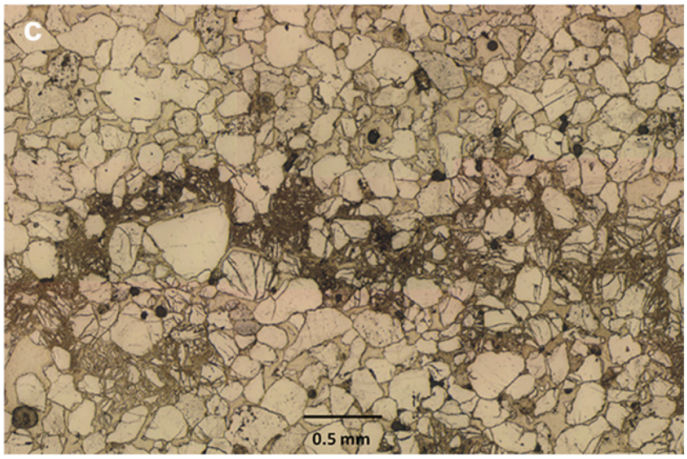

Figure 2.8: A close-up image of an individual compaction band (Wong and Baud, 2012). The relatively dark band exhibits clear evidence of extensive grain crushing and porosity reduction.

It has also been shown that sandstones with narrower grain size distributions are more likely to generate compaction bands than those with broader distributions (Cheung et al., 2012), providing evidence that the confined comminution model proposed by Sammis et al. (1987) is relevant to the deformation mechanism in both compaction and shear bands.

It should be noted that the formation of compaction bands has an effect on the overall macroscopic response of the sample.

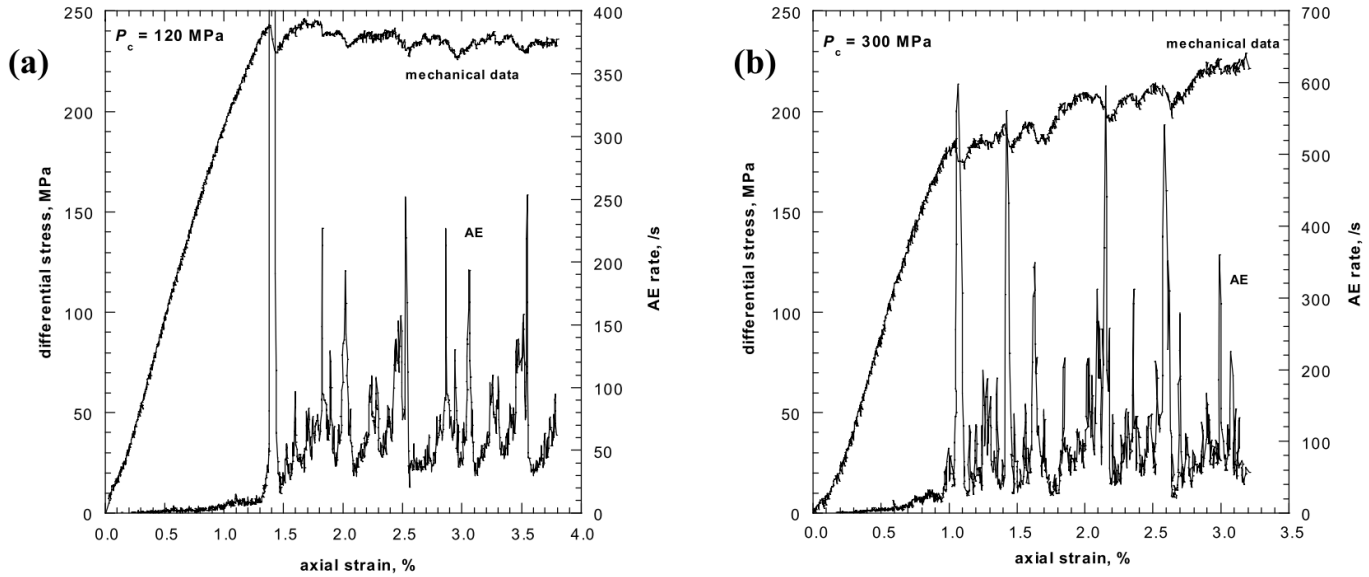

Figure 2.9: The macroscopic effect of compaction bands, with oscillations in the stress-strain curve of a Bentheim sandstone strongly correlated with peaks in the acoustic emissions data (Baud et al., 2004).

The formation of compaction bands, indicated by strong spikes in acoustic emissions data, induces stress drops in the stress strain curve, illustrated in Figure 2.9. The sequential formation of bands induces an oscillatory pattern Baud et al., 2004, 2006; Heap et al., 2015.

Shear bands

In contrast to the behaviour observed for compaction band formation, in the laboratory shear band formation is consistently favoured at low confining pressures for a range of different sandstones (Baud et al., 2004, 2006; Gajst et al., 2018; Guéguen and Fortin, 2013; Wong and Baud, 2012; Wong et al., 2001, 1997; Wu et al., 2000) as well as limestone (Vajdova et al., 2010), basalt (Zhu et al., 2016) and bassanite (Bedford et al., 2018) when submitted to standard triaxial compression testing. It should be noted that some rock types are capable of forming shear and compaction bands in overlapping regions of stress confinement (Olsson, 1999; Tembe et al., 2008).

Unlike compaction bands, which are consistently associated with substantial porosity reduction and grain crushing, the behaviour of shear bands depends on the confining pressure. At very low confining pressures, Berea and Vosges sandstones have been observed to form dilatant shear bands, while at low to moderate confining pressures they form shear bands associated with extensive grain cataclasis in a region of ≈ 1 mm thickness (Bésuelle et al., 2000; Menendez et al., 1996). The Vosges sandstone has also been observed to form pure dilation bands and dilating shear bands in triaxial extension tests (Bésuelle, 2001).

Several different researchers have observed that as the confinement increases the angle of the shear band with respect to the major principal stress also increases in triaxial (Bésuelle et al., 2000; Dewers et al., 2017; El Bied et al., 2002) and biaxial compression (Desrues and Viggiani, 2004).

The microstructure of shear bands has been extensively examined in Fontainebleau and Vosges sandstones and Hostun sand. In shear bands formed at low confining pressure, shear bands are thicker with some grain cracking and porosity increases, whereas at higher confining pressure the porosity reduces dramatically at the centre of the band accompanied by extensive cataclasis with some dilation at the band boundaries (El Bied et al., 2002), visible in Figure 2.10.

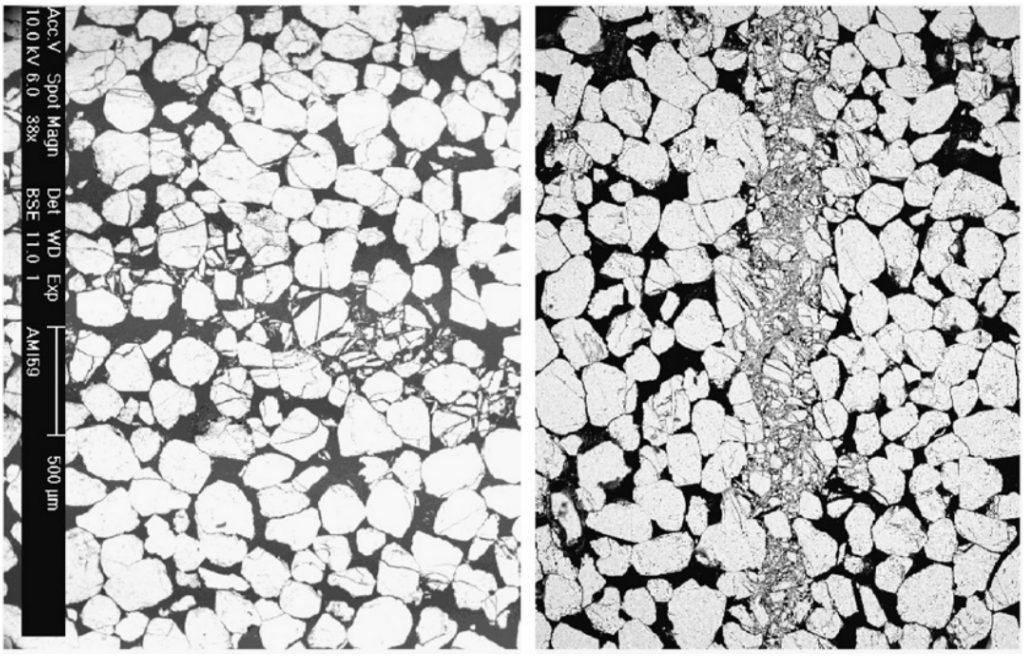

Figure 2.10: Shear bands in Fontainebleau sandstone (El Bied et al., 2002). On the left the sample was confined at 7 MPa then sheared, on the right the sample was saturated and confined at 28 MPa then sheared. Respective magnifications are 38 and 30×.

In undrained conditions bands formed under high confinement can form drainage channels, visible in Figure 2.11. Despite the increase of porosity in dilation bands, the permeability still reduces by 1-2 orders of magnitude due to an increase in tortuosity (Feia et al., 2016). In cataclastic shear bands the permeability can reduce by 3 orders of magnitude or more (Sulem and Ouffroukh, 2006).

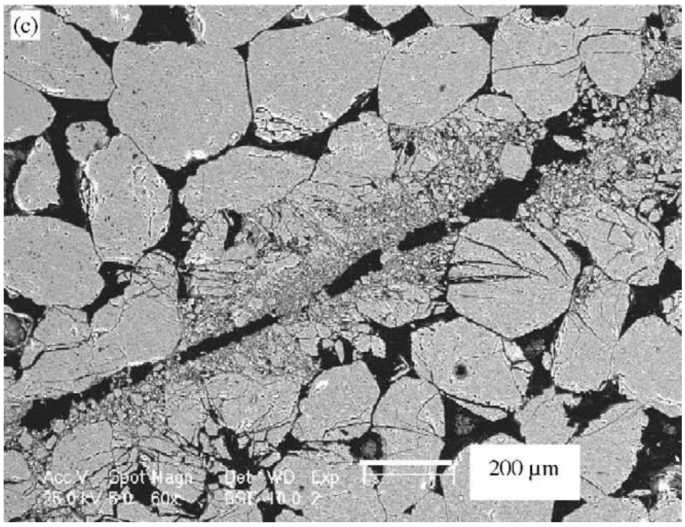

Figure 2.11: A drainage channel formed in a shear band during an undrained test on Fontainebleau sandstone confined at 50 MPa (Sulem and Ouffroukh, 2006).

Beyond direct post-mortem observation of shear bands in samples, new techniques from image analysis have enabled the observation of bands as they form in the sample. Digital image correlation (DIC) has been applied to geomaterials to observe their deformation mechanisms (Couture and Bésuelle, 2019; Desbois et al., 2017), and in particular has been used to observe bands in tests performed in a true triaxial device (Bésuelle and Lanatà, 2016).

The introduction of X-ray micro computed tomography (μCT) has allowed an unprecedented level of access to the interior of samples as they undergo deformation. Hall et al. (2010) demonstrated using volumetric digital image correlation (VDIC) that the shear band commences before the peak loading and narrows to 5 mm ($\approx$17 d_{50}) as the shearing increases. The authors do not report the granulometries before or after the test, but as the method relies on consistently identifying individual grains there is unlikely to be any significant grain breakage. The grain rotation is also observed to concentrate in the shear band, as shown in Figure 2.12.

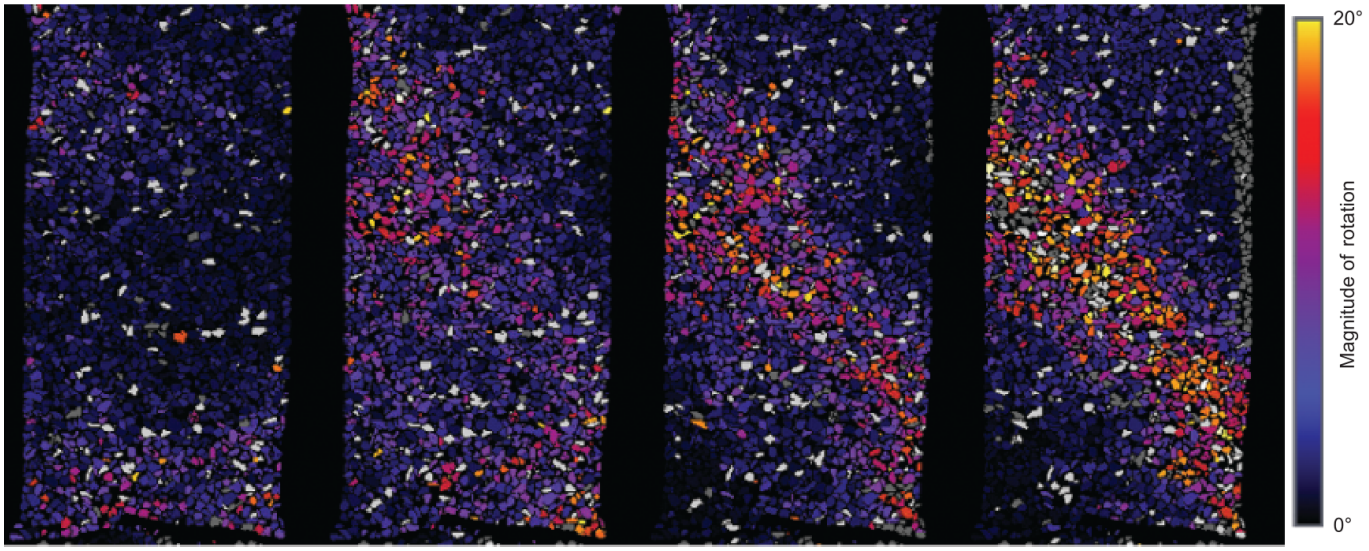

Figure 2.12: The grain rotations observed using X-ray μCT (Hall et al., 2010). The rotations are much more intense in the shear band compared to the rest of the sample.

This analysis was confirmed by Charalampidou et al. (2011) who verified the tomographic results with acoustic emissions and ultrasonic tomography. The shear strains determined using μCT are much more distinct than the volumetric strains, meaning that shear bands are more easily detected than compaction bands using this method. However, in the compaction bands the P-wave velocity is substantially reduced, offering another method of detecting

their formation. Andò and coworkers have obtained similar results in Hostun sand, both by applying a process similar to particle tracking velocimetry (Andò et al., 2012), as well as VDIC (Andò et al., 2017), in both cases to data obtained using μCT. These general localisation patterns have been confirmed to also occur in Yamazuna sand (Takano et al., 2015), Botucatu sandstones (Rodrigues et al., 2015) and Caicos ooids (Karatza et al., 2018). The method has also demonstrated that within the shear band there are fewer particles that form stable geometric networks (Fonseca et al., 2016), and that the particle size distribution is evolving faster inside the band (Karatza et al., 2018). Very recent results using μCT indicate that localisation appears to begin forming early in the test and gradually becomes more clearly defined as the test progresses (Desrues et al., 2018). It should be noted that macroscopic measures such as stress-strain curves do not give clear signals of shear band formation in the way that they do for compaction bands. However, the point of peak load on the load-displacement curve of a triaxial compression test typically appears to feature a through-going shear band (Desrues et al., 2018; Karatza et al., 2018; Tagliaferri et al., 2011) that subsequently narrows and fully develops as the global response appears to demonstrate strain softening. We may thus hypothesise that shear band formation is driving these macroscopic softening behaviours in triaxial compression tests.

Various authors have also submitted gouge samples to rotary (De Paola et al., 2015; Hou et al., 2012; Pozzi et al., 2019; Siman-Tov and Brodsky, 2018; Togo and Shimamoto, 2012) and ring-shear apparatuses (Kimura et al., 2014) and found broadly similar results to those tests conducted in biaxial and triaxial devices, particularly with respect to the formation of very localised bands with fine grain sizes.

Of special interest to this thesis are shear bands that are observed to form in the *Appareil Cisaillement Simple Annulaire* (ACSA), illustrated in Figure 2.13. This apparatus is a pseudo-Coutte cell allowing photographic observation and measurement of the boundary forces applied during shearing for large distances, described in detail in the theses of Patrick Lerat (Lerat, 1996) and Guillaume Chambon (Chambon, 2003) (both in French).

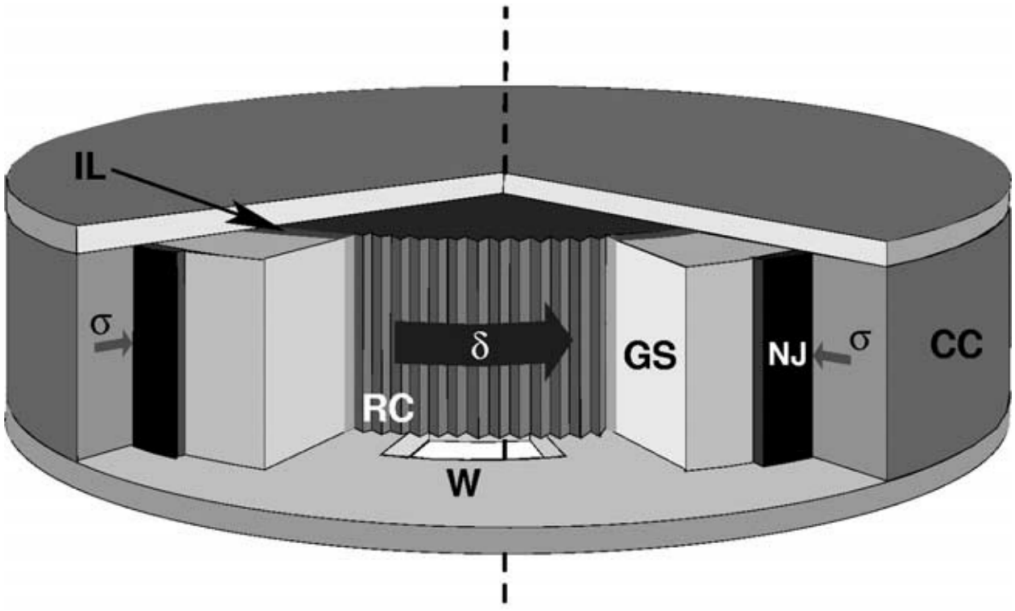

Figure 2.13: A sketch of the ACSA apparatus (Chambon and Schmittbuhl, 2002). RC indicates the roughened inner cylinder that rotates, GS the granular sample, NJ the encasing neoprene jacket pressurised by the water cell CC. A glass window W allows visual inspection of ≈80% of the sample, including the interface layer IL.

In particular, a series of experiments conducted by Chambon and co-workers aimed to explore experimentally some of the behaviours observed in faulting. They placed sand with a mean grain size of 1 mm into the apparatus, and the inner rotating wall had a roughness of 1 mm. They observed both velocity and slip weakening in their sample, and in a photo taken through a clear window in the base of the apparatus, shown in Figure 2.14, a cataclastic shear band of approximately 10 mm thickness is visible (Chambon and Schmittbuhl, 2002).

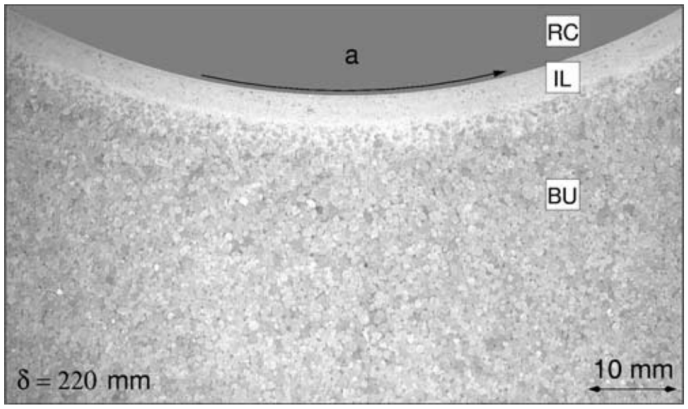

Figure 2.14: A view of the sample mounted in ACSA (Chambon and Schmittbuhl, 2002). RC is the cylinder, IL the interface layer (i.e. the cataclastic shear band) and BU the bulk of the sample.

An exponential decay of the velocity field oustide the shear band and evidence of a decoupling between the band and the bulk were observed using correlation imaging velocimetry (Chambon et al., 2003). The transition between the shear band and the bulk was observed to be ≈2 grains thick, and the shear band featured a significant evolution of grain sizes (Chambon et al., 2006c). In angular quartz sands with particle sizes of 1 and 0.6 mm, major slip weakening is observed, but glass beads demonstrate much less weakening for the same loading conditions (Chambon et al., 2006a,b). These experiments provide significant evidence of the important role of grain breakage in precipitating the formation of a shear band.

To conclude, we observe the formation of shear, compaction and dilation bands (and their combinations) in both nature and the laboratory. In particular, the relatively large number of observations of shear bands, whether taken directly from cores drilled through major faults, their surface outcroppings, small bands in rocks, and their pervasiveness as a mode of failure in the laboratory highlight the importance of developing accurate models to aid the understanding of their formation, and to predict their behaviour. Observations of compaction bands are comparatively rarer in the field, but can be generated in the laboratory under appropriate loading conditions with very common sandstones, highlighting the necessity of understanding their underlying physical mechanism so sample homogeneity can be maintained.

2.3 Modelling localisations

As previously discussed, the ability to model strain localisations is of high importance in geomechanics, relating to the accurate interpretation of laboratory experiments, fluid flow in reservoirs, geotechnical interventions and the mechanics of seismogenic faults. While there has been some attempts to understand and model compaction bands as the closing of a crack (i.e. the "anti-crack" model) (Fletcher and Pollard, 1981; Liu et al., 2015; Sternlof et al., 2005) or as the propagation of a shockwave (Olsson, 2001), it is most widely understood as being an example of a bifurcation phenomenon where an instability of the underlying constitutive model prompts a change from homogeneous deformation to an inhomogeneous and localised pattern (Rudnicki and Rice, 1975; Vardoulakis and Sulem, 1995). Shear bands appear to be universally understood in this fashion, and mathematical modelling approaches based on this are able to conceptually encapsulate compaction, shear and dilation bands as well as their combinations. As such, we also use this framework to present and discuss the modelling techniques that are required to develop an accurate understanding of localisation phenomena.

2.3.1 Bifurcation theory and its application to geomechanics

In order to understand how bifurcation theory is applied to geomechanics, it is necessary to clarify how systems respond to small perturbations around an equilibrium state. While there are various notions of stability current in engineering mechanics (see Bigoni and Hueckel (1991a,b) and Chambon et al. (2004) for extensive discussions), in this thesis

we exclusively use the notion of stability rigorously defined by Lyapunov in his doctoral thesis (and translated into English one century later). Explanations with the explicit mathematical framework are available (see Rattez (2018) and Stefanou and Alevizos (2016) and citations therein), but for our purposes it is sufficient to say that a system is unstable if, when subjected to a small perturbation, the perturbation continues to grow in time. A *bifurcation* occurs when the behaviour of a system changes at a *bifurcation point* (for our purposes, the system changes from stable to unstable in the Lyapunov sense). In geomechanics, this corresponds to a system deforming uniformly experiencing a bifurcation from an unstable uniform deformation mode to stable localised deformation.

When bifurcation analysis is conducted in the classical continuum, it can be shown that softening behaviour favours localisation. Localisation can also occur in hardening material provided it demonstrates sufficiently strong non-associative behaviour (Ord et al., 1991). Under these conditions, the governing equations change from an elliptic system to a hyperbolic system (Vardoulakis, 1985, 1986), resulting in an ill-posed problem. At this point, the homogeneous solution is unstable and is replaced by the localised band solution. In classical and rate-independent models we find that the predicted thickness of any localisation using techniques derived from bifurcation analysis will be zero (i.e. the perturbation with wavelength zero grows the fastest). Numerical implementation will lead to the observation of mesh-dependency of the results, with deformation typically concentrating in a band of one element width.

The root of this behaviour can be traced back to the absence of a length scale in the constitutive formulation. There are two principal ways to repair this deficiency in models:
1. Rate-dependent regularisation. In these theories some sort of rate-dependent term is added, often related to viscosity, temperature or both (Heeres et al., 2002; Olszak and Perzyna, 1969; Sulem, 2010). The length scale arises from the dimension of the viscosity material parameter(s). Importantly, in order for this form of regularisation to work the analysis must be dynamic.
2. Use of a higher order continuum such as Cosserat, second gradient, or non-local. In these theories, the continuum is enriched with either additional kinematic variables (Cosserat) (Cosserat and Cosserat, 1909; Vardoulakis, 2019), a dependence on higher gradients of the deformation (second gradient) (Triantafyllidis and Aifantis, 1986; Vardoulakis, 2000; Voyiadjis et al., 2014), or a dependence on a weighted average of the neighbouring points (Eringen, 1972, 1981; Pijaudier-Cabot and Bazant, 1988). All of these choices have the effect of introducing a material length scale.

In order to further explore the range of possible constitutive models that can be used to solve the problem of predicting deformation band formation and evolution, we examine some constitutive models of particular interest for this thesis.

2.3.2 Constitutive models

The introduction of the notions of bifurcation and stability to geomechanics is traceable to the pioneering works of Rice and Rudnicki (Rice, 1975, 1976; Rice and Rudnicki, 1980; Rudnicki and Rice, 1975). In particular, they highlighted the destabilising effects of non-associated plastic flow such as that associated with friction, which all models which hope to accurately model geomaterials must include.

However the understanding of the deeper underlying mathematical problem (as described above) and the diffusion of this knowledge to the geomechanics community must be attributed to Ioannis Vardoulakis and co-workers, building on the work of the Cosserat brothers (Cosserat and Cosserat, 1909), that had been re-formulated and re-popularised by Germain (1973). In a series of pioneering works in the 1980s, they introduced the Cosserat continuum (illustrated in Figure 2.15) as a means of regularising the problem and supplied a constitutive model that allowed them to predict the orientation of shear bands and their evolution in terms of thickness (Mühlhaus, 1985, 1986; Mühlhaus and Vardoulakis, 1987; Vardoulakis, 1985, 1986). In these works the internal length scale was taken to be a material parameter equal to the average grain size, based on experiments showing that the thickness of shear bands scales with d_{50} (Roscoe, 1970).

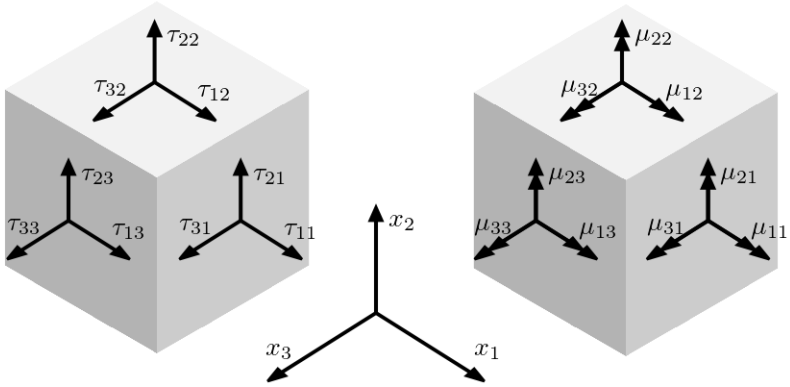

Figure 2.15: The Cosserat continuum concept (Cosserat and Cosserat, 1909).

This strand of analysis was extended to problems in rock mechanics (Sulem and Vardoulakis, 1990; Sulem et al., 1999) such as borehole breakouts (Papanastasiou and Vardoulakis, 1992; Vardoulakis and Sulem, 1993; Zervos et al., 2001), in particular surface instabilities (Vardoulakis and Papanastasiou, 1988) and size effects (Papanastasiou and Vardoulakis, 1989), and a comprehensive treatment of the applications of bifurcation analysis and various methods of regularising the problem was offered by Vardoulakis and Sulem (1995). There have been some continued efforts to model localisation without the benefit of the regularising Cosserat framework, either by focusing purely on band initiation (Buscarnera and Laverack, 2014; Dewers et al., 2017; Issen and Rudnicki, 2001; Olsson, 1999), directly modelling the micro-mechanics (Tordesillas et al., 2016; Wan et al., 2013) or enriching the model by including the bands post-facto (Nguyen et al., 2016). The post-facto model highlights the softening behaviour inside the band competing with hardening behaviour to create the overall macroscopic constitutive behaviour. While in the framework of regularised theories, there is some use of second gradient theory (Bésuelle and Chambon, 2007; Zhao et al., 2006), the concepts of Vardoulakis and coworkers appear to be the most popular way of regularising the problem for rate-independent models in geomechanics, bolstered at least in part by micro-mechanical arguments in favour of the asymmetry of the stress tensor in granular media (Bardet and Vardoulakis, 2001; Papanicolopulos and Veveakis, 2011) and the successful modelling of similar discrete systems (Stefanou et al., 2008, 2010).

An increasingly important strand of localisation modelling concerns that in systems with multi-physical couplings, driven primarily by the desire to model seismogenic faults. Certain authors have proceeded with their analysis relying on the rate-dependency induced by thermal effects (Molinari and Leroy, 1991; Rice, 2006; Sulem, 2010) or with a combination of visco-plastic and thermal effects (Got et al., 2019; Paesold et al., 2016; Platt et al., 2014; Rice et al., 2014; Veveakis et al., 2007) related to thermal pore-fluid pressurisation (Ghabezloo and Sulem, 2009) that prove to be sufficient to regularise the analysed system. In addition, the role of chemical reactions has been shown to play a crucial role in inducing a weakening behaviour but also limiting the associated rise in temperature and hence stopping thermal runaway (Brantut et al., 2017; Brantut and Sulem, 2012; Brantut et al., 2011; Platt et al., 2015; Stefanou and Sulem, 2013; Sulem and Famin, 2009; Veveakis et al., 2010). Models of this type have been shown to be able to explain creeping localisation, sudden seismic slip and periodic seismic slip patterns (Alevizos et al., 2014; Poulet et al., 2014b; Veveakis et al., 2014) that can account for kilometres of displacement on millimetric bands (Poulet et al., 2014a). The structures resulting from displacement of this magnitude are illustrated in Figure 2.16. Pure chemical changes in isothermal conditions have also been suggested to play a role in compaction band formation (Stefanou and Sulem, 2014).

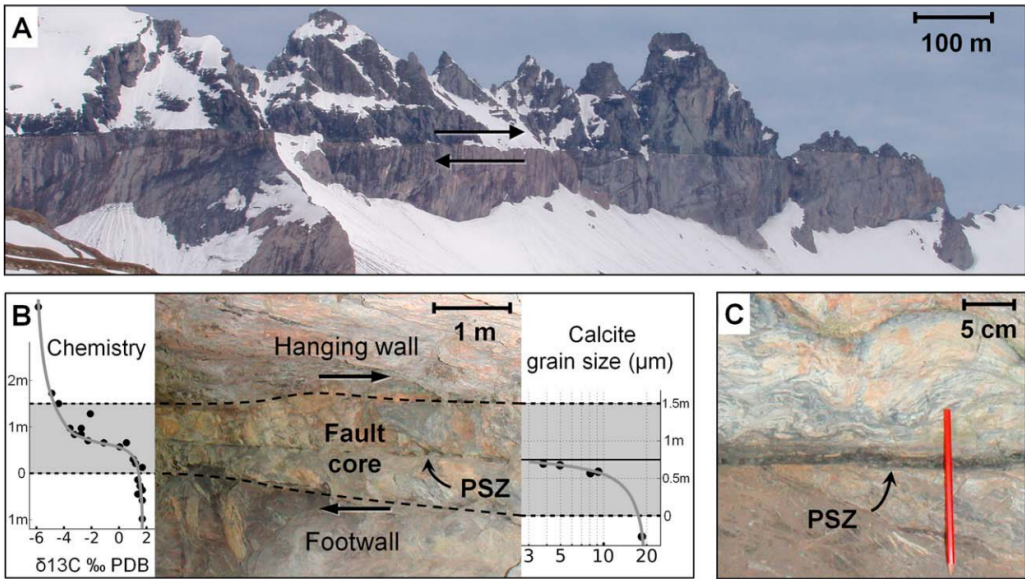

Figure 2.16: The Glarus thrust showing the sharp boundary at kilometre scale, the metre wide fault core and the centimetre wide principal slip zone (Poulet et al., 2014a). This level of displacement can be explained by coupled multiphysical models.

In addition, the multi-physical couplings can be analysed within the framework of the Cosserat continuum, following the concepts of Vardoulakis (Sulem et al., 2011; Veveakis et al., 2013). The thickness of bands formed using rate-dependent constitutive frameworks has been compared to that formed using a rate-independent Cosserat model, with the Cosserat continuum having the effect of thickening the band slightly (Sulem and Stefanou, 2016). Recently it has been demonstrated that the effect of the thermo-hydro couplings can introduce rate-dependent effects to a rate-independent mechanical model, that only become significant at seismic slip rates (Rattez, 2018; Rattez et al., 2018a,b,c), a behaviour illustrated in Figure 2.17.

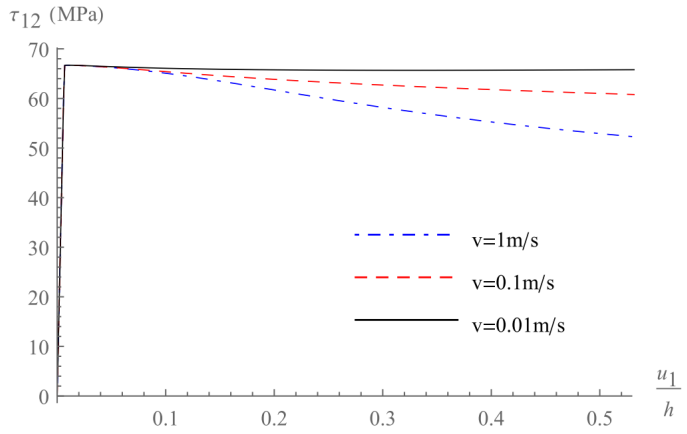

Figure 2.17: The effect of introducing thermo-hydro-mechanical couplings allows a rate-independent elastic-perfectly plastic model to reproduce rate-dependent effects at seismic slip rate without introducing spurious viscosity at low strain rates (Rattez et al., 2018c).

While the full suite of thermo-hydro-chemo-mechanical couplings are necessary for modelling fault behaviour, the regularising effect of these couplings cannot be called on to model localisations in dry granular media. Further, there does not appear to be any rate-dependence in terms of the thickness of the shear bands observed in experiments. As such, it is unlikely that a viscous regularisation is sufficient to model shear bands in these materials. This implies the necessity of using a higher-order continuum or non-local model to accurately explain the observed behaviour.

Further, previous regularisations using the Cosserat continuum have been conducted by treating the internal length as a fixed material constant. However, the abundance of field and experimental evidence demonstrating the presence

of grain cataclasis in localisation bands highlights the inadequacy of this assumption. In addition, the mechanical properties, hydraulic permeability, thermal conductivity and chemical reactivity all have a strong dependence on the grain size distribution, emphasising the importance of gaining access to this information at the modelling level. Recent work has also argued that ultra-cataclastic material plays an important role in the formation of injection veins surrounding faults (Lin, 2019). While there has been some recent attempts to include the idea of an evolving length scale in second gradient theories (Scherer et al., 2019) and non-local damage mechanics (Pijaudier-Cabot et al., 2004; Rastiello et al., 2018), or to account for system evolution by changing the non-local weighting function (Nguyen, 2011), length scale is not attached to any particular micro-mechanical quantity that could give it physical meaning, and the expressions for the length scale and its evolution must be imposed as a constitutive choice. Some recent work has included length scales that depend on the size of the unit cell used for homogenisation (Poh and Sun, 2017; Wang and Poh, 2018), and that decrease the interaction length as damage increases, which has been applied successfully to the case of one-dimensional shock loading a quasi-brittle bar. The micro-mechanics of the model are based on interactions between cracks that occur during very fast loading, and the accelerations and micro-inertial effects play a key role. In this thesis we are primarily interested in localisations that occur across a range of shear rates, meaning we focus on techniques that are also suitable for quasi-static loading cases. However, extending micro-inertial effects to three dimensions could be a fruitful area of future research, particularly in cases of fast shear such as during seismic slip.

By contrast to some of the non-local formulations, the rigid-body rotations of the Cosserat continuum have a clear physical analogue in the quasi-rigid rotations experienced by particles in shear bands (see e.g. Hall et al. (2010)), and as we shall show in Chapter 4 of this thesis, an expression for the internal length can be obtained as a natural consequence of energetic upscaling procedures.

Some recent works (Bauer, 2016; Bauer et al., 2015, 2017) have included an empirically based evolution equation for the mean grain size using a hypoplastic Cosserat formulation that is indifferent to thermodynamics, and thus cannot be used to correctly capture thermal processes in fault physics.

As such, we now introduce the Breakage Mechanics family of models, which provide a framework to evaluate the evolution of the grain-size distribution under mechanical loading.

Breakage Mechanics

The theory of Breakage Mechanics was introduced by Einav (Einav, 2007a,b) with the intention of modelling the effect of grain breakage on the bulk constitutive behaviour of brittle granular media. The model is constructed within the framework of hyperplasticity (Houlsby and Puzrin, 2007), guaranteeing that it is thermodynamically admissible. The essential point of the model is that an internal Breakage variable can be defined, denoted B, that ranges from 0 to 1 and tracks the grain size distribution's progression from its initial state to an assumed ultimate state. Based on extensive field observations of fault gouge grain size distributions (Chester and Chester, 1998; Sammis et al., 1987) and experimental evidence under arbitrarily large shearing (Coop et al., 2004), as well as theoretical considerations about confined comminution and the limits of particle breakage (Kendall, 1978; Turcotte, 1986), the ultimate grain size distribution was argued to follow a power law with a fractional exponent. It should be noted that the mathematics of the model behave equally well if some other ultimate distribution is substituted, but all the papers implementing Breakage Mechanics that we have cited adopt this hypothesis about the nature of the ultimate grain size distribution.

In concert with the breakage index that defines the relative position of the current grain size distribution between the initial and ultimate distributions, a new grading constant θ (in this thesis denoted θ_γ) was introduced in the initial paper (Einav, 2007a) that describes "how far apart" the initial and ultimate grain size distributions are. A larger value of θ_γ ($\approx$0.8-0.9) indicates that the initial and ultimate distributions are very different.

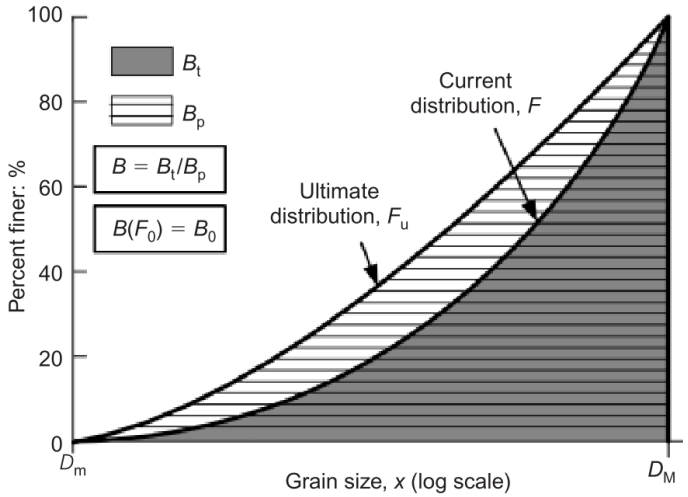

Figure 2.18: The definition of the Breakage internal variable as the ratio of the dark grey area to the striped area. The current and ultimate grain size distributions are indicated on the figure, while the initial distribution is indicated by the vertical line at the far right of the figure. This initial distribution indicates that all the particles were initially of size d_{Max}. The figure is taken from Buscarnera and Einav (2012), after a concept first discussed in Einav (2007a).

In the development of the simple elasto-breakage model in this paper, the energetic conjugate of the breakage was defined, namely the breakage energy E_B, that quantifies how much energy is available to break grains. A new material parameter E_c was also defined, initially arising as an integration constant. This parameter has the physical meaning of a crushing energy, i.e. how much energy it takes to begin the process of breaking grains.

In the process of extending the initial elasto-breakage model to an elasto-plasto-breakage model, the notion of a coupling angle ω was introduced, that describes how dissipation is allocated between grain crushing and plastic volumetric straining (Einav, 2007b). When $\omega = 0°$, there is no plastic volumetric straining and breakage growth is maximised. When $\omega = 90°$, there is no breakage growth and plastic volumetric straining is maximised.

The model was subsequently analogised to the classical Griffith crack model and a critical pressure for breakage growth was derived (Einav, 2007c). A refinement of the model to a "student's model" highlighted its usefulness for engineers (Einav, 2007d), with the corresponding yield surface illustrated in Figure 2.19.

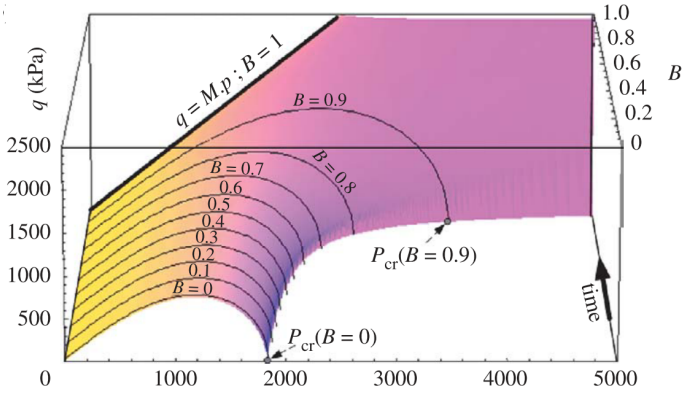

Figure 2.19: A yield surface in $p - q - B$ space, from Einav (2007d).

The model was further extended and refined to explore the behaviour of granular mixtures (Einav and Valdes, 2008) and the energetics of cataclastic processes (Einav and Nguyen, 2008; Nguyen and Einav, 2009). This extension of the model provides the basis of the model that we elaborate in Chapter 4 of this thesis. This model has subsequently been used to explore the formation of compaction bands (Das, 2013; Das et al., 2011, 2013) in porous rocks, as well as the end-bearing capacity of piles (Zhang, 2012; Zhang et al., 2012) being driven into sand.

In the context of studying unsaturated granular media, another material constant θ_H that regulates hydraulic energy has been introduced (Buscarnera and Einav, 2012), as well as the concept of the "universal initial distribution", that implements a mathematically favourable expression for the calculation of θ_γ and B. This model has been further refined to describe the couplings between the breakage processes and the water retention curve (Zhang and Buscarnera, 2015).

The inclusion of porosity as a state variable was first outlined in the context of a finite-strain formulation of Breakage Mechanics (Rubin and Einav, 2011) and further refined in a small-strain context that enables the accurate modelling of dilating behaviour and explains the critical-state dependence on grading (Tengattini et al., 2014a, 2016). The linkage between grain-size polydispersity and the porosity has recently been clarified (Guida et al., 2018). The modelling of cemented granular materials was accomplished by introducing a new state damage variable D that models the process of cement bridges being broken and crushed, using similar principles to the definitions of breakage (Das et al., 2014; Tengattini et al., 2014b). It should also be noted that breakage and damage have been combined to model the transition from a solid rock to a crushed granular media (Lyakhovsky and Ben-Zion, 2014a,b) and the dynamic rupture behaviour of the rock (Kurzon et al., 2019; Lyakhovsky et al., 2016), but that this model treats the behaviour as one similar to a phase transition between undamaged rock and entirely uncemented granular media, whereas the model outlined in Tengattini et al. (2014b) models cemented granular media as a distinct material in and of itself. The combination of the cemented and porous models is outlined in the thesis of Alessandro Tengattini (Tengattini, 2015). Recent work has extended the theory to transversely isotropic granular rocks (Marinelli and Buscarnera, 2019b).

Parallel to further research on the bulk constitutive laws modelled with Breakage Mechanics, research has been conducted to provide a clear link with the micro-mechanics of the grains themselves and the emergent macro-scale properties, principally the crushing energy E_c. Experiments (Stefanou and Sulem, 2016), theory (Zhang et al., 2016) and Discrete Element Modelling (DEM) (Cil and Buscarnera, 2016) have all shown that the grain-breakage process is best modelled by a (three parameter) Weibull distribution and there is an approximately linear scaling between the energy required to break individual grains and that required to begin crushing grain assemblies.

One of the fundamental strengths of Breakage Mechanics is its ability to provide a clear link between the underlying fabric of the material (the grains) and the macroscopic behaviour through an internal variable that is always measurable without knowledge of the material's history, an important feature that is necessary for physically accurate modelling (Rubin, 2001). The subsequent development of additional features of Breakage Mechanics such as the breakage energy and the critical breakage energy arise directly from thermodynamics and mathematical integration respectively. This renders the model family capable of elucidating the true underlying physics of processes such as localisation more clearly than phenomenological parameters based on macroscopic curve fitting are able to. Approaches based on curve fitting are also only valid within the range that they were calibrated, which can pose difficulties when passing from the laboratory to situations such as deep faults.

To conclude, the theory of Breakage Mechanics has been used to model brittle granular media with great success. Increasingly sophisticated models have been adopted that account for more physics and linkages have been drawn between the micro-mechanics of the grains and the macroscopic constitutive laws. While there have been some instances of using non-local (Nguyen and Einav, 2010) or viscous regularisation (Das et al., 2013, 2014) to enable Breakage Mechanics to predict strain localisations, the nature of this regularisation is ad-hoc and not related to any specific physical quantities of the medium. However, recent work has related rate dependence at the continuum scale to crack growth within the individual grains (Zhang and Buscarnera, 2017) which has been used to explain creep and delayed grain breakage (Sohn and Buscarnera, 2019). Rate-dependence may also result from chemical changes induced by surface-reactive environments (Zhang and Buscarnera, 2018). A rate-dependent Breakage model has also been implemented numerically with two different algorithms, with an algorithm based on consistency viscoplasticity

shown to be more efficient (Marinelli and Buscarnera, 2019a). A comparison of higher-order regularisation with viscous regularisation for Breakage Mechanics may provide an interesting future avenue to explore.

2.3.3 Numerical implementations

Any constitutive model of any significant complexity must be implemented numerically in order to derive results from it, as the underlying Partial Differential Equations (PDEs) will not be tractable analytically.

One approach is the Finite Difference method, which is frequently used to discretise the time-coordinate in PDEs. Refined versions such as the Runge-Kutta method (Butcher, 1963; Fehlberg, 1970) or Crank-Nicolson (Crank and Nicolson, 1947) are frequently implemented in practice. Implicit methods such as backwards-Euler are unconditionally numerically stable, at the cost of being more computationally expensive per time step.

Another approach is the Finite Element Method, which is typically used to discretise the spatial coordinate. Extensive treatments of various higher order continua implemented in finite elements for the solution of a range of geotechnical problems have been outlined in other works (see Collin et al. (2016), Papamichos (2016) and Papanastasiou and Zervos (2016) and citations therein for comprehensive treatments). Due to the enormous range of techniques and modifications to this method that have been published, dealing with a wide array of different problem types, we highlight only a select few publications illustrating the essential points for this thesis.

Various authors have highlighted the utility of the Cosserat continuum in ensuring that a unique solution is converged upon with appropriate mesh refinement (De Borst, 1991; Papanastasiou and Vardoulakis, 1989, 1992; Rattez et al., 2018b; Vardoulakis and Papanastasiou, 1988; Zervos et al., 2001). In particular, the utility of a mixed-element formulation has been argued (Godio et al., 2015; Li et al., 2014) for Cosserat finite elements, although it is not essential, as has been demonstrated in the recent thesis of Hadrien Rattez (Rattez, 2018) and associated works (Rattez et al., 2018a,b,c) performed using the REDBACK framework (Poulet et al., 2017).

Using material models that are based on enforcing a consistency condition on a yield surface demands a numerical implementation that allows the condition to be met, within numerical tolerance. There are multiple possible ways of doing this (see Einav et al. (2003)), and recently a robust projection algorithm has been implemented and validated for the Cosserat continuum (Godio et al., 2016).

It should also be noted that it is possible to retain the formal benefits of hyperplastic modelling while eliminating the yield surface, easing numerical integration (Einav, 2012).

Numerical techniques can be applied in order to model localisations without the underlying constitutive model featuring an internal length scale. Amongst these are the Enhanced Assumed Strain (EAS) method (Simo and Rifai, 1990) and the related Galerkin embedded strong discontinuity algorithm (Borja, 2000; Borja and Regueiro, 2001), and the Extended Finite Element Method (XFEM) (Moës and Belytschko, 2002; Moës et al., 1999; Sukumar et al., 2000). However, the performance and accuracy of these solutions can depend on exactly how the enhancement is implemented (Borja, 2008), and mean the problem can only be studied using the methodology the enhancement has been performed on (for example, no comparison with a linear stability analysis is possible). These techniques do not convey any additional information about the underlying physics that we are concerned with, and are mostly of interest from the perspective of obtaining better performance from classical models during localisation.

2.4 Conclusion

It is clear that the formation of localisation bands, particularly shear bands, is a significant failure mode for granular rocks observed in the field. Field observations highlight the importance of high porosity and large grain sizes, particularly in the formation of compaction bands. It appears to be exceedingly rare to encounter a shear band formed in the field that does not feature extensive grain cataclasis, emphasising that the microstructure changes extensively inside shear bands.

In the laboratory the formation of compaction bands occurs at high confining pressures (substantially higher than the pressure inferred from field measurements), while at low confining pressures, the failure of samples by shear band formation appears to be a pervasive mechanism. These shear bands can either be accompanied by extensive dilation and minimal grain fragmentation, or compaction and with extensive grain cataclasis.

While not being the sole tool used to model band formation, the theory of localisation of deformation based on bifurcation analysis is by far the most popular and well-developed method. It has been shown that in the absence of some regularisation that endows the constitutive model with an internal length, the predicted localisation width will be zero. The most popular method to regularise the problem in geomechanics is the use of the Cosserat continuum, but the imposition of the average grain size as a fixed internal length associated (up until now) with this method is clearly not viable given the extensive evidence for grain size evolution by cataclasis. It is also not clear from reported experimental results whether the polydispersity of the grain size distribution has a role to play with respect to the width of the shear band formation.

This absence in the literature suggests the need to perform some experiments focusing on the effect of polydispersity to obtain some insight for future modelling efforts. Thus, in the following chapter we present a series of experiments that we conducted to determine whether we need only to model the evolving mean grain size, or whether we must take into account the entire grain size distribution in some way.

Chapter 3

Continuous annular shear experiments with two-dimensional rod particles

3.1 Summary

In this chapter we present a series of experiments conducted in the *Appareil Cisaillement Simple Annulaire* (ACSA), with the aim of developing experimental techniques that in the future can be used to evaluate the success of models for polydisperse media, in particular their predictions of shear band formation. By selecting three mixtures with a constant mean grain size but different maximum grain sizes we develop the technique while also gaining insight into whether the mean grain size is an adequate descriptor of the micro-structure for the purposes of shear band modelling. In order to achieve this, we use techniques from image analysis to extract barycentric tangential velocity profiles over the radial coordinate, which are numerically differentiated to present strain rate profiles. By carrying out this analysis we are able to conclude that the mean grain size is inadequate to fully describe the continuum behaviour, and that some measure of polydispersity must be used to accurately represent the material. We are unable to conclude exactly what measure of polydispersity should be taken into account, as doing so would require carrying out an extensive experimental campaign that is beyond the scope of this thesis.

3.2 Introduction

In Chapter 2, we discussed the progression of Cosserat models intended to be able to predict the shear band thickness in granular media. These developments were motivated by the observation that the behaviour of granular media, particularly with respect to shear band formation, is strongly influenced by the size of the constituent grains (Roscoe, 1970). Previous developments in the theory of Cosserat modelling of geomaterials, in particular the classic works of Vardoulakis and coworkers (Mühlhaus and Vardoulakis, 1987; Vardoulakis and Sulem, 1995), have treated the mean grain size as a material parameter that is sufficient to capture the relevant behaviour based on observed experimental behaviour. In particular, the mean grain size plays a critical role in determining the thickness of shear and compaction bands in these models, by acting as the internal length of the Cosserat continuum that regularises the equations and allows the prediction of their characteristic width.

While these theories have been very successful and have been implemented in various extended models, particularly in the context of multi-physical coupling for fault mechanics (Rattez et al., 2018a,b,c), they rely on the assumption that the mean grain size is a fixed material parameter. However, a wide variety of evidence, from the laboratory scale (Coop et al., 2004; El Bied et al., 2002; Sulem and Ouffroukh, 2006) all the way to the fault scale (Chester and Chester, 1998; Sammis et al., 1987; Sulem, 2007) clearly demonstrates that when subjected to significant loading, grains undergo breakage and shear band structures form where the intensity of this breakage behaviour is particularly intense. As a consequence of the constituent particles of the media being crushed, the mean grain size must also change.

In addition to the change of the mean grain size due to crushing, the distribution also become more polydisperse as it evolves. This raises the question of whether the mean grain size alone is sufficient to model the behaviour of the material, or whether the polydispersity has a significant effect that must also be captured. Hence, we perform our tests on an assembly of grains with a constant mean grain size but varying maximum grain size, resulting in varying polydispersity of the system.

These grain size distributions are constructed out of Schneebelli material (that is to say, long cylindrical rods which we consider only in cross section). The simplifying effect of considering only 2 dimensions allows a clearer understanding of the underlying effects, and has been used successfully before in similar types of experiments relying on image analysis of particles of different sizes and their motion (Combe et al., 2013; Miller, 2014; Miller et al., 2013).

3.3 Experimental method

We prepare a series of experiments in the *Appareil Cisaillement Simple Annulaire* (ACSA). The complete details of the construction of the ACSA, are described in the PhD thesis of Patrick Lerat (Lerat, 1996) (in French). Further descriptions of the device have subsequently been published (Corfdir et al., 2004; Lerat et al., 1997), and the apparatus has been extensively used to explore the behaviour of fault gouge by Guillaume Chambon and coworkers (Chambon, 2003; Chambon and Schmittbuhl, 2002; Chambon et al., 2006a,b, 2003, 2006c), owing to its capacity to generate very large strains. We have replicated a sketch of the apparatus in Figure 2.13. For our purposes, it suffices to describe the apparatus as being a cylindrical Couette apparatus where the inner cylinder rotates to produce a shearing effect. The radius of the inner cylinder is 100 mm and that of the outer wall is 200 mm. Unlike other authors, we ran ACSA in "open face" mode, which means that we have a confining pressure applied to the outer edge of the apparatus, but no confinement above the sample. As a consequence the device is limited to small confining pressures. The bottom and internal faces of the machine are constructed out of stainless steel and hence disallow any displacements in those directions. The outer two centimetres of the device feature a small "step" to a lower level, which we filled with foam to try and obtain a consistent level. We attached a mask to the inner wall that has teeth of diameter 10 mm, allowing full engagement with the largest grain size. We illustrate the relevant components in Figure 3.1:

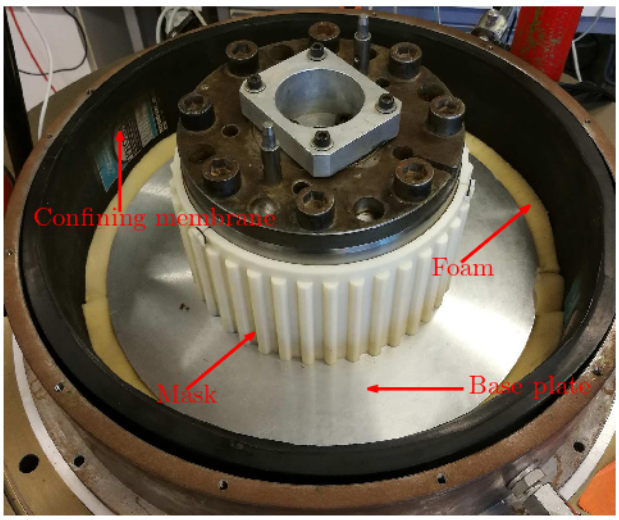

Figure 3.1: A photo of the ACSA in open-face mode, without any sample mounted, and the various parts annotated.

We note that the cylindrical shape of the ACSA means that it generates inhomogeneous stresses and strains. However, this does not preclude the generation of clear shear bands, such as that shown in Figure 2.14. Other workers using similar devices have also observed and modelled shear bands (Henann and Kamrin, 2013; Losert et al., 2000).

We prepared a range of PVC plastic cylinders, of height 60 mm (with some small variance), and diameters 1.6, 3, 4, 6, 8 and 10 mm. The larger cylinders were sanded so they were slightly rougher. We left the smaller cylinders as they are, as they already had a slightly roughened surface.

We then spray-painted the upper surfaces of the cylinders in a matte-white paint to aid the ability to accurately distinguish them from the surrounding void space. Any cylinders that were stuck together by the process of spray-painting were separated to avoid the formation of any compound grains.

The samples were prepared by including the desired grain size fractions in the appropriate weights to maintain the target mean grain size. The cylinders were placed in a series of moulds, shown in Figure 3.2 that prevent them from falling due to their slenderness (a factor which is particularly important for the smaller grain sizes), aided by the application of tape to the end and one of the open sides of the mould.

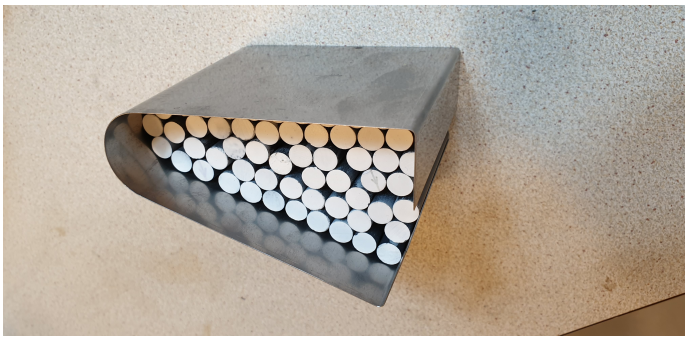

Figure 3.2: An example of rods (in this picture exclusively 10 mm rods) placed in a mould.

The tape on the open side was removed as the mould was placed in the ACSA. Once all of the moulds that could be fit into the ACSA were placed, the gaps between them were filled with the cylinders, and the moulds removed. Cylinders continued to be placed until the sample was sufficiently dense that no further cylinders could be inserted, or all of the prepared sample was placed.

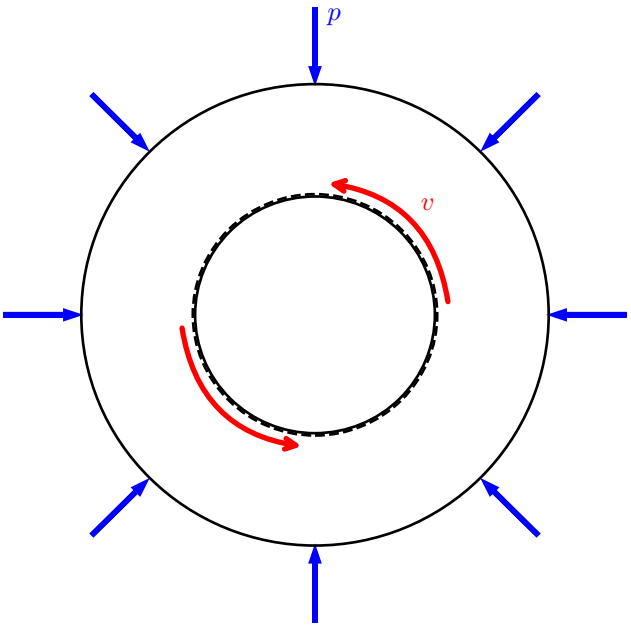

Figure 3.3: A schematic of the ACSA and the appropriate boundary conditions. The inner solid black line indicates the inner boundary, while the dotted black line indicates the outer edge of the teeth. We apply an initial confining pressure p uniformly to the outer boundary, and then commence shearing at a rate v at the inner wall.

The test geometry including the boundary conditions is illustrated in Figure 3.3. We set $p = 200$ kPa, and $v = 3.3495$ mm/min, and take a photo every five seconds.

	Set 1		Set 2		Set 3	
1.6 mm	813.46	g	949.91	g	1084.27	g
3 mm	1318.37	g	1539.50	g	1757.26	g
4 mm	1767.17	g	2063.59	g	2355.47	g
6 mm	1855	g	0	g	0	g
8 mm	0	g	1102	g	0	g
10 mm	0	g	0	g	803	g

Table 3.1: The weights for the different size fractions in each of the three sets of experiments. All three experiments have the same mean grain size by weight (4.2 mm), but different largest grain sizes.

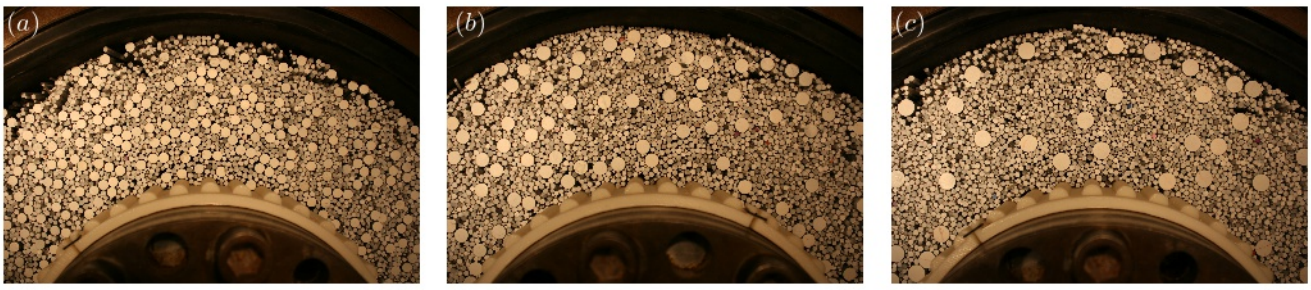

Figure 3.4: Three images showing the different materials. (a) is the material used in Set 1, (b) the material used in Set 2 and (c) the material used in Set 3.

The make-up of each set of experiments is listed in Table 3.1, and illustrated in Figure 3.4. We maintain the same

confining pressure p and the same shearing rate v for all the experiments, ensuring the only variable aspect is the polydispersity of the material that we test.

3.4 Data analysis

While the ACSA does have the capacity to measure the applied torque, in the geometry we use the data produced is unreliable, and so we turn to image analysis techniques to measure the velocity field. These techniques, namely spatio-temporal plotting, Fourier analysis and geometric fitting, are performed in order to obtain the tangential angular velocity over the radial coordinate.

3.4.1 Image treatment

We start with our original image in colour, shown in Figure 3.5. The image is 3888 by 2592 pixels and is obtained with a Canon EOS 400D digital camera, saving the file in JPEG format. The exposure time is 1/100th of a second, the f-number is f/5.0, the ISO value is 100 and the focal distance is 25 mm. A new image is taken every 5 seconds.

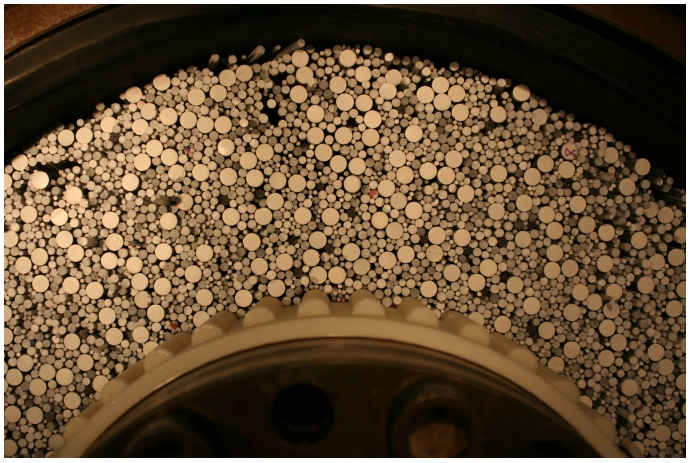

Figure 3.5: The original image in colour.

We convert the original image to greyscale and crop out the outer edge to reduce file size and increase processing efficiency (i.e. we remove the top 270 pixels). The greyscale is obtained by converting the red (R), green (G) and blue (B) colours into a single value using the ITU-R 601-2 luma transform:

$$L = R \times 299/1000 + G \times 587/1000 + B \times 114/1000 \tag{3.1}$$

This produces a greyscale image Figure 3.6 where all of the pixels values are transformed into values between 0 (absolute black) and 255 (absolute white):

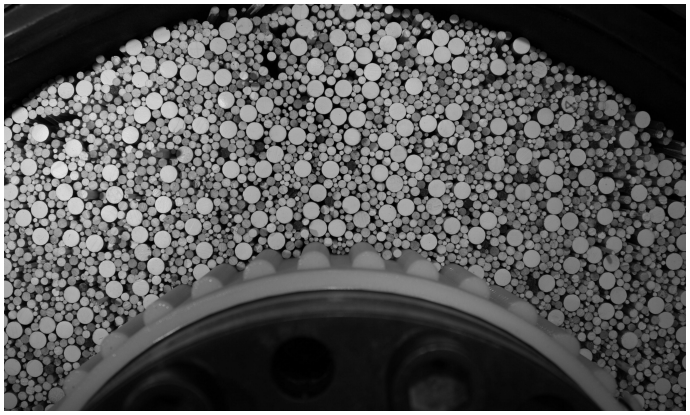

Figure 3.6: The image transformed to greyscale with redundant information cropped.

We consider a large number of equally-spaced arcs along the radius. We take arcs of equal length, centred along the centre line of the image, meaning that the arcs subtend increasingly small angles as the radial distance increases. We have no need to consider arcs that extend throughout the image in order to extract the desired information. In fact, it is better to take relatively short arcs owing to the distortion introduced by the parallax of the camera, which is more intense at the corners of the images. This causes arcs that are constant pixel distances apart to no longer represent constant physical distances.

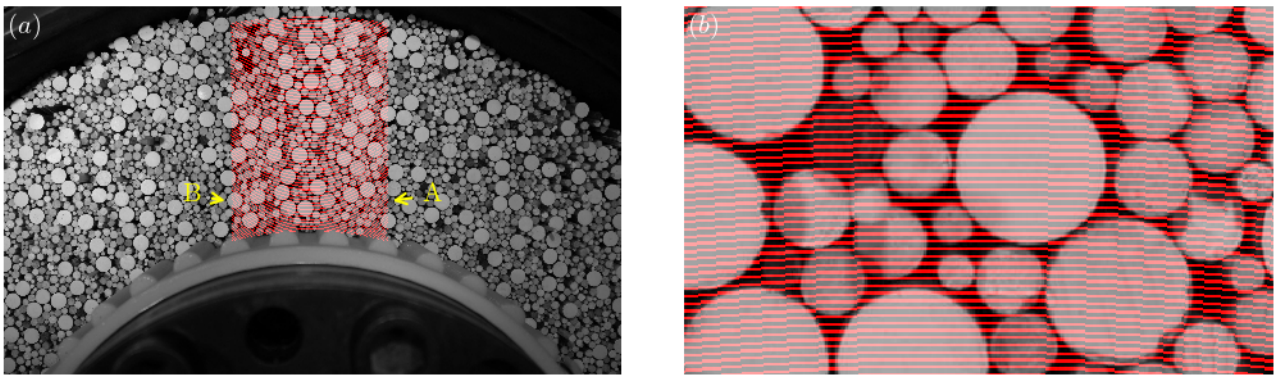

Figure 3.7: An illustration of the selected pixels lying along the arc. In (a) the entire region is visible. We highlight two points, A and B for later reference. In (b) we show a close-up, demonstrating that the arcs are sufficiently finely spaced to allow sub-grain resolution.

We select the arcs to have a five pixel spacing, as shown in Figure 3.7, allowing us to extract information below the length scale of the smallest particles present in the distribution, without being unduly computationally burdensome. We extract the greyscale values of each pixel that lies on the arc, and store them along with the spatial coordinates of that pixel.

Finally, we convert these values into a spatio-temporal plot, Figure 3.8, by plotting the greyscale values of the pixels on a given radial arc as a vertical column in order of increasing angular coordinate, and repeat this for every image, and subsequently for every radius. The spatio-temporal plot shows how the grey-scale values along a particular arc change over time. As a particle moves along the arc, the pixels lying in that particle will move upwards and to the right in the spatio-temporal plot. This creates a "stripey" pattern from which we can infer the velocity at that radial point.

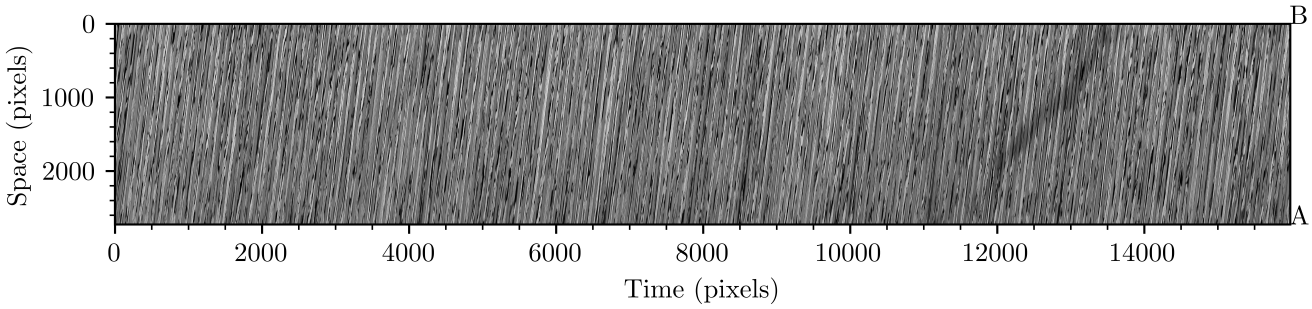

Figure 3.8: A spatio-temporal plot showing the continuity of the behaviour over time. Each column of pixels represents a five second time increment. Each row of pixels represents the same point in space, covering a region of 0.021 mm width. We label A and B the rows of pixels corresponding to the points A and B in Figure 3.7.

3.4.2 Fourier analysis

The spatio-temporal plots demonstrate a clear stripey pattern. The slope of this pattern in Figure 3.8 is a measure of the velocity, v_θ. The slope is more-or-less constant in time, with some degree of noise, and different radii will have different slopes, representing the decay of velocity as the radius increases.

The method we select in order to measure the slope is drawn from the work of Faug et al. (2015), based on the two dimensional fast Fourier transform (FFT). The FFT is a way to detect patterns in the image as well as their frequency and orientation. This will effectively collapse all of the slopes we observe in the stripey pattern into one set of data points that we will be able to apply fitting techniques to.

We wish to obtain a reliable statistical mean of the velocity that we measure using the FFT method. To this end, rather than performing an FFT of the entire spatio-temporal plot, which is extremely expensive numerically, we select a square sub-window at the left-most edge and perform the FFT analysis on that sub-window. We then slide the window along, such that the operation is performed 20 times and we have a well-defined statistical mean.

In order to aid the clarity of the signal, we can also pass the spatio-temporal plot through a threshold so that we treat values above the threshold as all equal to 255, and values below the threshold as equal to zero. This means that all shades of grey above the threshold will contribute equally, removing some of the effect of uneven paint application, overshadowing due to slightly unequal particle heights or slight tilting of the particles. This all adds to a "sharper" signal than present if we do not apply a binary threshold. We outline the specific details of the process in Appendix A. This produces a plot of the two dimensional FFT, as shown in Figure 3.9.

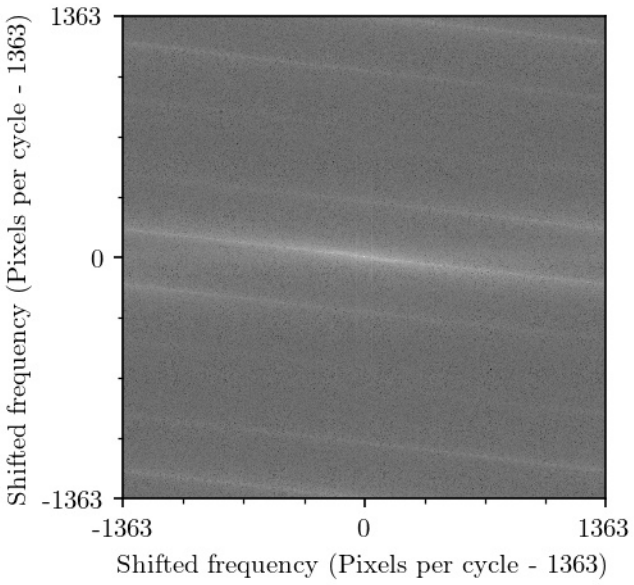

Figure 3.9: An image of the two dimensional fast Fourier transform after being appropriately phase-shifted and re-scaled for visualisation. The phase shifting (by half the image size) moves the low-frequency signal content to the centre of the image, while the re-scaling increases the contrast level. The horizontal axis is the frequency component of the pattern lying along the horizontal axis of the spatio-temporal plot, and the vertical axis is the frequency component of the pattern lying along the vertical axis of the spatio-temporal plot.

Clearly visible on Figure 3.9 are a series of white lines, with the brightest of those being at the centre. The slope of this line is a measure of the slope of the pattern in the spatio-temporal plot.

3.4.3 Velocity analysis

The slope of the line in Fourier space is more distinct and easier to measure than the pattern in the spatio-temporal space. We measure the slope of this line with two methods, linear best fit using orthogonal distance regression, and equivalent image moments.

The first step is to threshold the image, discarding any points that fall below the threshold value, so we retain only those points that display as "bright" on the image. We use 20 different threshold values, $t = 0.60, 0.61, \ldots, 0.80$, and discard any points less than $t \times I_{max}$.

In general, some points belonging to the fainter secondary lines will clear the thresholds. Although these lines have the same slope as the principal signal, their presence will serve to skew the fit. Hence, we apply a second threshold to discard any points that lie greater than n pixels distance away from the centre of the image (i.e. we discard high frequency information and seek the fundamental frequency). We set $n = 300$.

Finally, we binarise all the points that clear the threshold, setting the value of all points to either one or zero. Then we can perform our two fitting methods.

Orthogonal distance regression

Orthogonal distance regression (ODR) works similarly to classical linear regression. The essential difference is that rather than using only the vertical distance between the data point and the regression line, the ODR method takes the orthogonal distance between the data point and the regression line. This class of model is classically used to account for when there are errors in both the "independent" (x) and "dependent" (y) variables. This is suitable for our case as

they are both frequencies that are calculated from noisy spatio-temporal information. We outline the specific details of the method in Appendix B, but the general concept is illustrated in Figure 3.10

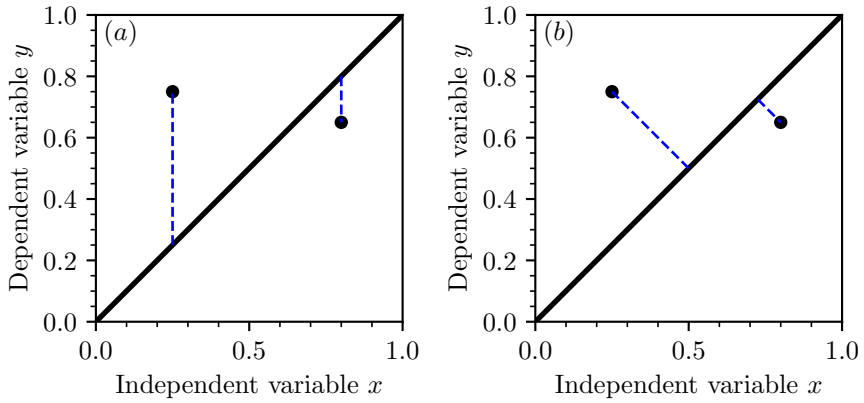

Figure 3.10: An illustration of the conceptual difference between classical linear and orthogonal distance regressions, for some arbitrary data. The classical linear regression is illustrated in (a), where we try to minimise the residuals (dotted blue lines) between the data points (black dots) and the regression line (black line) based on vertical distance. The orthogonal distance regression is illustrated in (b), where we try to minimise the residuals between the data points and regression line based on the orthogonal distance between the points and the line.

We note that much like the classical regression process, the ODR process can use an arbitrary function for the regression line. However, given the clear linear pattern evident in Figure 3.9, we use a linear function to determine the slope of the pattern. We further constrain the function to pass through the origin.

Image moments

An alternative method of determining the slope of the line is to find an ellipse that has the same "image moments" as the set of pixels in our image. This method was pioneered by Rocha et al. (2002). This method is typically used to measure the orientation of objects in an image. In our application the collection of bright pixels can be considered an object and its slope as the orientation. We outline the specific details of the method in Appendix C, but the general concept is illustrated in Figure 3.11

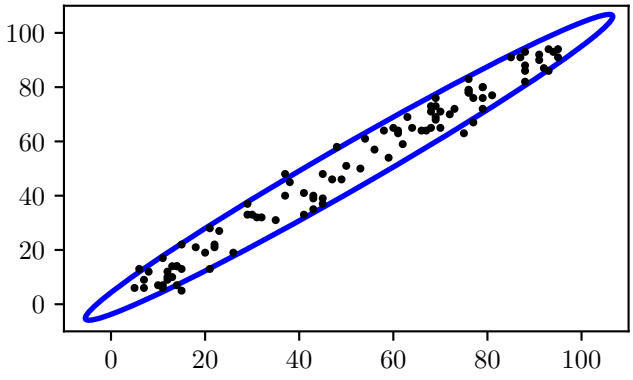

Figure 3.11: An illustration of the image moment concept, for some arbitrary data. The blue ellipse has the same set of image moments as the set of data points in black. In this particular instance the ellipse's major axis captures a region larger than the full extent of the data, while the minor axis excludes some data points. For the purposes of our velocity measurement, we are concerned only with the orientation of the ellipse relative to the signal we observe in the FFTs.

While the ODR method is well-established in the statistics community and known to be robust, the image moment method is a much more recent development from the field of image analysis that has the benefit of significantly greater

calculation speed. By using both methods we can check that our results are robust and not dependent on choice of method.

3.4.4 Determining the velocity distribution in space

In order to pass from the measurement of the slope of a pattern in Fourier space to an inferred velocity in the real world, we apply a range of processes to balance the quality of the fit with the robustness of the measurement, detailed in Appendix D. We discard any results that are unreliable due to either too few points clearing the threshold or "blow-up" due to measured angles near $\pi/2$. As the general quality of the fit increases with increasing threshold, we take the velocity measured using the highest threshold value that returns only reliable results.

We repeat this process at every radius and for each experiment to obtain a radial velocity distribution.

3.5 Results

The data that we recover from the above described process is noisy. In addition there are some errors induced by things like the camera moving slightly when the lens cap is replaced after an experiment. The information we are interested in is a description of the *shape* of the velocity distribution, rather than the absolute values. Hence we normalise the velocity by the velocity at the point at which the velocity begins to sharply decline. We manually inspect each velocity distribution to pick this point (as there are nine experiments this is not overly laborious). This point corresponds to the outer edge of the mask, and any points with a radius less than this give strongly fluctuating velocities and are harder to assign pixel-to-mm values due to the effect of the mask (which is physically closer to the camera than the particles in the sample, both of which are included in the spatio-temporal plots).

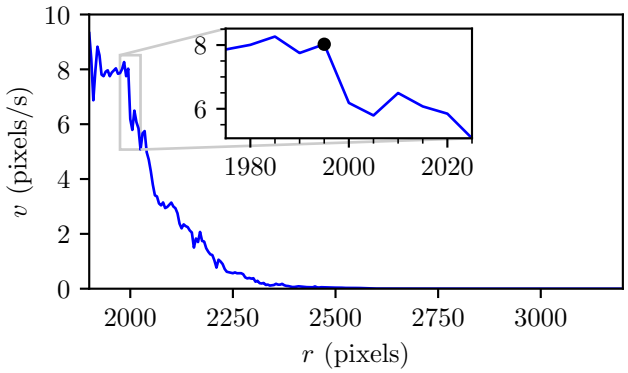

Figure 3.12: Un-normalised velocity in terms of pixels, with inset highlighting the region that we examine to pick the point at which the velocity begins to consistently decline rather than fluctuate about a relatively constant value. The inset is zoomed in on the region of interest in which we select the normalisation point, which we highlight in black. For the sake of clarity, we show only the velocity determined using the method of image moments. The data we show is taken from the first test of Set 1.

As is shown in Figure 3.12, the velocity distribution that we obtain from the above process described in § 3.4 is noisy while still showing some clear overall trends. Each of the experiments demonstrates the same trend which allows us to pick a point by which we can normalise the radius and velocity (highlighted in black in the image).

Thus, we can normalise each experiment by its appropriate normalisation point, so that they all normalised velocities have the value 1 at a normalised radius of 1. The shapes can then be compared in a meaningful way.

Figure 3.12 is typical of the velocity distributions in that the velocity measured is zero for most of the width of

the apparatus. This means that we can be confident that there is no effect due to the "step" at the outer edge of the apparatus that blocks any movement.

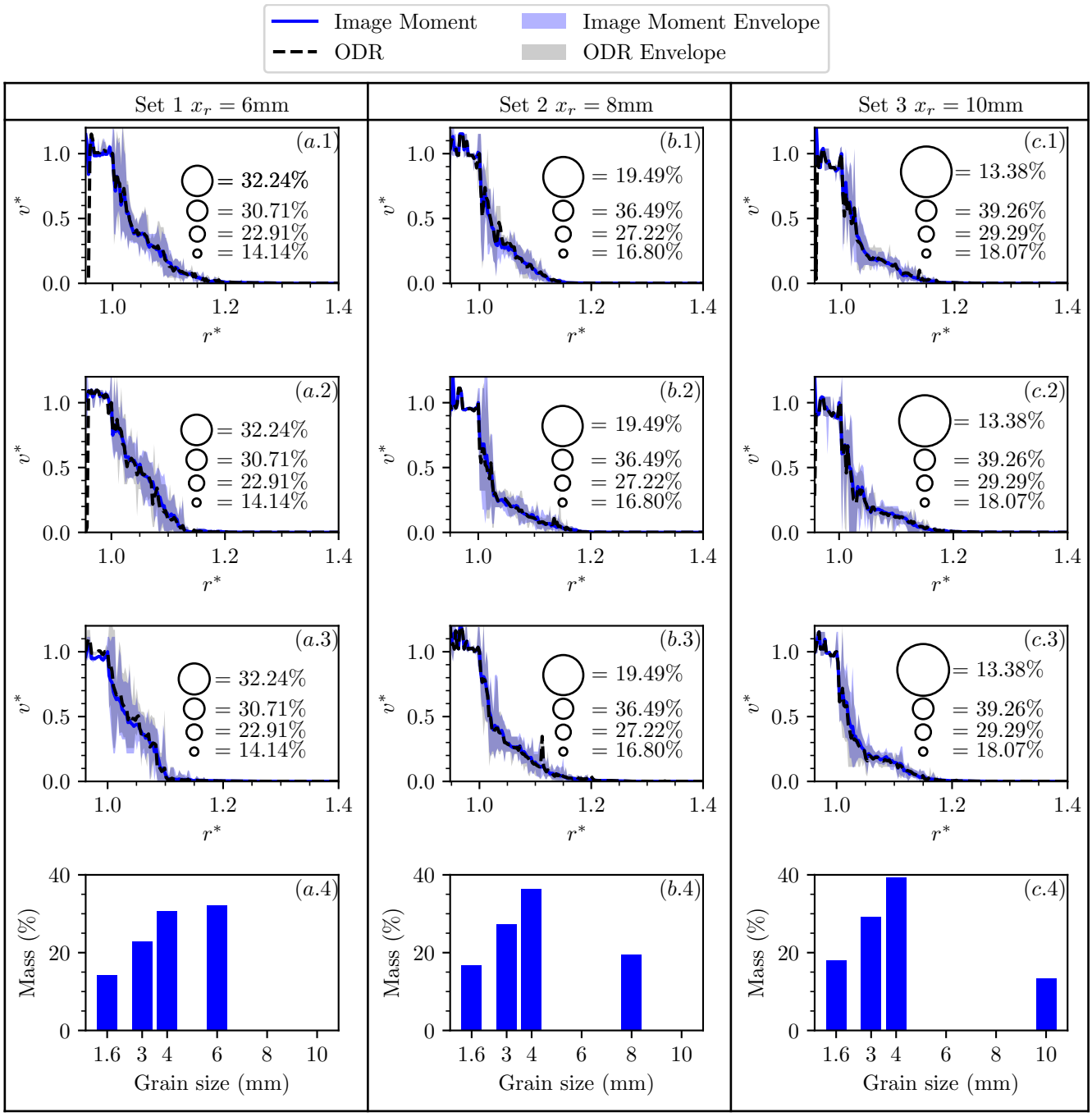

Figure 3.13: Normalised velocities for each experiment. The (a) column shows the experiments in Set 1, the (b) column the experiments in Set 2 and the (c) column the experiments in Set 3. (.1, .2, .3) indicate the first, second and third experiments in the set respectively. The normalisation point for each experiment is picked separately, and only the normalised radial distance containing interesting information is presented (for each experiment there is a large section of the apparatus with no velocity, which we exclude). Each column represents a set of experiments with the same material, with the mass percentage for each material shown in the fourth figure of the column. The envelopes in rows 1-3 are the minimum and maximum velocities over each of the 20 FFTs we perform on a given spatio-temporal plot.

For all experiments in Figure 3.13, the qualitative behaviour is similar, which is to say that there is a sharp decline in normalised velocity that reaches zero at a relatively small distance away from the wall in comparison to the overall size of the apparatus. The velocity is zero or sufficiently close to for the outer three quarters of the sample space in the apparatus. The two velocity distributions that we obtain for each experiment, using the image moment and orthogonal

distance regression methods are extremely similar in the overall distribution shape that they return, while the values at individual radial points may show some difference due to the noise. The size of the noise relative to the signal is enough that the data can benefit from a smoothing process, but not so much as to obscure the overall trends shown in the data.

To clarify the trends further, we can take the mean of each set of experiments, to more directly compare the behaviours that each exhibits.

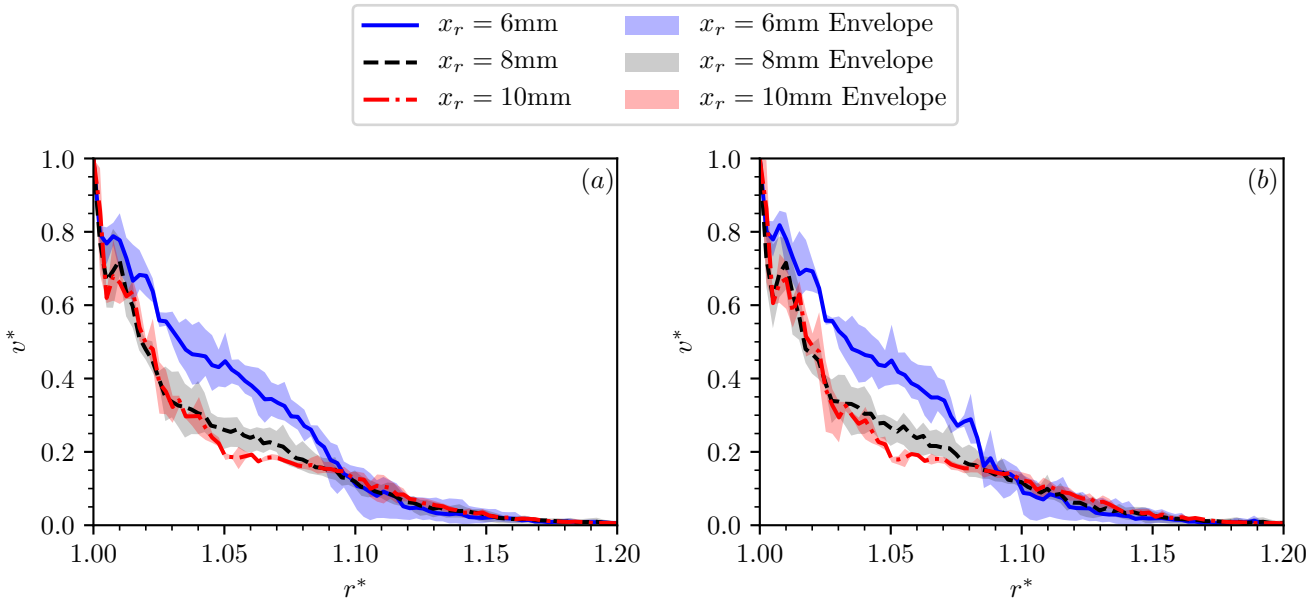

Figure 3.14: (a) The means of all three velocity distributions of each set of experiments, calculated using the method of image moments. (b) The means calculated using orthogonal distance regression. The envelopes are the minimum and maximum values from each of the three experiments done with the same material.

Figure 3.14 demonstrates that the continued good matching between the method of image moments and the orthogonal distance regression method. However, more importantly, it demonstrates a distinct difference between the distribution with $x_r = 6$mm, and those with $x_r = 8$ or 10mm. This difference is greater than the experimental error due to the method, expressed as the envelope around the mean line, and so we conclude that this most likely demonstrates a real effect due to the shape of the distribution.

3.6 Discussion

3.6.1 Smoothing

Although the tendencies of the experiments shown in Figure 3.14 are clear to the naked eye, there is still too much noise present to be able to use numerical differentiation to determine the strain rate distribution. We must smooth the data so that it is sufficiently amenable to further analysis without the noise overwhelming the signal. A simple but powerful method to smooth the data is the Savitzky-Golay filter (Savitzky and Golay, 1964), which acts as a type of low-pass filter, allowing the underlying signal through but blocking the higher frequency noise. We detail the algorithm in Appendix E, but the essential points are that we choose a smoothing window equivalent to the average particle size, and use an order one polynomial to fit. This allows for a better fit than the weighted moving average (which would correspond to an order zero polynomial), without introducing any additional "wigglyness" or over-fitting due to the selection of a higher-order polynomial.

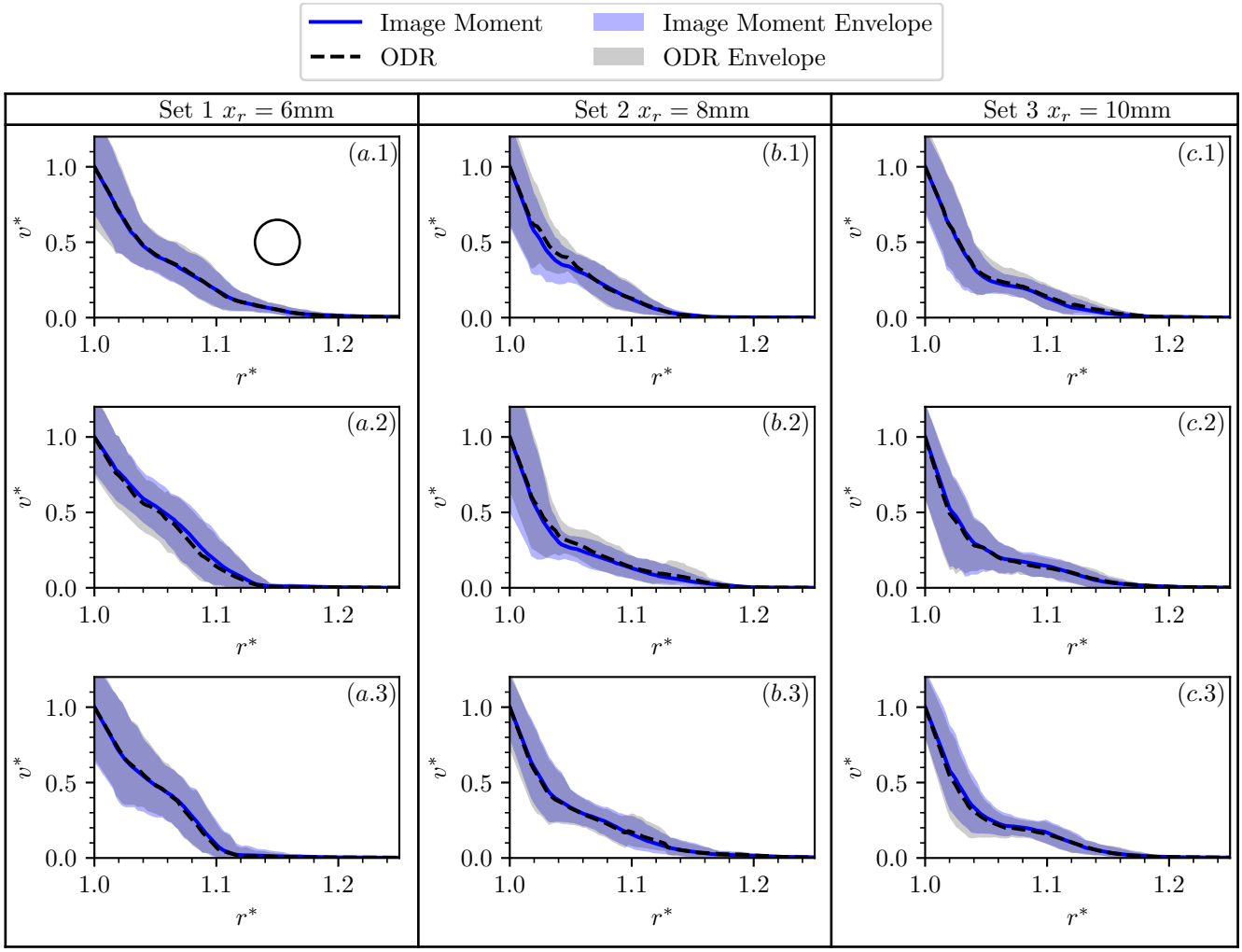

Figure 3.15: The results of the Savitzky-Golay smoothing algorithm after being applied to the normalised velocity distributions. The velocities have been renormalised so that the mean velocities once more pass through (1,1). The envelopes included are the smoothed envelopes of the minima and maxima in Figure 3.13, renormalised by the mean velocity. The average particle size (which is also the width of the smoothing window) is included on plot (a.1) for reference.

Visible in all of the sub-figures of Figure 3.15 is that there is once again good agreement between the two methods of velocity determination. Also visible is that the curves in Sets 2 and 3 display a distinct "kink" in their velocity profiles, featuring an initial region of sharp decline followed by a more gentle decline towards zero, whereas those in Set 1 have a more quasi-linear decline. These distributions may also feature a kink, but if so it is much less sharp than the kink that is very visible in Sets 2 and 3.

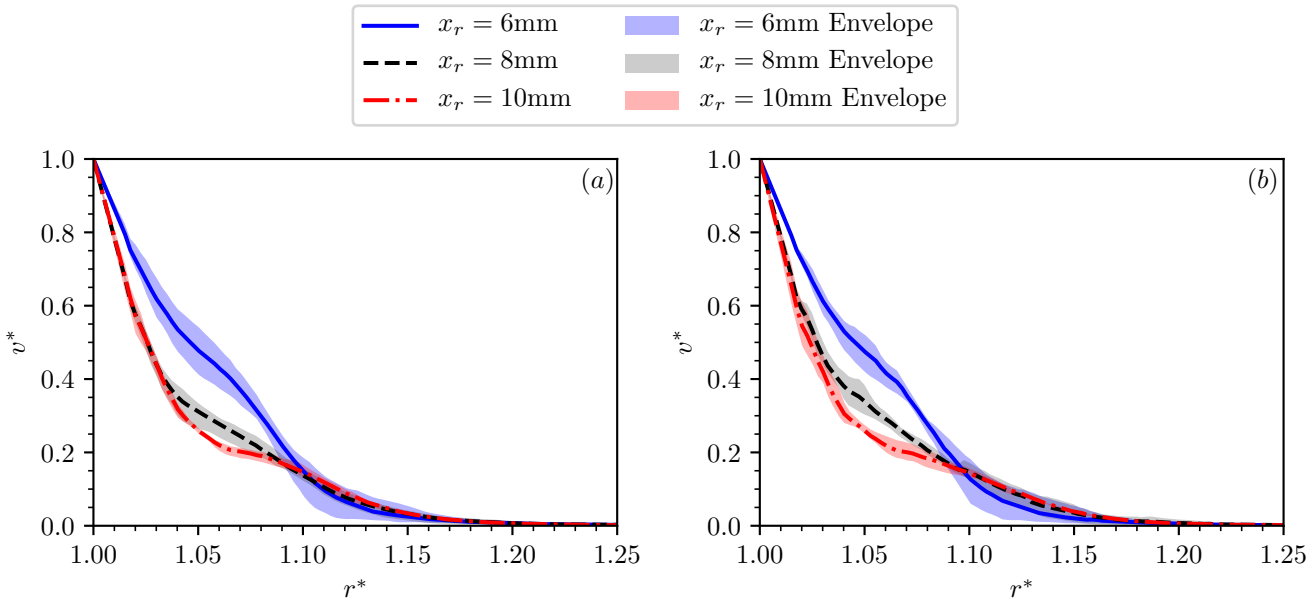

Figure 3.16: The results of the Savitzky-Golay smoothing algorithm after being applied to the mean normalised velocity distributions after the measurements inside the teeth have been discarded and renormalised. (a) are calculated using the method of image moments, and (b) are calculated with the orthogonal distance regression.

The mean velocity distributions in Figure 3.16 confirm the tendencies of the system, showing a clear separation between the first set of experiments, and the second and third.

The second and third sets of experiments demonstrate a sharper decline near the inner boundary, followed by a slower decline further away from the boundary. In the first set of experiments ($x_r = 6$mm), the slope of the initial decline is more gentle than in the other two sets, but is greater than the post-kink velocity gradient, so that it reaches zero before the other distributions.

The shape of all of the velocity distributions are strongly suggestive of the presence of shear band formation in the sample. Shear bands are characterised by the presence of a discontinuity in the strain rate gradient. We can characterise this discontinuity in one of two ways, either via the presence of the kink, or the decrease of the velocity to zero outside of a very narrow band.

3.6.2 Differentiation

In order to characterise the shear band, we need to obtain the radial shear strain rate distribution. In these conditions, the classical shear strain is simply the average of the two components of the Cosserat strain, and so we present only that as it is sufficiently illustrative of the behaviour. In addition, as the velocity declines with increasing radius, the strain rates will be negative. For the sake of clarity, we present the absolute values of the strains.

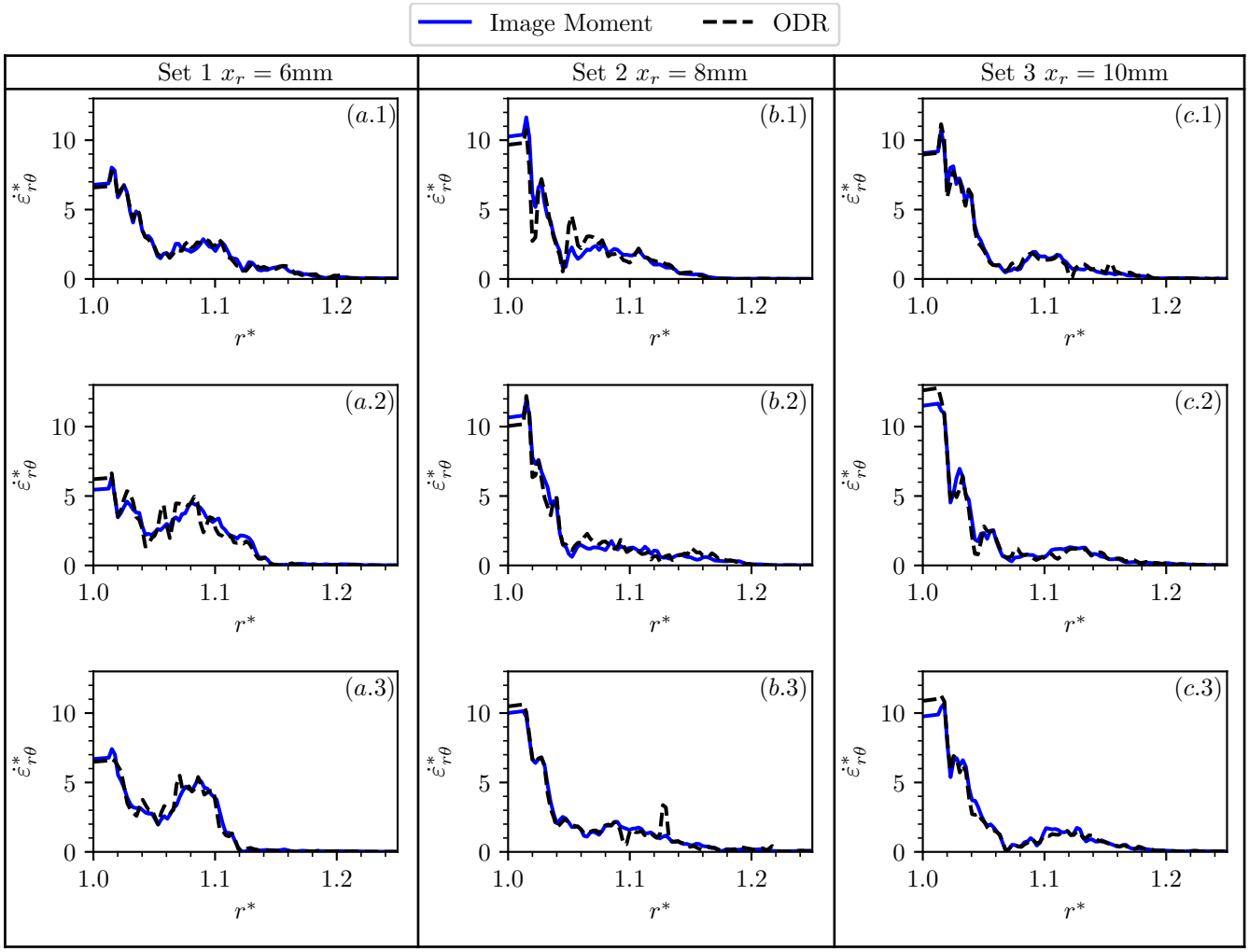

Figure 3.17: The absolute values of the (normalised) Cauchy shear strain rate $\dot{\varepsilon}_{r\theta}$. (a-c) are for the experiments with $x_r = 6$ mm,(d-f) are for those with $x_r = 8$ mm and (g-i) are for those with $x_r = 10$ mm.

We can see in Figure 3.17 that the strain rates associated with the first set of experiments have a consistently lower absolute value than those for the second and third sets in the region closest to the inner wall.

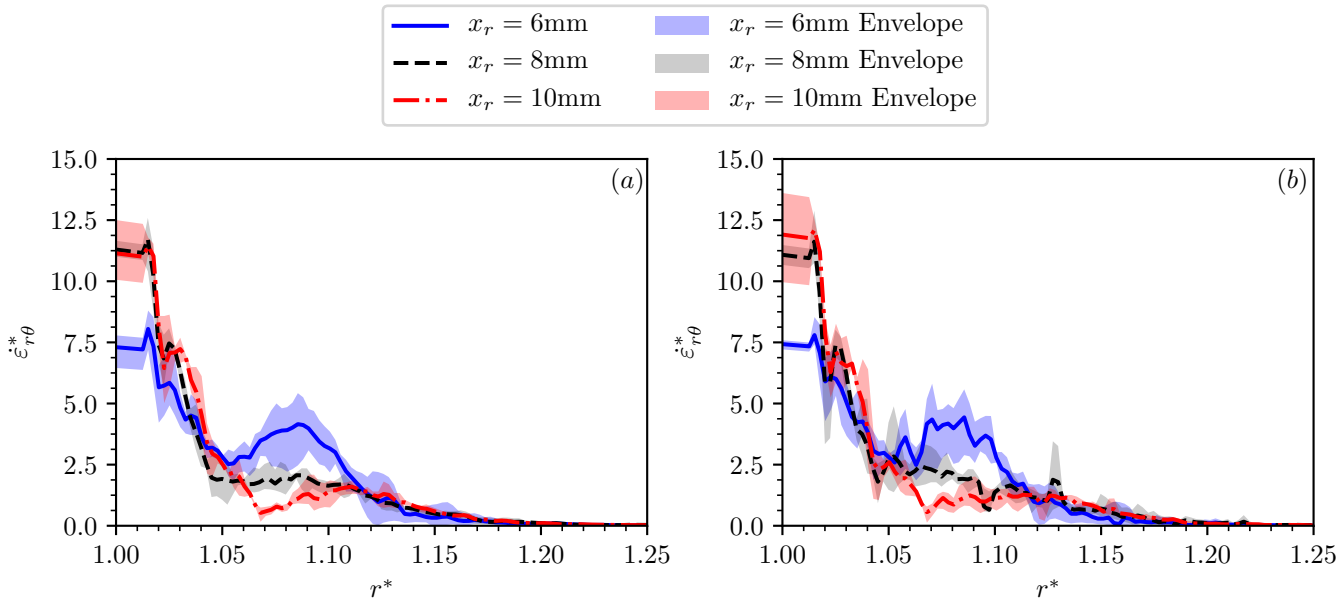

Figure 3.18: The strain rates calculated from the mean normalised velocity distribution. (a) The strain rates from the velocities calculated using the method of image moments, and (b) The strain rates from the velocities calculated using the ODR method.

Once again, from Figure 3.18 the trends of the different sets of experiments are clear, with those with $x_r = 8$mm or 10mm clearly different from those of $x_r = 6$mm. The change between a very steep decline followed by a much more gentle one is clear for Sets 2 and 3, both in terms of velocity (Figure 3.16) and shear strain rate whereas for Set 1 the velocity distribution does not show any clear signal of a kink, but the strain rate distribution, both the means in Figure 3.18 and each individual experiment in Figure 3.17, appear to show a significant kink, where the shear strain rate actually increases, suggesting that the velocity begins to decline even more rapidly. However, the noise compared to the signal is relatively large for this set of experiments, from the velocities through to the strain rates, and so it may be the case that this is not a real kink, and the true underlying behaviour is simply the quasi-linear behaviour visible on the velocity distribution.

3.6.3 Further discussion

The first set of experiments demonstrates a distinctly different behaviour from other two (b). Experiments 2 and 3 ((a.2) and (a.3) in Figure 3.13, Figure 3.15 and Figure 3.17) demonstrate a very rapid decline in velocity, reaching zero at a normalised radius of r^* of 1.14 and 1.12 respectively. Experiment 1 ((a.1) in the same figures) demonstrates a slightly different behaviour, more similar to those of Experiments 4-9, with a more gradual velocity decline reaching zero at r^* of 1.2. However it does not appear to display a strong kink, in common with the other experiments in Set 1. As a consequence of this experiment, the mean velocity distributions in Figure 3.14 and Figure 3.16 is non-zero at larger radii than it would be were this experiment excluded, which somewhat obscures the underlying trends. This is also the case for the strain rates, however Experiment 1 does appear to exhibit the same qualitative behaviour as experiments 2 and 3.

Turning to Sets 2 and 3 ((b.1-3) and (c.1-3) in Figure 3.13, Figure 3.15 and Figure 3.17), there appears to be very little difference in terms of the behaviours. When we consider both Figure 3.14 and Figure 3.16, we observe that there is a small region $\approx 1.04 \leq r^* \leq 1.09$, (occurring after the kinks in the distribution) where the velocity of Set 2 seems to be larger than that of Set 3, before once again following a very similar distribution towards zero as r^* increases. This difference is almost entirely accounted for by the experimental spread in the results from Set 2, meaning it is unlikely to be meaningful and is just due to normal experimental variance.

If we characterise the presence of the shear band by the region in which the velocity drops to zero, there is no apparent difference between Sets 2 and 3, while there is a difference between these two and Set 1. Further, if we characterise it by the kink in the velocity distribution, using the gradient of the strain rate to more precisely characterise it, there is some indication that the kink occurs at a slightly larger radii for Set 3 than for Set 2. The reason for this may be related to the nature of the particles that make up the distributions. Both Sets 2 and 3 feature "unnatural" grain size distributions in the sense that they are quite far from what would typically be found in nature (whereas Set 1 features a distribution that is consistent with natural soils). Both sets have grain size distributions with (close enough to) the same average, but this is achieved by using a bulk of smaller particles with relatively few much larger particles and nothing in between. The effect of this distribution may be to cause the behaviour to be governed largely by an "effective average grain size" that is the average of the bulk of smaller particles. This would explain why the behaviour of Sets 2 and 3 are largely very similar, because they are both sparse enough in large grains to trigger this sort of behaviour, whereas Set 1 has a smoother continuum type behaviour that engages all of the large particles in carrying the force chains. However, the difference between Sets 2 and 3 may be explained purely by the size of the largest particle present. These particles may disrupt the continuum flow and cause an even sharper decline than what may otherwise be the case. The kink may then occur at a larger radii for Set 3 than for Set 2 purely due to the largest particle size being slightly larger.

Finally, we note that in general, the decay in velocities that we observe is imposed by our choice of a cylindrical test geometry. However, given that we impose the same boundary conditions on all of our tests, but do not observe the same rate of velocity decay, we may infer that the rate of decay which determines the shear band thickness is governed in some way by the polydispersity. Our data does not allow us to determine whether the polydispersity affects only the plastic behaviour, or whether the elastic behaviour is also significantly changed. Future experiments could use techniques such as photoelasticimetry (Abed Zadeh et al., 2019) to trace the micro-mechanical origins of the bulk behaviour, and determine whether and to what extent inter-particle force distributions are changed by increasing the polydispersity of the medium. Further investigations in other geometries (such as the Stadium Shear Device (Miller, 2014)) would strengthen our conclusions by demonstrating that the behaviours we observe are truly micro-mechanical in origin and are not legacies of our experimental geometry. Experiments of this nature would allow modellers significant insight into how to include measures of polydispersity in their models.

3.7 Conclusion

These experiments were conducted in the context of inferring information that would be relevant to the construction of sophisticated models for granular media. In particular, Cosserat continuum models that are endowed with an internal length scale have used the average grain size as this length scale, and we wished to see whether this parameter was sufficient to characterise the material behaviour. By performing three sets of experiments, each of which used media with the same mean grain size, but different grain size distributions, we can conclude with confidence that the mean grain size is *insufficient* to fully characterise material behaviour. We may draw this conclusion on the basis that although the mean grain size was identical, different materials demonstrated different behaviours with respect to shear band formation. The material where the largest particle was 6 mm demonstrated a quasi-linear decline of velocity and in two out of the three experiments reached zero velocity at significantly smaller radii than the experiments with larger maximum grain size. Although the materials with maximum grain sizes of 8 mm and 10 mm declined to zero velocity at larger radii, they also demonstrated a distinct kink in their velocity profiles where they changed from an initial extremely rapid velocity decline to a much more gradual decline. In addition, the velocity profiles of these two experimental sets are very similar, with possibly the only difference being a kink point at a larger radius for the set with maximum grain size 10 mm compared to that for the set with maximum grain size 8 mm.

From this analysis we may infer that under constant mean grain size, increasing polydispersity increases the thickness of shear band, but perhaps only to a point. However, the increase of this thickness is significant, with the distributions

with 8 and 10 mm maximum particle sizes being on the order of 25-33% thicker than the distribution with 6 mm maximum particle size.

Based on the similar results returned by both the ODR and image moment methods for the velocity, and the size of the data spread we observe both within the experiments and over each set of experiments, we may conclude that these results are robust for these grain size distributions. However, as previously noted, this chapter serves mostly to develop a method by which we can validate future models for their predictions of shear bands, which required a large range of grain sizes. In order to develop truly robust experimental inferences about the interplay of grain size and polydispersity in forming shear bands, a much wider range of materials must be tested. In particular, more "realistic" grain size distributions with a smoother transition from large to small grains should be explored. It is possible that the observed difference in behaviour between Set 1 and Sets 2 and 3 could be explained as the difference between a polydisperse distribution (Set 1) and two relatively homogeneous distributions with occasional large intruder particles (Sets 2 and 3). However, if Sets 2 and 3 could be characterised in this way, we would expect smaller shear bands than those demonstrated in Set 1, given the well-known scaling of shear bands with mean grain size. While we could also imagine that it is in fact the larger grain sizes that dominate the behaviour, we would then expect an approximately 25% thicker shear band in Set 3 than in Set 2, which we do not observe. Hence we conclude that the most likely explanation is that all three sets are behaving as truly polydisperse distributions, and the observed differences in behaviour are due to the differences in polydispersity.

As the results of these experiments indicate, the effect of polydispersity on the size of shear bands may be less than that of the mean grain size, but it is not negligible. While a full experimental exploration of the exact relationship is beyond the scope of this thesis, the behaviour we have observed in these experiments contains important insights for modelling, namely that not only should modellers track the evolution of the mean grain size, they should also include measures of the polydispersity when developing models to predict deformation bands. With this in mind, in the following chapter we develop a model that includes information on the entire grain size distribution as well as the enriched kinematics that will allow it to predict shear band thickness.

Chapter 4

Formulating Breakage Mechanics in the Cosserat continuum

4.1 Summary

In this chapter we present the development of a model that combines Breakage Mechanics and the Cosserat continuum. The Breakage model chosen is that outlined in Nguyen and Einav (2009), as the simplest current model capable of being extended to the Cosserat continuum. Although there are currently a number of more general Breakage models, notably ones that include porosity and dilation (Tengattini, 2015), in the following we proceed with a simpler Breakage model to ease the implementation and understanding, as the Cosserat continuum introduces additional complexity due to the additional degrees of freedom. The benefit of this additional complexity is the ability to predict not only the existence but also the thickness of localisations such as shear bands. As discussed in the literature review, these structures are pervasive in both the field and the laboratory, meaning that any complete model of brittle granular media must be able to account for them. The model that we outline in this chapter can serve as a foundation for more complicated future models that take into account porosity, damage and pressure-dependent elasticity (Das et al., 2014; Tengattini et al., 2016, 2014b).

4.2 Introduction

This chapter is organised as follows: first, the definitions of strain $\dot{\gamma}_{ij}$ and curvature $\dot{\kappa}_{ij}$ rate tensors are introduced, and then the definitions of the stress τ_{ij} and couple-stress μ_{ij} tensors, as well as the breakage index B. An elastic upscaling procedure is detailed that allows the definition of two new material constants related to grading, θ_κ and θ_I, and a study of their limiting behaviours is conducted. A material length scale that arises naturally from the elastic upscaling is also defined. The constitutive model is then outlined, including a generalised definition of the second deviatoric invariants and methods to calibrate the Cosserat elastic stiffnesses as functions of the classical bulk and shear stiffnesses, assuming linear isotropic elasticity.

4.3 Definitions

4.3.1 Strain and curvature rates

In a Cosserat continuum, the material points have six degrees of freedom, those of translation that exist also in the classical continuum, and three degrees of rotational freedom.

The infinitesimal (non-symmetric) strain rate tensor is defined as

$$\dot{\gamma}_{ij} = \begin{bmatrix} \frac{\partial \dot{u}_1}{\partial x_1} & \frac{\partial \dot{u}_1}{\partial x_2} + \dot{\omega}_3^c & \frac{\partial \dot{u}_1}{\partial x_3} - \dot{\omega}_2^c \\ \frac{\partial \dot{u}_2}{\partial x_1} - \dot{\omega}_3^c & \frac{\partial \dot{u}_2}{\partial x_2} & \frac{\partial \dot{u}_2}{\partial x_3} + \dot{\omega}_1^c \\ \frac{\partial \dot{u}_3}{\partial x_1} + \dot{\omega}_2^c & \frac{\partial \dot{u}_3}{\partial x_2} - \dot{\omega}_1^c & \frac{\partial \dot{u}_3}{\partial x_3} \end{bmatrix}, \tag{4.1}$$

where $\dot{u}_i$ and $\dot{\omega}_i^c$ are the translation and rotation rates along and about the x_i axes.

The strain rate tensor can be split into symmetric and anti-symmetric parts, denoted $\dot{\gamma}_{(ij)}$ and $\dot{\gamma}_{[ij]}$ respectively. The symmetric part of the tensor is identical to the infinitesimal strain rate tensor in the classical continuum, so the equation may also be written

$$\dot{\gamma}_{ij} = \dot{\varepsilon}_{ij} + \dot{\gamma}_{[ij]}, \tag{4.2}$$

where

$$\dot{\varepsilon}_{ij} = \begin{bmatrix} \frac{\partial \dot{u}_1}{\partial x_1} & \frac{1}{2}\left(\frac{\partial \dot{u}_1}{\partial x_2} + \frac{\partial \dot{u}_2}{\partial x_1}\right) & \frac{1}{2}\left(\frac{\partial \dot{u}_1}{\partial x_3} + \frac{\partial \dot{u}_3}{\partial x_1}\right) \\ \frac{1}{2}\left(\frac{\partial \dot{u}_2}{\partial x_1} + \frac{\partial \dot{u}_1}{\partial x_2}\right) & \frac{\partial \dot{u}_2}{\partial x_2} & \frac{1}{2}\left(\frac{\partial \dot{u}_2}{\partial x_3} + \frac{\partial \dot{u}_3}{\partial x_2}\right) \\ \frac{1}{2}\left(\frac{\partial \dot{u}_3}{\partial x_1} + \frac{\partial \dot{u}_1}{\partial x_3}\right) & \frac{1}{2}\left(\frac{\partial \dot{u}_3}{\partial x_2} + \frac{\partial \dot{u}_2}{\partial x_3}\right) & \frac{\partial \dot{u}_3}{\partial x_3} \end{bmatrix}, \tag{4.3}$$

and

$$\dot{\gamma}_{[ij]} = \begin{bmatrix} 0 & \frac{1}{2}\left(\frac{\partial \dot{u}_1}{\partial x_2} - \frac{\partial \dot{u}_2}{\partial x_1}\right) + \dot{\omega}_3^c & \frac{1}{2}\left(\frac{\partial \dot{u}_1}{\partial x_3} - \frac{\partial \dot{u}_3}{\partial x_1}\right) - \dot{\omega}_2^c \\ \frac{1}{2}\left(\frac{\partial \dot{u}_2}{\partial x_1} - \frac{\partial \dot{u}_1}{\partial x_2}\right) - \dot{\omega}_3^c & 0 & \frac{1}{2}\left(\frac{\partial \dot{u}_2}{\partial x_3} - \frac{\partial \dot{u}_3}{\partial x_2}\right) + \dot{\omega}_1^c \\ \frac{1}{2}\left(\frac{\partial \dot{u}_3}{\partial x_1} - \frac{\partial \dot{u}_1}{\partial x_3}\right) + \dot{\omega}_2^c & \frac{1}{2}\left(\frac{\partial \dot{u}_3}{\partial x_2} - \frac{\partial \dot{u}_2}{\partial x_3}\right) - \dot{\omega}_1^c & 0 \end{bmatrix}. \tag{4.4}$$

In a Cosserat continuum, there also exists a curvature rate tensor, defined as

$$\dot{\kappa}_{ij} = \begin{bmatrix} \frac{\partial \dot{\omega}_1^c}{\partial x_1} & \frac{\partial \dot{\omega}_1^c}{\partial x_2} & \frac{\partial \dot{\omega}_1^c}{\partial x_3} \\ \frac{\partial \dot{\omega}_2^c}{\partial x_1} & \frac{\partial \dot{\omega}_2^c}{\partial x_2} & \frac{\partial \dot{\omega}_2^c}{\partial x_3} \\ \frac{\partial \dot{\omega}_3^c}{\partial x_1} & \frac{\partial \dot{\omega}_3^c}{\partial x_2} & \frac{\partial \dot{\omega}_3^c}{\partial x_3} \end{bmatrix}. \tag{4.5}$$

As with the strain rate tensor, the curvature rate tensor may also be decomposed into symmetric and anti-symmetric parts:

$$\dot{\kappa}_{ij} = \dot{\kappa}_{(ij)} + \dot{\kappa}_{[ij]}. \tag{4.6}$$

The total strain rate and curvature rate tensors (4.1) and (4.5) can also be compactly written respectively as

$$\dot{\gamma}_{ij} = \dot{u}_{i,j} + \epsilon_{ijk}\dot{\omega}_k^c, \tag{4.7}$$

and

$$\dot{\kappa}_{ij} = \dot{\omega}_{i,j}^c, \tag{4.8}$$

where the Einstein summation convention was used, which we follow from this point onward, and where ϵ_{ijk} is the Levi-Civita symbol, given by

$$\epsilon_{ijk} = \begin{cases} +1 \text{ if } (i,j,k) \text{ is } (1,2,3), (2,3,1) \text{ or } (3,1,2), \\ -1 \text{ if } (i,j,k) \text{ is } (3,2,1), (1,3,2) \text{ or } (2,1,3), \\ 0 \text{ otherwise.} \end{cases} \tag{4.9}$$

Both strain and curvature rate tensors can also be split into trace and deviatoric parts:

$$\dot{\gamma}_{ij} = \frac{1}{3}\dot{\varepsilon}_{kk}\delta_{ij} + \dot{e}_{ij}, \tag{4.10}$$

$$\dot{\kappa}_{ij} = \frac{1}{3}\dot{\kappa}_{kk}\delta_{ij} + \dot{k}_{ij}, \tag{4.11}$$

where δ_{ij} is the Kronecker delta, given by

$$\delta_{ij} = \begin{cases} 0 \text{ if } i \neq j, \\ 1 \text{ if } i = j. \end{cases} \tag{4.12}$$

The summation $\dot{\varepsilon}_{kk}$ is equivalent to the volumetric strain rate $\dot{\varepsilon}_v$. The deviatoric parts can be further decomposed into symmetric and anti-symmetric components

$$\dot{e}_{ij} = \dot{e}_{(ij)} + \dot{e}_{[ij]}, \tag{4.13}$$

$$\dot{k}_{ij} = \dot{k}_{(ij)} + \dot{k}_{[ij]}. \tag{4.14}$$

4.3.2 Plasticity framework

Later in this chapter, we develop a constitutive model within the context of rate-independent plasticity. The strain and curvature rates are decomposed into elastic (recoverable) and plastic (non-recoverable) parts:

$$\dot{\gamma}_{ij} = \dot{\gamma}^e_{ij} + \dot{\gamma}^p_{ij}, \tag{4.15}$$

$$\dot{\kappa}_{ij} = \dot{\kappa}^e_{ij} + \dot{\kappa}^p_{ij}. \tag{4.16}$$

The decompositions of the elastic and plastic parts into their respective volumetric and deviatoric, symmetric and anti-symmetric parts follow as for the total rate tensors above.

We hold to the convention that constitutive models must not rely on arbitrary reference-dependent variables (Rubin, 2001). As such, the elastic strain and curvature tensors, γ^e_{ij} and κ^e_{ij}, are used as state variables in the model, but not the plastic and total strain and curvature tensors.

4.3.3 Stresses and couple-stresses

The stress tensor in a Cosserat continuum is, in general, non-symmetric like the strain rate tensor. The tensor can be decomposed into symmetric and anti-symmetric parts, and the symmetric part is identified with the Cauchy stress tensor of the classical continuum:

$$\tau_{ij} = \sigma_{ij} + \tau_{[ij]}. \tag{4.17}$$

In the Cosserat continuum, there is also a couple-stress tensor, that can be decomposed similarly:

$$\mu_{ij} = \mu_{(ij)} + \mu_{[ij]}. \tag{4.18}$$

Both of these tensors can also be decomposed into volumetric and deviatoric parts:

$$\tau_{ij} = \frac{1}{3}\tau_{kk}\delta_{ij} + s_{ij}, \tag{4.19}$$

$$\mu_{ij} = \frac{1}{3}\mu_{kk}\delta_{ij} + m_{ij}. \tag{4.20}$$

$\frac{1}{3}\tau_{kk}$ is equivalent to the mean stress p. As with the strain, the deviatoric stresses can be further split into symmetric and anti-symmetric parts:

$$s_{ij} = s_{(ij)} + s_{[ij]}, \tag{4.21}$$

$$m_{ij} = m_{(ij)} + m_{[ij]}. \tag{4.22}$$

4.3.4 Breakage state variable

The breakage state variable B is defined by the ratio of the area between the current and initial cumulative grain size distributions (GSDs) to the area between the ultimate and initial cumulative grain size distributions, as shown in Figure 4.1.

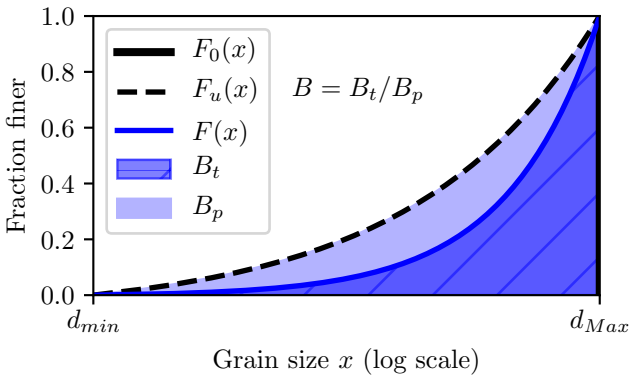

Figure 4.1: A plot showing the definition of the breakage variable B as the ratio of two grading areas. $F_0(x), F_u(x)$ and $F(x)$ are the initial, ultimate and current cumulative GSDs respectively. d_{min} and d_{Max} are the minimum and maximum grain sizes present in the GSDs.

The maximum grain size d_{Max} is constant between the initial and ultimate distributions, as grains cannot grow when undergoing a crushing process, and some proportion of the largest grains will remain intact even when the ultimate distribution is reached. d_{min} is the smallest grain size possible to obtain due to comminution, typically taken to be one micron (Kendall, 1978).

This definition of breakage is consistent with that given in Einav (2007a) and Buscarnera and Einav (2012). In particular, we make use of the universal initial distribution from Buscarnera and Einav (2012) (both in Figure 4.1 and throughout this thesis), given by

$$F_0(x) = H(x - d_{Max}), \tag{4.23}$$

for the cumulative distribution (where $H(\dots)$ represents the Heaviside step function). For the probability density function of the initial GSD, we may write

$$p_0(x) = \delta(x - d_{Max}), \tag{4.24}$$

where $\delta(\dots)$ represents the Dirac delta function.
The ultimate grain size distribution is assumed to follow a power-law distribution, based on evidence from exhumed fault gouges (Chester and Chester, 1998; Sammis et al., 1987) and arguments assuming self-similarity between grains of different sizes (Turcotte, 1986). The cumulative ultimate distribution is given by

$$F_u(x) = \frac{x^{3-\alpha} - {d_{min}}^{3-\alpha}}{{d_{Max}}^{3-\alpha} - {d_{min}}^{3-\alpha}}, \tag{4.25}$$

and the corresponding probability density function is given by

$$p_u(x) = (3-\alpha)\frac{x^{2-\alpha}}{{d_{Max}}^{3-\alpha} - {d_{min}}^{3-\alpha}}, \tag{4.26}$$

where α is a material constant defining the power law, with typical values between 2.5 and 2.7.

Using these definitions for the initial and ultimate grain size distributions, the current cumulative grain size distribution is defined as a function of the breakage:

$$F(x, B) = F_0(x)(1 - B) + F_u(x)B. \tag{4.27}$$

The corresponding probability density function is now given by

$$p(x, B) = p_0(x)(1 - B) + p_u(x)B. \tag{4.28}$$

The introduction of the breakage variable requires the introduction of its thermodynamic conjugate E_B, the breakage energy, that is a physical expression of how much energy can be liberated by the entire process of grain crushing from the initial GSD to the ultimate GSD.

4.4 Upscaling procedures

4.4.1 Elastic upscaling

The previous models of Breakage Mechanics that we discussed in the literature review have been formulated in either the classical continuum, or a non-local continuum. To formulate Breakage Mechanics in a Cosserat continuum, a statistical homogenisation process is undertaken that takes account of the contribution of the stored energy of the elastic curvatures when upscaled from the granular medium to the continuum formulation.

This process starts by considering the Helmholtz free energy density per unit volume. The function is given by

$$\Psi = \Psi(\gamma^e_{ij}, \kappa^e_{ij}, B) = \int_{d_{min}}^{d_{Max}} \hat{\psi}(\gamma^e_{ij}, \kappa^e_{ij}, x)p(x, B)\,\mathrm{d}x. \tag{4.29}$$

That is to say, the total Helmholtz free energy density is the Helmholtz free energy density at a given grain size x, weighted by the grain size distribution $p(x, B)$, integrated over the entire distribution.

The energy density is assumed to be further decomposed into a summation of elastic strain contributions and elastic curvature contributions:

$$\hat{\psi}(\gamma^e_{ij}, \kappa^e_{ij}, x) = \hat{\psi}_\gamma(\gamma^e_{ij}, x) + \hat{\psi}_\kappa(\kappa^e_{ij}, x). \tag{4.30}$$

Now we use the assumption of fractional independence from Einav (2007a) to make a separation of variables. This process was motivated by Discrete Element Method (DEM) simulations of granular media that revealed the underlying relationship between grain size and stored energy. The Helmholtz free energy contribution for a grain size x due to the strains is

$$\hat{\psi}_\gamma(\gamma^e_{ij}, x) = \left(\frac{x}{x_r}\right)^2 \psi_{r\gamma}(\gamma^e_{ij}), \tag{4.31}$$

where the subscript r represents a reference grain size fraction.

We can apply the same assumption of fractional independence to the contribution of the curvatures. However, in order for the energy density to have the correct dimensionality to contribute correctly to the Helmholtz free energy the elastic curvature terms must be further multiplied by some length scale ℓ^2. Micro-mechanically, smaller particle sizes

have fewer particle contacts and so participate in fewer force chains. They are also typically less angular, meaning there is less particle interlocking (Andò et al., 2012). Hence, we expect that the rotation rate of the grains and thus ultimately the elastic curvatures will scale with the grain size x. We also note that there is no information-passing mechanism that would allow an individual grain's behaviour to rely on any size other than its own. Hence, we set $\ell^2 = x^2$ and state that the Helmholtz free energy contribution for a grain size x due to the elastic curvatures is

$$\hat{\psi}_\kappa(\kappa^e_{ij}, x) = \left(\frac{x}{x_r}\right)^2 x^2 \hat{\psi}_{r\kappa}(\kappa^e_{ij}) = \left(\frac{x}{x_r}\right)^4 {x_r}^2 \psi_{r\kappa}(\kappa^e_{ij}). \tag{4.32}$$

Making successive back substitutions of the relevant expressions, the Helmholtz free energy expression becomes

$$\Psi = \int_{d_{min}}^{d_{Max}} \left(\left(\frac{x}{x_r}\right)^2 \hat{\psi}_{r\gamma}(\gamma^e_{ij}) + \left(\frac{x}{x_r}\right)^4 {x_r}^2 \psi_{r\kappa}(\kappa^e_{ij}) \right) p(x, B)\, \mathrm{d}x. \tag{4.33}$$

As the maximum grain size is the only one present in all the GSDs, from the initial to the ultimate, we select that as the reference grain size x_r:

$$x_r = d_{Max}. \tag{4.34}$$

We can split (4.33) into two integrals and insert (4.34):

$$\Psi = \Psi_\gamma + \Psi_\kappa = \frac{\psi_{r\gamma}(\gamma^e_{ij})}{{x_r}^2} \int_{d_{min}}^{d_{Max}} x^2 p(x, B)\, \mathrm{d}x + {x_r}^2 \frac{\psi_{r\kappa}(\kappa^e_{ij})}{{x_r}^4} \int_{d_{min}}^{d_{Max}} x^4 p(x, B)\, \mathrm{d}x. \tag{4.35}$$

Now, we note that the statistical moments of the distributions (about the origin) are defined by

$$J^n(B) = \int_{d_{min}}^{d_{Max}} x^n p(x, B)\, \mathrm{d}x. \tag{4.36}$$

Simple inspection of (4.35) shows that the two integrals give the second and fourth moments of the current grain size distribution. We first turn our attention to the strain integral Ψ_γ. Substituting in (4.28) and evaluating the integral returns the moments of the initial and ultimate grain size distributions. Conveniently, because of our choice of F_0, the nth statistical moment of the initial distribution $J^n_0 = {x_r}^n$. Introducing the material constant θ_γ by

$$\theta_\gamma = 1 - \frac{J^2_u}{{x_r}^2}, \tag{4.37}$$

allows us to re-arrange Ψ_γ to obtain

$$\Psi_\gamma = (1 - \theta_\gamma B)\psi_{r\gamma}(\gamma^e_{ij}), \tag{4.38}$$

which is the classical Breakage Mechanics expression for the Helmholtz free energy per Einav (2007a), noting however that the strain tensor is not symmetric here.

This expression can be further separated into symmetric and anti-symmetric contributions:

$$\Psi_\gamma = \Psi_{(\gamma)} + \Psi_{[\gamma]} = (1 - \theta_\gamma B)(\psi_{r(\gamma)}(\gamma^e_{(ij)}) + \psi_{r[\gamma]}(\gamma^e_{[ij]})). \tag{4.39}$$

This process can be repeated for the curvature integral Ψ_κ in (4.35), once again substituting in (4.28) and evaluating the integral to obtain the fourth moments of the initial and ultimate distributions. We can introduce a new material constant θ_κ defined by

$$\theta_\kappa = 1 - \frac{J^4_u}{{x_r}^4}, \tag{4.40}$$

which allows us to rewrite Ψ_κ in the form

$$\Psi_\kappa = (1 - \theta_\kappa B){x_r}^2 \psi^*_{r\kappa}(\kappa^e_{ij}). \tag{4.41}$$

This formulates the stored energy due to the elastic curvatures in a manner consistent with classical Breakage Mechanics.

Hence, the total Helmholtz free energy can be written

$$\Psi = (1-\theta_\gamma B)(\psi_{r(\gamma)}(\gamma^e_{(ij)}) + \psi_{r[\gamma]}(\gamma^e_{[ij]})) + (1-\theta_\kappa B){x_r}^2\psi_{r\kappa}(\kappa^e_{ij}). \tag{4.42}$$

We now compare this expression for the total elastic energy with that given in the extensive treatment of Cosserat continuum mechanics by Vardoulakis (2019) for isotropic linear Cosserat elasticity:

$$\Psi = \frac{2\nu G}{1-2\nu}\varepsilon^e_{ii}\varepsilon^e_{jj} + G\varepsilon^e_{ij}\varepsilon^e_{ij} + \eta_1 G\gamma^e_{[ij]}\gamma^e_{[ij]} + 6\eta_1 G\gamma^*_k\gamma^*_k + \frac{1}{2}G\ell^2(\kappa^e_{(ij)}\kappa^e_{(ij)} + \eta_2\kappa^e_{(ii)}\kappa^e_{(jj)} + \eta_3\kappa^e_{[ij]}\kappa^e_{[ij]}). \tag{4.43}$$

The elastic length terms multiplying the terms associated with the elastic curvatures can be directly identified in the form given by Vardoulakis (2019), and this comparison makes explicit the identification of the elastic length when Breakage Mechanics is upscaled as above:

$$\ell^e = x_r\sqrt{1-\theta_\kappa B}. \tag{4.44}$$

We highlight here that the elastic length scale we have derived depends on the *entire* grain size distribution through the new material constant θ_κ, and evolves as the Breakage variable evolves.

It should also be noted that as a consequence of the length scale being multiplied out of the expression for the energy due to curvature, the elastic parameters will have units solely of stress, and not couple-stress unlike other authors (Rattez et al., 2018a).

4.4.2 Inertial upscaling

The momentum balance equations of the Cosserat continuum are given by

$$\tau_{ij,j} - \rho\frac{\partial^2 u_i}{\partial t^2} = 0, \tag{4.45}$$

$$\mu_{ij,j} - \epsilon_{ijk}\tau_{jk} - I\frac{\partial^2 \omega^c_i}{\partial t^2} = 0. \tag{4.46}$$

Importantly, at the level of the Representative Volume Element (RVE), the rotational momentum balance is included, and hence the moment of rotational inertia, I, of the medium must be defined in order to fully specify the continuum. Previously, this has been taken as the moment of inertia associated only with the average particle size (Rattez et al., 2018a,b,c; Sulem et al., 2011). However, Breakage Mechanics enables consideration of the entire grain size distribution, and so the average of the moments of inertia of all the particles is selected, and how it changes as a function of grain breakage must be modelled.

An upscaling on the three dimensional case is performed, as it necessitates the definition of a new material parameter, whereas the two dimensional case does not.

The rotational moment of inertia of a solid sphere of diameter x about its own axis is given by

$$I = \frac{\pi}{60}\rho x^5, \tag{4.47}$$

where ρ is the density of the particle.

As particle breakage progresses, more (and smaller) particles appear inside the RVE. It is assumed that each of these particles rotates around its own proper axis, but not around any other point.

Now, to find the average of the moments of inertia, the integration is performed over the continuous particle size distribution:

$$I(B) = \frac{\pi}{60}\rho \int_{d_{min}}^{d_{Max}} x^5 p(x,B)\,\mathrm{d}x = \frac{\pi}{60}\rho {x_r}^5 \int_{d_{min}}^{d_{Max}} \left(\frac{x}{x_r}\right)^5 \big(p_0(x)(1-B) + p_u(x)B\big)\,\mathrm{d}x. \tag{4.48}$$

Evaluating the integral and using the definitions of the fifth moments J_0^5 and J_u^5 results in

$$I(B) = \frac{\pi}{60}\rho {x_r}^5 \frac{(1-B)J_0^5 + BJ_u^5}{{x_r}^5}. \tag{4.49}$$

Once again exploiting that $J_0^5 = {x_r}^5$ and introducing another material constant:

$$\theta_I = 1 - \frac{J_u^5}{{x_r}^5}, \tag{4.50}$$

the expression for the rotational inertia can be re-arranged to

$$I(B) = \frac{\pi}{60}(1-\theta_I B)\rho {x_r}^5, \tag{4.51}$$

in three dimensions.

It should be noted that the rotational moment of inertia for a disc of diameter x in two dimensions is

$$I = \frac{\pi}{32}\rho x^4 \tag{4.52}$$

If the above analysis were repeated in two dimensions, there would be identical definitions between θ_I and θ_κ. Hence, the rotational inertia is

$$I(B) = \begin{cases} \frac{\pi}{32}(1-\theta_\kappa B)\rho {x_r}^4 & \text{in two dimensions,} \\ \frac{\pi}{60}(1-\theta_I B)\rho {x_r}^5 & \text{in three dimensions.} \end{cases} \tag{4.53}$$

4.4.3 Limit values

The expressions for θ_γ, θ_κ and θ_I can be written by evaluating the integrals in their explicit forms. Using the universal initial distribution (4.24) and the ultimate fractal distribution (4.26) consistent with Buscarnera and Einav (2012) and Einav (2007d), the expressions are

$$\theta_\gamma = 1 - \frac{3-\alpha}{5-\alpha}\left(\frac{1-(d_{min}/d_{Max})^{5-\alpha}}{1-(d_{min}/d_{Max})^{3-\alpha}}\right), \tag{4.54}$$

$$\theta_\kappa = 1 - \frac{3-\alpha}{7-\alpha}\left(\frac{1-(d_{min}/d_{Max})^{7-\alpha}}{1-(d_{min}/d_{Max})^{3-\alpha}}\right), \tag{4.55}$$

$$\theta_I = 1 - \frac{3-\alpha}{8-\alpha}\left(\frac{1-(d_{min}/d_{Max})^{8-\alpha}}{1-(d_{min}/d_{Max})^{3-\alpha}}\right). \tag{4.56}$$

First, considering the limit $d_{min} \to 0$

$$\theta_\gamma = \frac{2}{5-\alpha}, \tag{4.57}$$

$$\theta_\kappa = \frac{4}{7-\alpha}, \tag{4.58}$$

$$\theta_I = \frac{5}{8-\alpha}. \tag{4.59}$$

For typical values of α (2.5-2.7 (Sammis et al., 1987)), $\theta_\gamma = 0.8 - 0.83$, $\theta_\kappa = 0.89 - 0.91$ and $\theta_I = 0.91 - 0.93$.

Next, considering the limit $\alpha \to 3$

$$\theta_\gamma = 1 + \frac{1 - (d_{min}/d_{Max})^2}{2\ln\left(d_{min}/d_{Max}\right)}, \tag{4.60}$$

$$\theta_\kappa = 1 + \frac{1 - (d_{min}/d_{Max})^4}{4\ln\left(d_{min}/d_{Max}\right)}, \tag{4.61}$$

$$\theta_I = 1 + \frac{1 - (d_{min}/d_{Max})^5}{5\ln\left(d_{min}/d_{Max}\right)}. \tag{4.62}$$

If a value such as $d_{min} = 0.00001 d_{Max}$ is assigned, $\theta_\gamma = 0.957, \theta_\kappa = 0.978$ and $\theta_I = 0.98$.

From this analysis it can be concluded that θ_γ, θ_κ and θ_I approach 1 only in the extreme limit as both $\alpha \to 3$ and $d_{min} \to 0$ at the same time. Hence, they must be retained in the model, as for typical values of the parameters their absence will lead to oversimplification and loss of information.

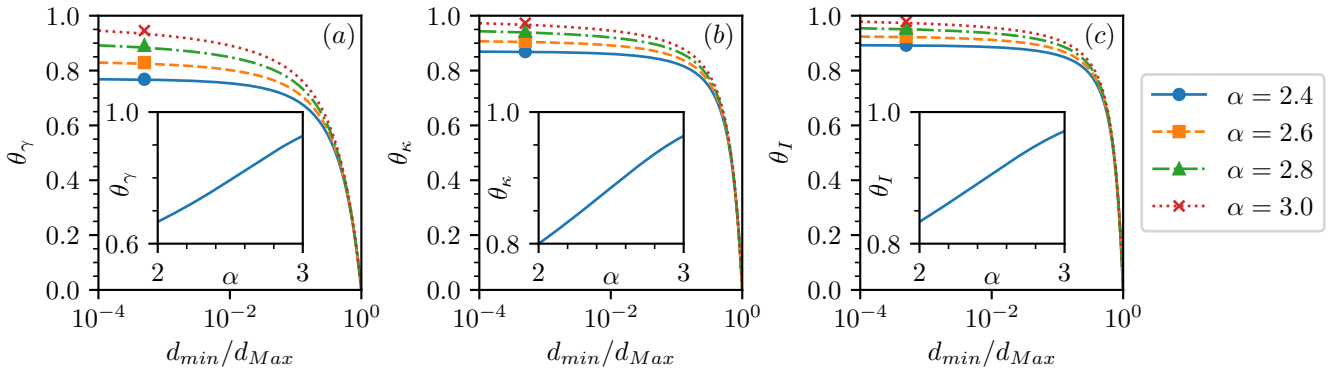

Figure 4.2: The three plots of (a) θ_γ, (b) θ_κ and (c) θ_I all present qualitatively the same behaviour as a function of d_{min}/d_{Max} and α. The insets are the respective plots holding $d_{min}/d_{Max} = 10^{-3}$ and varying α between 2 and 3.

In Figure 4.2, we observe that θ_γ, θ_κ and θ_I exhibit qualitatively the same behaviour, with stable values over a wide range of d_{min}/d_{Max} ratios.

4.5 Constitutive model

4.5.1 Thermodynamic considerations

We introduce a constitutive model to describe and predict the behaviour of the granular medium. The model is drawn from Nguyen and Einav (2009) and Einav (2007a), modified for consistency with the Cosserat continuum.

The model is constructed in the framework of hyperplasticity (Houlsby and Puzrin, 2007), so the first step is to make a statement encapsulating the First and Second laws of Thermodynamics:

$$W = \dot{\Psi} + \Phi, \qquad \Phi \geq 0. \tag{4.63}$$

Only the Helmholtz free energy is a proper state function, so its time rate is denoted with a dot. The rate of work and rate of dissipation are definable only as rates, and so are left without a dot to denote this conceptual distinction.

For the time being we take the general form of Ψ given in (4.42), and leave the explicit specification until later.

4.5.2 Dissipation

The total dissipation rate can always be written as the sum of the products of the dissipative variables and their respective conjugate stresses, i.e.

$$\Phi(\dot{B}, \dot{\varepsilon}_v^p, \dot{\gamma}^p) = E_B\dot{B} + p\dot{\varepsilon}_v^p + q\dot{\gamma}^p. \tag{4.64}$$

However, the dissipation pseudo-potential can be written in a more specific form, namely

$$\Phi(\dot{B}, \dot{\varepsilon}_v^p, \dot{\gamma}^p) = \sqrt{[D_B(\dot{B})]^2 + [D_v(\dot{\varepsilon}_v^p)]^2 + [D_s(\dot{\gamma}^p)]^2}, \tag{4.65}$$

where each of D_B, D_v and D_s are homogeneous first order functions of the dissipative rates.

The Legendre transformation and some re-arranging are used to pass from the dissipation pseudo-potential to the yield surface in dissipative stress space.

First, (4.65) is substituted into (4.64), and differentiated with respect to the dissipative variables. This gives

$$E_B = \frac{\partial\Phi(\dot{B}, \dot{\varepsilon}_v^p, \dot{\gamma}^p)}{\partial\dot{B}} = \frac{D_B(\dot{B})}{\Phi(\dot{B}, \dot{\varepsilon}_v^p, \dot{\gamma}^p)}\frac{\partial D_B(\dot{B})}{\partial\dot{B}}, \tag{4.66}$$

$$p = \frac{\partial\Phi(\dot{B}, \dot{\varepsilon}_v^p, \dot{\gamma}^p)}{\partial\dot{\varepsilon}_v^p} = \frac{D_v(\dot{\varepsilon}_v^p)}{\Phi(\dot{B}, \dot{\varepsilon}_v^p, \dot{\gamma}^p)}\frac{\partial D_v(\dot{\varepsilon}_v^p)}{\partial\dot{\varepsilon}_v^p}, \tag{4.67}$$

$$q = \frac{\partial\Phi(\dot{B}, \dot{\varepsilon}_v^p, \dot{\gamma}^p)}{\partial\dot{\gamma}^p} = \frac{D_s(\dot{\gamma}^p)}{\Phi(\dot{B}, \dot{\varepsilon}_v^p, \dot{\gamma}^p)}\frac{\partial D_s(\dot{\gamma}^p)}{\partial\dot{\gamma}^p}. \tag{4.68}$$

As the total dissipation potential (4.64) is first order in the dissipative rates, the Legendre transform is degenerate and hence can be written

$$\lambda y_\Phi(E_B, p, q) = E_B\dot{B} + p\dot{\varepsilon}_v^p + q\dot{\gamma}^p - \Phi(\dot{B}, \dot{\varepsilon}_v^p, \dot{\gamma}^p) = 0, \tag{4.69}$$

where λ is an undetermined scalar (the plastic multiplier), and the transformation is from $\dot{B}, \dot{\varepsilon}_v^p, \dot{\gamma}^p$ to a function entirely in E_B, p, q.

This function is found by first re-arranging (4.66), (4.67) and (4.68):

$$\frac{E_B}{\partial D_B(\dot{B})/\partial\dot{B}} = \frac{D_B(\dot{B})}{\Phi(\dot{B}, \dot{\varepsilon}_v^p, \dot{\gamma}^p)}, \tag{4.70}$$

$$\frac{p}{\partial D_v(\dot{\varepsilon}_v^p)/\partial\dot{\varepsilon}_v^p} = \frac{D_v(\dot{\varepsilon}_v^p)}{\Phi(\dot{B}, \dot{\varepsilon}_v^p, \dot{\gamma}^p)}, \tag{4.71}$$

$$\frac{q}{\partial D_s(\dot{\gamma}^p)/\partial\dot{\gamma}^p} = \frac{D_s(\dot{\gamma}^p)}{\Phi(\dot{B}, \dot{\varepsilon}_v^p, \dot{\gamma}^p)}. \tag{4.72}$$

Squaring each equation and then adding them together gives

$$\left(\frac{E_B}{\partial D_B(\dot{B})/\partial\dot{B}}\right)^2 + \left(\frac{p}{\partial D_v(\dot{\varepsilon}_v^p)/\partial\dot{\varepsilon}_v^p}\right)^2 + \left(\frac{q}{\partial D_s(\dot{\gamma}^p)/\partial\dot{\gamma}^p}\right)^2 = \frac{[D_B(\dot{B})]^2 + [D_v(\dot{\varepsilon}_v^p)]^2 + [D_s(\dot{\gamma}^p)]^2}{[\Phi(\dot{B}, \dot{\varepsilon}_v^p, \dot{\gamma}^p)]^2}. \tag{4.73}$$

Inserting the specific form of dissipation potential given in (4.65) leads naturally to

$$\left(\frac{E_B}{\partial D_B(\dot{B})/\partial\dot{B}}\right)^2 + \left(\frac{p}{\partial D_v(\dot{\varepsilon}_v^p)/\partial\dot{\varepsilon}_v^p}\right)^2 + \left(\frac{q}{\partial D_s(\dot{\gamma}^p)/\partial\dot{\gamma}^p}\right)^2 - 1 = 0. \tag{4.74}$$

This relationship satisfies the requirements for y_Φ, i.e. that it is identically equal to zero and expressed solely in terms of the (generalised) stresses and not the dissipative variables. It should be noted that equations (4.66), (4.67) and (4.68) are true only when dissipation is active i.e. when the generalised stress state is on the yield surface. We re-write

the equation with a less than or equal to in order to account for when the state is inside the yield surface, to obtain the yield function in the generalised stress space:

$$y_\Phi(E_B, p, q) = \left(\frac{E_B}{\partial D_B(\dot{B})/\partial \dot{B}}\right)^2 + \left(\frac{p}{\partial D_v^p(\dot{\varepsilon}_v^p)/\partial \dot{\varepsilon}_v^p}\right)^2 + \left(\frac{q}{\partial D_s^p(\dot{\gamma}^p)/\partial \dot{\gamma}^p}\right)^2 - 1 \leq 0. \tag{4.75}$$

The mathematical form of the dissipation potentials can now be specified:

$$D_B(\dot{B}) = \frac{\sqrt{E_B E_c}}{(1-B)\cos(\omega)}\dot{B}, \tag{4.76}$$

$$D_v^p(\dot{\varepsilon}_v^p) = \frac{p}{(1-B)\sin(\omega)}\sqrt{\frac{E_c}{E_B}}\dot{\varepsilon}_v^p, \tag{4.77}$$

$$D_s^p(\dot{\gamma}^p) = Mp|\dot{\gamma}^p|, \tag{4.78}$$

where E_c is the critical breakage energy, M is the critical state parameter satisfying $q = Mp$ in triaxial compression and ω is a coupling angle between dissipation due to breakage and dissipation due to plastic volumetric straining, as per Einav (2007a,d).

The evolution of the breakage state variable B, and the rates of the plastic strains and plastic curvatures are given by the flow rules:

$$\dot{B} = \lambda\frac{\partial y_\Phi}{\partial E_B} = \lambda\frac{2E_B}{\left[\partial D_B(\dot{B})/\partial \dot{B}\right]^2} = \lambda\frac{2(1-B)^2\cos^2(\omega)}{E_c}, \tag{4.79}$$

$$\begin{aligned}\dot{\gamma}_{ij}^p &= \lambda\frac{\partial y_\Phi}{\partial \tau_{ij}} = \lambda\left(\frac{\partial y_\Phi}{\partial p}\frac{\partial p}{\partial \tau_{ij}} + \frac{\partial y_\Phi}{\partial q}\frac{\partial q}{\partial \tau_{ij}}\right) = \lambda\left(\frac{2p}{\left[\partial D_v^p(\dot{\varepsilon}_v^p)/\partial \dot{\varepsilon}_v^p\right]^2}\frac{1}{3}\delta_{ij} + \frac{2q}{\left[\partial D_s^p(\dot{\gamma}^p)/\partial \dot{\gamma}^p\right]^2}\frac{1}{q}(h_1^* s_{ij} + h_2^* s_{ji})\right) \\ &= \lambda\left(\frac{2E_B(1-B)^2\sin^2(\omega)}{3pE_c}\delta_{ij} + \frac{2(h_1^* s_{ij} + h_2^* s_{ji})}{(Mp)^2}\right),\end{aligned} \tag{4.80}$$

$$\dot{\kappa}_{ij}^p = \lambda\frac{\partial y_\Phi}{\partial \mu_{ij}} = \lambda\frac{\partial y_\Phi}{\partial q}\frac{\partial q}{\partial \mu_{ij}} = \lambda\frac{2q}{\left[\partial D_s^p(\dot{\gamma}^p)/\partial \dot{\gamma}^p\right]^2}\frac{1}{\ell^{e2}q}(h_3^* m_{ij} + h_4^* m_{ji}) = \lambda\frac{2(h_3^* m_{ij} + h_4^* m_{ji})}{\ell^{e2}(Mp)^2}. \tag{4.81}$$

It should be noted that the yield surface is not a function of the trace part of the couple-stress tensor, simplifying the full expansion of the flow rule in the curvatures (4.81) by allowing us to set the trace part of the derivatives to zero.

It may also be noted that these flow rules are associated to the yield surface in the generalised stress space, but will appear non-associated if viewed only in the true stress space.

As a matter of convenience, a change from the yield surface in dissipative stress space to the yield surface in mixed stress-breakage-energy space can be achieved by directly substituting (4.76), (4.77) and (4.78) into (4.75) to obtain

$$y_{mix} = \frac{E_B(1-B)^2}{E_c} + \left(\frac{q}{Mp}\right)^2 - 1 \leq 0. \tag{4.82}$$

4.5.3 Elasticity

The elastic behaviour can be recovered by specifying the Helmholtz free energy density in the reference grain fraction so that linear Cosserat elasticity is recovered from the generic potential (4.42). This can be specified by

$$\Psi = \frac{1-\theta_\gamma B}{2}C_{ijkl}^e\gamma_{ij}^e\gamma_{kl}^e + {x_r}^2\frac{1-\theta_\kappa B}{2}D_{ijkl}^e\kappa_{ij}^e\kappa_{kl}^e, \tag{4.83}$$

where

$$C^e_{ijkl} = \left(K - \frac{2}{3}G\right)\delta_{ij}\delta_{kl} + (G + G_c)\delta_{ik}\delta_{jl} + (G - G_c)\delta_{il}\delta_{jk}, \tag{4.84}$$

$$D^e_{ijkl} = \left(L - \frac{2}{3}H\right)\delta_{ij}\delta_{kl} + (H + H_c)\delta_{ik}\delta_{jl} + (H - H_c)\delta_{il}\delta_{jk}. \tag{4.85}$$

K and G are the bulk and shear elastic moduli as per the classical continuum, and G_c, L, H and H_c are additional elastic parameters introduced for the Cosserat continuum. As previously noted in §4.4.1, the parameters L, H, and H_c have units of stress in this work.

Now the thermodynamic stresses can be derived from the Helmholtz free energy (4.83):

$$\tau_{ij} = \frac{\partial \Psi}{\partial \gamma^e_{ij}} = (1 - \theta_\gamma B) C^e_{ijkl}\gamma^e_{kl}, \tag{4.86}$$

$$\mu_{ij} = \frac{\partial \Psi}{\partial \kappa^e_{ij}} = {x_r}^2(1 - \theta_\kappa B) D^e_{ijkl}\kappa^e_{kl}, \tag{4.87}$$

$$E_B = -\frac{\partial \Psi}{\partial B} = \frac{\theta_\gamma}{2} C^e_{ijkl}\gamma^e_{ij}\gamma^e_{kl} + \frac{{x_r}^2\theta_\kappa}{2} D^e_{ijkl}\kappa^e_{ij}\kappa^e_{kl}. \tag{4.88}$$

4.5.4 Plastic multiplier

The model is completely specified by determining an explicit expression for the plastic multiplier λ. λ is obtained by applying the consistency condition, i.e. when the stress state is on the yield surface $y = 0$, so for any further inelastic loading $\dot{y} = 0$. By expansion of any expression for $\dot{y}$, such as $\dot{y}_{mix}$, an expression in terms of the rates of the state variables $\dot{\gamma}^e_{ij}, \dot{\kappa}^e_{ij}$ and $\dot{B}$ is obtained. The rates of elastic strains and curvatures are replaced with the rates of total and plastic strains and curvatures via (4.15) and (4.16). Finally, the rates of the plastic strains and curvatures and the rate of breakage are replaced with their flow rules (4.79), (4.80) and (4.81) in which λ appears as an unknown variable. Rearrangement gives an explicit expression for λ in terms of the state variables and the rates of total strains and curvatures, closing the model. This process gives

$$\lambda = \frac{A_1\dot{\gamma}_{kl} + A_2\dot{\kappa}_{kl}}{A_3 \times A_4 + A_5 + A_6 \times A_7 + A_8}, \tag{4.89}$$

where

$$A_1 = \left(\frac{-2q^2}{3M^2p^3}\delta_{ij} + \frac{2}{(Mp)^2}\left(h^*_1 s_{ij} + h^*_2 s_{ji}\right)\right)\left(1 - \theta_\gamma B\right) C^e_{ijkl} + \frac{(1-B)^2}{E_c}\frac{\theta_\gamma}{2} C^e_{ijkl}\gamma^e_{ij}, \tag{4.90}$$

$$A_2 = \frac{2}{(Mp)^2}\frac{1}{{\ell_q}^2}\left(h^*_3 m_{ij} + h^*_4 m_{ji}\right)\left(1 - \theta_\kappa B\right) D^e_{ijkl} + \frac{(1-B)^2}{E_c}\frac{{x_r}^2\theta_\kappa}{2} D^e_{ijkl}\kappa^e_{ij}, \tag{4.91}$$

$$A_3 = \frac{-2q^2}{3M^2p^3}\delta_{ij} + \frac{2}{(Mp)^2}\left(h^*_1 s_{ij} + h^*_2 s_{ji}\right), \tag{4.92}$$

$$A_4 = \left(1 - \theta_\gamma B\right) C^e_{ijkl}\left(\frac{2E_B(1-B)^2\sin^2(\omega)}{3pE_c}\delta_{kl} + \frac{2\left(h^*_1 s_{kl} + h^*_2 s_{lk}\right)}{(Mp)^2}\right) + \theta_\gamma C^e_{ijkl}\gamma^e_{kl}\frac{2(1-B)^2\cos^2(\omega)}{E_c}, \tag{4.93}$$

$$A_5 = \frac{2}{(Mp)^2}\frac{1}{{\ell_q}^2}\left(h^*_3 m_{ij} + h^*_4 m_{ji}\right)\left(\left(1 - \theta_\kappa B\right) D^e_{ijkl}\frac{2\left(h^*_3 m_{kl} + h^*_4 m_{lk}\right)}{{\ell_q}^2(Mp)^2} + \theta_\kappa D^e_{ijkl}\kappa^e_{kl}\frac{2(1-B)^2\cos^2(\omega)}{E_c}\right), \tag{4.94}$$

$$A_6 = \frac{(1-B)^2}{E_c}, \tag{4.95}$$

$$A_7 = \frac{\theta_\gamma}{2} C^e_{ijkl}\gamma^e_{ij}\left(\frac{2E_B(1-B)^2\sin^2(\omega)}{3pE_c}\delta_{kl} + \frac{2\left(h^*_1 s_{kl} + h^*_2 s_{lk}\right)}{(Mp)^2}\right) + \frac{{x_r}^2\theta_\kappa}{2} D^e_{ijkl}\kappa^e_{ij}\frac{2\left(h^*_3 m_{kl} + h^*_4 m_{lk}\right)}{{\ell_q}^2(Mp)^2}, \tag{4.96}$$

$$A_8 = \frac{2E_B(1-B)}{E_c}\frac{2(1-B)^2\cos^2(\omega)}{E_c}. \tag{4.97}$$

For the purposes of performing numerical integrations, a smoothing can be achieved by implementation in the framework of h^2plasticity (Einav, 2012). This framework allows the evolution equations to be smooth and continuous while ensuring compatibility with the laws of thermodynamics. Some some small modifications to the flow rules (4.79), (4.80) and (4.81) result in:

$$\dot{B} = \langle\lambda\rangle(1+y)^{\xi}\frac{2(1-B)^2\cos^2(\omega)}{E_c}, \tag{4.98}$$

$$\dot{\gamma}^p_{ij} = \langle\lambda\rangle(1+y)^{\xi}\left(\frac{2E_B(1-B)^2\sin^2(\omega)}{3pE_c}\delta_{ij} + \frac{2(h^*_1 s_{ij} + h^*_2 s_{ji})}{(Mp)^2}\right), \tag{4.99}$$

$$\dot{\kappa}^p_{ij} = \langle\lambda\rangle(1+y)^{\xi}\frac{2(h^*_3 m_{ij} + h^*_4 m_{ji})}{{\ell^e}^2(Mp)^2}, \tag{4.100}$$

where $\langle\cdot\rangle$ are Macaulay brackets, y is the yield function (any expression of y will work as they all have the same scalar value, so we use y_{mix} as the most compact form), and ξ is a parameter controlling the stiffness of the response. As $\xi \to \infty$, the classical hyper-plastic model is recovered. Smaller values of ξ represent "softer" behaviours with dissipation being more significantly activated at lower values of load.

4.5.5 Incremental constitutive response

In order to complete the description of the model, the expression for the incremental stiffness relationship is required. Even though the expressions for τ_{ij} and μ_{ij} are independent of κ^e_{ij} and γ^e_{ij} respectively, there is coupling present in the incremental relationship due to λ being a function of both $\dot{\gamma}_{kl}$ and $\dot{\kappa}_{kl}$. A linear decomposition of (4.89) is performed to obtain

$$\lambda = \lambda^{\gamma}_{kl}\dot{\gamma}_{kl} + \lambda^{\kappa}_{kl}\dot{\kappa}_{kl}. \tag{4.101}$$

Using (4.101), the incremental constitutive relationship under increasing load in a compact differential form is given by:

$$\begin{bmatrix}\dot{\tau}_{ij}\\ \dot{\mu}_{ij}\end{bmatrix} = \begin{bmatrix}\frac{\partial\tau_{ij}}{\partial\gamma^e_{kl}} - \lambda^{\gamma}_{kl}(1+y)^{\xi}\left(\frac{\partial y_\Phi}{\partial\tau_{ij}} - \frac{\partial\tau_{ij}}{\partial B}\frac{\partial y_\Phi}{\partial E_B}\right) & -\lambda^{\kappa}_{kl}(1+y)^{\xi}\left(\frac{\partial y_\Phi}{\partial\tau_{ij}} - \frac{\partial\tau_{ij}}{\partial B}\frac{\partial y_\Phi}{\partial E_B}\right)\\ -\lambda^{\gamma}_{kl}(1+y)^{\xi}\left(\frac{\partial y_\Phi}{\partial\mu_{ij}} - \frac{\partial\mu_{ij}}{\partial B}\frac{\partial y_\Phi}{\partial E_B}\right) & \frac{\partial\mu_{ij}}{\partial\kappa^e_{kl}} - \lambda^{\kappa}_{kl}(1+y)^{\xi}\left(\frac{\partial y_\Phi}{\partial\mu_{ij}} - \frac{\partial\mu_{ij}}{\partial B}\frac{\partial y_\Phi}{\partial E_B}\right)\end{bmatrix}\begin{bmatrix}\dot{\gamma}_{kl}\\ \dot{\kappa}_{kl}\end{bmatrix}. \tag{4.102}$$

It is convenient to write this relationship as

$$\begin{bmatrix}\dot{\tau}_{ij}\\ \dot{\mu}_{ij}\end{bmatrix} = \begin{bmatrix}E^{ep}_{ijkl} & F^{ep}_{ijkl}\\ K^{ep}_{ijkl} & M^{ep}_{ijkl}\end{bmatrix}\begin{bmatrix}\dot{\gamma}_{kl}\\ \dot{\kappa}_{kl}\end{bmatrix}. \tag{4.103}$$

4.5.6 Invariants

The formulation of the first stress and strain invariants in a Cosserat continuum is the same as for the classical continuum, as outlined above in §4.3.1 and §4.3.3. However, the formulations of the second deviatoric stress and strain invariants are not trivial in the Cosserat continuum. Micro-mechanical arguments have been advanced by several different authors (Mühlhaus and Vardoulakis, 1987; Rattez et al., 2018a; Vardoulakis and Sulem, 1995), allowing the invariant for plastic shear strain to be defined by consideration of kinematics, or the invariant for the deviatoric stress to be defined by consideration of statics. They are respectively

$$\dot{\gamma}^p = \sqrt{g^*_1\dot{e}^p_{ij}\dot{e}^p_{ij} + g^*_2\dot{e}^p_{ij}\dot{e}^p_{ji} + {\ell_\gamma}^2(g^*_3\dot{k}^p_{ij}\dot{k}^p_{ij} + g^*_4\dot{k}^p_{ij}\dot{k}^p_{ji})}, \tag{4.104}$$

$$q = \sqrt{h^*_1 s_{ij}s_{ij} + h^*_2 s_{ij}s_{ji} + \frac{1}{{\ell_q}^2}(h^*_3 m_{ij}m_{ij} + h^*_4 m_{ij}m_{ji})}. \tag{4.105}$$

Certain weighting factors are given to the values of g^*_i in the kinematic expression of $\dot{\gamma}^p$, and h^*_i in the static expression of q, in order to recover the classical expressions when the Cosserat effects vanish. Two pairs of values are defined, $q - \dot{\gamma}^p$ kinematic and $q - \dot{\gamma}^p$ static, with different weighting factors g^*_i and h^*_i. The length scale ℓ_γ is identified with

the grain size in the micro-mechanical derivations. It is essential to note here that the definition of these invariants in the work of Vardoulakis and co-workers implicitly takes $\ell_\gamma = \ell_q = R$, that is to say that both lengths are equal to some constant multiple of the mean grain radius (Mühlhaus and Vardoulakis, 1987; Vardoulakis and Sulem, 1995). As a consequence, the derivation of the weighting factors relies on all particles having the same diameter. In a medium featuring grain breakage, this will certainly not be the case, and so the invariants must be at least partially re-visited to determine appropriate expressions for the medium.

By relaxing the assumption that the internal length is the same for the stress and strain invariants, but retaining the assumption of coaxiality (that is to say that the stress and strain increments act in the same direction), and taking the weighting factors h_i^* in the static formulation and g_i^* in the kinematic formulation on an ad-hoc basis, new expressions can be determined.

Now, we apply the flow rule to obtain the plastic strain and curvature rates (see (4.80) and (4.81) for the application of the chain rule). We only require the deviatoric parts of the rates:

$$\begin{aligned}\dot{e}_{ij}^p &= \lambda \frac{\partial y_\Phi}{\partial q}\frac{\partial q}{\partial \tau_{ij}},\\ &= \lambda \frac{\partial y_\Phi}{\partial q}\frac{1}{q}(h_1^* s_{ij} + h_2^* s_{ji}),\end{aligned} \tag{4.106}$$

and similarly, the deviatoric plastic curvature rate by

$$\begin{aligned}\dot{k}_{ij}^p &= \lambda \frac{\partial y_\Phi}{\partial q}\frac{\partial q}{\partial \mu_{ij}},\\ \dot{k}_{ij}^p &= \lambda \frac{\partial y_\Phi}{\partial q}\frac{1}{{\ell_q}^2 q}(h_3^* m_{ij} + h_4^* m_{ji}).\end{aligned} \tag{4.107}$$

Now, the plastic strain rate invariant is defined to be the derivative of the dissipative yield surface with respect to the stress invariant:

$$\dot{\gamma}^p = \lambda \frac{\partial y_\Phi}{\partial q}. \tag{4.108}$$

Using the assumption of coaxiality detailed above, the strain rate terms in the strain rate invariant (4.104) can be replaced with their equivalent expressions phrased in terms of stresses, i.e. (4.106) and (4.107). Cancelling and re-arranging transforms the expression of the strain invariant into an expression of the stress invariant:

$$q = \sqrt{\begin{array}{c} g_1^*(h_1^* s_{ij} + h_2^* s_{ji})(h_1^* s_{ij} + h_2^* s_{ji}) + g_2^*(h_1^* s_{ij} + h_2^* s_{ji})(h_1^* s_{ji} + h_2^* s_{ij}) + \\ \dfrac{{\ell_\gamma}^2}{{\ell_q}^4}(g_3^*(h_3^* m_{ij} + h_4^* m_{ji})(h_3^* m_{ij} + h_4^* m_{ji}) + g_4^*(h_3^* m_{ij} + h_4^* m_{ji})(h_3^* m_{ji} + h_4^* m_{ij})) \end{array}}. \tag{4.109}$$

There are now two expressions for the stress invariant, (4.105) and (4.109) which must be equivalent, but the constants g_i^* are present only in (4.109), allowing the formation of relationships between g_i^* and h_i^*. The deviatoric stress is expanded into its symmetric and anti-symmetric parts, per (4.21). By exploiting that the product of a symmetric and anti-symmetric tensor is identically zero, that $s_{(ij)} = s_{(ji)}$ and that $s_{[ij]} = -s_{[ji]}$, both (4.109) and (4.105) can be written in terms of the symmetric and anti-symmetric parts:

$$\sqrt{(h_1^* + h_2^*)s_{(ij)}s_{(ij)} + (h_1^* - h_2^*)s_{[ij]}s_{[ij]} + \frac{1}{{\ell_q}^2}((h_3^* + h_4^*)m_{(ij)}m_{(ij)} + (h_3^* - h_4^*)m_{[ij]}m_{[ij]})}, \tag{4.110}$$

when considering (4.105), and

$$\sqrt{\begin{array}{c}(h_1^*+h_2^*)^2(g_1^*+g_2^*)s_{(ij)}s_{(ij)}+(h_1^*-h_2^*)^2(g_1^*-g_2^*)s_{[ij]}s_{[ij]}+\\ \frac{\ell_\gamma{}^2}{\ell_q{}^4}((h_3^*+h_4^*)^2(g_3^*+g_4^*)m_{(ij)}m_{(ij)}+(h_3^*-h_4^*)^2(g_3^*-g_4^*)m_{[ij]}m_{[ij]})\end{array}}, \tag{4.111}$$

when considering (4.109). Now, the coefficients of the symmetric and anti-symmetric parts on each side can be directly equated to arrive at two sets of simultaneous equations:

$$h_1^*+h_2^*=\frac{1}{g_1^*+g_2^*}, \tag{4.112}$$

$$h_1^*-h_2^*=\frac{1}{g_1^*-g_2^*}, \tag{4.113}$$

for the stress weighting factors, and

$$h_3^*+h_4^*=\left(\frac{\ell_q}{\ell_\gamma}\right)^2\frac{1}{g_3^*+g_4^*}, \tag{4.114}$$

$$h_3^*-h_4^*=\left(\frac{\ell_q}{\ell_\gamma}\right)^2\frac{1}{g_3^*-g_4^*}, \tag{4.115}$$

for the moment weighting factors. These expressions differ from other authors (Rattez et al. (2018a) for example) in leaving open the possibility that $\ell_\gamma \neq \ell_q$, and hence give a slightly more general expression.

We identify ℓ^q with ℓ^e, defined as per (4.44). However, there is no immediately obvious identification to make that will give an explicit expression for ℓ_γ. As such, it is supposed that it may also evolve with breakage in a similar way to the elastic length, and the ratio between the elastic and plastic length is a fixed ratio ζ, which acts as a new material property.

It should also be noted that the definition of q used in previous examples of Breakage Mechanics is consistent with $q=\sigma_a-\sigma_r$, that is to say with the difference between the axial and radial stresses in a triaxial test. This leads to a tensorial definition of

$$q=\sqrt{\frac{3}{2}s_{ij}s_{ij}} \tag{4.116}$$

in the classical continuum, which the definition must collapse to in the absence of Cosserat effects. A table of weighting factors for the invariants (4.104) and (4.105) is arrived at:

	2D model	3D model
Static model	$g_i^*=\{1/2,1/6,\zeta^2/3,0\}$ $h_i^*=\{9/4,-3/4,3,0\}$	$g_i^*=\{8/15,2/15,8\zeta^2/15,2\zeta^2/15\}$ $h_i^*=\{2,-1/2,2,-1/2\}$
Kinematic model	$g_i^*=\{1,-1/3,4/3,0\}$ $h_i^*=\{9/8,3/8,3\zeta^2/4,0\}$	$g_i^*=\{8/9,-2/9,8/9,-2/9\}$ $h_i^*=\{6/5,3/10,6\zeta^2/5,3\zeta^2/10\}$

Table 4.1: Values of the coefficients for stress and plastic strain rate invariants in a Cosserat continuum made consistent with Breakage Mechanics

The values listed in Table 4.1 are compatible with previous works (Mühlhaus and Vardoulakis, 1987; Sulem and Vardoulakis, 1990), adjusted appropriately to account for the slightly different definition of the stress invariant.

4.6 Model calibration

4.6.1 Cosserat stiffness relationships

Before specifying the parameter values, it is convenient to derive some relationships between the stiffnesses present in the classical continuum and the new Cosserat stiffnesses. As the stiffnesses are those of the unbroken material, we set $B = 0$, which also has the benefit of simplifying the analysis somewhat. In order to do this, we derive the Gibbs free energy, Γ, by performing a Legendre transform from the Helmholtz energy

$$\begin{aligned}\Gamma &= \Psi - \tau_{ij}\gamma^e_{ij} - \mu_{ij}\kappa^e_{ij},\\ &= -\frac{1}{2}C^{el}_{ijkl}\gamma^e_{ij}\gamma^e_{kl} - {x_r}^2 D^{el}_{ijkl}\kappa^e_{ij}\kappa^e_{kl},\\ &= -\frac{1}{2}C^{comp}_{ijkl}\tau_{ij}\tau_{kl} - \frac{1}{2{x_r}^2}D^{comp}_{ijkl}\mu_{ij}\mu_{kl},\end{aligned} \tag{4.117}$$

where C^{comp}_{ijkl} and D^{comp}_{ijkl} are the isotropic linear elastic compliance tensors, that are obtained by inverting (4.84) and (4.85).

We now write the energy in terms of the stress invariants:

$$\Gamma = -\frac{1}{2}\left(\frac{p^2}{K} + \frac{q^2}{3G}\right). \tag{4.118}$$

The elastic strains and curvatures are given by differentiating with respect to the stresses:

$$\begin{aligned}\gamma^e_{ij} &= -\frac{\partial G}{\partial \tau_{ij}} = -\frac{\partial \Gamma}{\partial p}\frac{\partial p}{\partial \tau_{ij}} - \frac{\partial \Gamma}{\partial q}\frac{\partial q}{\partial \tau_{ij}},\\ &= \frac{1}{2}\left(\frac{2p}{K}\frac{1}{n}\delta_{ij} + \frac{2q}{3G}\frac{1}{q}(h^*_1 s_{ij} + h^*_2 s_{ji})\right),\\ &= \frac{p}{nK}\delta_{ij} + \frac{1}{3G}(h^*_1 s_{ij} + h^*_2 s_{ji}),\end{aligned} \tag{4.119}$$

where n is the dimension of the problem ($n = 2$ or $n = 3$).

The relationship must be expressed in terms of τ_{kl} to obtain a compliance tensor. Where appropriate, the substitution $\tau_{ij} = \delta_{ik}\delta_{jl}\tau_{kl}$ is made:

$$\begin{aligned}\gamma^e_{ij} &= \left(\frac{1}{n^2 K}\delta_{ij}\delta_{kl} + \frac{1}{3G}\left(h^*_1\left(\delta_{ik}\delta_{jl} - \frac{1}{n}\delta_{kl}\delta_{ij}\right) + h^*_2\left(\delta_{jk}\delta_{il} - \frac{1}{n}\delta_{kl}\delta_{ij}\right)\right)\right)\tau_{kl},\\ &= \left(\left(\frac{1}{n^2 K} - \frac{1}{3nG}(h^*_1 + h^*_2)\right)\delta_{ij}\delta_{kl} + \frac{1}{3G}\left(h^*_1\delta_{ik}\delta_{jl} + h^*_2\delta_{jk}\delta_{il}\right)\right)\tau_{kl}.\end{aligned} \tag{4.120}$$

This compliance relationship expressed in terms of K, G, h_1*, h^*_2 may be compared with that in (4.117), which is expressed in terms of K, G, G_c. This allows the derivation of a formula for the value of G_c. Comparing the results considering the 1212 and 2112 entries of the two compliance relationships gives:

$$\frac{h^*_1}{3G} = \frac{G + G_c}{4GG_c}, \tag{4.121}$$

$$\frac{h^*_2}{3G} = \frac{-G + G_c}{4GG_c}, \tag{4.122}$$

$$\frac{h^*_1 - h^*_2}{3G} = \frac{(G + G_c) - (-G + G_c)}{4GG_c} = \frac{1}{2G_c}, \tag{4.123}$$

$$G_c = \frac{3G}{2(h^*_1 - h^*_2)} \tag{4.124}$$

Now turning to the curvatures, the expressions can be derived in a similar way:

$$\begin{aligned}\kappa^e_{ij} &= \frac{\partial \Gamma}{\partial \mu_{ij}} = \frac{\partial \Gamma}{\partial q}\frac{\partial q}{\partial \mu_{ij}},\\ &= \frac{1}{2}\frac{2q}{3G}\frac{1}{q{\ell^e}^2}(h^*_3 m_{ij} + h^*_4 m_{ji}),\\ &= \frac{1}{3G{\ell^e}^2}(h^*_3 \mu_{ij} + h^*_4 m_{ji}),\\ &= \frac{1}{3G{\ell^e}^2}(h^*_3 \delta_{ik}\delta_{jl} + h^*_4 \delta_{jk}\delta_{il})\mu_{kl}. \end{aligned} \tag{4.125}$$

As $B = 0$, $\ell^e = x_r$. Once again, by comparing the compliance relationship with that in (4.117), specifically the 1212 and 2112 entries, we may derive two relationships:

$$\frac{h^*_3}{3{x_r}^2 G} = \frac{H + H_c}{4{x_r}^2 H H_c}, \tag{4.126}$$

$$\frac{h^*_4}{3{x_r}^2 G} = \frac{-H + H_c}{4H H_c}, \tag{4.127}$$

$$\frac{h^*_3 + h^*_4}{3{x_r}^2 G} = \frac{(H + H_c) + (-H + H_c)}{4{x_r}^2 H H_c} = \frac{1}{2H}, \tag{4.128}$$

$$H = \frac{3G}{2(h^*_3 + h^*_4)}, \tag{4.129}$$

and

$$\frac{h^*_3 - h^*_4}{3{x_r}^2 G} = \frac{(H + H_c) - (-H + H_c)}{4{x_r}^2 H H_c} = \frac{1}{2H_c}, \tag{4.130}$$

$$H_c = \frac{3G}{2(h^*_3 - h^*_4)}. \tag{4.131}$$

Finally, it should be noted that the Gibbs free energy expression excludes any contribution from the trace part of the elastic curvatures, similarly to how the flow rules for the plastic curvatures ignore the trace component. This is equivalent to stating that there are no twisting motions contributing to the model, and hence the material parameter L makes no contribution to the model.

This series of differentiations has allowed the definition of three additional Cosserat stiffnesses directly as a function of the shear stiffness G, and the choice of static or kinematic model in two or three dimensions.

4.6.2 Experimental methods

In order to apply the model to a real geomaterial, certain experiments must be carried out in order to determine the values of the various parameters in the model.

By measuring the granulometry, x_r is immediately obtained as the largest grain size present. Either the particular material can be placed in some sort of apparatus that allows arbitrarily large shear, in order to determine an ultimate grading, or one may select values of the power law coefficient from the literature. Hence, the full initial granulometry either allows calculation of $\theta_\gamma, \theta_\kappa, \theta_I$ by taking the appropriate moments of the initial distribution and setting $B = 0$, or they may be calculated using the universal initial distribution and the ratio of the areas under the initial and ultimate granulometries calculated to give an initial value of $B \geq 0$.

The density of the material can be easily measured using standard techniques (i.e. measuring the mass of a known volume of material), or if the composition of the grains is known, their solid density divided by the initial solid volume fraction will give the bulk density.

The bulk and shear moduli K and G can be measured using standard techniques such as shear wave measurements. While in reality, these moduli are pressure dependent, we assume isotropic linear elasticity for this model, meaning that the calibration should be done at as low a pressure as practicable. We may calculate G_c, H, H_c from these values after selecting the kinematic or static model and the choice of dimension.

The critical state parameter M is the slope of the critical state line in $p - q$ space, typically obtained in a triaxial test.

The critical breakage energy can be found by subjecting a sample to isotropic compression until grain crushing starts. By rearranging (4.82) with $q = 0$, an expression for E_c is straightforwardly obtained. It should be noted that this value can also be inferred from scaling laws based on the grain size (Zhang et al., 2016).

The only parameter of the model which can be adjusted to fit the plastic response is the coupling angle ω. Calibration may be performed by seeing which value of ω best matches the stress-strain response after plasticity.

4.7 Conclusion

In this chapter, we first expanded the upscaling procedures of Breakage Mechanics consistent with Einav (2007a) to the Cosserat continuum. This allows us to include the contributions of the elastic curvatures to the total stored energy, by making use of a new material constant θ_κ that can be measured without making any constitutive assumptions about the material. This material constant and the upscaling procedure allow us to define a new internal length for the system, ℓ^e, that takes into account the entire grain size distribution, and evolves as that distribution evolves.

The upscaling techniques were further extended to account for the moment of rotational inertia, allowing the definition of another new material constant θ_I that allows the entire grain size distribution and its evolution to be taken into account when analysing the momentum balance equations of the Cosserat continuum.

A limit analysis of the new granulometry parameters was undertaken, which confirmed the necessity of including all of the parameters in the model in order to retain sufficient information about the grain size distribution.

We then outlined a constitutive model, expanding a previously developed model into the Cosserat continuum using our newly developed upscaled relationships. In doing so, we derived certain relationships between the second deviatoric stress and strain invariants that are slightly more general than in previous works, and consistent with the definition of the deviator stress used in triaxial tests.

Finally, we derived relationships between the bulk and shear moduli of the classical continuum and three additional Cosserat stiffness moduli and presented methods to calibrate the values of all parameters. We emphasise here that the change to the Cosserat continuum requires no additional calibration over the same model expressed in the classical continuum, as all new material parameters can be calculated with the same information necessary to calculate their classical equivalents.

However, in order to draw conclusions about the thickness of localisations predicted by the model, which is the principal reason to develop a Cosserat model, we must explore it numerically. These explorations are conducted by means of linear stability analyses and finite element modelling, presented in the following chapter.

Chapter 5

Numerical applications

5.1 Summary

In this chapter we apply the model developed in the previous chapter to predict the thickness of localisation phenomena. The two principal methods that we implement are the linear stability analysis (LSA) and the finite element method (FEM). Using these two methods we focus our investigation on constant volume shearing. We also use the LSA to examine the system tendencies under constant confining pressure shearing, œdometric compression and biaxial compression. By investigating a range of load paths equivalent to well-understood experimental tests or important field phenomena, we develop understanding of the strengths and limitations of the model in explaining the physics of the processes that we are interested in.

5.2 Introduction

This chapter is organised as follows: first, we present the methods used to predict localisation thickness. Then we apply these methods to a range of different load cases and compare between the two methods for each case. Finally, we discuss the results in the context of what they reveal about the underlying physical mechanisms of each system.

5.3 Methods

We will use two different methods to determine the localisation thickness predicted by the new Cosserat Breakage Mechanics model. The first method is the linear stability analysis (LSA). This method is semi-analytical, and involves perturbing an assumed homogeneous system then studying the evolution in time of those perturbations to determine if strain localisation can occur, and if so what the localised zone width and orientation angle are. This technique is applied to a single element implementing the material model in Mathematica or Python that takes strain and curvature rates as inputs.

The second method is the finite element method (FEM). Displacements or tractions are applied to the boundaries of the system and a numerical solution for the evolution of the system is searched for by implementing the material model at each node while maintaining equilibrium in the system. The displacements and Cosserat rotations are interpolated between the nodes with basis functions. The finite element system simulates the response of a structure that can deform inhomogeneously.

5.3.1 Linear stability analysis

The linear stability analysis is conducted on the momentum balance equations for the Cosserat continuum:

$$\tau_{ij,j} - \rho \frac{\partial^2 u_i}{\partial t^2} = 0, \tag{5.1}$$

$$\mu_{ij,j} - \epsilon_{ijk}\tau_{jk} - I\frac{\partial^2 \omega_i^c}{\partial t^2} = 0. \tag{5.2}$$

We assume that there is a homogeneous solution obeying the governing balance equations and following the above constitutive laws, and perform a perturbation about said solution. We may re-write the kinematic fields as

$$u(x_i, t) = u^0(x_i, t) + \tilde{u}(x_i, t), \tag{5.3}$$

$$\omega^c(x_i, t) = \omega^{c0}(x_i, t) + \tilde{\omega}^c(x_i, t), \tag{5.4}$$

where the 0 superscript denotes the homogeneous solution and $\tilde{}$ the perturbation term. We assume that the resultant perturbations in stresses, strains, couple-stresses and curvatures follow the incremental constitutive relationships (4.103), linearised around the homogeneous solution.

The governing equations are satisfied by the homogeneous field, and hence by subtraction they must also be satisfied by the perturbation terms. In order to obtain an appropriate linear system allowing a bifurcation analysis, we insert the incremental constitutive relationships (4.103) and the definitions of the strain and curvature rates (4.7) and (4.8) into the perturbations of (5.1) and (5.2) to obtain

$$E^{ep}_{jklm}(\tilde{u}_{l,mk} + \epsilon_{lmo}\tilde{\omega}^c_{o,k}) + F^{ep}_{jklm}\tilde{\omega}^c_{l,mk} - \rho\frac{\partial^2 \tilde{u}_k}{\partial t^2} = 0, \tag{5.5}$$

$$K^{ep}_{jklm}(\tilde{u}_{l,mk} + \epsilon_{lmo}\tilde{\omega}^c_{o,k}) + M^{ep}_{jklm}\tilde{\omega}^c_{l,mk} - \epsilon_{jkl}(E^{ep}_{klmo}(\tilde{u}_{m,o} + \epsilon_{mop}\tilde{\omega}^c_p) + F^{ep}_{klmo}\tilde{\omega}^c_{m,o}) - I\frac{\partial^2 \tilde{\omega}^c_j}{\partial t^2} = 0. \tag{5.6}$$

We now have a set of 6 equations with 6 unknowns, $\tilde{u}_j$ and $\tilde{\omega}^c_j$. Within the framework of linear stability analysis we seek solutions for the unknowns in time and space with the following form:

$$U^*_j(x_k, t) = \bar{U}_j e^{st + \frac{2\pi \mathrm{i}}{\Lambda} x_k n_k}, \tag{5.7}$$

$$\Omega^*_j(x_k, t) = \bar{\Omega}_j e^{st + \frac{2\pi \mathrm{i}}{\Lambda} x_k n_k}, \tag{5.8}$$

where $\bar{U}_j$ and $\bar{\Omega}_j$ are vectors of coefficients, s is the growth coefficient in time of the perturbation (also known as the Lyapunov exponent), i is the imaginary unit, Λ is the perturbation wavelength, n_k the polarisation direction and $U^*_j(x_k, t)$ and $\Omega^*_j(x_k, t)$ are vectors that contain the unknown perturbation fields. We can insert (5.7) and (5.8) into (5.5) and (5.6) to obtain

$$E^{ep}_{jklm}\left(\frac{4\pi^2 \mathrm{i}^2}{\Lambda^2} n_m n_k \bar{U}_l e^{st + \frac{2\pi \mathrm{i}}{\Lambda} x_o n_o} + \epsilon_{lmo}\frac{2\pi \mathrm{i}}{\Lambda} n_k \bar{\Omega}_o e^{st + \frac{2\pi \mathrm{i}}{\Lambda} x_p n_p}\right) + F^{ep}_{jklm}\frac{4\pi^2 \mathrm{i}^2}{\Lambda^2} n_m n_k \bar{\Omega}_l e^{st + \frac{2\pi \mathrm{i}}{\Lambda} x_o n_o} - \rho s^2 \bar{U}_j e^{st + \frac{2\pi \mathrm{i}}{\Lambda} x_k n_k} = 0, \tag{5.9}$$

$$K^{ep}_{jklm}\left(\frac{4\pi^2 \mathrm{i}^2}{\Lambda^2} n_m n_k \bar{U}_l e^{st + \frac{2\pi \mathrm{i}}{\Lambda} x_o n_o} + \epsilon_{lmo}\frac{2\pi \mathrm{i}}{\Lambda} n_k \bar{\Omega}_o e^{st + \frac{w\pi \mathrm{i}}{\Lambda} x_p n_p}\right) + M^{ep}_{jklm}\frac{4\pi^2 \mathrm{i}^2}{\Lambda^2} n_m n_k \bar{\Omega}_l e^{st + \frac{2\pi \mathrm{i}}{\Lambda} x_o n_o}$$
$$-\epsilon_{jkl}\left(E^{ep}_{klmo}\left(\frac{2\pi \mathrm{i}}{\Lambda} n_o \bar{U}_l e^{st + \frac{2\pi \mathrm{i}}{\Lambda} x_p n_p} + \epsilon_{mop}\bar{\Omega}_p e^{st + \frac{2\pi \mathrm{i}}{\Lambda} x_q n_q}\right) + F^{ep}_{klmo}\frac{2\pi \mathrm{i}}{\Lambda} n_o \bar{\Omega}_m e^{st + \frac{2\pi \mathrm{i}}{\Lambda} x_p n_p}\right)$$
$$-Is^2 \bar{\Omega}_j e^{st + \frac{2\pi \mathrm{i}}{\Lambda} x_k n_k} = 0. \tag{5.10}$$

This is a linear system for the coefficients $\bar{U}_1, \bar{U}_2, \bar{U}_3, \bar{\Omega}_1, \bar{\Omega}_2, \bar{\Omega}_3$. We are interested in when the system becomes singular, and after removing the common factor of the exponential (which can never be equal to zero) from all equations,

we may write a (6 by 6) coefficient matrix, which we call the bifurcation matrix. While conceptually straightforward to describe and obtain with appropriate software, each individual entry is unwieldy, making the matrix proper too long to be written here.

We now find the determinant of the matrix, which results in a characteristic polynomial in s. As s^2 terms are present in the matrix, there will be apparent roots that are not actually true solutions of the system, as a consequence of mirror roots being introduced by the squaring process. A simple variable substitution will reduce the polynomial to the correct order of 6.

We explore how the roots of the polynomial change as a function of the changing parameters and state variables of the system, as well as the wavelength of the perturbation Λ. We may characterise the roots as being one of four types, depending on whether s:

1. has negative real part. This indicates that the perturbation decreases in time and the system is stable.
2. is complex with a positive real part. This indicates a flutter instability where the system will cycle between loading and unloading. However, if the constitutive model consists of an elastic and an elasto-plastic region, the unloading will result in a return to the elastic region, stabilising the system. It is hence unclear if we may conclude anything from a result of this type.
3. is real with positive real part. This indicates that the perturbation grows in time and the system is unstable. Hence, we have a bifurcation.
4. has real part equal to zero. We cannot conclude anything in this case.

For a given set of state variables, we may search over a range of wavelengths and orientations to find the largest real positive s, which will be the fastest growing perturbation. The wavelength Λ_{max} associated with this perturbation is interpreted as the width of the localisation band. Λ_{min} is the wavelength where the real part of $s = 0$, and any perturbation with a smaller wavelength than this cannot propagate. These values are indicated in Figure 5.1:

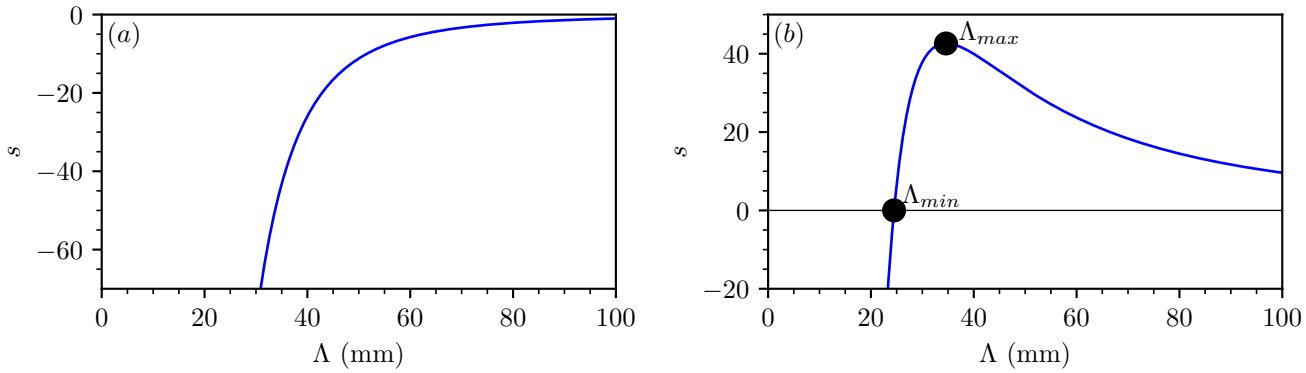

Figure 5.1: A typical example of the behaviour of the Lyapunov exponent s versus the perturbation wavelength Λ: (a) before a bifurcation has occurred, and (b) after a bifurcation has occurred, with the points defining Λ_{min} and Λ_{max} highlighted.

We consider a reference state corresponding to homogeneous deformation, so that all Cosserat terms are zero. As a consequence, the bifurcation matrix is significantly simplified, as setting $\kappa^e_{ij} = 0$ results in $F^{ep}_{ijkl} = K^{ep}_{ijkl} = 0$, and only the elastic component of M^{ep}_{ijkl} remains. This reduces the equation we seek to solve to

$$\begin{vmatrix} E^{ep}_{jklm}\frac{4\pi^2\mathrm{i}^2}{\Lambda^2}n_m n_k - \rho s^2\delta_{jl} & E^{ep}_{jklm}\epsilon_{lmo}\frac{2\pi\mathrm{i}}{\Lambda}n_k \\ -\epsilon_{jkl}E^{ep}_{klmo}\frac{2\pi\mathrm{i}}{\Lambda}n_o & M^{ep}_{jklm}\frac{4\pi^2\mathrm{i}^2}{\Lambda^2}n_m n_k\delta_{lp} - \epsilon_{jkl}E^{ep}_{klmo}\epsilon_{mop} - Is^2\delta_{jp} \end{vmatrix} = 0 \tag{5.11}$$

We may then apply specific loading conditions to investigate the model's behaviour under particular physical config-

urations.

It should also be noted that beyond the point of initial bifurcation, the homogeneous solution we assume for the linear stability analysis is no longer valid. However, by continuing to integrate the model (assuming homogeneity), we can explore the tendencies of the system close to the homogeneous state by continuing to integrate the mathematical equations (assuming homogeneity) beyond the bifurcation point.

5.3.2 Finite element method

The finite element method permits the exploration of the post-localisation regime in a rigorous fashion as there is no need for any part of the system to be assumed to be homogeneous.

The system to be integrated with the FEM consists of the (static) momentum balance equations of the Cosserat continuum, namely

$$\tau_{ij,j} = 0, \tag{5.12}$$

$$\mu_{ij,j} - \epsilon_{ijk}\tau_{jk} = 0. \tag{5.13}$$

The boundary of the system $\partial\Omega$ can be partitioned into two parts, $\partial\Omega_D$ where Dirichlet boundary conditions are applied, and $\partial\Omega_N$ where Neumann boundary conditions are applied, noting that $\partial\Omega = \partial\Omega_D + \partial\Omega_N$.

The Dirichlet conditions on $\partial\Omega_D$ are

$$u_i = u_i^d, \tag{5.14}$$

$$\omega_i^c = \omega_i^{cd}, \tag{5.15}$$

where u_i^d and ω_i^{cd} are the prescribed displacements and Cosserat rotations respectively.

The Neumann conditions on $\partial\Omega_N$ are

$$\tau_{ij}n_j = t_i^d, \tag{5.16}$$

$$\mu_{ij}n_j = m_i^d, \tag{5.17}$$

where t_i^d and m_i^d are the prescribed tractions for the stresses and couple-stresses respectively.

The weak form of the balance equations can be written as

$$-\int_\Omega \tau_{ij}\psi_{i,j}\,\mathrm{d}\Omega + \int_{\partial\Omega_N} \tau_{ij}n_j\psi_i\,\mathrm{d}S = 0, \tag{5.18}$$

$$-\int_\Omega \mu_{ij}\psi_{i,j}\,\mathrm{d}\Omega + \int_{\partial\Omega_N} \mu_{ij}n_j\psi_i\,\mathrm{d}S - \int_\Omega \epsilon_{ijk}\tau_{jk}\psi_i\,\mathrm{d}\Omega = 0, \tag{5.19}$$

where ψ_i are test functions.

The system is integrated in the Numerical Geolab framework, which provides a generalised continuum layer on top of the finite element solver FEniCS (Stefanou, 2018). We use an implicit backwards Euler method, and select quadratic test functions for the displacements and linear test functions for the Cosserat rotations (Godio et al., 2015). This general formulation allows us to implement our model and compare with results obtained from experiments and field observations.

5.4 Parameter values

5.4.1 Calibrated values

We take the values of the Breakage model that we explore from those used in Das et al. (2011) modelling Bentheim sandstone, which in turn were calculated from Baud et al. (2004, 2006), Tembe et al. (2008) and Wong et al. (2001). Following these papers, we also set the ultimate fractal parameter $\alpha = 2.6$ and take 0.105 mm as the maximum grain size. Consistent with Buscarnera and Einav (2012) and Kendall (1978) and the arguments therein, we set the minimum grain size to 0.001 mm. These choices set the values for $\theta_\gamma, \theta_\kappa$ and θ_I. We have additional sets of model parameters associated with our re-framing of the model in the Cosserat continuum, which are calculated as per §4.6.1. The kinematic model in three dimensions is selected, and the model parameter relating the elastic and plastic length scales is set $\zeta = 1$. We treat the h^2 parameter ξ merely as a numerical smoothing parameter that allows the system to be numerically integrated more easily. Hence, we set $\xi = 100$ so that we are close to the response of the underlying hyper-plastic model. Finally, the total set of physical parameters in units of grams/millimetres/milliseconds is

Mechanical Parameters			Granulometry Parameters		
K	13833	MPa	θ_γ	0.80	
G	7588	MPa	θ_κ	0.89	
G_c	12646.7	MPa	θ_I	0.91	
H	7588	MPa	d_{Max}	0.105	mm
H_c	12646.7	MPa	ρ	2.5×10^{-3}	g/mm^3
E_c	4.65	MPa			
M	1.7				
ω	70	$^\circ$			

Table 5.1: List of material constants.

Unless otherwise specified, all calculations in this thesis use the values listed in Table 5.1 and start from $B = 0$.

5.4.2 Sensitivity analyses

Here, we focus on the coupling angle ω and the breakage variable B. Both of these parameters are not available to models outside of the Breakage Mechanics framework, and hence we can gain new understanding of the importance of different physical processes that cannot be inferred from other model families. We focus on these two parameters because they reveal important information about the underlying physics of the process. ω characterises whether grain breakage or pore collapse is the favoured method of energy dissipation in the system. B tells us about the grain size distribution and how much energy is available to be dissipated in grain crushing. Both of these aspects of the system are particularly salient to our focus on the formation of cataclastic shear bands, making an analysis of the system sensitivity to changes in these parameters potentially illuminating for both our understanding of the physics, and the strengths and limitations of our model.

5.5 Load conditions

We can in principle use our methods to explore a wide variety of load conditions. First we use the LSA to determine where on the yield surface bifurcation is likely to occur. We do this by fixing a value of B (hence determining the yield surface) and setting $\kappa^e_{ij} = 0$ as we remain in the Cauchy continuum up until localisation. We then find the set of elastic strains that apply to the load conditions and lie on the yield surface. For each member of this set of elastic strains, we check to see if there is a positive value of the growth coefficient s at a very large wavelength ($\Lambda = 10000$ mm). If so we conclude that this region of the yield surface supports a localisation.

We then simulate an individual load path using with a single element implementing the h^2plasticity version of the model, and pass the set of state variables at each step in time to the analysis code, which returns whether there is a

localisation, and if so the corresponding minimum and maximum wavelengths.

The result of this LSA analysis is used to size the system that we simulate using the FEM. We ensure that the total size of our system is at least five times that of Λ_{min} at first localisation, and that we have at least ten elements spanning the expected width Λ_{max} of the band at first localisation. These values are drawn from experience, but we verify the adequacy of the choices in Appendix G. The results of the LSA and the FEM can then be compared.

In this thesis we focus on shearing under constant volume. Shearing under constant volume corresponds to fast undrained shear that can be seen in seismogenic faults, and allows us to reduce our system to a pseudo-one-dimensional problem.

We also examine three other loading conditions, using only the LSA technique, shearing under constant confining stress, œdometric compression and biaxial compression. Shearing under constant confining stress corresponds to seismogenic faults when undergoing drained shear. Œdometric compression corresponds to the standard laboratory œdometric test. Both of these load conditions allow a reduction to a pseudo-one-dimensional system. While the biaxial compression test is less common than the triaxial compression test, it allows us to reduce our system to a pseudo-two-dimensional problem, and to make a comparison to literature that is specifically focused on shear band formation.

5.5.1 Constant volume shearing

As discussed in §5.5, a system undergoing shear at a constant volume is analogous to the undrained shear that occurs during seismic slip. While our model does not feature any hydraulic coupling, it is still important to understand how the model behaves under these conditions.

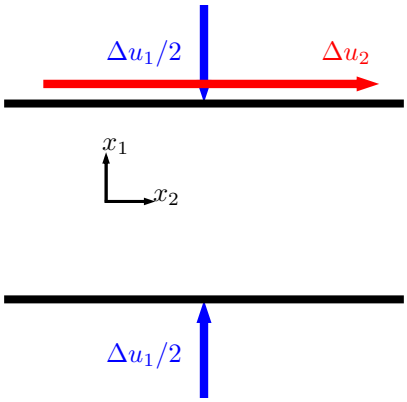

Figure 5.2: A schematic of the system that we consider. We apply a total displacement of Δu_1 in the x_1 direction that acts as a pre-confinement, marked in blue. We then start our test at $t = 0$ and apply a displacement Δu_2 in the x_2 direction to induce shearing, marked in red. During shearing we maintain constant volume (no further Δu_1 is applied). The system is invariant in the x_3 direction.

The system that we consider is illustrated in Figure 5.2. Applying the appropriate simplifications to (4.1) and (4.5) results in reduced strain and curvature rate tensors for both the pre-confinement stage and the constant volume shearing test:

$$\dot{\gamma}_{ij} = \begin{bmatrix} \frac{\partial \dot{u}_1}{\partial x_1} & \dot{\omega}_3^c & 0 \\ \frac{\partial \dot{u}_2}{\partial x_1} - \dot{\omega}_3^c & 0 & 0 \\ 0 & 0 & 0 \end{bmatrix}, \tag{5.20}$$

and

$$\dot{\kappa}_{ij} = \begin{bmatrix} 0 & 0 & 0 \\ 0 & 0 & 0 \\ \frac{\partial \dot{\omega}_3^c}{\partial x_1} & 0 & 0 \end{bmatrix}. \tag{5.21}$$

Linear stability analysis

The first step is using the LSA to understand the behaviour of the system in a general sense. In order to do this, we examine where on the yield surface can support bifurcation. This is a *qualitative* description that gives an indication of the behaviour. If we limit our analysis to consider only the pairs of elastic strains γ^e_{11} and γ^e_{21} that place the system described above on the yield surface, there appears to be no bifurcation supported by the system. This behaviour can ultimately be traced to the fact that $\gamma^e_{22/33} = 0$ during elastic loading.

However, if we were to imagine following an individual load path, $\gamma^e_{22/33}$ will start to accumulate as we enter the plastic region of the load path, which ultimately allows the system to bifurcate. To represent this behaviour, we consider systems with *isotropic* values of the elastic strains. This allows the determination of which parts of the yield surface can *in principle* support bifurcation for our load conditions.
Thus, the calculation steps are:

1. Fix a value of B (thus determining the yield surface),
2. Set an isotropic value of $\gamma^e_{11/22/33}$ less than or equal to $\gamma^e_{p_{crit}}$, the isotropic elastic strain that corresponds to the critical pressure for that value of B,
3. Calculate the shearing strain γ^e_{21} that places the system on the yield surface,
4. Check whether for a very large wavelength ($\Lambda = 10000$ mm) there is a value of s with positive real part.

If the condition in step 4 is fulfilled, there is a bifurcation and the system will form a shear band. We checked a range of representative values and in each instance observed that the horizontal orientation $n_i = 1, 0, 0$ results in the maximal value of s for these load conditions. Hence in this case we assume a horizontal band orientation, resulting in a significant calculation speed-up relative to requiring the system perform an optimisation of the value of s with respect to n_i.

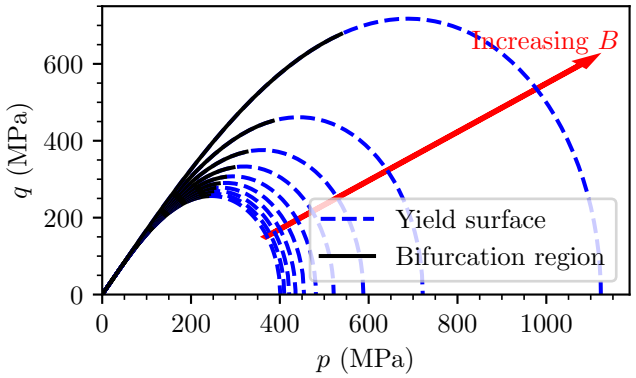

Figure 5.3: The regions of the yield surface that can in principle support localisation parallel to the shear direction when sheared under constant volume conditions, using the calibrated values of the material parameters. The analysis is performed for $B = 0, 0.1, \ldots, 0.9$, with the corresponding yield surfaces above.

In Figure 5.3 we can observe that the region that supports shear band formation for the calibrated values consistently occurs on the lower confining pressure side of the yield surfaces, where plastic shear straining is the dominant form of dissipation. We can also see that that as B increases, the fraction of the yield surface that supports bifurcation decreases gradually. This indicates that as the grain size distribution approaches its ultimate value, the possibility to

dissipate energy via grain crushing reduces, and the set of stress states that support band formation are those that favour dissipation via plastic shearing.

We can now follow an individual load path to observe the favoured localisation width and the predicted post-localisation behaviour. For this analysis we apply the confinement as described in Figure 5.2, rather than the isotropic confinement we have used to study the localisation regions of the yield surface. Thus, we impose γ_{11} while setting $\gamma_{22} = \gamma_{33} = 0$. It should also be noted that the homogeneous reference state of the LSA is in the classical continuum, and as rotational equilibrium must be obeyed, the strains will be symmetric per (4.3) rather than the Cosserat form in (5.20). Hence, we apply shear strain γ_{21} and γ_{12}.

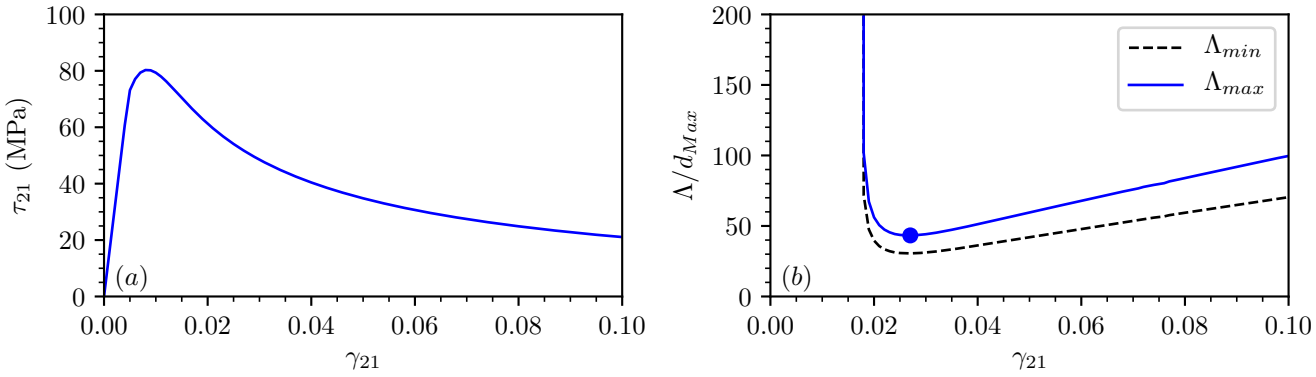

Figure 5.4: The system behaviour at constant volume with increasing shear strain. (a) The shear stress τ_{21}, and (b) the minimum wavelength for perturbation growth Λ_{min} and the fastest growing wavelength Λ_{max}. Both wavelengths have been normalised by the largest grain size d_{Max}. We place a marker on the minimum value of Λ_{max} for clarity. We will later use this value in sizing our FEM system.

In Figure 5.4 we observe that a shear band forms during shear at constant volume for the calibrated values we have chosen. We interpret the minimum value attained by the Λ_{max} curve to be the predicted thickness of the shear band in these conditions. It should be noted that the shear bands form at $\gamma_{21} \approx 0.02$, which is more than twice the strain associated with the peak of the $\tau_{21} - \gamma_{21}$ curve. In the $\tau_{21} - \gamma_{21}$ curve we observe some apparent softening. We emphasise that this softening is only *apparent*, and that the system is actually hardening in the classical sense (the yield surface is expanding).

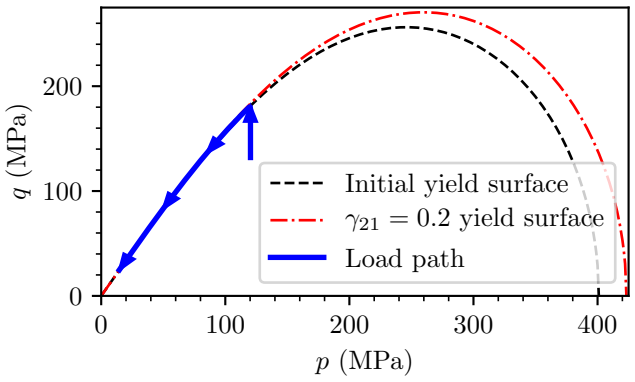

Figure 5.5: A comparison of the $p - q$ points that lie on the initial yield surface for $B = 0$, and for $B = 0.217$ (corresponding to $\gamma_{21} = 0.2$), with the load path of the curve in Figure 5.4.

In Figure 5.5 we demonstrate the contrast between the apparent softening and the true hardening. For the sake of clarity we have continued the load path integration to $\gamma_{21} = 0.2$ to show the growth of the yield surface. This behaviour arises as the growth of the breakage variable B contributes to an expanded yield surface, while also reducing

the effective stiffness of the material.

As well as the calibrated values of the system, we can explore how the system changes when we change some of the parameters related to Breakage Mechanics. In particular, we are interested in how the behaviour changes as we change the maximum grain size, the initial value of the breakage, and the tendency of the system to dissipate via either grain crushing or plastic volumetric straining. We focus on these three parameters because they reveal important information about the underlying physics of the process. ω characterises whether grain breakage or pore collapse is the favoured form of energy dissipation in the system. d_{Max} and B tell us about the grain size distribution, which in turn informs us about how much capacity to dissipate energy via grain crushing remains in the system before it saturates. Both of these aspects of the system are particularly salient to our focus on the formation of cataclastic shear bands, making an analysis of the system sensitivity to changes in these parameters potentially illuminating for both our understanding of the physics, and the strengths and limitations of our model.

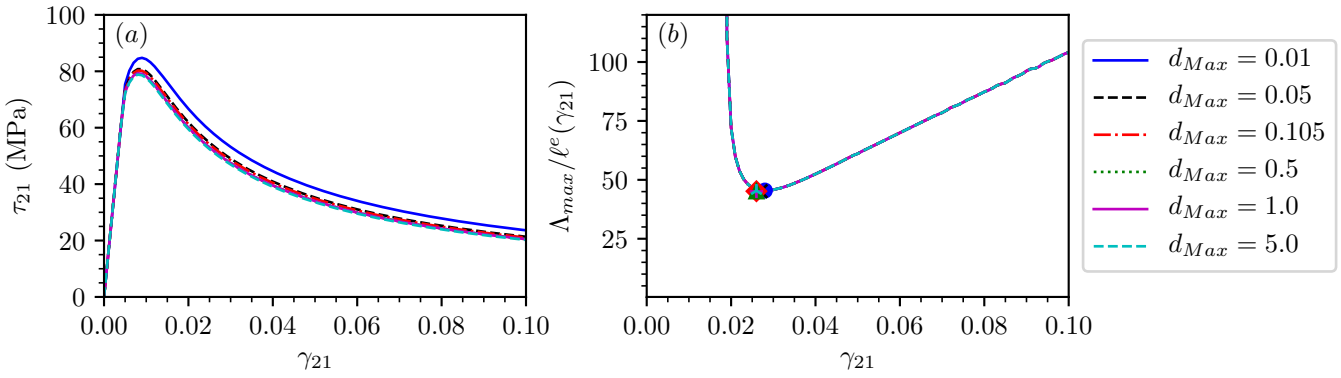

Figure 5.6: The system behaviour at constant volume with increasing shear strain, for six different values of maximum grain size d_{Max}. (a) The shear stress τ_{21}, and (b) the fastest growing wavelength Λ_{max}. The wavelengths have been normalised by the internal length scale of the respective material. Each of these curves were confined to the same initial γ^e_{11} before shearing commenced. A marker is placed on the minimum values of Λ_{max} for clarity.

In Figure 5.6 we observe that when we normalise the curves by their respective internal lengths ℓ^e, we observe that the system effectively collapses onto one curve, despite orders of magnitude difference in the absolute size of the predicted shear band. It is important to note here that the normalising length is not constant here, and evolves due to the increase in B. We can see that in this instance the internal length sufficiently captures all of the relevant physics (both the absolute grain size and the relative polydispersity) to serve as an ideal normalisation length. In this case, the polydispersity is characterised purely by the ratio of the smallest to the largest particle size. However, we can also investigate a more complex measure of polydispersity by changing the relative weight of intermediate particle sizes, via changing the initial values of B. In this case, our plot in Figure 5.3 remains valid to characterise which regions of the yield surface can support shear band formation.

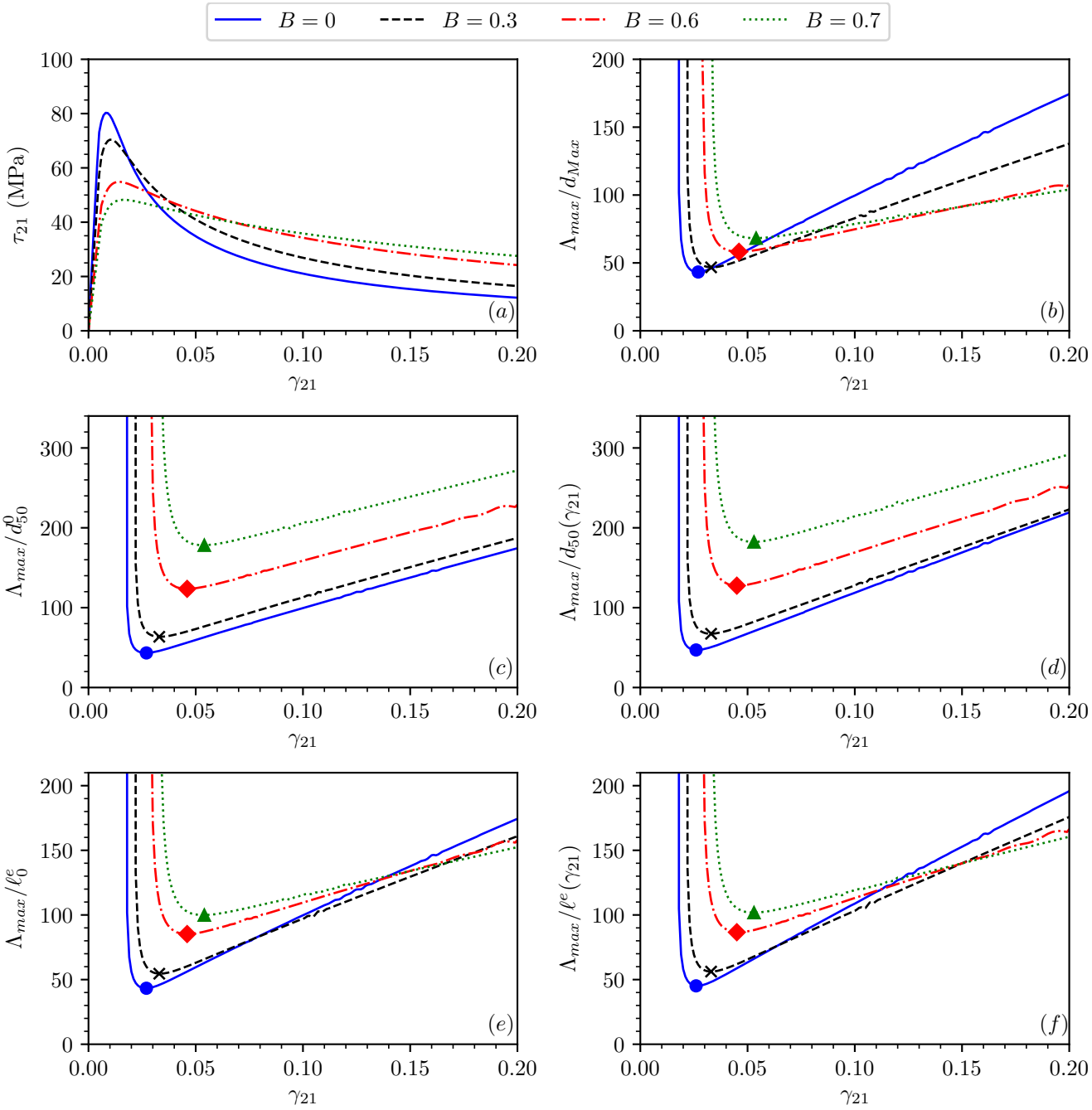

Figure 5.7: The system behaviour at constant volume with increasing shear strain, for four different initial values of B. (a) The shear stress τ_{21}, (b) the fastest growing wavelength Λ_{max} normalised by d_{Max}, (c) Λ_{max} normalised by the respective initial values of d_{50}, (d) Λ_{max} normalised by the respective values of d_{50} as they evolve, (e) Λ_{max} normalised by the respective initial values of ℓ^e, and (f) Λ_{max} normalised by the respective values of ℓ^e as they evolve. Each of these curves were confined to the same initial γ_{11}^e before shearing commenced. A marker is placed on the minimum values of Λ_{max} for clarity.

We plot in Figure 5.7 a number of different means of normalising the width of the predicted shear band. We also continue to shear up to $\gamma_{21} = 0.2$ to observe the longer-term tendencies of the behaviour. Firstly, we observe that the same qualitative behaviour is observed for all of the different initial values of B. However, as the initial particle breakage is increased, the formation of a shear band requires increasingly more shear strain, and the initial band width is wider, but also grows at a slower rate. This last effect is sufficiently pronounced that after $\gamma_{21} \approx 0.1$ the shear band associated with the initially unbroken material is predicted to be thicker relative to its grains than the bands with already broken grains.

In particular, when we study different normalisation strategies, we observe that normalising by the largest grain size d_{Max} gives the closest grouping of initial widths, and thus the most accurate indication of potential shear band widths, particularly at lower values of B, and thus polydispersity. We also note that when we normalise by the evolving internal length scale ℓ^e, the curves converge faster than if we normalise solely by the respective initial values ℓ^e_0. At larger values of shear, the normalisation with evolving length scale causes the three curves for $B \geq 0.3$ to converge. From these normalisation comparisons, we observe that normalising either by the initial or evolving mean grain size d_{50}, we obtain the largest spread between the initial localisation widths, and no or very slow convergence.

Now, by changing the material parameter ω we may instead examine the tendency of the system to favour dissipation via plastic volumetric straining over dissipation via grain crushing. In this instance the regions of the yield surface which can support shear band formation must be recalculated.

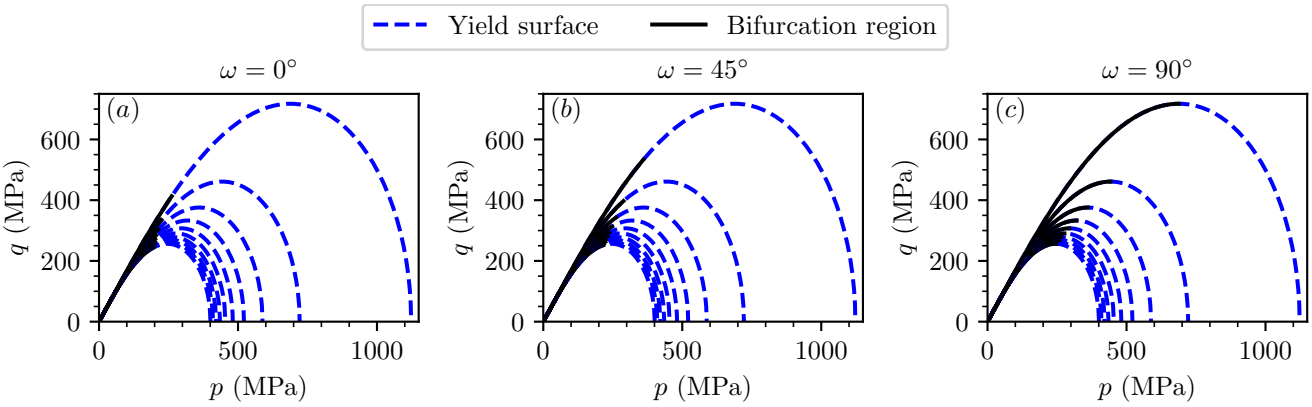

Figure 5.8: The regions of the yield surface that can in principle support localisation parallel to the shear direction when sheared under constant volume conditions, for (a) $\omega = 0°$, (b) $\omega = 45°$, and (c) $\omega = 90°$. The analysis is once again performed for $B = 0, 0.1, \ldots, 0.9$, with the corresponding yield surfaces shown above.

In Figure 5.8 we can see that changing the value of the parameter ω has a significant effect on the ability of the system to support shear band formation. In the system where $\omega = 0°$ (i.e. where grain crushing is most strongly favoured) only low confining pressures allow the formation of shear bands. The fraction of the yield surface that can support band formation also dramatically reduces as B increases. By contrast, the system where $\omega = 90°$ (i.e. where pore collapse is most strongly favoured) supports shear band formation for any region of the yield surface to the left of the maximum value of q. This behaviour does not change with increasing values of B. The system where $\omega = 45°$ (i.e. where the two dissipative mechanisms are balanced) is intermediate between the two end members in both the extent of the bifurcation region at $B = 0$, and the behaviour of the bifurcation region as B grows.

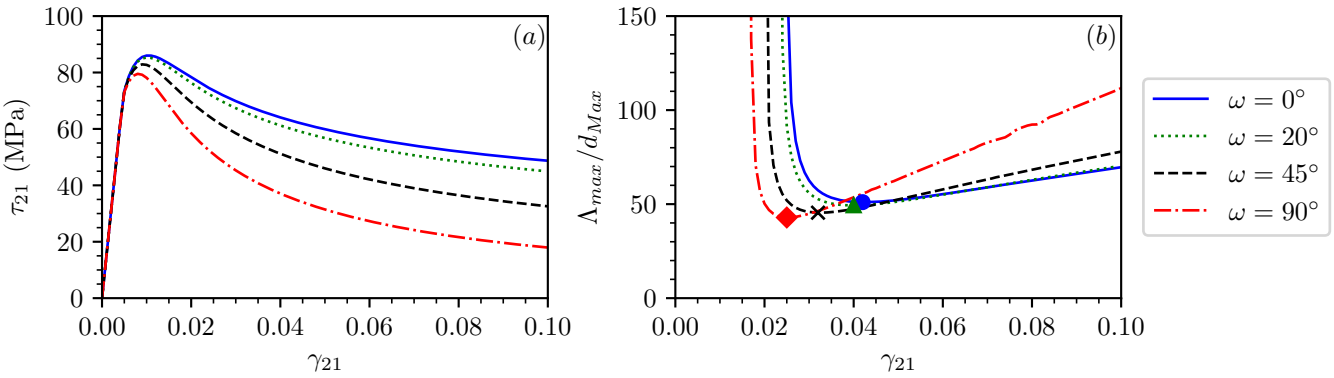

Figure 5.9: The system behaviour at constant volume with increasing shear strain, for four different values of ω. (a) The shear stress τ_{21}, and (b) the fastest growing wavelength Λ_{max}. The wavelengths have been normalised by the largest grain size d_{Max}.

In Figure 5.9 we can see the different behaviour of the system following a given load path, for various values of ω. When considering the $\tau_{21} - \gamma_{21}$ plot we can see that the for smaller ω the apparent softening is smaller. When we consider the localisation behaviour, we observe that increasing the value of ω results in localisation at a smaller value of shear strain, and the localisation is thinner relative to the constituent grains. The thickness of the band grows faster as ω increases.

Finite element method

Using the analysis from the LSAs, we may size our finite element system. We select a system that is 35 mm in total, which is slightly more than 5 times the widest initial localisation that we expect. We simulate the system with 641 elements. The choice of these two values is discussed in Appendix G. We also make use of a rescaling factor (1000 or 10000) that is applied to the displacements and strains. The displacements are multiplied by the factor, while the strains are divided. This has the effect of increasing the number of time steps, while reducing the number of iterations required to converge at each time step. The net effect is a slight loss in accuracy relative to an unscaled system, which is more than made up for by a significant calculation speed-up.

For our boundary conditions, we fix zero Cosserat rotations at both boundaries. The physical meaning of this choice is that at the boundaries of the system, the Cosserat effects are eliminated. We then compress one side of the system until the displacement associated with our target strain is reached. The displacement in this direction is then fixed, and shear displacement is applied in the other direction, up until the target displacement is reached.

The calculation times of the system depend on a variety of factors, including the exact parameter values, the amount of scaling, how much deformation is applied and how the computing resources are allocated within the cluster carrying out the computations. Certain parameter values can lead to the system being relatively stiffer than other possible systems. The scaling factors change the number of Newton iterations at a given time step, which is an expensive operation. The calculation will run much faster for elastic and homogeneous plastic deformations, but once localisation starts will require very small time steps. However, once the localisation is well established, the calculation speeds up again. Computing on multiple nodes of a cluster adds a certain amount of overhead cost as at least one CPU core on each node must devote part of its run time to allocating the distribution of calculations between the other cores on that machine, and passing information back and forth between the machines. For the same amount of computing resources, calculations on one node will be more efficient as no CPU time needs to be dedicated to passing information between nodes. While we ran a variety of different simulations, varying all of these factors, we take as being approximately representative a simulation that we ran using 8 CPUs on two nodes, with 641 elements, scaling factor of 1000, and targeting a homogeneous strain value of $\gamma_{21} = 0.2$. The simulation completed in 13 hours, 22 minutes and 6 seconds, with CPU utilisation at 92.2% and 89.3% on the two nodes. This gives a computational efficiency of 375.4 seconds per element per unit of strain i.e. at the rate that the overall system was calculated, a single element system could be calculated to a strain of $\gamma_{21} = 1.0$ in just over six minutes. We note also that this calculation time can be considerably reduced by forcing the system to converge towards a particular bifurcation state, but the result will then obscure the true behaviour of the underlying system.

We start by considering the calibrated values listed in Table 5.1 and starting from $B = 0$. To illustrate the behaviour of the system as we increase shear, we can plot the values of B across the spatial coordinate and observe the signal of the shear band. We select B as the variable that we use to indicate the shear band formation (as opposed to other possible choices such as γ_{21}^p or λ (Rattez et al., 2018c)) as the primary interest of this thesis is the formation of cataclastic shear bands. B is a unique feature of Breakage Mechanics models that allows us to track this form of localisation.

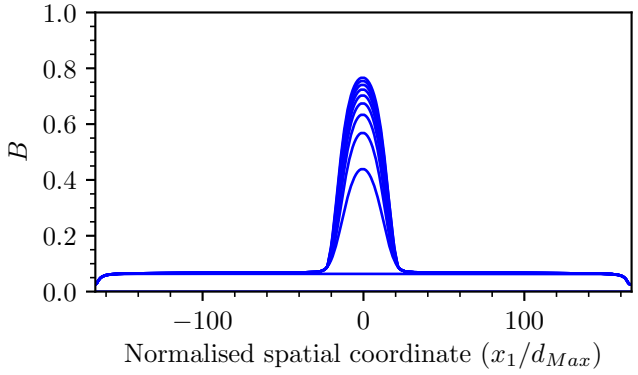

Figure 5.10: The total value of B, plotted over the spatial coordinate normalised by the reference grain size x_r, for the calibrated parameter values. The increment between each curve is kept constant ($\Delta\gamma_{21} = 0.035$).

In Figure 5.10 we observe a clear localisation of the value of B, with a very clear band forming in the centre of the system, well away from the wall effects visible at the edge. We plot for consistent increments of homogeneous strain γ_{21}^h (that is to say, the shear strain calculated as if the deformation was accommodated homogeneously across the system, neglecting the contribution of the Cosserat rotations). However, we note that for the calibrated value of ω (and high values of ω generally) in this load condition, the system becomes very difficult to resolve as the system moves into the bottom left corner of the yield surface at large strains. Figure 5.5 illustrates this behaviour. However, we succeed in applying more than enough strain to observe and understand the behaviour of the system.

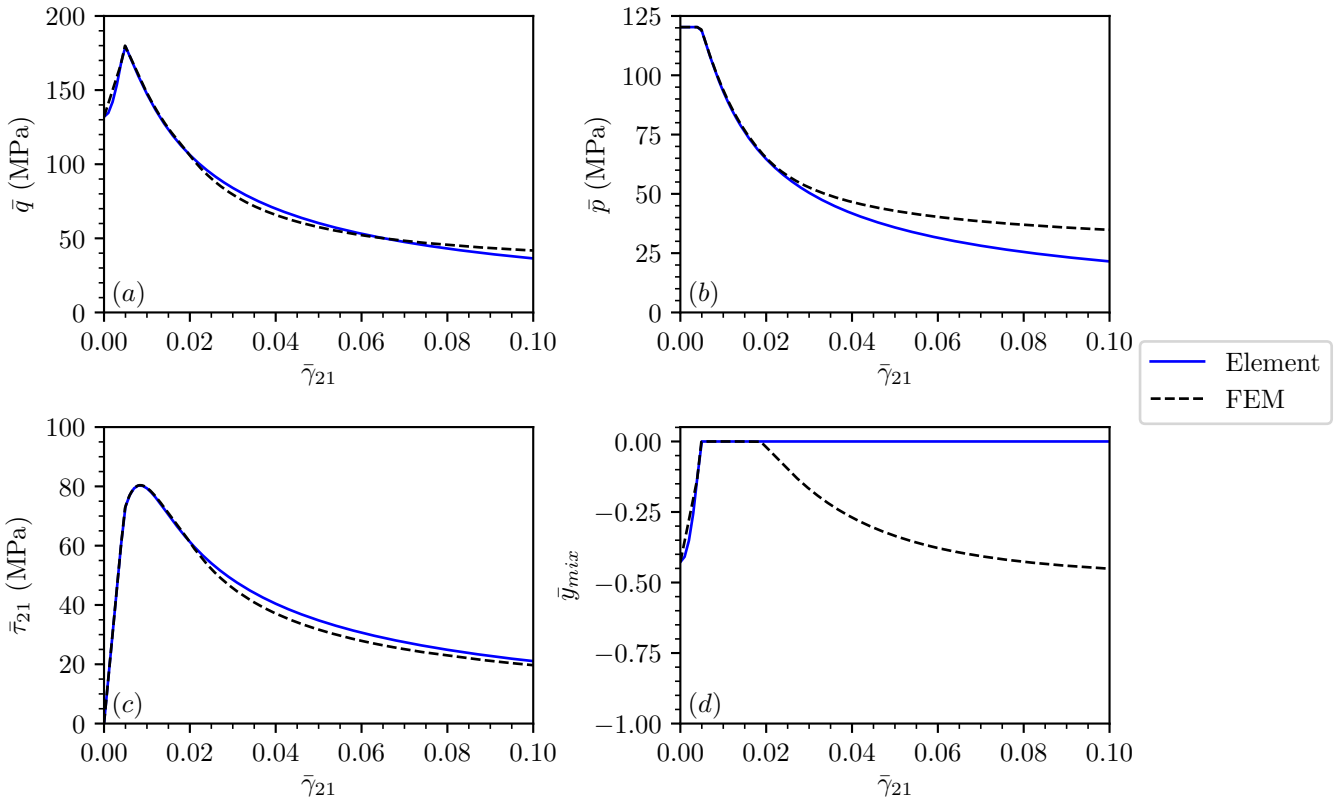

Figure 5.11: The macroscopic response of the finite element system relative to the response of a single element submitted to the same strains for the calibrated parameter values. We plot the average values over the entire FEM system of (a) $\bar{q}$, (b) $\bar{p}$, (c) $\bar{\tau}_{21}$, and (d) $\bar{y}_{mix}$, against the value of $\bar{\gamma}_{21}$, once again averaged over the entire system.

Figure 5.11 demonstrates differences between the macro-response of the FEM system compared to that of the single element. By comparing the behaviours in Figure 5.11(c), we may infer that this arises due to the presence of

couple-stresses. In the single element simulation, the system takes $\dot{\gamma}_{ij}$ (in this case $\dot{\gamma}_{21}$ and $\dot{\gamma}_{12}$) as inputs and has $\dot{\kappa}_{ij} = 0$ at all times. However, the FEM system can obey rotational equilibrium with asymmetric stresses so long as there is a counter-balancing couple stress. This results in slightly lower stress values of τ_{21} in the FEM system, as shown in Figure 5.11(c), due to the formation of a stress-couple. However, in Figure 5.11(a), we observe that these effects are captured in q, meaning that the FEM system and the single element follow a similar paths with respect to q space, but that the components of q differ between the two. Figure 5.11(b) demonstrates an eventual divergence in the values of p between the two systems, suggesting that in the FEM system eventually changes to the couple-stresses are favoured over changes to the stresses. We also observe in Figure 5.11(d) the very clear macroscopic signal of shear band formation after the onset of plasticity. While the single element reaches plasticity and then remains on the yield surface, the FEM system deforms homogeneously before the formation of the shear band. The band formation is indicated by the average value of the yield function $\bar{y}_{mix}$ decreasing despite continued straining. The local value of y_{mix} will remain zero in the shear band, but will decrease outside of it as the system unloads elastically.

Much like with our LSAs, we can also benefit from a sensitivity analysis of the system conducted in FEM. We start by considering the systems that start with different initial values of B. In this instance, we shear our system only as far as $\gamma^h_{21} = 0.2$, so that we have file sizes that are small enough that we can visualise them, while still being well past the point of localisation. We start by plotting the evolution of the breakage variable.

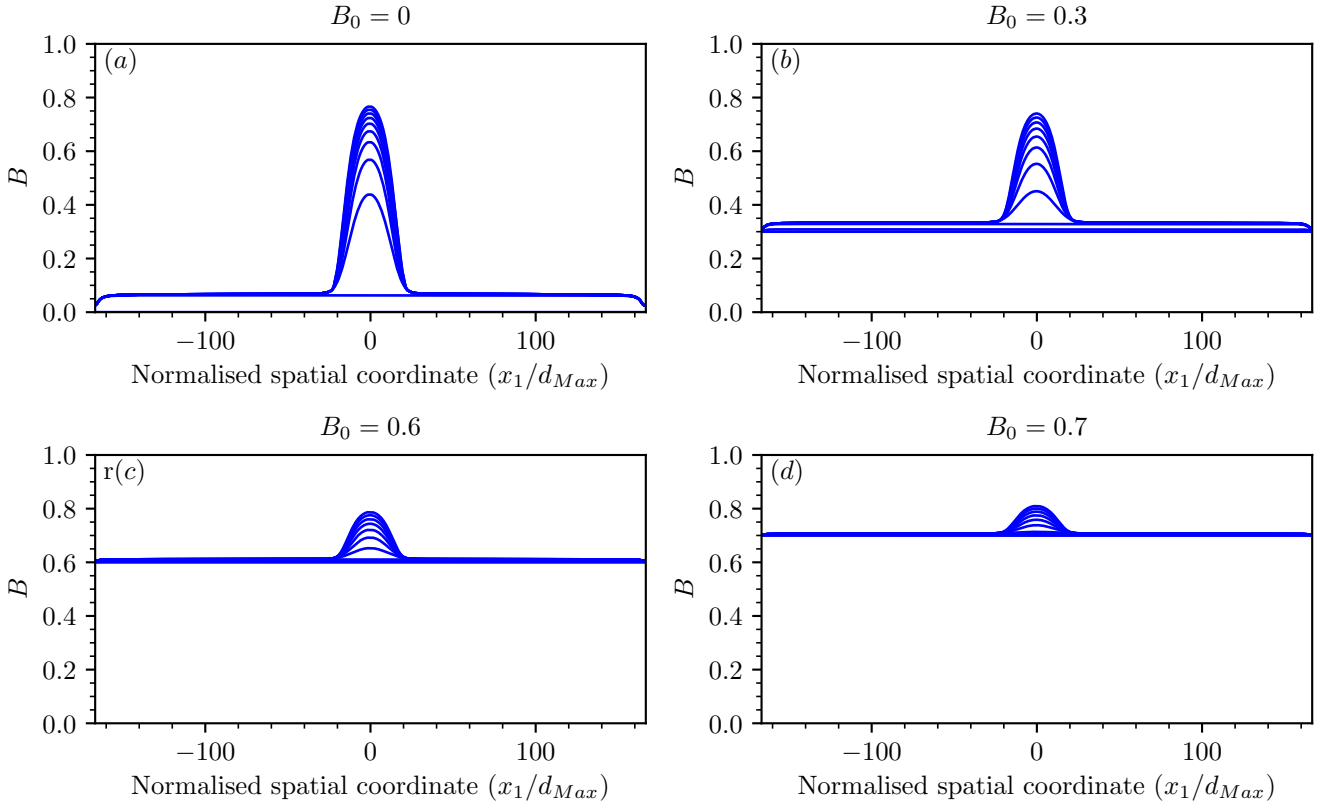

Figure 5.12: The evolution of B for (a) initial $B = 0.3$, with increments of homogeneous strain between the lines being $\Delta\gamma^h_{21} = 0.02$, and (b) initial $B = 0.6$, with increments of homogeneous strain between the lines being $\Delta\gamma^h_{21} = 0.02$.

From Figure 5.12 we can observe that in both instances the shear band formation is well-behaved, remaining stable at the centre of the system, with no influence from the boundaries visible.

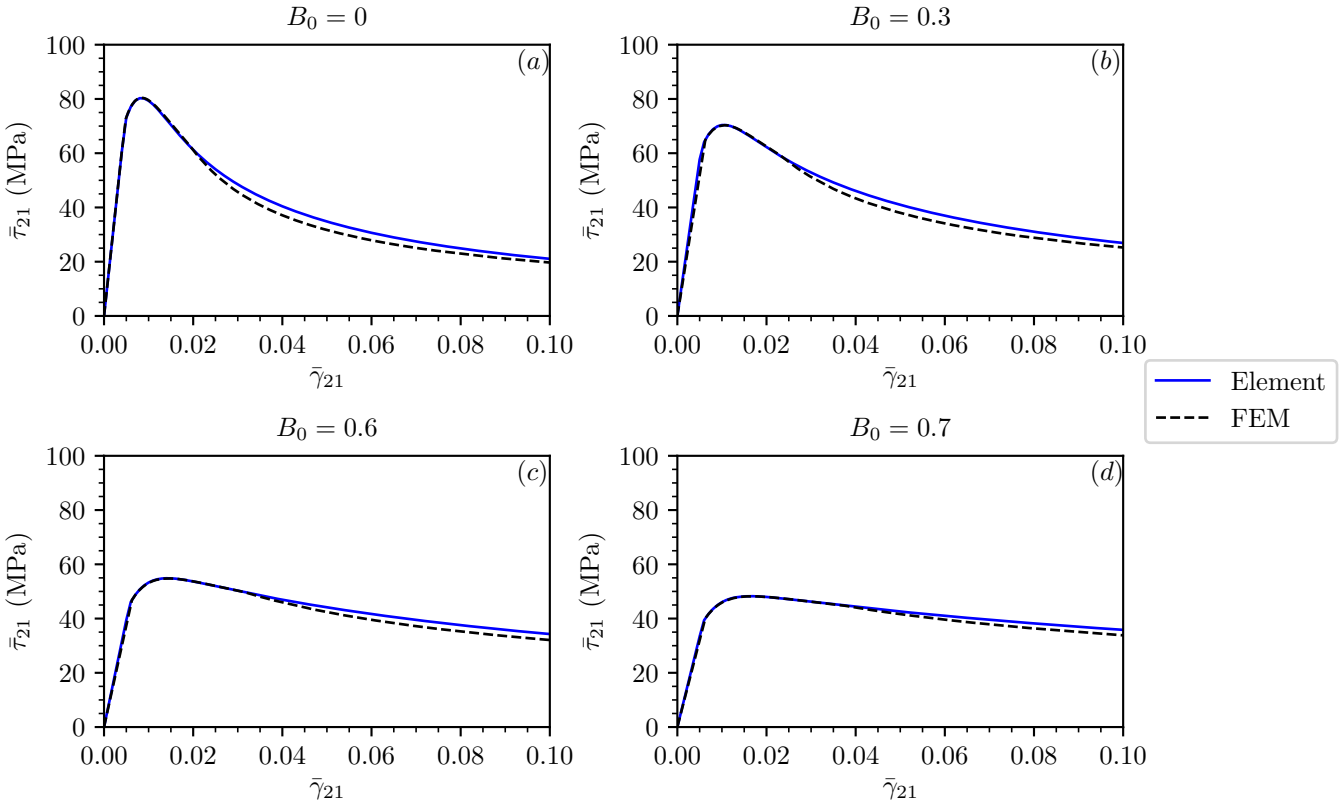

Figure 5.13: The macroscopic average stress response $\bar{\tau}_{21}$ of the finite element system relative to the response of a single element submitted to the same strains for (a) $B_0 = 0$, (b) $B_0 = 0.3$, (c) $B_0 = 0.6$ and (d) $B_0 = 0.7$.

Figure 5.13 demonstrates that when changing the initial value of B, we observe qualitatively the same behaviour as for the calibrated values, with the same underlying causes, of couple-stresses compensating for shear stresses. It should be noted that the difference between the overall response and the single element response increases as we increase B, with much lower peak stresses obtained, but also correspondingly smaller apparent softening behaviour demonstrated.

By examining both the progression of the value of B as the shear band forms, and the macroscopic effect on the shear band behaviour, we may conclude that changing the initial value of B in the system does not induce substantive qualitative changes in the overall system behaviour, but that the quantitative effects are notable.

We may also examine the changes to the system that arise when we change the values of ω, indicating a change in the system's preference between dissipation via grain crushing or pore collapse.

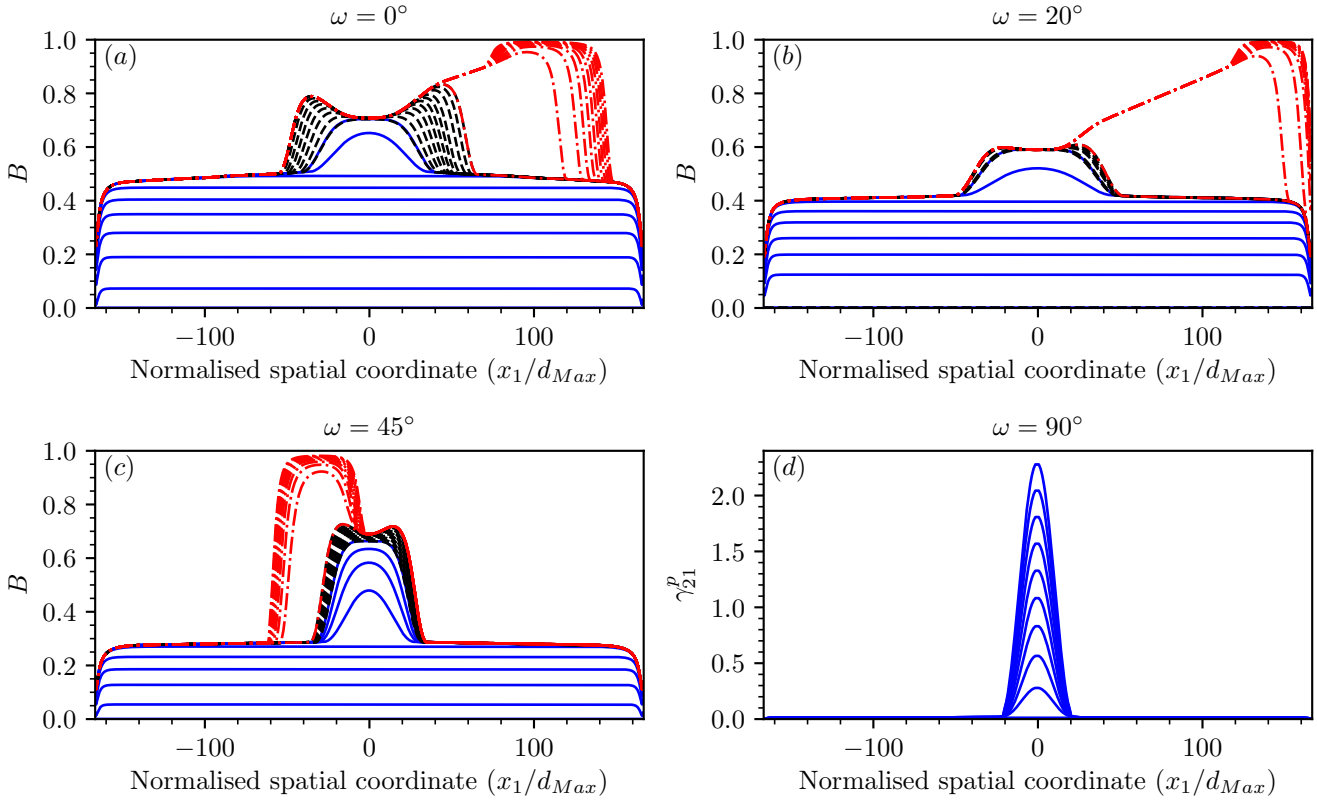

Figure 5.14: The evolution of B for: (a) $\omega = 0°$, with increments of homogeneous strain between the blue lines being $\Delta\gamma_{21}^h = 0.0076$, between the black lines $\Delta\gamma_{21}^h = 0.0036$, and between the red lines $\Delta\gamma_{21}^h = 0.1888$, (b) $\omega = 20°$, with increments of homogeneous strain between the blue lines being $\Delta\gamma_{21}^h = 0.006$, between the black lines $\Delta\gamma_{21}^h = 0.0005$, and between the red lines $\Delta\gamma_{21}^h = 0.1935$, (c) $\omega = 45°$, with increments of homogeneous strain between the blue lines being $\Delta\gamma_{21}^h = 0.0077$, between the black lines $\Delta\gamma_{21}^h = 0.0022$, and between the red lines $\Delta\gamma_{21}^h = 0.1901$. (d) The evolution of γ_{21}^p for $\omega = 90°$, with increments of homogeneous strain between the blue lines being $\Delta\gamma_{21}^h = 0.0329$.

We can observe several important behaviours when we analyse the plots in Figure 5.14. We have plotted homogeneous and single-band evolution in blue, the evolution between a single band and a double-band structure in black, and the off-centre single band evolution to saturation in red.

Observable in Figure 5.14(a,b,c) is the formation of a double-band structure for values of $\omega \leq 45°$. These double band structures saturate after a relatively small amount of additional straining, and one of the bands becomes dominant and continues to grow. We observe that the shear band width essentially saturates past a certain point, with there being very little breakage growth even for large strain increments. It should be noted that as the band width is defined in terms of the *rate* of B, the bands at large shear values are actually narrow strips growing at the edge of regions with saturated values of B. That is to say, while the regions featuring crushed and broken grains become increasingly large, the shear bands that are growing the size of the region become increasingly small.

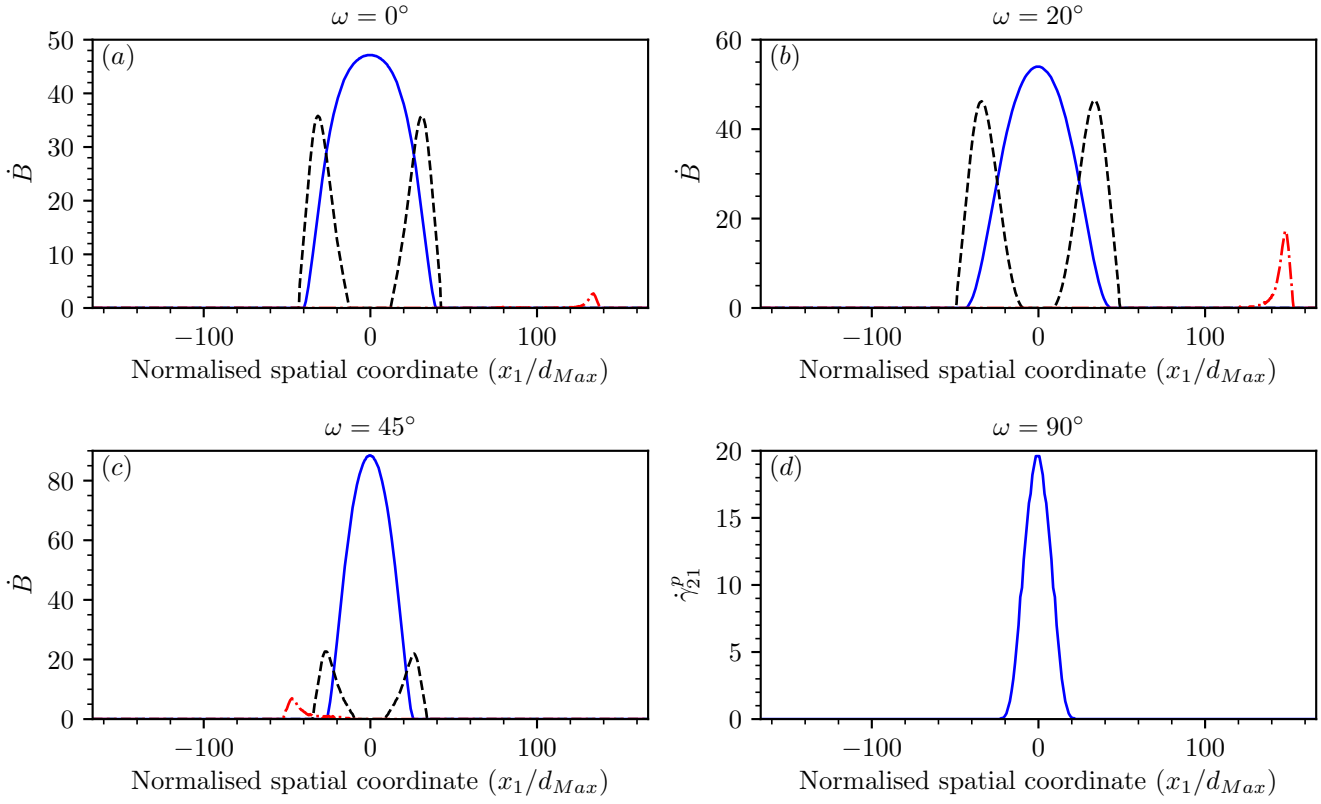

Figure 5.15: The evolution of $\dot{B}$ for (a) $\omega = 0°$, with the blue curve at a homogeneous strain level of $\gamma_{21}^h = 0.0620$, the black curve at a homogeneous strain level of $\gamma_{21}^h = 0.0792$, and the red curve at a homogeneous strain level of $\gamma_{21}^h = 0.8669$, (b) $\omega = 20°$, with the blue curve at a homogeneous strain level of $\gamma_{21}^h = 0.05298$, the black curve at a homogeneous strain level of $\gamma_{21}^h = 0.0615$, and the red curve at a homogeneous strain level of $\gamma_{21}^h = 0.2570$, (c) $\omega = 45°$, with the blue curve at a homogeneous strain level of $\gamma_{21}^h = 0.0486$, the black curve at a homogeneous strain level of $\gamma_{21}^h = 0.0946$, and the red curve at a homogeneous strain level of $\gamma_{21}^h = 0.2307$, (d) $\omega = 90°$, with the blue curve at a homogeneous strain level of $\gamma_{21}^h = 0.0657$.

In Figure 5.15, we plot the distribution of breakage rates, using just one representative curve for each phase of shear band development for the sake of clarity. We can clearly see that as the band development progresses, the active zone that defines the shear band becomes increasingly thin, as well as asymmetrically distributed in space. We may also observe the saturation of the grain breakage, with the asymmetric band growing at a much slower rate than the double bands, which in turn grow more slowly than the single shear band.

It is also important to note that in the case of $\omega = 0/20°$, the shear band migrates towards the system boundary. This may result in a certain amount of interference from boundary effects (particularly for $\omega = 20°$). However, while we should not put too much store in the precise numerical values of the model at large strains (noting that it is a small-strain model, and involves many simplifications), the behaviour is at least indicative of phenomena observed in the field and laboratory and discussed in Chapter 2, namely the presence of bands of ultra-cataclastic material in zones that have undergone arbitrarily large shearing, in a range of load conditions (Das et al., 2013).

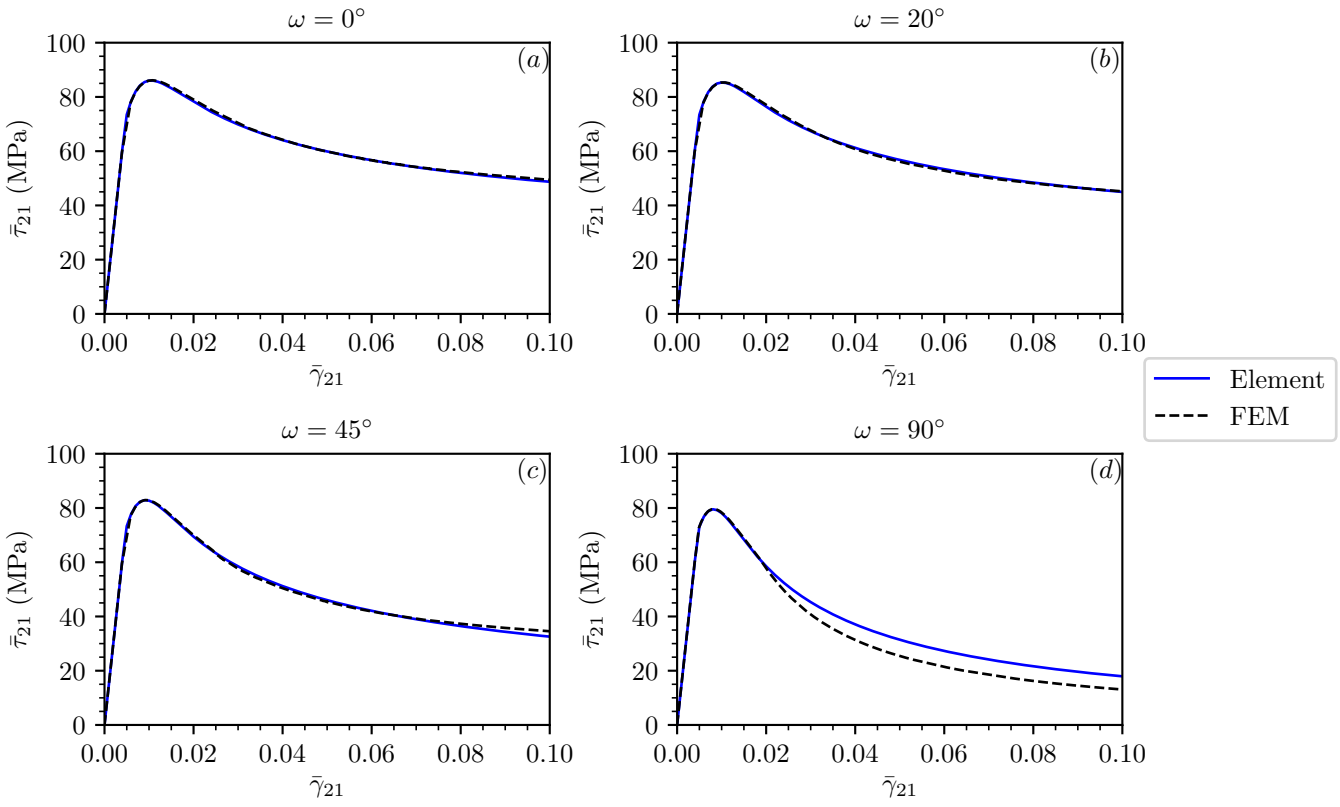

Figure 5.16: The macroscopic average stress response $\bar{\tau}_{21}$ of the finite element system relative to the response of a single element submitted to the same strains for (a) $\omega = 0°$, (b) $\omega = 20°$, (c) $\omega = 45°$ and (d) $\omega = 90°$.

Figure 5.16 demonstrates that when changing the initial value of ω, we observe qualitatively the same behaviour as for Figure 5.11. The macroscopic response follows the single element response for each of the four different cases, with there being notably softer macroscopic behaviour only for the system with $\omega = 90°$. This behaviour suggests that the broader bands observed for the lower values of ω induce very little stress asymmetry, and hence only have negligible stress couples relative to the narrower bands of the systems with higher values of ω.

These results illustrate several important tendencies of the system. For the lower values of ω, we observe a clear tendency to form two bands (this is not contradictory with our LSA per se, as once the system loses uniqueness several solutions become possible, including multiple localisations). One of these bands eventually dominates, and the long term behaviour of this band is towards a much narrower localisation than both the initial localisation width, and the width predicted by the LSA at large strains (indeed, the LSA predicts a steadily widening band). However, for the two larger values of ω, we see behaviour that is qualitatively similar to that predicted by the corresponding LSA, in that the width (very gradually) grows as strain increases, albeit at a much slower rate than predicted by the LSA. We may observe that the localisation gradually becomes wider for $\omega = 70°$, but that for $\omega = 90°$ it is almost constant. This difference in behaviour can be explained by the state variables remaining almost constant in the case of $\omega = 90°$, due to the absence of grain crushing. Hence, from this analysis we may conclude that the tendency of the system to favour either grain crushing or plastic volumetric deformation has a clear effect on the initial localisation behaviour, but that the behaviour under large strains is much less clear and requires further investigation.

5.6 Discussion

There are several underlying physical behaviours that are illustrated by our study of the model applied under several different loading conditions.

5.6.1 Constant volume shearing

Firstly considering the results we have obtained under constant volume shear in §5.5.1, we observe certain trends across both our analyses using the calibrated values, and the sensitivity analyses we have also conducted. Importantly, we note that the linear stability analysis provides a reasonably accurate prediction for the initial thickness of the shear band that we observe in the finite element implementation, albeit after following a different stress-strain curve than predicted. We speculate that this is because the Cosserat rotations are not taken into account in the LSA or in the calculation of the homogeneous shear strain. The effect of accumulating elastic curvatures results in yield after less apparent straining in certain elements, softening the overall response. However, these curvatures also contribute to making the $\tau_{21} - \gamma_{21}$ curve soften at a slower rate.

Turning to our sensitivity analyses, we may observe that the initial value of B does not have a very strong effect on the system behaviour. We observe good agreement between the linear stability analysis and finite element method results, with increasing initial values of B leading to very similar shear band structures, despite substantial changes in the value of the mean grain size. This trend in behaviour may be able to explain why researchers are yet to determine a constant scaling between d_{50} and the band thickness, as it also depends on the polydispersity of the grain size distribution. Figure 5.7 indicates that for the initial band width, d_{Max} is actually a more indicative value, while for increasing strains, the evolving internal length scale ℓ^e converges more rapidly than any other length. However, the indications from this plot are that no single length scale is sufficient to accurately and fully characterise the predicted shear band width once the polydispersity in the system involves a continuous distribution of grain sizes that are constantly changing.

By contrast to the behaviour as we change the initial value of B, we see that the value of ω has a very strong effect on the overall behaviour. The LSA predicts the trend of diminishing initial thickness with increasing ω. However, the LSA consistently predicts an initial rapid increase in band thickness post localisation. However, this is largely not what we observe in the FEM system. We see that in the case of $\omega = 0/20/45°$, two separate and smaller shear bands form on either side of the initial shear band. Once one of these bands becomes dominant, we observe that the tendency of the band is to become significantly *narrower* than its initial thickness. This band thickness also stabilises, with little to no change and a value of B very close to 1. These smaller values of ω appear to exhibit the essential behaviour that we observe in ultra-cataclastic shear bands in seismic faults, which is to say that there is a band of stable thickness with extremely crushed grains, surrounded by a band of less broken grains, which is in turn surrounded by the broader damage zone. However, when considering the behaviour at larger values of ω, we can see there is a qualitative change in the post-localisation behaviour of the material. For some (as yet undetermined) value of ω, the system transitions between a single stable shear band that grows slowly (for high values of ω), and an unstable band that degenerates into firstly two bands, and then one thin band where the centre moves in space. These results are at least suggestive that it is the porosity which is the true controlling factor of the behaviour that we observe, with systems that are capable of exhibiting pore collapse behaving very differently to those that are not. Nevertheless, while ω represents in some sense this behaviour, the reality is that the evolutions of the pore space and the grain size distribution are closely tied together, and our simple model that poses them as competing processes is not refined enough to accurately determine the role of porosity.

The ability of the model to predict the formation of double-bands in material that strongly favours grain crushing is paralleled by the observations that field geologists have made.

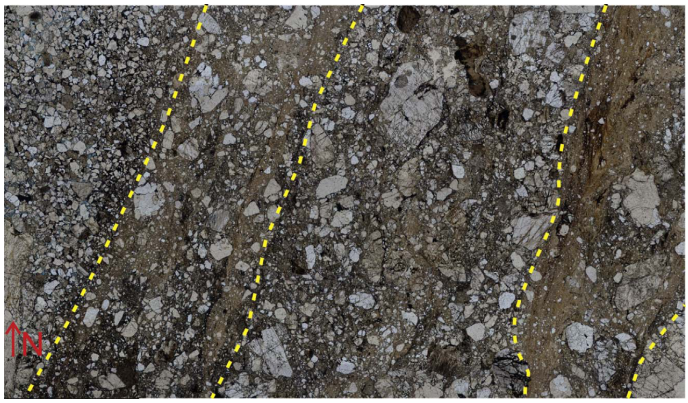

Figure 5.17: An image of two ultra-cataclastic zones sandwiching a cataclastic zone, from Nicchio et al. (2018). The zone boundaries are highlighted in yellow.

In Figure 5.17, we see the clear presence of two zones of ultra-cataclastic material that have formed in feldspar rich conglomerates. These zones lie on either side of a zone with significantly less cataclasis. Similar observations can also be found in Aydin and Johnson (1978), Bürgi et al. (2001) and Wibberley and Shimamoto (2002) amongst others, in a variety of different rock types and locales. Our model predicts this phenomenon for material that strongly favours grain crushing, and not in material that strongly favours pore collapse, illustrated in Figure 5.14. This aspect of the model behaviour can be used to infer material properties and calibrate models (specifically ω) from field observations of double-band presence or absence, and draw conclusions about which dissipative mechanisms were dominant at different points in the geological history of the rock.

It should be noted that the inferences we can draw for the long-term behaviour of the systems with high ω are limited by the failure of the system to converge. Ultimately it is because under these load conditions, the system moves to very small $p-q$ values in the left-hand corner of the yield surfaces (the tendency is illustrated in Figure 5.5), which eventually reach sufficiently small values that the numerical material model is unable to resolve them satisfactorily. The most promising way in which this problem can be resolved in future research is to implement a model that incorporates a true critical state, i.e. one that includes the porosity ϕ as an internal variable (Tengattini et al., 2016). The current model only includes the critical state in $p-q$ space, rather than the more traditional $p-q-\phi$ space, or indeed $p-q-\phi-B$ for breakage models with porosity. In our model the $p-q$ space critical state is not actually accessible, serving instead as an asymptote for the system. Introducing porosity to the model would not only have the effect of introducing a physical and accessible critical state to stabilise the numerical implementation, but would also increase the fidelity of the model towards the underlying physics of the system. Our current model which represents porosity change through plastic volumetric strain that is ultimately controlled by ω, can accommodate arbitrarily large volumetric strains. However, introducing a porosity state variable puts appropriate physical bounds on the system behaviour, allowing pore collapse processes to saturate. Implementing an accurate pore-scale model is also essential in order to be able to expand the model to hydro-mechanical processes, where the collapse of pore space can lead to dramatic increases in pore pressure that in turn cause dramatic decreases in the effective stress and overall sliding resistance of the system.

The role of the evolving internal length scale, the key contribution of this thesis, is to consistently reduce the characteristic length scale of the system. Ultimately this will result in narrower predicted shear bands than if the internal length was some fixed value, which causes the grain crushing to be further localised within an intense cataclastic shear band. However, while it is possible to specify evolving length scales using empirical evolution laws, for the mean grain size, this will not include the effects of the other sizes present in the grain size distribution. These other grain sizes interact with each other in complex ways such as small grains acting as cushions for larger grains, which ensures that even in the ultimate grain size distribution there are still large grains present. Mathematically this is reflected in the evolving length scale having a maximum size (d_{Max}), but also a minimum size that reflects the presence of the larger

grains. This minimum size prevents the system from becoming stuck in a feedback loop of grain crushing resulting in a smaller length scale which results in a smaller band which in turn results in more intense grain crushing and so on. Our length scale is not only based in a rich physical description, but also demonstrates mathematically favourable properties, which are particularly useful when considering multi-physical couplings.

5.6.2 Constant confining stress shearing

Turning now to our results on the system under constant confining stress rather than constant volume elaborated in §H, we have observed some unexpected behaviours. The first behaviour that we note is that when varying the value of B, the predicted localisation widths collapse onto a single curve, indicating that d_{Max} is a better indication of localisation width than d_{50} under these load conditions. The second behaviour we observe is that the system consistently produces bands that form at an angle relative to the shear plane, namely Riedel shear bands. As discussed in §H, the consequence of this behaviour is that we can study this load case using LSAs, but studying it using the FEM is more difficult as we are unable to apply the appropriate boundary conditions.

Our model predicts the formation of the antithetic Riedel band that is at a high angle to the shear plane. We note that in this model, synthetic Riedel bands demonstrate ill-posed behaviour, most likely due to their featuring a dilating component, something that this model cannot implement. Once again, the inclusion of porosity in the model enables the exploration of a wider range of possibilities, specifically dilative shear bands all the way up to pure dilation bands (although we note that much like pure compaction bands, pure dilation bands would require some additional method of regularisation to be implemented). Exploring the formation of these bands using a more sophisticated model would be an interesting route for further research, albeit still restricted to the LSA technique only.

5.6.3 Œdometric compression

Now, considering our analysis of the system under œdometric compression in §I, we can see that the behaviour imparts information about which regularisation technique is most appropriate under these conditions. Essentially, the Cosserat continuum fails to regularise under œdometric compression, suggesting that at least for the regularisation of pure compaction or dilation bands, we require either a full first-order micromorphic theory, or some form of viscous regularisation. An interesting and important aspect to explore in future research is whether the viscous rate-dependent effects that arise from the internal grain damage processes (Marinelli and Buscarnera, 2019a; Sohn and Buscarnera, 2019; Zhang and Buscarnera, 2017, 2018) predict a sufficiently thick compaction band, or whether the full first order micromorphic continuum must be adopted for continuum modelling of granular media.

In spite of the Cosserat continuum's failure to regularise in the pure compaction band limit, the breakage mechanics model still conveys important information about the conditions that enable band formation. Figure I.2 and Figure I.3 demonstrate that only the systems which strongly favour pore collapse (i.e. have high values of ω) and have low to moderate values of B are able to form compaction bands. Similarly, Figure I.4 illustrates that the maximum grain size also has a strong effect on the size of localisation zone on the yield surface. These two behaviours align with the observations made by geologists both in the field and experimentally, that highly porous rocks favour the formation of compaction bands (Castellanza et al., 2009; Papazoglou et al., 2017; Wong and Baud, 2012; Wong et al., 2001), and that rocks with narrower grain size distributions are more likely to generate compaction bands than those with broader distributions (Cheung et al., 2012).

We may conclude from our model and the results of other authors (Das, 2013; Das et al., 2011) that the essential conditions for band formation are that the material has the capacity for both extensive pore collapse and grain crushing, with these two processes being intertwined. We would further suggest that the apparent discrepancy between the conditions in which bands form in the laboratory (and in our model), i.e. under relatively high pressure, and that which geologists have inferred to be the field conditions during band formation can be explained by the transformation of the material over time as it underwent lithification. At the time of the band formation, we expect that these

æolian sands were extremely loose and with large grains, creating a material that formed compaction bands at very low *absolute* pressures, but which nevertheless corresponded to pressures near p_{crit} for the material at that time. The lithification process that transformed the sand into sandstone has served to expand the range of pressures over which the material acts elastically, leading to the discrepancy in band formation pressures.

5.6.4 Biaxial compression

Our biaxial results presented in §J demonstrate the importance of ω in determining whether a localisation forms. For systems that favour grain crushing (or even that are balanced between grain crushing and pore collapse) we see that the system fails to localise, as the hardening tendency of the system is sufficient to overwhelm any tendency to localise that may be induced by the non-associated evolution laws. For those systems that do localise, we observe that using the LSA, the band width appears to be stable, growing only very slowly and with only gradual angular change predicted. This behaviour is also true for systems that start with more broken grains, however these systems also take longer to converge on a stable localisation width than those with initially unbroken grains. The ultimate predicted localisation width also demonstrates very little variation with changing values of B, indicating once again that d_{Max} is a better indication than d_{50}.

It should be noted that other theories have been able to successfully predict localisation in biaxial tests with dilatant shear bands (Zervos et al., 2001, 2007), which is not possible in our model. This further points to the necessity of equipping future models with a porosity state variable which can be used to model dilative behaviour.

Recent workers using digital image correlation have observed deformation in a biaxial test being accommodated by a series of intermittent shear bands (Lanatà, 2015; Le Bouil et al., 2014), although the reported tests eventually demonstrate permanent shear bands. There have also been similar results reported by workers making use of three-dimensional X-ray tomography (Desrues et al., 2018) on a triaxial compression test.

However, for tests performed on Gosford sandstone (Ord et al., 1991), the presence of a single through-going shear band is visible on specimen-scale experimental photographs, and scanning electron micrographs reveal a narrow region of intense cataclasis surrounded by a region of cracked grains which is in turn surrounded by undamaged matrix. These tests also feature a through-going crack, which provides an indication of the limitations of our model. Future modelling attempts on cohesive granular rocks require us to include some form of damage variable that can replicate a cracking process, which will also have the effect of easing the convergence issues our model suffered at low pressures by expanding the elastic region (Das et al., 2014; Tengattini et al., 2014b). A damage model must either be appropriately constructed to account for interfaces (Guiamatsia and Nguyen, 2014) and re-meshed as needed, or be integrated in a framework capable of supporting discontinuities such as the extended finite element method (XFEM) (Moës and Belytschko, 2002; Moës et al., 1999; Sukumar et al., 2000) if it is to be able to predict true through-going cracks and model the motion along them.

5.7 Conclusion

To conclude, we have implemented two distinct methods for examining localisations predicted by our constitutive model. Linear stability analyses are able to provide a description of which areas of the yield surface are capable of supporting localisation, as well as indicating the expected initial localisation width. Finite element methods for constant volume shearing have been able to confirm the general accuracy of the predictions of the linear stability analyses with respect to the initial width of the localisation. However, the finite element studies reveal that we require more strain to trigger localisation than predicted by the stability analyses, and that the shear band width either grows considerably more slowly (in the case of strong tendency to pore collapse) or actually localises further (in the case of strong tendency to crush grains), rather than increasing rapidly.

Using linear stability analyses of the system undergoing shear with constant confining stress have revealed that the model does not predict ultra-cataclastic shear bands parallel to the shear plane, as would be found in faults, but does predict Riedel shear bands with a stable width. However, the nature of these bands relative to the geometry of the problem means that we are unable to apply the appropriate boundary conditions to generate them using the finite element method.

Our linear stability analyses have shown that the Cosserat continuum does not regularise the system under œdometric compression, but these analyses can nevertheless be used to draw conclusions about the behaviour that confirm experimental and field observations of compaction bands, namely that their formation is favoured in rocks with high porosity and narrow grain size distributions.

Finally, our analysis of the system under biaxial loading conditions reveals that localisation in our model only occurs in systems that exhibit a strong preference for pore collapse over grain crushing, and that the band behaviour is stable in terms of its width and angle.

We have demonstrated that our model is capable of successfully modelling conditions corresponding to fast undrained shearing. By considering different load conditions, we have obtained predictions of Riedel band formation, while also highlighting possibilities for future work by expanding the model.

Chapter 6

Conclusions and Perspectives

6.1 Conclusions

This thesis has investigated the importance of grain sizes and their distribution to the macroscopic response of brittle granular media, in particular the formation of localised bands of deformation. We structured this thesis by considering the cycle of experiments, model development and numerical implementation. Each step of this cycle provides important insights for the next, as well as indicating possible future research directions to further progress our understanding of brittle granular media.

We described in Chapter 3 a series of experiments that were performed in the *Appareil Cisaillement Simple Annulaire*, typically referred to as ACSA. These experiments were conducted for two reasons:

1. To develop a method of image processing that can reliably extract velocity distributions and be used for the verification of future models, and
2. To provide some indicative evidence of whether shear band thickness varied only with the mean grain size, or if there was a more complex relationship at work that depended on the polydispersity.

The method that we developed involves performing a series of transformations on the photographs of the experiments that ultimately allow the extraction of time-averaged velocities with sub-particle resolution, which is more than sufficient to test the predictions that models may make about the spatial distribution of radial velocities in the ACSA device.

Using our image processing method, we examined the set of experiments and came to the conclusion that they were insufficient to formulate a strong claim about the laws that govern shear band width formation with respect to their constituent grains. However, they did show that materials with identical mean grain size but different levels of polydispersity produced shear bands of differing thickness.

We then moved to the development of a constitutive model that would be suitable for the prediction of localisations in brittle granular material, taking account of the evolving grain size distribution as the material undergoes crushing, described in Chapter 4. We accomplished this by developing a model that combined two distinct formulations of constitutive models, the Cosserat model formulation, and the Breakage Mechanics model formulation, to create a new Cosserat Breakage Mechanics model that combines the strengths of both model families while ameliorating some of their respective weaknesses. The general framework for the model was obtained by performing an elastic upscaling that was consistent with Breakage Mechanics in the classical continuum, but that included the energetic contributions of the elastic curvatures. As a natural consequence of this upscaling, we obtained a new internal Cosserat length that evolves as the grain size distribution does, and that includes information from the entire grain size distribution,

aligning with the insights we gained from our experiments.

In this chapter we also defined and analysed some new granulometry parameters, made a slight generalisation of the second deviatoric stress and strain invariants for the Cosserat continuum, and defined relationships between the stiffnesses in the classical continuum, and three new stiffnesses introduced with the Cosserat continuum. The final outcome of this is that we were able to specify an enriched Cosserat constitutive model that requires no additional calibration relative to the same model in the classical continuum, but also has additional predictive power due to the equations remaining well-posed during localisation processes.

Our model offers some theoretical justifications for the behaviour we observed in our experiments in Chapter 3, noting however that we are modelling a different type of material. This is further indication that conducting a more systematic set of experiments to determine precisely the effect of polydispersity would be a useful future research direction.

In Chapter 5, we studied the behaviour of the model with respect to its predictions of localisation behaviour. We used two methods to do so, linear stability analyses, typically referred to as LSA, and the finite element method, typically referred to as FEM. Using the combination of these methods, we were able to study a number of different loading conditions that related to common experimental or field conditions. The LSA enabled us to study how changing the material parameters, in particular the tendency of the model to dissipate energy either via grain crushing or pore collapse, would affect the loads required to induce a localisation. This method allowed us to obtain insights even in systems which the Cosserat continuum does not regularise, such as œdometric compression.

We also applied LSA to material-point integrations of our model. This method allowed us to predict the initial width of localisation thicknesses, and their predicted post-localisation tendency, which could be subsequently compared to the results obtained using the FEM. Of particular note is that under constant confining pressure, the model predicts Riedel shear bands that lie at an angle to the shear plane. This prediction offers a significant clue to how these cataclastic bands form as co-seismic structures. Similarly, when analysing the system under biaxial conditions, we observe that our model predictions agree with experimental observations of cataclastic bands forming at an angle to the applied tractions.

The FEM results showed generally good agreement with those of the LSA, and also enables the rigorous study of the post-bifurcation behaviour. This revealed the tendency of the system to form thin bands of ultra-cataclastic material in those systems that favoured grain breakage, when sheared at constant volume. This load condition is analogous to the fast undrained shearing observed in faults, and the formation of these thin ultra-cataclastic bands is consistent with field observations of the structure of faults.

6.2 Perspectives

In this thesis, we provided the foundations for further detailed study of a number of different questions that arose.

Firstly, and most obviously, the method of image analysis that we developed to study localisation in the ACSA can be applied to any number of experimental geometries, and can be used to inform further model development, or to test the predictions given by future models.

To the first end, a much more comprehensive series of experiments with different sets of grain sizes, different confining pressures and different velocities can be explored in order to experimentally determine the effect of polydispersity on the shear band thickness. As the ACSA is a large device featuring difficult-to-prepare samples, a comprehensive suite of experiments may well be a thesis-worth of work in and of itself. An alternative possibility is constructing a much smaller ACSA and scaling the particles down appropriately. This may also allow the extension of the experimental

techniques from conventional photography to X-ray imaging, as well as from two to three dimensions (Guillard et al., 2017). The potential of this technique to obtain a full and rich experimental understanding of the dependence of the system behaviour on polydispersity could underpin the development of not only new Cosserat Breakage Mechanics models, but also segregation models and refinements of well-known granular flow models such as the $\mu(I)$-rheology (GDR Midi, 2004).

Secondly, there is significant scope for refinement in the model that we have presented. The upscaling that we presented is almost entirely general for Cosserat Breakage Mechanics models, in the same way that the original Breakage Mechanics paper framed a general upscaling procedure in the classical continuum (Einav, 2007a). The only constitutive assumption our upscaling makes is that the energetic contributions of the elastic strains and curvatures are uncoupled. Hence, within this framework we can develop significantly more refined models.

In developing our model, we made a choice to use the most simple already existing Breakage Mechanics model that is capable of being re-framed in the Cosserat continuum (Das et al., 2011; Nguyen, 2011). This choice was made so that the model and its behaviour could be understood despite the additional complexity that the Cosserat continuum necessarily introduces. However, now that we understand the behaviour of the simplest Cosserat Breakage Mechanics model, there is ample possibility to add in the wide variety of additional physics that have been accounted for in recent years by a wide variety of workers in classical Breakage Mechanics.

The most important additional physical feature to include in the model is the porosity. This inclusion would allow both a description of the dilative behaviour that is impossible in the current model, and a much more refined compressive and shear behaviour that may have the benefit of numerically stabilising the model. In addition to the porosity, non-linear elasticity due to Hertzian contacts must be included for accurate representation of material behaviour, particularly at small strains (Tengattini et al., 2016). The model can be made to more accurately account for the presence of cement bridges between grains via the addition of a damage variable (Das et al., 2014; Tengattini et al., 2014b), which can further refine our ability to model tests on granular rocks. Breakage Mechanics has also been framed in a finite strain framework (Rubin and Einav, 2011) that would be more appropriate for the large shear strain simulations we have undertaken in this thesis, and for fault modelling in general. Finally, phenomena arising from fracture behaviour at the grain scale such as grain-size dependence of yielding (Zhang et al., 2016) and rate-dependence (Zhang and Buscarnera, 2017) may also be included in the model to increase its physical fidelity.

Hence, it is possible for us to imagine that simply by combining the state-of-the-art aspects of various models, we could straightforwardly arrive at an extremely comprehensive model that would be accurate at small strains and low confining pressures all the way to geological confining pressures and arbitrarily large strains, while also being well-regularised in shear due to Cosserat effects, and in compaction/dilation due to rate-dependent effects. It is conceivable that it may be necessary to move from Cosserat to a full-first order micromorphic continuum (i.e. one that includes second-gradient terms) in the event that the rate-dependent regularisation is insufficient, but in any event the possibility of an extremely physically rich and predictively powerful constitutive model would appear to be in reach.

Finally, we may wish in future to implement our models in conjunction with thermo-hydro-chemo-mechanical coupling. Recent research (Rattez, 2018; Rattez et al., 2018a,b,c) has revealed the importance of these couplings in localising behaviour, particularly within the physical context of seismogenic faults. There are a range of ways in which the information that we can in principle access through Cosserat Breakage Mechanics can significantly improve the modelling of these processes. The collapse of pore space and subsequent decrease in permeability, the amount of dissipation attributable to grain crushing and hence unavailable for frictional heating, and the amount of grain surface area for chemical reactions to take place, are all tightly intertwined with the overall behaviour of faults. Cosserat Breakage Mechanics offers the promise of greatly improving the physical fidelity and thus modelling accuracy of each component of these mathematically and physically complex systems. Even in typical laboratory situations such as undrained tri-

axial tests, researchers have witnessed the interaction of crushed grains with water pressure to form drainage channels (Sulem and Ouffroukh, 2006). Modelling complex systems such as these may necessitate a corresponding increase in the complexity of the numerical method we use to model it, such as extended finite element method (XFEM), material point method (MPM) or smoothed-particle hydrodynamics (SPH).

Overall, we may conclude that this thesis has formed a solid framework that advances both the experimental study of polydispersity in granular media, and the development of rich constitutive models that can capture a wide variety of physical phenomena.

Bibliography

Abed Zadeh, Aghil et al. (2019). "Enlightening force chains: a review of photoelasticimetry in granular matter". In: *Granular Matter* 21.4. ISSN: 1434-5021. DOI: 10.1007/s10035-019-0942-2. URL: https://doi.org/10.1007/s10035-019-0942-2.

Alevizos, Sotiris, Emmanuil Veveakis and Thomas Poulet (2014). "Thermo-poro-mechanics of chemically active creeping faults. 1: Theory and steady state considerations". In: *Journal of Geophysical Research: Solid Earth* 119.6, pp. 4583–4605. ISSN: 21699356. DOI: 10.1002/2013JB010071.

Andò, Edward et al. (2012). "Grain-scale experimental investigation of localised deformation in sand: A discrete particle tracking approach". In: *Acta Geotechnica* 7.1, pp. 1–13. ISSN: 18611125. DOI: 10.1007/s11440-011-0151-6.

Andò, Edward et al. (2017). "Strain Localisation in Sand in Cycles of Triaxial Compression and Extension: Continuum and Grain-Scale Analysis". In: *Bifurcation and Degradation of Geomaterials with Engineering Applications*. Ed. by Euripides Papamichos et al. Springer International Publishing, pp. 489–497. ISBN: 978-3-319-56396-1. DOI: 10.1007/978-3-319-56397-8. URL: http://link.springer.com/10.1007/978-3-319-56397-8.

Ando, Masataka (2001). "Geological and geophysical studies of the Nojima Fault from drilling: An outline of the Nojima Fault zone probe". In: *Island Arc* 10.3-4, pp. 206–214. ISSN: 10384871. DOI: 10.1111/j.1440-1738.2001.00349.x.

Aydin, Atilla and Ramil Ahmadov (2009). "Bed-parallel compaction bands in aeolian sandstone: Their identification, characterization and implications". In: *Tectonophysics* 479.3-4, pp. 277–284. ISSN: 00401951. DOI: 10.1016/j.tecto.2009.08.033. URL: http://dx.doi.org/10.1016/j.tecto.2009.08.033.

Aydin, Atilla and Arvid M. Johnson (1978). "Development of Faults as Zones of Deformation Bands and as Slip Surfaces in Sandstone". In: *Pure and Applied Geophysics* 116, pp. 931–942.

— (1983). "Analysis of faulting in porous sandstones". In: *Journal of Structural Geology* 5.1, pp. 19–31. ISSN: 01918141. DOI: 10.1016/0191-8141(83)90004-4.

Ballas, Gregory et al. (2013). "Shear-enhanced compaction bands formed at shallow burial conditions; implications for fluid flow (Provence, France)". In: *Journal of Structural Geology* 47, pp. 3–15. ISSN: 01918141. DOI: 10.1016/j.jsg.2012.11.008. URL: http://dx.doi.org/10.1016/j.jsg.2012.11.008.

Bardet, Jean-Pierre and Ioannis Vardoulakis (2001). "The asymetry of stress in granular media". In: *Int. J. Solids Structures* 38, pp. 353–367. ISSN: 00207683. DOI: 10.1016/S0020-7683(00)00021-4. URL: http://www.sciencedirect.com/science/article/pii/S0020768300000214.

Baud, Patrick, Emmanuelle Klein and Teng-fong Wong (2004). "Compaction localization in porous sandstones : spatial evolution of damage and acoustic emission activity". In: *Journal of Structural Geology* 26, pp. 603–624. DOI: 10.1016/j.jsg.2003.09.002.

Baud, Patrick, Veronika Vajdova and Teng-fong Wong (2006). "Shear-enhanced compaction and strain localization: Inelastic deformation and constitutive modeling of four porous sandstones". In: *Journal of Geophysical Research: Solid Earth* 111.12, pp. 1–17. ISSN: 21699356. DOI: 10.1029/2005JB004101.

Bauer, Erich (2016). "Simulation of the Influence of Grain Damage on the Evolution of Shear Strain Localization". In: *Continuous Media with Microstructure 2*. Ed. by B. Albers and M. Kuczma. Springer International Publishing, pp. 231–244. ISBN: 9783319282411. DOI: 10.1007/978-3-319-28241-1.

Bauer, Erich, Linke Li and Wenxiong Huang (2015). "Hypoplastic Constitutive Modelling of Grain Damage Under Plane Shearing". In: *Bifurcation and Degradation of Geomaterials in the New Millenium: Proceedings of the 10th*

International Workshop on Bifurcation and Degradation in Geomaterials. Ed. by Kam-Tim Chau and Jidong Zhao, pp. 181–187. ISBN: 9783319135052. DOI: 10.1007/978-3-319-13506-9.

Bauer, Erich, Linke Li and Mohammedkeya Khosravi (2017). "Modelling Grain Damage Under Plane Strain Compression Using a Micro-polar Continuum". In: *Bifurcation and Degradation of Geomaterials with Engineering Applications: Proceedings of the 11th International Workshop on Bifurcation and Degradation in Geomaterials dedicated to Hans Muhlhaus, Limassol, Cyprus, 21-25 May 2017*. Ed. by Euripides Papamichos et al. Springer International Publishing, pp. 349–359. ISBN: 9783319563961. DOI: 10.1007/978-3-319-56397-8. URL: http://dx.doi.org/10.1007/978-3-319-56397-8.

Bedford, John D. et al. (2018). "High-Resolution Mapping of Yield Curve Shape and Evolution for Porous Rock: The Effect of Inelastic Compaction on Porous Bassanite". In: *Journal of Geophysical Research: Solid Earth* 123.2, pp. 1217–1234. ISSN: 21699356. DOI: 10.1002/2017JB015250.

Beke, Barbara et al. (2019). "Deformation band formation as a function of progressive burial: Depth calibration and mechanism change in the Pannonian Basin (Hungary)". In: *Marine and Petroleum Geology* 105.April, pp. 1–16. ISSN: 02648172. DOI: 10.1016/j.marpetgeo.2019.04.006. URL: https://doi.org/10.1016/j.marpetgeo.2019.04.006.

Bésuelle, Pierre (2001). "Compacting and dilating shear bands in porous rock: Theoretical and experimental conditions". In: *Journal of Geophysical Research* 106.B7, pp. 435–442.

Bésuelle, Pierre and René Chambon (2007). "Étude de la localisation de la déformation à l'aide de modèles second gradient". In: *18ème Congrès Français de Mécanique*. Grenoble.

Bésuelle, Pierre, Jacques Desrues and Suzanne Raynaud (2000). "Experimental characterisation of the localisation phenomenon inside a Vosges sandstone in a triaxial cell". In: *International Journal of Rock Mechanics and Mining Sciences* 37, pp. 1223–1237. ISSN: 1365-1609. DOI: 10.1016/S1365-1609(00)00057-5.

Bésuelle, Pierre and Patrizia Lanatà (2016). "A new true triaxial cell for field measurements on rock specimens and its use in the characterization of strain localization on a vosges sandstone during a plane strain compression test". In: *Geotechnical Testing Journal* 39.5, pp. 879–890. ISSN: 01496115. DOI: 10.1520/GTJ20150227.

Bigoni, Davide and Tomasz Hueckel (1991a). "Uniqueness and localization - I. Associative and non-associative elastoplasticity". In: *International Journal of Solids and Structures* 28.2, pp. 197–213.

— (1991b). "Uniqueness and localization - II. Coupled elastoplasticity". In: *International Journal of Solids and Structures* 28.2, pp. 215–224. ISSN: 0020-7683. DOI: 10.1016/0020-7683(91)90206-U. URL: http://dx.doi.org/10.1016/0020-7683(91)90206-U.

Borja, Ronaldo I. (2000). "Finite element model for strain localization analysis of strongly discontinuous fields based on standard Galerkin approximation". In: *Computer Methods in Applied Mechanics and Engineering* 190.11-12, pp. 1529–1549. ISSN: 00457825. DOI: 10.1016/S0045-7825(00)00176-6.

— (2008). "Assumed enhanced strain and the extended finite element methods: A unification of concepts". In: *Computer Methods in Applied Mechanics and Engineering* 197.33-40, pp. 2789–2803. ISSN: 00457825. DOI: 10.1016/j.cma.2008.01.019.

Borja, Ronaldo I. and Richard A. Regueiro (2001). "Strain localization in frictional materials exhibiting displacement jumps". In: *Computer Methods in Applied Mechanics and Engineering* 190.20-21, pp. 2555–2580. ISSN: 00457825. DOI: 10.1016/S0045-7825(00)00253-X.

Brantut, Nicolas, Ioannis Stefanou and Jean Sulem (2017). "Dehydration-induced instabilities at intermediate depths in subduction zones". In: *Journal of Geophysical Research: Solid Earth* 122.8, pp. 6087–6107. ISSN: 21699356. DOI: 10.1002/2017JB014357.

Brantut, Nicolas and Jean Sulem (2012). "Strain Localization and Slip Instability in a Strain-Rate Hardening, Chemically Weakening Material". In: *Journal of Applied Mechanics* 79.3, p. 031004. ISSN: 00218936. DOI: 10.1115/1.4005880.

Brantut, Nicolas, Jean Sulem and A. Schubnel (2011). "Effect of dehydration reactions on earthquake nucleation: Stable sliding, slow transients, and unstable slip". In: *Journal of Geophysical Research: Solid Earth* 116.5, pp. 1–16. ISSN: 21699356. DOI: 10.1029/2010JB007876.

Bürgi, C., A. Parriaux and G. Franciosi (2001). "Geological characterization of weak cataclastic fault rocks with regards to the assessment of their geomechanical properties". In: *Quarterly Journal of Engineering Geology and Hydrogeology* 34.2, pp. 225–232. ISSN: 14709236. DOI: 10.1144/qjegh.34.2.225.

Buscarnera, Giuseppe and Itai Einav (2012). "The yielding of brittle unsaturated granular soils". In: *Géotechnique* 62.2, pp. 147–160. ISSN: 0016-8505. DOI: 10.1680/geot.10.P.118.

Buscarnera, Giuseppe and Reed T. Laverack (2014). "Path dependence of the potential for compaction banding: Theoretical predictions based on a plasticity model for porous rocks". In: *Journal of Geophysical Research: Solid Earth* 119, pp. 1882–1903. DOI: 10.1002/2013JB010562.Received.

Butcher, John C. (1963). "Coefficients for the study of Runge-Kutta integration processes". In: *Journal of the Australian Mathematical Society* 3.May, pp. 185–201. ISSN: 1446-7887. DOI: 10.1017/S1446788700027932.

Cashman, S. and K. Cashman (2000). "Cataclasis and deformation-band formation in unconsolidated marine terrace sand, Humboldt County, California". In: *Geology* 28.2, pp. 111–114. ISSN: 00917613. DOI: 10.1130/0091-7613(2000)28<111:CADFIU>2.0.CO;2.

Castellanza, Riccardo, Eleni Gerolymatou and Roberto Nova (2009). "Experimental observations and modelling of compaction bands in oedometric tests on high porosity rocks". In: *Strain* 45.5, pp. 410–423. ISSN: 00392103. DOI: 10.1111/j.1475-1305.2008.00578.x.

Cavailhes, Thibault and Atle Rotevatn (2018). "Deformation bands in volcaniclastic rocks – Insights from the Shihtiping tuffs, Coastal Range of Taiwan". In: *Journal of Structural Geology* 113.January, pp. 155–175. ISSN: 01918141. DOI: 10.1016/j.jsg.2018.06.004. URL: https://doi.org/10.1016/j.jsg.2018.06.004.

Chambon, Guillaume (2003). "Caractérisation expérimentale du frottement effectif des zones de faille". PhD thesis. Paris XI Orsay.

Chambon, Guillaume and Jean Schmittbuhl (2002). "Laboratory gouge friction: Seismic-like slip weakening and secondary rate- and state-effects". In: *Geophysical Research Letters* 29.10, pp. 5–8. ISSN: 00948276. DOI: 10.1029/2001gl014467.

Chambon, Guillaume, Jean Schmittbuhl and Alain Corfdir (2006a). "Frictional response of a thick gouge sample: 1. mechanical measurements and microstructures". In: *Journal of Geophysical Research: Solid Earth* 111.9, pp. 1–17. ISSN: 21699356. DOI: 10.1029/2003JB002731.

— (2006b). "Frictional response of a thick gouge sample: 2. friction law and implications for faults". In: *Journal of Geophysical Research: Solid Earth* 111.9, pp. 1–12. ISSN: 21699356. DOI: 10.1029/2004JB003339.

Chambon, Guillaume et al. (2003). "Shear with comminution of a granular material: Microscopic deformations outside the shear band". In: *Physical Review E - Statistical Physics, Plasmas, Fluids, and Related Interdisciplinary Topics* 68.1, p. 8. ISSN: 1063651X. DOI: 10.1103/PhysRevE.68.011304.

Chambon, Guillaume et al. (2006c). "The thickness of faults: From laboratory experiments to field scale observations". In: *Tectonophysics* 426.1-2, pp. 77–94. ISSN: 00401951. DOI: 10.1016/j.tecto.2006.02.014.

Chambon, René, Denis Caillerie and Gioacchino Viggiani (2004). "Loss of uniqueness and bifurcation vs instability : some remarks". In: *Revue Française de Génie Civil* 8.5-6, pp. 517–535.

Charalampidou, Elli Maria et al. (2011). "Characterization of shear and compaction bands in a porous sandstone deformed under triaxial compression". In: *Tectonophysics* 503.1-2, pp. 8–17. ISSN: 00401951. DOI: 10.1016/j.tecto.2010.09.032. URL: http://dx.doi.org/10.1016/j.tecto.2010.09.032.

Chester, Frederick M. and Judith S. Chester (1998). "Ultracataclasite structure and friction processes of the Punchbowl fault, San Andreas system, California". In: *Tectonophysics* 295.1-2, pp. 199–221. ISSN: 00401951. DOI: 10.1016/S0040-1951(98)00121-8.

Cheung, Cecilia S.N., Patrick Baud and Teng-fong Wong (2012). "Effect of grain size distribution on the development of compaction localization in porous sandstone". In: *Geophysical Research Letters* 39.21, pp. 6–10. ISSN: 00948276. DOI: 10.1029/2012GL053739.

Cil, Mehmet B. and Giuseppe Buscarnera (2016). "DEM assessment of scaling laws capturing the grain size dependence of yielding in granular soils". In: *Granular Matter* 18.3, pp. 1–15. ISSN: 14347636. DOI: 10.1007/s10035-016-0638-9.

Collettini, Cristiano et al. (2014). "Fault structure and slip localization in carbonate-bearing normal faults: An example from the Northern Apennines of Italy". In: *Journal of Structural Geology* 67.PA, pp. 154–166. ISSN: 01918141. DOI: 10.1016/j.jsg.2014.07.017. URL: http://dx.doi.org/10.1016/j.jsg.2014.07.017.

Collin, Frédéric, Panagiotis Kortronis and Benoît Pardoen (2016). "Numerical modelling of Multiphysics couplings and strain localization". In: *Modelling of instabilities and bifurcation in Geomechanics*. Ed. by Jean Sulem et al. Grenoble: The Alliance of Laboratories in Europe for Education, Research and Technology, pp. 133–164.

Combe, Gaël et al. (2013). "Experimental evidence of granulence". In: *AIP Conference Proceedings* 1542.June 2013, pp. 453–456. ISSN: 0094243X. DOI: 10.1063/1.4811965.

Coop, M. R. et al. (2004). "Particle breakage during shearing of a carbonate sand". In: *Géotechnique* 3, pp. 157–163. ISSN: 0016-8505. DOI: 10.1680/geot.2004.54.3.157. URL: https://arxiv.org/ftp/arxiv/papers/1410/1410.6002.pdf.

Corfdir, Alain, Patrick Lerat and Ioannis Vardoulakis (2004). "A cylinder shear apparatus". In: *Geotechnical Testing Journal* 27.5, pp. 447–455. ISSN: 01496115.

Cornet, François H. et al. (2004). "Forage au travers de la faille active d'Aigion : L'observatoire constitué par le puits AIG10". In: *Comptes Rendus - Geoscience* 336.4-5, pp. 395–406. ISSN: 16310713. DOI: 10.1016/j.crte.2004.02.002.

Cosserat, François and Eugène Cosserat (1909). *Théorie des corps déformables*. Paris: Librairie Scientifique A. Hermann et Fils.

Couture, Cyrille and Pierre Bésuelle (2019). "Diffuse and localized deformation of a porous Vosges sandstone in true triaxial conditions". In: *IS-Glasgow 2019*. Vol. 92. E3S Web of Conferences.

Crank, John and Phyllis Nicolson (1947). "A practical method for numerical evaluation of partial differential equations of the heat-conduction type". In: *Mathematical Proceedings of the Cambridge Philosophical Society* 43.1, pp. 50–67.

Das, Arghya (2013). "A theoretical study of grain crushing induced compaction localization in porous sandstones". PhD thesis. The University of Sydney. ISBN: 9783642328145.

Das, Arghya, Giang D. Nguyen and Itai Einav (2011). "Compaction bands due to grain crushing in porous rocks: A theoretical approach based on breakage mechanics". In: *Journal of Geophysical Research: Solid Earth* 116.8, pp. 1–14. ISSN: 21699356. DOI: 10.1029/2011JB008265.

— (2013). "The propagation of compaction bands in porous rocks based on breakage mechanics". In: *Journal of Geophysical Research: Solid Earth* 118.5, pp. 2049–2066. ISSN: 21699356. DOI: 10.1002/jgrb.50193.

Das, Arghya et al. (2014). "A thermomechanical constitutive model for cemented granular materials with quantifiable internal variables. Part II - Validation and localization analysis". In: *Journal of the Mechanics and Physics of Solids* 70.1, pp. 382–405. ISSN: 00225096. DOI: 10.1016/j.jmps.2014.05.022. URL: http://dx.doi.org/10.1016/j.jmps.2014.05.022.

Davis, George H. et al. (2000). "Conjugate Riedel deformation band shear zones". In: *Journal of Structural Geology* 22.2, pp. 169–190. ISSN: 01918141. DOI: 10.1016/S0191-8141(99)00140-6.

De Borst, René (1991). "Simulation of Strain Localization: a Reappraisal of the Cosserat Continuum". In: *Engineering Computations* 8.4, pp. 317–332. ISSN: 0264-4401. DOI: 10.1108/eb023842.

De Paola, Nicola et al. (2008). "Fault zone architecture and deformation processes within evaporitic rocks in the upper crust". In: *Tectonics* 27.4, pp. 1–21. ISSN: 02787407. DOI: 10.1029/2007TC002230.

De Paola, Nicola et al. (2015). "Can grain size sensitive flow lubricate faults during the initial stages of earthquake propagation?" In: *Earth and Planetary Science Letters* 431, pp. 48–58. ISSN: 0012821X. DOI: 10.1016/j.epsl.2015.09.002. URL: http://dx.doi.org/10.1016/j.epsl.2015.09.002.

Del Sole, Leonardo and Marco Antonellini (2019). "Microstructural, petrophysical, and mechanical properties of compactive shear bands associated to calcite cement concretions in arkose sandstone". In: *Journal of Structural Geology* 126.January, pp. 51–68. ISSN: 01918141. DOI: 10.1016/j.jsg.2019.05.007. URL: https://doi.org/10.1016/j.jsg.2019.05.007.

Delle Piane, Claudio et al. (2017). "Carbonate hosted fault rocks: A review of structural and microstructural characteristic with implications for seismicity in the upper crust". In: *Journal of Structural Geology* 103, pp. 17–36. ISSN: 01918141. DOI: 10.1016/j.jsg.2017.09.003. URL: https://doi.org/10.1016/j.jsg.2017.09.003.

Deng, Shang and Atilla Aydin (2012). "Distribution of compaction bands in 3D in an aeolian sandstone: The role of cross-bed orientation". In: *Tectonophysics* 574-575, pp. 204–218. ISSN: 00401951. DOI: 10.1016/j.tecto.2012.08.037. URL: http://dx.doi.org/10.1016/j.tecto.2012.08.037.

Desbois, Guillaume et al. (2017). "Deformation in cemented mudrock (Callovo-Oxfordian Clay) by microcracking, granular flow and phyllosilicate plasticity: Insights from triaxial deformation, broad ion beam polishing and scanning electron microscopy". In: *Solid Earth* 8.2, pp. 291–305. ISSN: 18699529. DOI: 10.5194/se-8-291-2017.

Desrues, Jacques and Gioacchino Viggiani (2004). "Strain localization in sand: An overview of the experimental results obtained in Grenoble using stereophotogrammetry". In: *International Journal for Numerical and Analytical Methods in Geomechanics* 28.4, pp. 279–321. ISSN: 03639061. DOI: 10.1002/nag.338.

Desrues, Jacques et al. (2018). "How does strain localise in standard triaxial tests on sand: Revisiting the mechanism 20 years on". In: *Mechanics Research Communications* 92, pp. 142–146. ISSN: 00936413. DOI: 10.1016/j.mechrescom.2018.08.007. URL: https://doi.org/10.1016/j.mechrescom.2018.08.007.

Dewers, Thomas A. et al. (2017). "Strain localization and elastic-plastic coupling during deformation of porous sandstone". In: *International Journal of Rock Mechanics and Mining Sciences* 98.May 2016, pp. 167–180. ISSN: 13651609. DOI: 10.1016/j.ijrmms.2017.06.005. URL: http://dx.doi.org/10.1016/j.ijrmms.2017.06.005.

Du Bernard, Xavier, Peter Eichhubl and Atilla Aydin (2002). "Dilation bands: A new form of localized failure in granular media". In: *Geophysical Research Letters* 29.24, pp. 21–29. ISSN: 0094-8276. DOI: 10.1029/2002GL015966. URL: http://www.scopus.com/inward/record.url?eid=2-s2.0-0038066524%5C%5C%5C&partnerID=40%5C%5C%5C&md5=d864961e5dc1e96a1a4e1b89954e82f3.

Eichhubl, Peter, John N. Hooker and Stephen E. Laubach (2010). "Pure and shear-enhanced compaction bands in Aztec Sandstone". In: *Journal of Structural Geology* 32.12, pp. 1873–1886. ISSN: 01918141. DOI: 10.1016/j.jsg.2010.02.004. URL: http://dx.doi.org/10.1016/j.jsg.2010.02.004.

Einav, Itai (2007a). "Breakage mechanics-Part I: Theory". In: *Journal of the Mechanics and Physics of Solids* 55.6, pp. 1274–1297. ISSN: 00225096. DOI: 10.1016/j.jmps.2006.11.003.

— (2007b). "Breakage mechanics-Part II: Modelling granular materials". In: *Journal of the Mechanics and Physics of Solids* 55.6, pp. 1298–1320. ISSN: 00225096. DOI: 10.1016/j.jmps.2006.11.004.

— (2007c). "Fracture propagation in brittle granular matter". In: *Proceedings of the Royal Society A* 463.August, pp. 3021–3035. ISSN: 1364-5021. DOI: 10.1098/rspa.2007.1898.

— (2007d). "Soil mechanics : breaking ground". In: *Philosophical Transactions of The Royal Society A* 365.1861, pp. 2985–3002. ISSN: 1364-503X. DOI: 10.1098/rsta.2007.0009.

— (2012). "The unification of hypo-plastic and elasto-plastic theories". In: *International Journal of Solids and Structures* 49.11-12, pp. 1305–1315. ISSN: 00207683. DOI: 10.1016/j.ijsolstr.2012.02.003. URL: http://dx.doi.org/10.1016/j.ijsolstr.2012.02.003.

Einav, Itai and Giang D. Nguyen (2008). "Hardening plasticity for geomaterials : micromechanical roots and alternative formulations". In: *5th. European Congress on Computational Methods in Applied Sciences and Engineering*.

Einav, Itai, Alexander M. Puzrin and Guy T. Houlsby (2003). "Numerical studies of hyperplasticity with single, multiple and a continuous field of yield surfaces". In: *International Journal for Numerical and Analytical Methods in Geomechanics* 27.10, pp. 837–858. ISSN: 03639061. DOI: 10.1002/nag.303.

Einav, Itai and Julio R. Valdes (2008). "On comminution and yield in brittle granular mixtures". In: *Journal of the Mechanics and Physics of Solids* 56.6, pp. 2136–2148. ISSN: 00225096. DOI: 10.1016/j.jmps.2008.02.002.

Einav, Itai et al. (2018). "Faults Get Colder Through Transient Granular Vortices". In: *Geophysical Research Letters* 45.6, pp. 2625–2632. ISSN: 19448007. DOI: 10.1002/2017GL076029.

El Bied, Amine, Jean Sulem and François Martineau (2002). "Microstructure of shear zones in Fontainebleau sandstone". In: *International Journal of Rock Mechanics and Mining Sciences* 39.7, pp. 917–932. ISSN: 13651609. DOI: 10.1016/S1365-1609(02)00068-0.

Eringen, Ahmed Cemal (1972). "Nonlocal polar elastic continua". In: *International Journal of Engineering Science* 10.1, pp. 1–16. ISSN: 00207225. DOI: 10.1016/0020-7225(72)90070-5.

— (1981). "On nonlocal plasticity". In: *International Journal of Engineering Science* 19.12, pp. 1461–1474. ISSN: 00207225. DOI: 10.1016/0020-7225(81)90072-0.

Exner, Ulrike, Jasmin Kaiser and Susanne Gier (2013). "Deformation bands evolving from dilation to cementation bands in a hydrocarbon reservoir (Vienna Basin, Austria)". In: *Marine and Petroleum Geology* 43, pp. 504–515. ISSN: 02648172. DOI: 10.1016/j.marpetgeo.2012.10.001. URL: http://dx.doi.org/10.1016/j.marpetgeo.2012.10.001.

Exner, Ulrike and Cornelius Tschegg (2012). "Preferential cataclastic grain size reduction of feldspar in deformation bands in poorly consolidated arkosic sands". In: *Journal of Structural Geology* 43, pp. 63–72. ISSN: 01918141. DOI: 10.1016/j.jsg.2012.08.005. URL: http://dx.doi.org/10.1016/j.jsg.2012.08.005.

Faug, Thierry et al. (2015). "Standing jumps in shallow granular flows down smooth inclines". In: *Physics of Fluids* 27.7. ISSN: 10897666. DOI: 10.1063/1.4927447.

Fehlberg, E. (1970). "Klassische Runge-Kutta-Formeln vierter und niedrigerer Ordnung mit Schrittweiten-Kontrolle und ihre Anwendung auf Wärmeleitungsprobleme". In: *Computing* 6.1-2, pp. 61–71. ISSN: 0010485X. DOI: 10.1007/BF02241732.

Feia, Sadok et al. (2016). "Changes in permeability of sand during triaxial loading: effect of fine particles production". In: *Acta Geotechnica* 11.1, pp. 1–19. ISSN: 18611133. DOI: 10.1007/s11440-014-0351-y.

Ferraro, Francesco et al. (2018). "Space-time evolution of cataclasis in carbonate fault zones". In: *Journal of Structural Geology* 110.June 2017, pp. 45–64. ISSN: 01918141. DOI: 10.1016/j.jsg.2018.02.007. URL: https://doi.org/10.1016/j.jsg.2018.02.007.

Ferraro, Francesco et al. (2019). "Structural diagenesis of carbonate fault rocks exhumed from shallow crustal depths: An example from the central-southern Apennines, Italy". In: *Journal of Structural Geology* 122.January, pp. 58–80. ISSN: 01918141. DOI: 10.1016/j.jsg.2019.02.008. URL: https://doi.org/10.1016/j.jsg.2019.02.008.

Fisher, Q. J. and R. J. Knipe (2001). "The permeability of faults within siliciclastic petroleum reservoirs of the North Sea and Norwegian Continental Shelf". In: *Marine and Petroleum Geology* 18.10, pp. 1063–1081. ISSN: 02648172. DOI: 10.1016/S0264-8172(01)00042-3.

Fletcher, Raymond C. and David D. Pollard (1981). "Anticrack model for pressure solution surfaces". In: *Geology* 9.9, pp. 419–424.

Fonseca, J. et al. (2016). "Image-based investigation into the primary fabric of stress-transmitting particles in sand". In: *Soils and Foundations* 56.5, pp. 818–834. ISSN: 00380806. DOI: 10.1016/j.sandf.2016.08.007. URL: http://dx.doi.org/10.1016/j.sandf.2016.08.007.

Fossen, Haakon (2010). "Deformation bands formed during soft-sediment deformation: Observations from SE Utah". In: *Marine and Petroleum Geology* 27.1, pp. 215–222. ISSN: 02648172. DOI: 10.1016/j.marpetgeo.2009.06.005. URL: http://dx.doi.org/10.1016/j.marpetgeo.2009.06.005.

Fossen, Haakon, Richard A. Schultz and Anita Torabi (2011). "Conditions and implications for compaction band formation in the Navajo Sandstone, Utah". In: *Journal of Structural Geology* 33.10, pp. 1477–1490. ISSN: 01918141. DOI: 10.1016/j.jsg.2011.08.001. URL: http://dx.doi.org/10.1016/j.jsg.2011.08.001.

Fossen, Haakon et al. (2007). "Deformation bands in sandstone: a review". In: *Journal of the Geological Society* 164.4, pp. 755–769. ISSN: 0016-7649. DOI: 10.1144/0016-76492006-036.

Fossen, Haakon et al. (2015). "Contractional deformation of porous sandstone: Insights from the Aztec Sandstone, SE Nevada, USA". In: *Journal of Structural Geology* 74, pp. 172–184. ISSN: 01918141. DOI: 10.1016/j.jsg.2015.02.014. URL: http://dx.doi.org/10.1016/j.jsg.2015.02.014.

Gajst, Hannah et al. (2018). "Effects of pre-existing faults on compaction localization in porous sandstones". In: *Tectonophysics* 747-748.April, pp. 1–15. ISSN: 00401951. DOI: 10.1016/j.tecto.2018.09.002.

GDR Midi (2004). "On dense granular flows." In: *The European physical journal. E* 365, pp. 1–26. ISSN: 1292-8941. DOI: 10.1140/epje/i2003-10153-0. arXiv: 0312502v1 [arXiv:cond-mat]. URL: http://www.ncbi.nlm.nih.gov/pubmed/15340859.

Germain, P (1973). “The Method of Virtual Power in Continuum Mechanics - Part II: Microstructure”. In: *SIAM Journal on Applied Mathematics* 25.3, pp. 556–575.

Ghabezloo, Siavash and Jean Sulem (2009). “Stress dependent thermal pressurization of a fluid-saturated rock”. In: *Rock Mechanics and Rock Engineering* 42.1, pp. 1–24. ISSN: 07232632. DOI: `10.1007/s00603-008-0165-z`. arXiv: `0808.3886`.

Godio, Michele et al. (2015). “Dynamic finite element formulation for Cosserat elastic plates”. In: *International Journal for Numerical Methods in Engineering* 101, pp. 992–1018. ISSN: 17359260. DOI: `10.1002/nme`.

— (2016). “Multisurface plasticity for Cosserat materials : Plate element implementation and validation”. In: *International Journal for Numerical Methods in Engineering* April, pp. 456–484. DOI: `10.1002/nme`.

Got, Jean Luc et al. (2019). “Damage and Strain Localization Around a Pressurized Shallow-Level Magma Reservoir”. In: *Journal of Geophysical Research: Solid Earth* Figure 1, pp. 1–16. ISSN: 21699356. DOI: `10.1029/2018JB016407`.

Griffiths, Joshua et al. (2018). “Deformation band development as a function of intrinsic host-rock properties in Triassic Sherwood Sandstone”. In: *Reservoir Quality of Clastic and Carbonate Rocks: Analysis, Modelling and Prediction.* Ed. by P.J. Armitgage et al. Vol. 435. 1. The Geological Society of London, pp. 161–176. DOI: `10.1144/sp435.11`.

Guéguen, Yves and Jérôme Fortin (2013). “Elastic envelopes of porous sandstones”. In: *Geophysical Research Letters* 40.July, pp. 3550–3555. DOI: `10.1002/grl.50676`.

Guiamatsia, Irene and Giang D. Nguyen (2014). “A thermodynamics-based cohesive model for interface debonding and friction”. In: *International Journal of Solids and Structures* 51.3-4, pp. 647–659. ISSN: 00207683. DOI: `10.1016/j.ijsolstr.2013.10.032`. URL: `http://dx.doi.org/10.1016/j.ijsolstr.2013.10.032`.

Guida, Giulia et al. (2018). “Linking micro grainsize polydispersity to macro porosity”. In: *International Journal of Solids and Structures.* ISSN: 00207683. DOI: `10.1016/j.ijsolstr.2018.11.032`. URL: `https://doi.org/10.1016/j.ijsolstr.2018.11.032`.

Guillard, François, Benjy Marks and Itai Einav (2017). “Dynamic X-ray radiography reveals particle size and shape orientation fields during granular flow”. In: *Scientific Reports* 7.1, pp. 1–11. ISSN: 20452322. DOI: `10.1038/s41598-017-08573-y`.

Hall, Stephen A. et al. (2010). “Discrete and continuum analysis of localised deformation in sand using X-ray μCT and volumetric digital image correlation”. In: *Géotechnique* 60.5, pp. 315–322. ISSN: 0016-8505. DOI: `10.1680/geot.2010.60.5.315`. URL: `http://www.icevirtuallibrary.com/doi/10.1680/geot.2010.60.5.315`.

Heap, Michael J et al. (2015). “Time-dependent compaction band formation in sandstone”. In: *Journal of Geophysical Research: Solid Earth* 120, pp. 4808–4830. DOI: `10.1002/2015JB012022.Received`.

Heeres, Otto M., Akke S. J. Suiker and René De Borst (2002). “A comparison between the Perzyna viscoplastic model and the consistency viscoplastic model”. In: *European Journal of Mechanics, A/Solids* 21.1, pp. 1–12. ISSN: 09977538. DOI: `10.1016/S0997-7538(01)01188-3`.

Heermance, Richard, Zoe K. Shipton and James P. Evans (2003). “Fault structure control on fault slip and ground motion during the 1999 rupture of the Chelungpu fault, Taiwan”. In: *Bulletin of the Seismological Society of America* 93.3, pp. 1034–1050. ISSN: 00371106. DOI: `10.1785/0120010230`.

Henann, David L. and Kenneth N. Kamrin (2013). “A predictive, size-dependent continuum model for dense granular flows.” In: *Proceedings of the National Academy of Sciences of the United States of America* 110.17, pp. 6730–5. ISSN: 1091-6490. DOI: `10.1073/pnas.1219153110`. URL: `http://www.pubmedcentral.nih.gov/articlerender.fcgi?artid=3637726%5C%5C%5C%5C%5C%5C%5C%5C%5C%5C%5C&tool=pmcentrez%5C%5C%5C%5C%5C%5C%5C%5C%5C%5C%5C&rendertype=abstract`.

Hill, R.E. (1990). “Analysis of deformation bands in the Aztec Sandstone, Valley of Fire, Nevada”. Masters Thesis. University of Nevada, Las Vegas.

Holcomb, David J. et al. (2007). “Compaction localization in the Earth and the laboratory: State of the research and research directions”. In: *Acta Geotechnica* 2.1, pp. 1–15. ISSN: 18611125. DOI: `10.1007/s11440-007-0027-y`.

Hou, Linfeng et al. (2012). “Internal structures and high-velocity frictional properties of a bedding-parallel carbonate fault at Xiaojiaqiao outcrop activated by the 2008 Wenchuan earthquake”. In: *Earthquake Science* 25.3, pp. 197–217. DOI: `10.1007/s11589-012-0846-2`.

Houlsby, Guy T. and Alexander M. Puzrin (2007). *Principles of Hyperplasticity*. London: Springer-Verlag London, p. 351. ISBN: 978-1-84628-240-9. DOI: 10.1007/978-1-84628-240-9. arXiv: arXiv:1011.1669v3. URL: http://link.springer.com/10.1007/978-1-84628-240-9.

Issen, Kathleen A. and John W. Rudnicki (2001). "Theory of compaction bands in porous rock". In: *Physics and Chemistry of the Earth, Part A: Solid Earth and Geodesy* 26.1-2, pp. 95–100. ISSN: 14641895. DOI: 10.1016/S1464-1895(01)00031-X.

Janssen, C. et al. (2016). "Microstructures and their implications for faulting processes -Insights from DGLab core samples from the Gulf of Corinth". In: *Journal of Structural Geology* 86, pp. 62–74. ISSN: 01918141. DOI: 10.1016/j.jsg.2016.03.008. URL: http://dx.doi.org/10.1016/j.jsg.2016.03.008.

Karatza, Z. et al. (2018). "Evolution of deformation and breakage in sand studied using X-ray tomography". In: *Géotechnique* 68.2, pp. 107–117. ISSN: 0016-8505. DOI: 10.1680/jgeot.16.P.208. URL: http://www.icevirtuallibrary.com/doi/10.1680/jgeot.16.P.208.

Kendall, K. (1978). "The impossibility of comminuting small particles by compression". In: *Nature* 272, pp. 710–711.

Kimura, Sho et al. (2014). "The effect of effective normal stress on particle breakage, porosity and permeability of sand: Evaluation of faults around methane hydrate reservoirs". In: *Tectonophysics* 630.C, pp. 285–299. ISSN: 00401951. DOI: 10.1016/j.tecto.2014.05.031.

Klein, Emmanuelle et al. (2001). "Mechanical behaviour and failure mode of Bentheim sandstone under triaxial compression". In: *Physics and Chemistry of the Earth, Part A: Solid Earth and Geodesy* 26.1-2, pp. 21–25. ISSN: 14641895. DOI: 10.1016/S1464-1895(01)00017-5.

Kurzon, Ittai, Vladimir Lyakhovsky and Yehuda Ben-Zion (2019). "Dynamic Rupture and Seismic Radiation in a Damage–Breakage Rheology Model". In: *Pure and Applied Geophysics* 176.3, pp. 1003–1020. ISSN: 14209136. DOI: 10.1007/s00024-018-2060-1.

Lanatà, Patrizia (2015). "Full-field experimental characterization of mechanical behaviour and failure in a porous rock in plane strain compression : homogeneous deformation and strain localization". PhD thesis. Université de Grenoble.

Le Bouil, Antoine et al. (2014). "A biaxial apparatus for the study of heterogeneous and intermittent strains in granular materials". In: *Granular Matter* 16.1, pp. 1–8. ISSN: 14345021. DOI: 10.1007/s10035-013-0477-x.

Lerat, Patrick (1996). "Etude de l'interface sol-structure dans les milieux granulaires à l'aide d'un nouvel appareil de cisaillement annulaire". PhD thesis. École Nationale des Ponts et Chaussées.

Lerat, Patrick, Marc Boulon and François Schlosser (1997). "Étude expérimentale de I'interface sol-structure dans les milieux granulaires". In: *Revue Française de Génie Civil* 1.2, pp. 345–366. ISSN: 1279-5119. DOI: 10.1080/12795119.1997.9692123.

Li, Xikui et al. (2014). "A mixed finite element procedure of gradient Cosserat continuum for second-order computational homogenisation of granular materials". In: *Computational Mechanics* 54.5, pp. 1331–1356. ISSN: 01787675. DOI: 10.1007/s00466-014-1062-9.

Lin, Aiming (2019). "Thermal pressurization and fluidization of pulverized cataclastic rocks formed in seismogenic fault zones". In: *Journal of Structural Geology* 125.December 2017, pp. 278–284. ISSN: 01918141. DOI: 10.1016/j.jsg.2017.12.010. URL: https://doi.org/10.1016/j.jsg.2017.12.010.

Lin, Aiming and Masayuki Nishikawa (2011). "Riedel shear structures in the co-seismic surface rupture zone produced by the 2001 Mw 7.8 Kunlun earthquake, northern Tibetan Plateau". In: *Journal of Structural Geology* 33.9, pp. 1302–1311. ISSN: 01918141. DOI: 10.1016/j.jsg.2011.07.003. URL: http://dx.doi.org/10.1016/j.jsg.2011.07.003.

Liu, Chun et al. (2015). "Mechanism of formation of wiggly compaction bands in porous sandstone: 1. Observations and conceptual model". In: *Journal of Geophysical Research: Solid Earth* 120.12, pp. 8138–8152. ISSN: 21699356. DOI: 10.1002/2015JB012372.

Lommatzsch, Marco et al. (2015). "Dilatant shear band formation and diagenesis in calcareous, arkosic sandstones, Vienna Basin (Austria)". In: *Marine and Petroleum Geology* 62, pp. 144–160. ISSN: 02648172. DOI: 10.1016/j.marpetgeo.2015.02.002. URL: http://dx.doi.org/10.1016/j.marpetgeo.2015.02.002.

Losert, W. et al. (2000). "Particle dynamics in sheared granular matter". In: *Physical Review Letters* 85.7, pp. 1428–1431. ISSN: 00319007. DOI: 10.1103/PhysRevLett.85.1428. arXiv: 0004401 [cond-mat].

Losh, Steven et al. (1999). "Vertical and lateral fluid flow related to a large growth fault, South Eugene Island Block 330 field, offshore Louisiana". In: *American Association of Petroleum Geologists Bulletin* 83.2, pp. 244–276. ISSN: 01491423. DOI: 10.1306/00AA9A5C-1730-11D7-8645000102C1865D.

Lyakhovsky, Vladimir and Yehuda Ben-Zion (2014a). "A Continuum Damage–Breakage Faulting Model and Solid-Granular Transitions". In: *Pure and Applied Geophysics* 171.11, pp. 3099–3123. ISSN: 14209136. DOI: 10.1007/s00024-014-0845-4.

— (2014b). "Damage-breakage rheology model and solid-granular transition near brittle instability". In: *Journal of the Mechanics and Physics of Solids* 64.1, pp. 184–197. ISSN: 00225096. DOI: 10.1016/j.jmps.2013.11.007. URL: http://dx.doi.org/10.1016/j.jmps.2013.11.007.

Lyakhovsky, Vladimir et al. (2016). "Dynamic rupture in a damage-breakage rheology model". In: *Geophysical Journal International* 206.2, pp. 1126–1143. ISSN: 1365246X. DOI: 10.1093/gji/ggw183.

Marinelli, Ferdinando and Giuseppe Buscarnera (2019a). "A Generalized Backward Euler algorithm for the numerical integration of a viscous breakage model". In: *International Journal for Numerical and Analytical Methods in Geomechanics* 43.1, pp. 3–29. ISSN: 10969853. DOI: 10.1002/nag.2841.

— (2019b). "Anisotropic breakage mechanics: From stored energy to yielding in transversely isotropic granular rocks". In: *Journal of the Mechanics and Physics of Solids* 129, pp. 1–18. ISSN: 00225096. DOI: 10.1016/j.jmps.2019.04.013.

Menendez, Beatriz, Wenlu Zhu and Teng-fong Wong (1996). "Micromechanics of brittle faulting and cataclastic flow in Tavel limestone". In: *Journal of Structural Geology* 32.l, pp. 1158–1169. ISSN: 01918141. DOI: 10.1016/j.jsg.2010.07.007.

Miller, Thomas (2014). "The kinematics of dense granular materials under indefinite plane-shear". PhD thesis. The University of Sydney.

Miller, Thomas et al. (2013). "Eddy viscosity in dense granular flows". In: *Physical Review Letters* 111.5, pp. 2–5. ISSN: 00319007. DOI: 10.1103/PhysRevLett.111.058002.

Moës, Nicolas and Ted Belytschko (2002). "Extended finite element method for cohesive crack growth". In: *Engineering Fracture Mechanics* 69.7, pp. 813–833. ISSN: 00137944. DOI: 10.1016/S0013-7944(01)00128-X.

Moës, Nicolas, John Dolbow and Ted Belytschko (1999). "A finite element method for crack growth without remeshing". In: *International Journal for Numerical Methods in Engineering* 46.1, pp. 131–150. ISSN: 00295981. DOI: 10.1002/(SICI)1097-0207(19990910)46:1<131::AID-NME726>3.0.CO;2-J.

Molinari, Alain and Yves M. Leroy (1991). "Structures in shear zones due to thermal effects". In: *Comptes Rendus de l'Académie des Sciences - Series IIB - Mechanics - Physics - Astronomy* 313.1, pp. 7–13.

Mollema, P. N. and M. A. Antonellini (1996). "Compaction bands: A structural analog for anti-mode I cracks in aeolian sandstone". In: *Tectonophysics* 267.1-4, pp. 209–228. ISSN: 00401951. DOI: 10.1016/S0040-1951(96)00098-4.

Mühlhaus, Hans-Bernd (1985). "Oberflächen-Instabilität bei geschichtetem Halbraum mit Biegesteifigkeit". In: *Ingenieur-Archiv* 55, pp. 388–400.

— (1986). "Scherfugenanalyse bei granularem Material im Rahmen der Cosserat-Theorie". In: *Ingenieur-Archiv* 56, pp. 389–399. DOI: 10.1007/BF02570619.

Mühlhaus, Hans-Bernd and Ioannis Vardoulakis (1987). "The thickness of shear bands in granular materials". In: *Géotechnique* 37.3, pp. 271–283.

Nguyen, Giang D. (2011). "A damage model with evolving nonlocal interactions". In: *International Journal of Solids and Structures* 48.10, pp. 1544–1559. ISSN: 00207683. DOI: 10.1016/j.ijsolstr.2011.02.002. arXiv: j.ijsolstr.2011.02.002 [10.1016]. URL: http://dx.doi.org/10.1016/j.ijsolstr.2011.02.002.

Nguyen, Giang D. and Itai Einav (2009). "The Energetics of Cataclasis Based on Breakage Mechanics". In: *Pure and Applied Geophysics* 166, pp. 1693–1724. DOI: 10.1007/978-3-0346-0138-2. URL: http://link.springer.com/10.1007/978-3-0346-0138-2.

Nguyen, Giang D. and Itai Einav (2010). "Nonlocal regularisation of a model based on breakage mechanics for granular materials". In: *International Journal of Solids and Structures* 47.10, pp. 1350–1360. ISSN: 0020-7683. DOI: 10.1016/j.ijsolstr.2010.01.020. URL: http://dx.doi.org/10.1016/j.ijsolstr.2010.01.020.

Nguyen, Giang D. et al. (2016). "Constitutive modelling of compaction localisation in porous sandstones". In: *International Journal of Rock Mechanics and Mining Sciences* 83, pp. 57–72. ISSN: 13651609. DOI: 10.1016/j.ijrmms.2015.12.018. URL: http://dx.doi.org/10.1016/j.ijrmms.2015.12.018.

Nicchio, Matheus A. et al. (2018). "Development of cataclastic foliation in deformation bands in feldspar-rich conglomerates of the Rio do Peixe Basin, NE Brazil". In: *Journal of Structural Geology* 107.July 2017, pp. 132–141. ISSN: 01918141. DOI: 10.1016/j.jsg.2017.12.013. URL: https://doi.org/10.1016/j.jsg.2017.12.013.

Olsson, William A. (1999). "Theoretical and experimental investigation of compaction bands in porous rock". In: *Journal of Geophysical Research* 104.B4, pp. 7219–7228.

— (2001). "Quasistatic propagation of compaction fronts in porous rock". In: *Mechanics of Materials* 33.11, pp. 659–668. ISSN: 01676636. DOI: 10.1016/S0167-6636(01)00078-3.

Olsson, William A. and David J. Holcomb (2000). "Compaction localization in porous sandstones". In: *Geophysical Research Letters* 27.21, pp. 3537–3540.

Olszak, Wacław and Piotr Perzyna (1969). "On thermal effects in viscoplasticity". In: *Zeitschrift für angewandte Mathematik und Physik ZAMP* 20.5, pp. 676–680. ISSN: 0044-2275. DOI: 10.1007/bf01590623.

Ord, Alison, Ioannis Vardoulakis and R. Kajewski (1991). "Shear band formation in Gosford Sandstone". In: *International Journal of Rock Mechanics and Mining Sciences* 28.5, pp. 397–409. ISSN: 01489062. DOI: 10.1016/0148-9062(91)90078-Z.

Paesold, Martin et al. (2016). "Conditions for the localisation of plastic deformation in temperature sensitive viscoplastic materials". In: *Journal of Mechanics of Materials and Structures* February. DOI: 10.2140/jomms.2016.11.113.

Papamichos, Euripides (2016). "Numerical modeling of bifurcation: Applications to borehole stability, multilayer buckling, and rock bursting". In: *Modelling of instabilities and bifurcation in Geomechanics*. Ed. by Jean Sulem et al. Grenoble: The Alliance of Laboratories in Europe for Education, Research and Technology, pp. 166–187.

Papanastasiou, Panos and Ioannis Vardoulakis (1989). "Bifurcation analysis of deep boreholes: II. Scale effect". In: *International Journal for Numerical and Analytical Methods in Geomechanics* 13.2, pp. 183–198. ISSN: 01489062. DOI: 10.1016/0148-9062(89)90982-0.

— (1992). "Numerical treatment of progressive localization in relation to borehole stability". In: *International Journal for Numerical and Analytical Methods in Geomechanics* 16.6, pp. 389–424. ISSN: 10969853. DOI: 10.1002/nag.1610160602.

Papanastasiou, Panos and Antonios Zervos (2016). "Numerical modelling of strain localisation". In: *Modelling of instabilities and bifurcation in Geomechanics*. Ed. by Jean Sulem et al. Grenoble: The Alliance of Laboratories in Europe for Education, Research and Technology, pp. 133–165.

Papanicolopulos, Stefanos-Aldo and Emmanuil Veveakis (2011). "Sliding and rolling dissipation in Cosserat plasticity". In: *Granular Matter* 13, pp. 197–204. DOI: 10.1007/s10035-011-0253-8.

Papazoglou, Athanasios et al. (2017). "Localized Compaction in Tuffeau de Maastricht: Experiments and Modeling". In: *Bifurcation and Degradation of Geomaterials with Engineering Applications*. Ed. by Euripides Papamichos et al. Springer International Publishing, pp. 481–488. ISBN: 978-3-319-56396-1. DOI: 10.1007/978-3-319-56397-8. URL: http://link.springer.com/10.1007/978-3-319-56397-8.

Pijaudier-Cabot, Gilles and Zdenek P. Bazant (1988). "Nonlocal Damage Theory". In: *Journal of Engineering Mechanics* 113.10, pp. 1512–1533.

Pijaudier-Cabot, Gilles, Khalil Haidar and Jean François Dubé (2004). "Non-local damage model with evolving internal length". In: *International Journal for Numerical and Analytical Methods in Geomechanics* 28.7-8, pp. 633–652. ISSN: 03639061. DOI: 10.1002/nag.367.

Platt, John D., Nicolas Brantut and James R. Rice (2015). "Strain localization driven by thermal decomposition during seismic shear". In: *Journal of Geophysical Research: Solid Earth* 120.6, pp. 4405–4433. ISSN: 21699356. DOI: 10.1002/2014JB011493.

Platt, John D., John W. Rudnicki and James R. Rice (2014). "Stability and localization of rapid shear in fluid-saturated fault gouge: 2. Localized zone width and strength evolution". In: *Journal of Geophysical Research: Solid Earth* 119.5, pp. 4334–4359. ISSN: 21699356. DOI: 10.1002/2013JB010711.

Poh, Leong Hien and Gang Sun (2017). "Localizing gradient damage model with decreasing interactions". In: *International Journal for Numerical Methods in Engineering* 110.6, pp. 503–522. ISSN: 10970207. DOI: 10.1002/nme.5364.

Poulet, Thomas, Martin Paesold and Emmanuil Veveakis (2017). "Multi-Physics Modelling of Fault Mechanics Using REDBACK: A Parallel Open-Source Simulator for Tightly Coupled Problems". In: *Rock Mechanics and Rock Engineering* 50.3. ISSN: 07232632. DOI: 10.1007/s00603-016-0927-y.

Poulet, Thomas et al. (2014a). "Modeling episodic fluid-release events in the ductile carbonates of the Glarus thrust". In: *Geophysical Research Letters* 41.20, pp. 7121–7128. ISSN: 19448007. DOI: 10.1002/2014GL061715.

Poulet, Thomas et al. (2014b). "Thermo-poro-mechanics of chemically active creeping faults: 3. The role of serpentinite in episodic tremor and slip sequences, and transition to chaos". In: *Journal of Geophysical Research: Solid Earth* 119.6, pp. 4583–4605. ISSN: 21699356. DOI: 10.1002/2013JB010071.

Pozzi, Giacomo et al. (2019). "Coseismic ultramylonites: An investigation of nanoscale viscous flow and fault weakening during seismic slip". In: *Earth and Planetary Science Letters* 516, pp. 164–175. ISSN: 0012821X. DOI: 10.1016/j.epsl.2019.03.042. URL: https://doi.org/10.1016/j.epsl.2019.03.042.

Rao, Gang et al. (2011). "Co-seismic Riedel shear structures produced by the 2010 Mw 6.9 Yushu earthquake, central Tibetan Plateau, China". In: *Tectonophysics* 507.1-4, pp. 86–94. ISSN: 00401951. DOI: 10.1016/j.tecto.2011.05.011. URL: http://dx.doi.org/10.1016/j.tecto.2011.05.011.

Rastiello, Giuseppe et al. (2018). "From diffuse damage to strain localization from an Eikonal Non-Local (ENL) Continuum Damage model with evolving internal length". In: *Computer methods in applied mechanics and engineering* 331, pp. 650–674. DOI: 10.1016/j.cma.2017.12.006.

Rattez, Hadrien (2018). "Couplages Thermo-Hydro-Mécaniques et localisation dans les milieux de Cosserat : Application à l'analyse de stabilité du cisaillement rapide des failles". PhD thesis. Université Paris-Est.

Rattez, Hadrien, Ioannis Stefanou and Jean Sulem (2018a). "The importance of Thermo-Hydro-Mechanical couplings and microstructure to strain localization in 3D continua with application to seismic faults. Part I: Theory and linear stability analysis". In: *Journal of the Mechanics and Physics of Solids* 115, pp. 54–76. ISSN: 00225096. DOI: 10.1016/j.jmps.2018.03.004. URL: https://doi.org/10.1016/j.jmps.2018.03.004.

Rattez, Hadrien et al. (2018b). "Numerical Analysis of Strain Localization in Rocks with Thermo-hydro-mechanical Couplings Using Cosserat Continuum". In: *Rock Mechanics and Rock Engineering* 51.10, pp. 3295–3311. ISSN: 07232632. DOI: 10.1007/s00603-018-1529-7. URL: http://dx.doi.org/10.1007/s00603-018-1529-7.

— (2018c). "The importance of Thermo-Hydro-Mechanical couplings and microstructure to strain localization in 3D continua with application to seismic faults. Part II: Numerical implementation and post-bifurcation analysis". In: *Journal of the Mechanics and Physics of Solids* 115, pp. 54–76. ISSN: 00225096. DOI: 10.1016/j.jmps.2018.03.004. URL: https://doi.org/10.1016/j.jmps.2018.03.003.

Rawling, Geoffrey C. and Laurel B. Goodwin (2003). "Cataclasis and particulate flow in faulted, poorly lithified sediments". In: *Journal of Structural Geology* 25.3, pp. 317–331. ISSN: 01918141. DOI: 10.1016/S0191-8141(02)00041-X.

Rice, James R. (1975). "On the Stability of Dilatant Hardening for Saturated Rock Masses". In: *Journal of Geophysical Research* 80.11, pp. 1531–1536.

— (1976). "The localization of plastic deformation". In: *14th International Congress on Theoretical and Applied Mechanics*, pp. 207–220. DOI: 10.1.1.160.6740.

— (2006). "Heating and weakening of faults during earthquake slip". In: *Journal of Geophysical Research: Solid Earth* 111.5, pp. 1–29. ISSN: 21699356. DOI: 10.1029/2005JB004006.

Rice, James R. and John W. Rudnicki (1980). "A note on some features of the theory of localization of deformation". In: *International Journal of Solids and Structures* 16.7, pp. 597–605. ISSN: 00207683. DOI: 10.1016/0020-7683(80)90019-0.

Rice, James R., John W. Rudnicki and John D. Platt (2014). "Stability and localization of rapid shear in fluid-saturated fault gouge: 1. Linearized stability analysis". In: *Journal of Geophysical Research: Solid Earth* 119.5, pp. 4311–4333. ISSN: 21699356. DOI: 10.1002/2013JB010710.

Robert, Romain et al. (2018). "Deformation bands, early markers of tectonic activity in front of a fold-and-thrust belt: Example from the Tremp-Graus basin, southern Pyrenees, Spain". In: *Journal of Structural Geology* 110.February, pp. 65–85. ISSN: 01918141. DOI: 10.1016/j.jsg.2018.02.012. URL: https://doi.org/10.1016/j.jsg.2018.02.012.

Rocha, Lourena, Luiz Velho and Paulo Cezar Pinto Carvalho (2002). "Image moments-based structuring and tracking of objects". In: *15th Brazilian Symposium on Computer Graphics and Image Processing (SIBGRAPI 2002), 7-10 October 2002, Fortaleza-CE, Brazil*, pp. 99–105. ISBN: 076951846X. DOI: 10.1109/SIBGRA.2002.1167130.

Rodrigues, Mérolyn C. N. L., Barbara Trzaskos and Angela P. Lopes (2015). "Influence of deformation bands on sandstone porosity: A case study using three-dimensional microtomography". In: *Journal of Structural Geology* 72, pp. 96–110. ISSN: 01918141. DOI: 10.1016/j.jsg.2015.01.003.

Roscoe, K. H. (1970). "The Influence of Strains in Soil Mechanics". In: *Géotechnique* 20.2, pp. 129–170. ISSN: 0016-8505. DOI: 10.1680/geot.1970.20.2.129. URL: http://www.icevirtuallibrary.com/doi/10.1680/geot.1970.20.2.129.

Rotevatn, Atle et al. (2008). "Slipped deformation bands: A new type of cataclastic deformation bands in Western Sinai, Suez rift, Egypt". In: *Journal of Structural Geology* 30.11, pp. 1317–1331. ISSN: 01918141. DOI: 10.1016/j.jsg.2008.06.010. URL: http://dx.doi.org/10.1016/j.jsg.2008.06.010.

Rotevatn, Atle et al. (2016). "Sequential growth of deformation bands in carbonate grainstones in the hangingwall of an active growth fault: Implications for deformation mechanisms in different tectonic regimes". In: *Journal of Structural Geology* 90, pp. 27–47. ISSN: 01918141. DOI: 10.1016/j.jsg.2016.07.003. URL: http://dx.doi.org/10.1016/j.jsg.2016.07.003.

Rubin, Miles B. (2001). "Physical reasons for abandoning plastic deformation measures in plasticity and viscoplasticity theory". In: *Archives of Mechanics* 53.4-5, pp. 519–539.

Rubin, Miles B. and Itai Einav (2011). "A large deformation breakage model of granular materials including porosity and inelastic distortional deformation rate". In: *International Journal of Engineering Science* 49.10, pp. 1151–1169. ISSN: 00207225. DOI: 10.1016/j.ijengsci.2011.05.002. URL: http://dx.doi.org/10.1016/j.ijengsci.2011.05.002.

Rudnicki, John W. and James R. Rice (1975). "Conditions for the localization of deformation in pressure-sensitive dilatant materials". In: *Journal of the Mechanics and Physics of Solids* 23.6, pp. 371–394. ISSN: 00225096. DOI: 10.1016/0022-5096(75)90001-0.

Sakaguchi, Arito et al. (2011). "Seismic slip propagation to the updip end of plate boundary subduction interface faults: Vitrinite reflectance geothermometry on Integrated Ocean Drilling Program NanTro SEIZE cores". In: *Geology* 39.4, pp. 395–398. ISSN: 00917613. DOI: 10.1130/G31642.1.

Sammis, Charles, Geoffrey King and Ronald Biegel (1987). "The kinematics of gouge deformation". In: *Pure and Applied Geophysics PAGEOPH* 125.5, pp. 777–812. ISSN: 00334553. DOI: 10.1007/BF00878033.

Savitzky, Abraham and Marcel J.E. Golay (1964). "Smoothing and Differentiation of Data by Simplified Least Squares Procedures". In: *Analytical Chemistry* 36.8, pp. 1627–1639. ISSN: 15206882. DOI: 10.1021/ac60214a047.

Scherer, Jean-Michel et al. (2019). "Strain gradient crystal plasticity with evolving length scale: Application to voided irradiated materials". In: *European Journal of Mechanics - A/Solids*. ISSN: 09977538. DOI: 10.1016/j.euromechsol.2019.04.003. URL: https://linkinghub.elsevier.com/retrieve/pii/S0997753818309458.

Schultz, Richard A. (2009). "Scaling and paleodepth of compaction bands, Nevada and Utah". In: *Journal of Geophysical Research* 114.B3, pp. 1–13. ISSN: 0148-0227. DOI: 10.1029/2008jb005876.

Schultz, Richard A., Chris H. Okubo and Haakon Fossen (2010). "Porosity and grain size controls on compaction band formation in Jurassic Navajo Sandstone". In: *Geophysical Research Letters* 37.22, pp. 1–5. ISSN: 00948276. DOI: 10.1029/2010GL044909.

Schutjens, P.M.T.M. et al. (1995). "The influence of intergranular microcracks on the petrophysical properties of sandstone-experiments to quantify effects of core damage". In: *Proceedings of the Society of Core Analysts*.

Shipton, Zoe K. et al. (2006). "How Thick is a Fault? Fault Displacement-Thickness Scaling Revisited". In: *Earthquakes: Radiated Energy and the Physics of Faulting*. American Geophysical Union, pp. 193–198. ISBN: 978-0-87590-435-1. DOI: 10.1029/170GM19.

Sibson, Richard H. (2003). "Thickness of the seismic slip zone". In: *Bulletin of the Seismological Society of America* 93.3, pp. 1169–1178. ISSN: 00371106. DOI: 10.1785/0120020061.

Siman-Tov, Shalev and Emily E. Brodsky (2018). "Gravity-Independent Grain Size Segregation in Experimental Granular Shear Flows as a Mechanism of Layer Formation". In: *Geophysical Research Letters* 45.16, pp. 8136–8144. ISSN: 19448007. DOI: 10.1029/2018GL078486.

Simo, J. C. and M. S. Rifai (1990). "A class of mixed assumed strain methods and the method of incompatible modes". In: *International Journal for Numerical Methods in Engineering* 29.8, pp. 1595–1638. ISSN: 10970207. DOI: 10.1002/nme.1620290802.

Skurtveit, Elin et al. (2013). "Experimental investigation of deformation mechanisms during shear-enhanced compaction in poorly lithified sandstone and sand". In: *Journal of Geophysical Research: Solid Earth* 118, pp. 4083–4100. DOI: 10.1002/jgrb.50342.

Sohn, Changbum and Giuseppe Buscarnera (2019). "Measurement of comminution rate in granular materials subjected to creep tests". In: *Granular Matter* 21.60. ISSN: 1434-7636. DOI: 10.1007/s10035-019-0912-8. URL: https://doi.org/10.1007/s10035-019-0912-8.

Soliva, Roger et al. (2016). "Tectonic regime controls clustering of deformation bands in porous sandstone". In: *Geology* 44.6, pp. 423–426. ISSN: 19432682. DOI: 10.1130/G37585.1.

Stanchits, Sergei et al. (2009). "Initiation and propagation of compaction bands in dry and wet bentheim sandstone". In: *Pure and Applied Geophysics* 166.5-7, pp. 843–868. ISSN: 00334553. DOI: 10.1007/s00024-009-0478-1.

Stefanou, Ioannis (2018). *Numerical Geolab*. Nantes.

Stefanou, Ioannis and Sotiris Alevizos (2016). "Fundamentals of bifurcation theory and stability analysis". In: *Modelling of instabilities and bifurcation in Geomechanics*. Ed. by Jean Sulem et al. Grenoble: The Alliance of Laboratories in Europe for Education, Research and Technology, pp. 29–68.

Stefanou, Ioannis and Jean Sulem (2013). "Formation de bandes de compaction dans les geomatériaux causée par une dégradation chimique". In: *21ème Congrès Français de Mécanique*.

— (2014). "Chemically induced compaction bands: Triggering conditions and band thickness". In: *Journal of Geophysical Research: Solid Earth* 119.100, pp. 8964–8975. ISSN: 21699313. DOI: 10.1002/2014JB011567.Received.

— (2016). "Existence of a threshold for brittle grains crushing strength : two-versus three-parameter Weibull distribution fitting". In: *Granular Matter* 18.2, pp. 1–10. ISSN: 1434-7636. DOI: 10.1007/s10035-015-0603-z.

Stefanou, Ioannis, Jean Sulem and Ioannis Vardoulakis (2008). "Three-dimensional Cosserat homogenization of masonry structures: Elasticity". In: *Acta Geotechnica* 3.1, pp. 71–83. ISSN: 18611125. DOI: 10.1007/s11440-007-0051-y.

— (2010). "Homogenization of interlocking masonry structures using a generalized differential expansion technique". In: *International Journal of Solids and Structures* 47.11-12, pp. 1522–1536. ISSN: 00207683. DOI: 10.1016/j.ijsolstr.2010.02.011.

Sternlof, Kurt R., John W. Rudnicki and David D. Pollard (2005). "Anticrack inclusion model for compaction bands in sandstone". In: *Journal of Geophysical Research: Solid Earth* 110.11, pp. 1–16. ISSN: 21699356. DOI: 10.1029/2005JB003764.

Sukumar, N. et al. (2000). "Extended finite element method for three-dimensional crack modelling". In: *International Journal for Numerical Methods in Engineering* 48, pp. 1549–1570. ISSN: 0029-5981. DOI: 10.1002/1097-0207(20000820)48:11<1549::AID-NME955>3.0.CO;2-A.

Sulem, Jean (2007). "Stress orientation evaluated from strain localisation analysis in Aigion Fault". In: *Tectonophysics* 442.1-4, pp. 3–13. ISSN: 00401951. DOI: 10.1016/j.tecto.2007.03.005. arXiv: 0808.2012.

— (2010). "Bifurcation theory and localization phenomena". In: *European Journal of Environmental and Civil Engineering* 14.8-9, pp. 989–1009. ISSN: 1964-8189. DOI: 10.1080/19648189.2010.9693276.

Sulem, Jean and V Famin (2009). "Thermal decomposition of carbonates in fault zones: Slip-weakening and temperature-limiting effects". In: *Journal of Geophysical Research* 114.B6, pp. 1–14. ISSN: 0148-0227. DOI: 10.1029/2009JB006576.

Sulem, Jean and Hicham Ouffroukh (2006). "Shear banding in drained and undrained triaxial tests on a saturated sandstone: Porosity and permeability evolution". In: *International Journal of Rock Mechanics and Mining Sciences* 43.2, pp. 292–310. ISSN: 13651609. DOI: 10.1016/j.ijrmms.2005.07.001.

Sulem, Jean and Ioannis Stefanou (2016). "Thermal and chemical effects in shear and compaction bands". In: *Geomechanics for Energy and the Environment* 6, pp. 4–21. ISSN: 2352-3808. DOI: 10.1016/j.gete.2015.12.004. URL: http://dx.doi.org/10.1016/j.gete.2015.12.004.

Sulem, Jean, Ioannis Stefanou and Emmanuil Veveakis (2011). "Stability analysis of undrained adiabatic shearing of a rock layer with Cosserat microstructure". In: *Granular Matter* 13.3, pp. 261–268. ISSN: 14345021. DOI: 10.1007/s10035-010-0244-1.

Sulem, Jean and Ioannis Vardoulakis (1990). "Bifurcation analysis of the triaxial test on rock specimens. A theoretical model for shape and size effect". In: *Acta Mechanica* 83.3-4, pp. 195–212. ISSN: 00015970. DOI: 10.1007/BF01172981.

Sulem, Jean et al. (1999). "Elasto-plastic modelling of Red Wildmoor sandstone". In: *Mechanics of Cohesive-Frictional Materials* 4, pp. 215–245.

Tagliaferri, Francesco et al. (2011). "Observing strain localisation processes in bio-cemented sand using x-ray imaging". In: *Granular Matter* 13.3, pp. 247–250. ISSN: 14345021. DOI: 10.1007/s10035-011-0257-4.

Takano, Daiki et al. (2015). "Localised deformation in a wide-grained sand under triaxial compression revealed by X-ray tomography and digital image correlation". In: *Soils and Foundations* 55.4, pp. 906–915. ISSN: 00380806. DOI: 10.1016/j.sandf.2015.06.020. URL: http://dx.doi.org/10.1016/j.sandf.2015.06.020.

Tavani, S. et al. (2018). "Shear-enhanced compaction-solution bands in quartz-rich calcarenites of the Cotiella Massif (Spanish Pyrenees)". In: *Journal of Structural Geology* 114.November 2017, pp. 274–279. ISSN: 01918141. DOI: 10.1016/j.jsg.2017.11.018. URL: https://doi.org/10.1016/j.jsg.2017.11.018.

Tembe, Sheryl, Patrick Baud and Teng-fong Wong (2008). "Stress conditions for the propagation of discrete compaction bands in porous sandstone". In: *Journal of Geophysical Research: Solid Earth* 113.9, pp. 1–16. ISSN: 21699356. DOI: 10.1029/2007JB005439.

Tengattini, Alessandro (2015). "A micro-mechanical study of cemented granular materials". PhD thesis. The University of Sydney.

Tengattini, Alessandro, Arghya Das and Itai Einav (2014a). "A theory predicting breakage dependence of critical state in sand". In: *Geomechanics from Micro to Macro*. Vol. 1. 1. London: Taylor & Francis Group, pp. 695–698. ISBN: 9781138027077. DOI: 10.1201/b17395-124. URL: http://www.crcnetbase.com/doi/abs/10.1201/b17395-124.

— (2016). "A constitutive modelling framework predicting critical state in sand undergoing crushing and dilation". In: *Géotechnique* 66.9, pp. 695–710. ISSN: 0016-8505. DOI: 10.1680/jgeot.14.P.164. URL: http://www.icevirtuallibrary.com/doi/10.1680/jgeot.14.P.164.

Tengattini, Alessandro et al. (2014b). "A thermomechanical constitutive model for cemented granular materials with quantifiable internal variables. Part I—Theory". In: *Journal of the Mechanics and Physics of Solids* 70.1, pp. 281–296. ISSN: 00225096. DOI: 10.1016/j.jmps.2014.05.021. URL: http://linkinghub.elsevier.com/retrieve/pii/S0022509614001185.

Togo, Tetsuhiro and Toshihiko Shimamoto (2012). "Energy partition for grain crushing in quartz gouge during subseismic to seismic fault motion: An experimental study". In: *Journal of Structural Geology* 38, pp. 139–155. ISSN: 01918141. DOI: 10.1016/j.jsg.2011.12.014. URL: http://dx.doi.org/10.1016/j.jsg.2011.12.014.

Torabi, Anita (2014). "Cataclastic bands in immature and poorly lithified sandstone, examples from Corsica, France". In: *Tectonophysics* 630.C, pp. 91–102. ISSN: 00401951. DOI: 10.1016/j.tecto.2014.05.014. URL: http://dx.doi.org/10.1016/j.tecto.2014.05.014.

Torabi, Anita et al. (2015). "The dynamics and interaction of compaction bands in Valley of Fire State Park, Nevada (USA): Implications for their growth, evolution, and geostatistical property". In: *Tectonophysics* 657, pp. 113–128. ISSN: 00401951. DOI: 10.1016/j.tecto.2015.06.029. URL: http://dx.doi.org/10.1016/j.tecto.2015.06.029.

Tordesillas, Antoinette et al. (2016). "Granular vortices : Identification , characterization and conditions for the localization of deformation". In: *Journal of the Mechanics and Physics of Solids* 90, pp. 215–241. ISSN: 0022-5096. DOI: 10.1016/j.jmps.2016.02.032. URL: http://dx.doi.org/10.1016/j.jmps.2016.02.032.

Triantafyllidis, Nicolas and Elias C. Aifantis (1986). "A gradient approach to localization of deformation. I. Hyperelastic materials". In: *Journal of Elasticity* 16.3, pp. 225–237. ISSN: 03743535. DOI: 10.1007/BF00040814.

Turcotte, D. L. (1986). "Fractals and Fragmentation". In: *Journal of Geophysical Research* 91.5, pp. 1921–1926.

Vajdova, Veronika and Teng-fong Wong (2003). "Incremental propagation of discrete compaction bands: Acoustic emission and microstructural observations on circumferentially notched samples of Bentheim". In: *Geophysical Research Letters* 30.14, pp. 1–4. ISSN: 00948276. DOI: 10.1029/2003GL017750.

Vajdova, Veronika et al. (2010). "Micromechanics of brittle faulting and cataclastic flow in Tavel limestone". In: *Journal of Structural Geology* 32.8, pp. 1158–1169. ISSN: 01918141. DOI: 10.1016/j.jsg.2010.07.007. URL: http://dx.doi.org/10.1016/j.jsg.2010.07.007.

Vannucchi, Paola and Lorenzo Leoni (2007). "Structural characterization of the Costa Rica décollement: Evidence for seismically-induced fluid pulsing". In: *Earth and Planetary Science Letters* 262.3-4, pp. 413–428. ISSN: 0012821X. DOI: 10.1016/j.epsl.2007.07.056.

Vardoulakis, Ioannis (1985). "Stability and bifurcation of undrained, plane rectilinear deformations on water-saturated granular soils". In: *International Journal for Numerical and Analytical Methods in Geomechanics* 9.5, pp. 399–414. ISSN: 10969853. DOI: 10.1002/nag.1610090502.

— (1986). "Dynamic stability analysis of undrained simple shear on water-saturated granular soils". In: *International Journal for Numerical and Analytical Methods in Geomechanics* 10.2, pp. 177–190. ISSN: 10969853. DOI: 10.1002/nag.1610100206.

— (2000). "2nd Gradient constitutive models". In: *Constitutive Modelling of Granular Materials*. Ed. by Dimitrios Kolymbas. Berlin: Springer Berlin Heidelberg, pp. 225–248.

— (2019). *Cosserat Continuum Mechanics*. Ed. by Eleni Gerolymatou et al. Cham: Springer International Publishing. ISBN: 978-3-319-95155-3. DOI: 10.1007/978-3-319-95156-0. URL: http://link.springer.com/10.1007/978-3-319-95156-0.

Vardoulakis, Ioannis and Panos Papanastasiou (1988). "Bifurcation analysis of deep boreholes: I. Surface instabilities". In: *International Journal for Numerical and Analytical Methods in Geomechanics* 12.4, pp. 379–399. ISSN: 10969853. DOI: 10.1002/nag.1610120404.

Vardoulakis, Ioannis and Jean Sulem (1993). "Application of Bifurcation Theory to Rock Mechanics Problems". In: *Comprehensive Rock Engineering Volume 1*. Ed. by J. Hudson. Pergamon Press. Chap. 23, pp. 575–609.

— (1995). *Bifurcation analysis in geomechanics*. Glasgow: Blackie Academic & Professional, p. 466. ISBN: 0203697030. DOI: 10.1061/(ASCE)0733-9399(2006)132:9(952).

Veveakis, Emmanuil, Sotiris Alevizos and Ioannis Vardoulakis (2010). "Chemical reaction capping of thermal instabilities during shear of frictional faults". In: *Journal of the Mechanics and Physics of Solids* 58.9, pp. 1175–1194. ISSN: 00225096. DOI: 10.1016/j.jmps.2010.06.010.

Veveakis, Emmanuil, Thomas Poulet and Sotiris Alevizos (2014). "Thermo-poro-mechanics of chemically active creeping faults: 2. Transient considerations". In: *Journal of Geophysical Research: Solid Earth* 119.6, pp. 4583–4605. ISSN: 21699356. DOI: 10.1002/2013JB010071.

Veveakis, Emmanuil, Ioannis Stefanou and Jean Sulem (2013). "Failure in shear bands for granular materials : thermo-hydro-chemomechanical effects". In: *Géotechnique Letters* 3.2, pp. 31–26.

Veveakis, Emmanuil, Ioannis Vardoulakis and Giulio Di Toro (2007). "Thermoporomechanics of creeping landslides : The 1963 Vaiont slide , northern Italy". In: *Journal of Geophysical Research* 112.April, pp. 1–21. DOI: 10.1029/2006JF000702.

Voyiadjis, George Z., Danial Faghihi and Yida Zhang (2014). "A theory for grain boundaries with strain-gradient plasticity". In: *International Journal of Solids and Structures* 51.10, pp. 1872–1889. ISSN: 00207683. DOI: 10.1016/j.ijsolstr.2014.01.020. URL: http://dx.doi.org/10.1016/j.ijsolstr.2014.01.020.

Wan, Richard et al. (2013). "Diffuse instabilities with transition to localization in loose granular materials". In: *International Journal for Numerical and Analytical Methods in Geomechanics* February 2012, pp. 1292–1311. DOI: 10.1002/nag.

Wang, Zhao and Leong Hien Poh (2018). "A homogenized localizing gradient damage model with micro inertia effect". In: *Journal of the Mechanics and Physics of Solids* 116, pp. 370–390. ISSN: 00225096. DOI: 10.1016/j.jmps.2018.04.007. URL: https://doi.org/10.1016/j.jmps.2018.04.007.

Wibberley, Christopher A J and Toshihiko Shimamoto (2002). "Internal structure and permeability of major strike-slip fault zones: The Median Tectonic Line in Mie Prefecture, Southwest Japan". In: *Journal of Structural Geology* 25.1, pp. 59–78. ISSN: 01918141. DOI: 10.1016/S0191-8141(02)00014-7.

Wong, Teng-fong and Patrick Baud (2012). "The brittle-ductile transition in porous rock: A review". In: *Journal of Structural Geology* 44, pp. 25–53. ISSN: 01918141. DOI: 10.1016/j.jsg.2012.07.010. URL: http://dx.doi.org/10.1016/j.jsg.2012.07.010.

Wong, Teng-fong, Patrick Baud and Emmanuelle Klein (2001). "Localized failure modes in a compactant porous rock". In: *Geophysical Research Letters* 28.13, pp. 2521–2524.

Wong, Teng-fong, Christian David and Wenlu Zhu (1997). "The transition from brittle faulting to cataclastic flow in porous sandstones: Mechanical deformation". In: *Journal of Geophysical Research* 102.B2, pp. 3009–3025. DOI: 10.1029/96jb03281.

Wu, Xiang Yang, Patrick Baud and Teng-fong Wong (2000). "Micromechanics of compressive failure and spatial evolution of anisotropic damage in Darley Dale sandstone". In: *International Journal of Rock Mechanics and Mining Sciences* 37.1-2, pp. 143–160. ISSN: 01489062. DOI: 10.1016/S1365-1609(99)00093-3.

Zervos, Antonios, Panos Papanastasiou and Ioannis Vardoulakis (2001). "Modelling of localisation and scale effect in thick-walled cylinders with gradient elastoplasticity". In: *International Journal of Solids and Structures* 38.30-31, pp. 5081–5095. ISSN: 00207683. DOI: 10.1016/S0020-7683(00)00337-1.

Zervos, Antonios, Ioannis Vardoulakis and Panos Papanastasiou (2007). "Influence of nonassociativity on localization and failure in geomechanics based on gradient elastoplasticity". In: *International Journal of Geomechanics* 7.1, pp. 63–74. ISSN: 15323641. DOI: 10.1061/(ASCE)1532-3641(2007)7:1(63).

Zhang, Chunshun (2012). "Breakage mechanics in large granular flow problems". PhD thesis. The University of Sydney, pp. 1–158.

Zhang, Chunshun, Itai Einav and Giang D. Nguyen (2012). "The end-bearing capacity of piles penetrating into crushable soils". In: *Géotechnique* 63.5, pp. 1–14. ISSN: 0016-8505. DOI: 10.1680/geot.11.P.117.

Zhang, Jiaxiang, Teng-Fong Wong and Daniel M. Davis (1990a). "Micromechanics of pressure-induced grain crushing in porous rocks". In: *Journal of Geophysical Research* 95.B1, p. 341. ISSN: 0148-0227. DOI: 10.1029/jb095ib01p00341.

Zhang, Jiaxiang et al. (1990b). "Pressure-induced microcracking and grain crushing in berea and boise sandstones: acoustic emission and quantitative microscopy measurements". In: *Mechanics of Materials* 9.1, pp. 1–15. ISSN: 01676636. DOI: 10.1016/0167-6636(90)90026-C.

Zhang, Yida and Giuseppe Buscarnera (2015). "Prediction of breakage-induced couplings in unsaturated granular soils". In: *Géotechnique* 65.2, pp. 135–140.

— (2017). "A rate-dependent breakage model based on the kinetics of crack growth at the grain scale". In: *Géotechnique* 67.11, pp. 953–967. ISSN: 0016-8505. DOI: 10.1680/jgeot.16.p.181.

— (2018). "Breakage mechanics for granular materials in surface-reactive environments". In: *Journal of the Mechanics and Physics of Solids* 112, pp. 89–108. ISSN: 00225096. DOI: 10.1016/j.jmps.2017.11.008. URL: https://doi.org/10.1016/j.jmps.2017.11.008.

Zhang, Yida, Giuseppe Buscarnera and Itai Einav (2016). "Grain size dependence of yielding in granular soils interpreted using fracture mechanics, breakage mechanics and Weibull statistics". In: *Géotechnique* 66.2, pp. 149–160. ISSN: 0016-8505. DOI: 10.1680/jgeot.15.P.119. URL: http://www.icevirtuallibrary.com/doi/10.1680/jgeot.15.P.119.

Zhao, Jidong, Daichao Sheng and Ian F. Collins (2006). "Thermomechanical formulation of strain gradient plasticity for geomaterials". In: *Journal of Mechanics of Materials and Structures* 1.5.

Zhu, Wei et al. (2016). "Micromechanics of brittle faulting and cataclastic flow in Mount Etna basalt". In: *Journal of Geophysical Research: Solid Earth*, pp. 3782–3803. DOI: 10.1002/2015JB012608.Received.

Zoback, Mark D., Stephen Hickman and William Ellsworth (2011). "Scientific drilling into the San Andreas fault zone - An overview of SAFOD's first five years". In: *Scientific Drilling* 1, pp. 14–28. ISSN: 18168957. DOI: 10.2204/iodp.sd.11.02.2011.

Zoback, Mark D. et al. (1988). "The Cajon Pass Scientific Drilling Experiment: Overview of Phase 1". In: *Geophysical Research Letters* 15.9, pp. 933–936.

Zuluaga, Luisa F., Haakon Fossen and Atle Rotevatn (2014). "Progressive evolution of deformation band populations during laramide fault-propagation folding: Navajo Sandstone, San Rafael monocline, Utah, U.S.A." In: *Journal of Structural Geology* 68.PA, pp. 66–81. ISSN: 01918141. DOI: 10.1016/j.jsg.2014.09.008. URL: http://dx.doi.org/10.1016/j.jsg.2014.09.008.

Acknowledgements

Over the course of the four and a bit years it took me to finish this thesis, I met and spent time with an enormous number of people, both in France and Australia. Being able to split my time between Sydney and Paris has been an enormous privilege, and I am eternally grateful to everyone who shared the journey with me.

Firstly I must thank my supervisor at the University of Sydney, Professor Itai Einav, for his constant guidance, questioning spirit, and relentless drive to improve both the thesis and me as a scientist. It's no exaggeration to say that the experience has changed the way I think.

Next, my housemates permanent and not-so-permanent; Grac, Henry, Zaina, Rosie, Chloe, Lindsay, Polly and Steph, all of whom showed an inordinate amount of tolerance for my attempts at baking, my neurotic rules about correct placement of kitchen objects, and my vague and unhelpful attempts at explaining myself. It would have been a much less fun time (and probably a much worse thesis) without all of you, and I hope the occasional successful baking project and numerous Mario Kart sessions can go part of the way to repaying the debt of friendship I owe you all.

I must also thank the reviewers of this thesis, Professors Panos Papanastasiou, Giang Nguyen and Leong Hien Poh, for kindly donating their time to read and thoroughly comment on this work. In particular, I thank the president of the jury, Professor Gwénaëlle Proust, for going above and beyond at short notice to conduct the defence and organise all of the subsequent administrative burden.

Finally, the extended SciGEM group at Sydney; Benjy, Ebrahim, Eranga, François, James and Mara. Having some sceptics force me to explain what I was doing in a comprehensible way was a massive aid to me in writing this monster, not to mention defending it (and an extra-special thanks for organising the party).

Given the theme of this thesis is very much localisation, it seems apropos to also briefly localise these acknowledgements into something that might resemble French.

Ici, il faut remercier surtout mon directeur de thèse, Professeur Jean Sulem, et mon encadrant Professeur Ioannis Stefanou. Ils m'ont soutenu avec leurs vastes réserves de patience, intelligence et bonne humeur, et ils ont ma reconnaissance éternelle.

Les pauvres qui ont partagé un bureau avec moi mérite une mention particulière aussi pour supporter mes bêtises innombrables. Hung, Tien, Marcos, Sara, Tri, Layal, Tan, Youssouf, j'espère que le premier accès aux gâteaux était un peu de compensation.

L'équipe technique, Emmanuel, Baptiste, Loic, Marine et Xavier m'ont aidé énormément, ce n'est pas une exagération de dire que sans eux, cette thèse n'aurait pas été fait. Leur aide avec l'ACSA et leur compagnie pendant des longues heures de remplissage était précieux, et sans eux il n'y aurait pas un chapitre entier de la thèse dédié à l'appareil.

Enfin, il faut remercier tous les autres doctorants et post-doctorants de l'équipe CERMES (et un saupoudrage de MSA) ; Abdelali, Agustin, Alessandra, Alexandre, Alexandros, Anaïs, Axelle, Benjamin, Dong, Edoardo, Filippo, Giorgos, Hadrien, Hao, Hugo, Lina, Malik, Manuel, Nam Nghia, Phil, Radja, Rawaz, Sadek, Timos, Xiu, Yichun, Yu and Zi. Leur bonne humeur, leur tolérance et leurs corrections de mes crimes innombrable contre la langue française, ont rendu mon séjour à Paris un vrai plaisir.

It would be remiss of me not to thank my friends; Alex, Arie, Ed, Lyndell, Kieran, Max, Nick and Rupert, whose support got me through some tough times in a new country whose language I barely spoke.

Last, but certainly not least, I have to thank my parents for their constant and unwavering love and support, from go to whoa. It really wouldn't have been possible without you.

Financing

Funding from the University of Sydney is gratefully acknowledged, in particular the Australian Postgraduate Award, a Merit Scholarship and the Postgraduate Research Support Scheme.

In addition, the work undertaken in this thesis was supported by Australian Research Council Discovery Projects DP160104310 and DP190103487. The numerical developments (Numerical Geolab) were supported by the European Research Council (ERC) under the European Union Horizon 2020 research and innovation program (Grant agreement 757848 CoQuake).

Appendix A

Fast Fourier transform algorithm

In order to present the FFT as an image that shows distinct features, we must perform a standard set of rescalings. The algorithm to obtain a two dimensional FFT image (with a specific implementation using scipy's fftpack) then becomes:

1. Threshold the spatio-temporal plot, then
2. Extract the square window that we are performing the FFT on, then
3. Perform the FFT, then
4. Phase-shift the FFT so that the zero-component appears at the centre rather than the edge of the image, then
5. Take the absolute value of the FFT (we include both the real and imaginary parts of the transform), then
6. Take the $\log_{10}$ of every value, then
7. Find the contrast range i.e. the difference between the maximum and minimum values present, then
8. Subtract the minimum value from each value and divide that value by the contrast range, and multiply by 255.

Appendix B

Orthogonal distance regression algorithm

To perform the fitting by orthogonal distance regression, we exploit scipy's ODR module. We assume that the observed data (x_i, y_i) are expressible as deviations from the values (x_i^*, y_i^*) that lie on the regression line:

$$x_i = x_i^* + \eta_i, \tag{B.1}$$

$$y_i = y_i^* + \varepsilon_i. \tag{B.2}$$

We define a parameter δ that is the ratio of their variances:

$$\delta = \frac{\sigma_\varepsilon^2}{\sigma_\eta^2}. \tag{B.3}$$

As the method for generating the x and y data is the same, the variances can be assumed the same and hence $\delta = 1$.

We define a line of best fit that must pass through the origin

$$y^* = \beta x^*, \tag{B.4}$$

and then seek to minimise the weighted sum of squared residuals

$$\beta = \underset{\beta \in \mathbb{R}}{\operatorname{argmin}} \left(\frac{1}{\sigma_\varepsilon^2} \sum_{i=1}^{N} \left((y_i - \beta x_i^*)^2 + (x_i - x_i^*) \right) \right). \tag{B.5}$$

This will return a value of β that results in the line of best fit from the ODR method.

Appendix C

Image moment algorithm

In order to calculate the equivalent ellipse, first we must calculate the area (the total number of pixels), where x and y are the coordinates of the pixel, and P is the set of those coordinates:

$$A = \sum_{x,y \in \mathrm{P}} x^0 y^0. \tag{C.1}$$

The normalised moments (i.e. the mean positions in the horizontal and vertical directions) are then given by

$$\bar{x} = \frac{1}{A} \sum_{x,y \in P} x^1 y^0, \tag{C.2}$$

$$\bar{y} = \frac{1}{A} \sum_{x,y \in P} x^0 y^1. \tag{C.3}$$

The respective horizontal, vertical and mixed second order moments are calculated by

$$\mu_{xx} = \frac{1}{A} \sum_{x,y \in P} x^2 y^0 - \bar{x}^2, \tag{C.4}$$

$$\mu_{yy} = \frac{1}{A} \sum_{x,y \in P} x^0 y^2 - \bar{y}^2, \tag{C.5}$$

$$\mu_{xy} = \frac{1}{A} \sum_{x,y \in P} x^1 y^1 - \bar{x}\bar{y}. \tag{C.6}$$

The covariance matrix of the set of pixels is then given by

$$\mathrm{Cov}(P) = \begin{bmatrix} \mu_{xx} & \mu_{xy} \\ \mu_{xy} & \mu_{yy} \end{bmatrix}. \tag{C.7}$$

The eigenvectors of the covariant matrix give the major and minor axis lengths, and the orientation of the major axis:

$$l = \sqrt{8\left(\mu_{xx} + \mu_{yy} + \sqrt{4{\mu_{xy}}^2 + (\mu_{xx} - \mu_{yy})^2}\right)}, \tag{C.8}$$

$$w = \sqrt{8\left(\mu_{xx} + \mu_{yy} - \sqrt{4{\mu_{xy}}^2 + (\mu_{xx} - \mu_{yy})^2}\right)}, \tag{C.9}$$

$$\theta = 0.5 \tan^{-1}\left(\frac{2\mu_{xy}}{\mu_{xx} - \mu_{yy}}\right). \tag{C.10}$$

It should be noted that the angle returned is the angle between the major axis of the ellipse and the nearest Cartesian axis, so it may require adjustment to return a consistent value with respect to the x-axis.

Appendix D

Data robustness

We first note that the slope of the line in the frequency space is orthogonal to the slope of the pattern in the spatio-temporal plot, so the returned angles, $\tan(\beta)$ and θ from the ODR and image moment analyses respectively need to be subtracted from $\pi/2$ in order to correctly give the angle on the spatio-temporal plot.

Now, in order to determine the specific velocity value that we measure, we consider the different threshold values. In general the quality of the fit increases with the value of the threshold, up to the point at which it collapses due to an insufficient number of points. In this instance our method numerically returns a 'NaN' value.

We also have to be careful that the analysis does not return unreasonable values. Occasionally, due to taking the $\tan(\theta)$ of angles close to $\pi/2$, we can experience rapid blow up. Hence, we must implement a procedure to discard unreasonable values. We start by discarding any obviously wrong values (greater than 20, when maximal values are otherwise of order eight), setting these to NaN. We then take the average of the highest threshold value that returns a non-NaN value for a given radius, averaging across the number of separate FFT images produced. We calculate the standard deviation σ and if it is greater than five (already much larger than what the "true" value would be), we set it to five.

We then select a z-score (in this case two), and set any value that is greater than $z \times \sigma$ to NaN.

Finally, for a given experiment at a given radial distance, we search for the value associated with the maximal threshold value that does not return a NaN, and select that as the velocity returned for that point.

Appendix E

Savitzky-Golay smoothing algorithm

A window of m data points (x_i, y_i) is selected (where m is odd) and the order of a fitting polynomial is specified (where the order is less than m). The filter slides the window along the full set of data, fitting the data with the expression

$$y_j^* = \sum_{i=\frac{1-m}{2}}^{\frac{m-1}{2}} C_i y_{j+i}, \tag{E.1}$$

where the window is centred on y_j, and C_i are convolution coefficients that act to more heavily weight data closer to the centre of the fitting window. The convolution coefficients are determined by the least squares method (which has an analytical solution if the x_i are evenly spaced, which is the case with our data).

We then select a window size of 13 points, and a fitting polynomial of order one. We perform the smoothing by exploiting scipy.signal's savgol_filter algorithm.

Because the method of determining the velocity by ODR is slightly more prone to generating NaNs, we pass through our matrix of velocities and replace all NaNs with zeros (failure to replace with a real number means that the Savitzky-Golay method will not work). The method only returns NaNs for small velocities which are very close to zero anyway, and these velocities occur outside the window that we plot, and so have no effect on the region of interest.

As the filter does not respect the need to retain a normalised velocity of one at a radius of one, we renormalise by the smoothed velocity at this radius to produce the final result.

Appendix F

Numerical differentiation

In the classical continuum the strain rate entries denoting shear are symmetric ($\dot{\varepsilon}_{r\theta} = \dot{\varepsilon}_{\theta r}$) and are given by

$$\dot{\varepsilon}_{r\theta} = \frac{1}{2}\left(\frac{1}{r}\frac{\partial v_r}{\partial \theta} + \frac{\partial v_\theta}{\partial r} - \frac{v_\theta}{r}\right). \tag{F.1}$$

In the Cosserat continuum the corresponding entries are given by

$$\dot{\gamma}_{r\theta} = \frac{1}{r}\frac{\partial v_r}{\partial \theta} - \frac{v_\theta}{r} + \omega_z^c, \tag{F.2}$$

$$\dot{\gamma}_{\theta r} = \frac{\partial v_\theta}{\partial r} - \omega_z^c. \tag{F.3}$$

The geometry of ACSA is perfectly rotationally symmetric, and hence the system must be invariant in θ. We also have no capacity to track the Cosserat rotations ω_z^c, so we will ignore these in the formulations. We are left with

$$\dot{\varepsilon}_{r\theta} = \frac{1}{2}\left(\frac{\partial v_\theta}{\partial r} - \frac{v_\theta}{r}\right), \tag{F.4}$$

in the classical continuum, and

$$\dot{\gamma}_{r\theta} = -\frac{v_\theta}{r}, \tag{F.5}$$

$$\dot{\gamma}_{\theta r} = \frac{\partial v_\theta}{\partial r}, \tag{F.6}$$

in the Cosserat continuum.

We need to establish a method to determine the velocity gradient. We choose the central-difference method as its accuracy is greater than the forward- and backward-difference methods (which we use only for the gradient at the first and last points). Hence we have

$$\frac{\partial v_\theta^0}{\partial r} \approx \frac{v_\theta^1 - v_\theta^0}{\Delta r}, \tag{F.7}$$

for the first point,

$$\frac{\partial v_\theta^N}{\partial r} \approx \frac{v_\theta^N - v_\theta^{N-1}}{\Delta r}, \tag{F.8}$$

for the last point, and

$$\frac{\partial v_\theta^i}{\partial r} \approx \frac{v_\theta^{i+1} - v_\theta^{i-1}}{2\Delta r}, \tag{F.9}$$

for all the points in between.

Appendix G

Convergence analysis

We conduct an analysis to confirm the appropriate sizing of our constant volume shear system. We use our calibrated values, with the exception of $\omega = 0°$, as this value of ω is predicted to produce the widest shear band. Thus, if the system is suitably sized for this value, it is suitably sized for all values of ω.

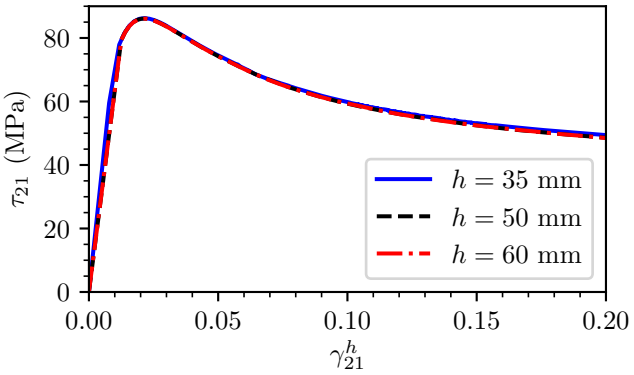

Figure G.1: We plot the value of the shearing stress τ_{21} at the boundary against the homogeneous strain γ^h_{21} for a variety of total system heights.

In Figure G.1, we compare the shear stress at the boundary against the homogeneous shear strain as a means of verifying adequate behaviour, as per Rattez et al. (2018b). This test is also conducted well past the point of localisation, verifying that it converges for elasticity, homogeneous plasticity and localised plasticity. We observe that the behaviour is essentially identical for all three curves, so we may select the smallest system size (even for the same number of elements, physically smaller systems are computationally slightly faster to compute).

We then conduct an analysis to confirm the appropriate number of elements to distribute across the system.

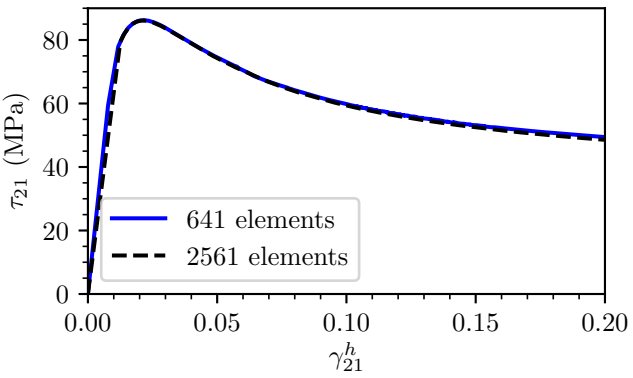

Figure G.2: We plot the value of the shearing stress τ_{21} at the boundary against the homogeneous strain γ_{21}^h for two different numbers of elements.

In Figure G.2, we observe that the two curves are converged, and hence we may select the system with fewer elements as being significantly more computationally efficient.

Hence, we may proceed with our scientific analysis, noting that the system is both sufficiently large and sufficiently finely resolved to produce satisfactory results.

Appendix H

Constant confining stress shearing

As detailed in Chapter 2, the cataclastic shear bands found in seismic faults are an object of interest in this thesis. This case is best modelled as a band being sheared under constant confining stress.

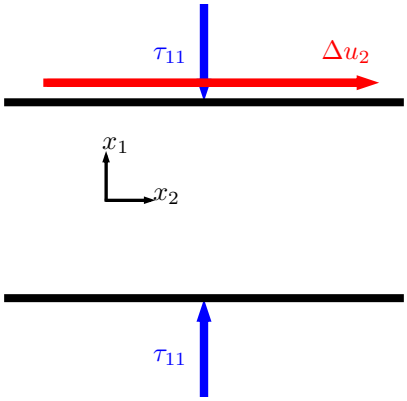

Figure H.1: A schematic of the system that we consider. We apply a constant confining stress τ_{11} in the x_1 direction that acts as a pre-confinement, marked in blue. We then start our test at $t = 0$ and apply a displacement Δu_2 in the x_2 direction to induce shearing, marked in red. During shearing we maintain a constant value of τ_{11}. The system is invariant in the x_3 direction.

The system that we consider is illustrated in Figure H.1. Applying the appropriate simplifications to (4.1) and (4.5) results in reduced strain and curvature rate tensors:

$$\dot{\gamma}_{ij} = \begin{bmatrix} \frac{\partial \dot{u}_1}{\partial x_1} & \dot{\omega}_3^c & 0 \\ \frac{\partial \dot{u}_2}{\partial x_1} - \dot{\omega}_3^c & 0 & 0 \\ 0 & 0 & 0 \end{bmatrix}, \tag{H.1}$$

and

$$\dot{\kappa}_{ij} = \begin{bmatrix} 0 & 0 & 0 \\ 0 & 0 & 0 \\ \frac{\partial \dot{\omega}_3^c}{\partial x_1} & 0 & 0 \end{bmatrix}. \tag{H.2}$$

H.1 Linear stability analysis

We apply the same steps as in §5.5.1, other than allowing the value of n_1 to vary. This allows a qualitative understanding of where the system is likely to support bifurcation.

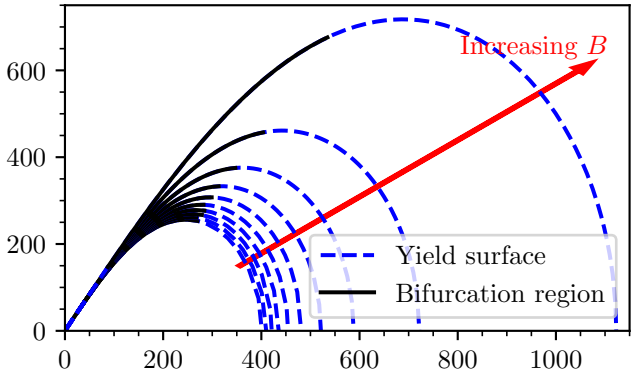

Figure H.2: The regions of the yield surface that can in principle support localisation when sheared under constant confining stress, using the calibrated values of the material parameters. The analysis is performed for $B = 0, 0.1, \ldots, 0.9$, with the corresponding yield surfaces above.

In Figure H.2 we observe substantially similar behaviour to that in Figure 5.3. The only difference is that the localisation region is shifted slightly towards the high pressure regions, particularly at low values of B.

Now, we may follow an individual load curve to examine the behaviour of the system as it transitions from homogeneous deformation to localisation. We apply our confining stress such that $p_0 = 0.3p_{crit}$, which in this case means we apply $\tau_{11} = 208.3$ MPa for all our analyses. As shown in Figure H.2, this level of confining stress places our system within the region that is most favourable for the appearance of strain localisation.

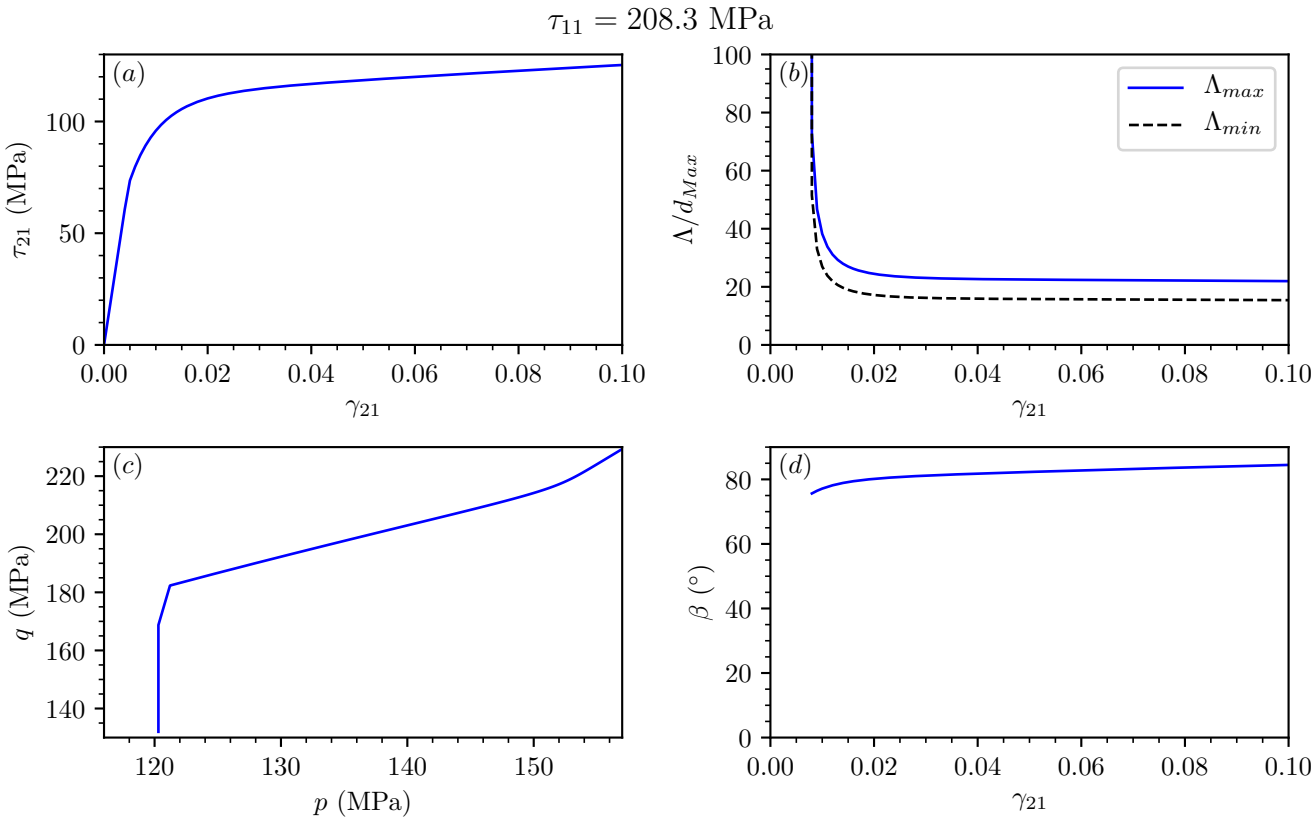

Figure H.3: (a) The shear stress τ_{21} against the total shear strain γ_{21} under constant confining stress $\tau_{11} = 208.3$ MPa. (b) The minimum wavelength for perturbation growth Λ_{min}, and the fastest growing wavelength Λ_{max} against the total shear strain γ_{21}. Both wavelengths have been normalised by the maximum grain size d_{Max}. (c) The system evolution in $p - q$ space. The initial value of q is non-zero because $\tau_{11} \neq \tau_{22/33}$. (d) The evolution of the angle β of the band relative to the shear plane.

In Figure H.3 we observe that under the pseudo-one-dimensional conditions we have specified, a shear band forms during shear at constant confining stress for the calibrated values we have chosen. Firstly, we observe that the system always experiences an apparent hardening when following the $q-\gamma_{21}$ curve. Secondly, Λ_{max} and Λ_{min} reach particular values and then very slowly decline. Finally, the angle at which the shear band forms is steep, and grows steeper as the shear progresses.

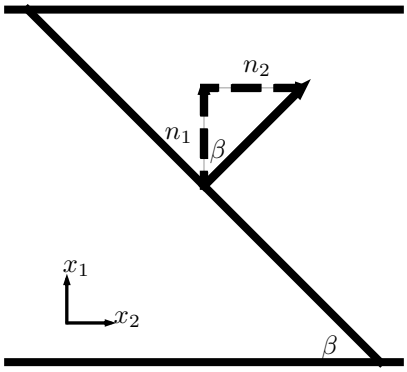

Figure H.4: Illustration of the band geometry with the definition of β.

We illustrate the definition of β for this loading condition in Figure H.4. The bands have this inclination (antithetic) because both the n_1 and n_2 normal components are positive. A synthetic band would have negative n_2 component.

Once again, we can gain insight into the physical behaviour of the system by varying different physical parameters. If we once again start by changing the initial value of the breakage variable B, the plot in Figure H.2 will remain valid as indicative of which regions support shear band formation.

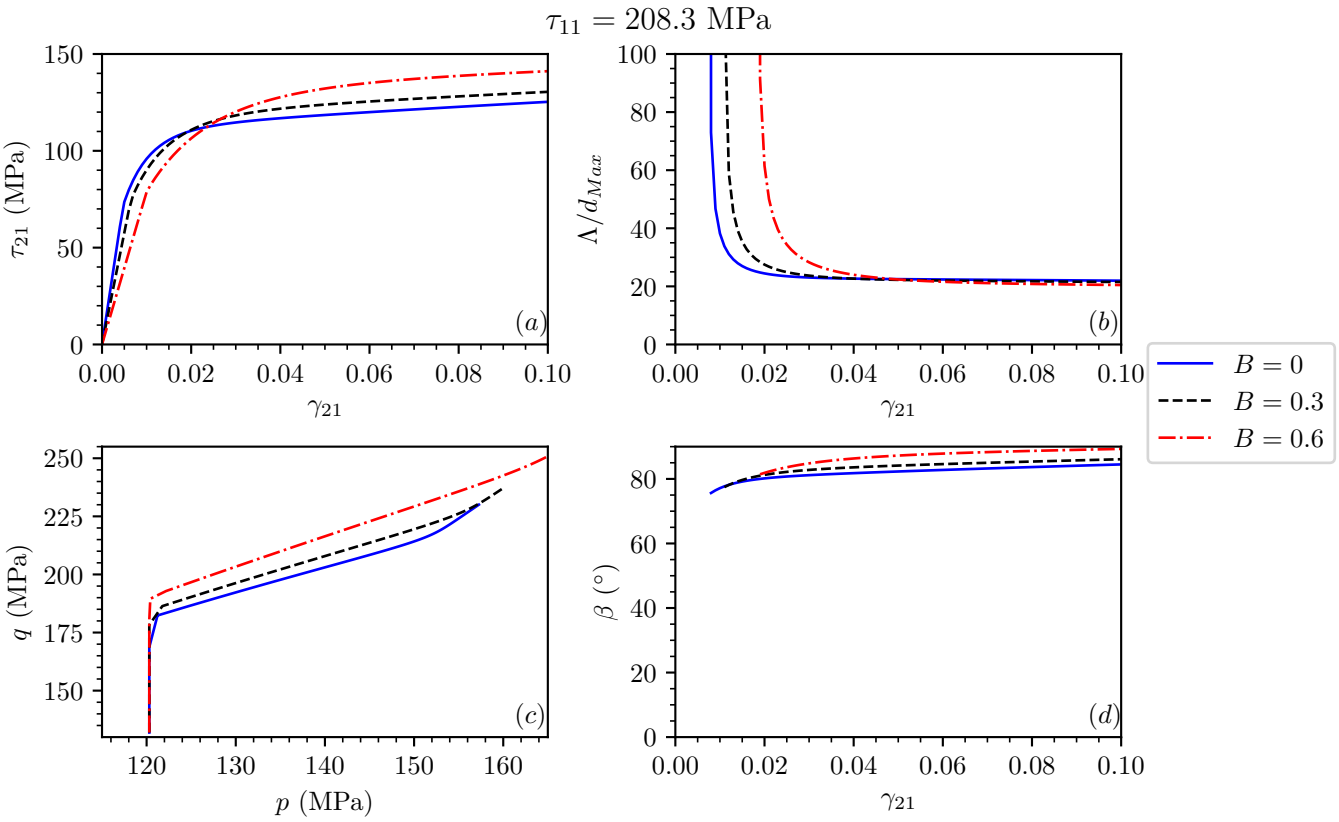

Figure H.5: (a) The shear stress τ_{21} against the total shear strain γ_{21} under constant confining stress $\tau_{11} = 208.3$ MPa, for three different initial values of B. (b) The fastest growing wavelength Λ_{max} against the total shear strain γ_{21} for three different initial values of B. The wavelengths have all been normalised by the largest grain size d_{Max}. (c) The deviatoric stress invariant q against the mean stress p. (d) The angle β of the fastest growing wavelength against the total shear strain γ_{21}.

We can see in Figure H.5 that changing the initial value of B has no strong effect on the behaviour of the model under these conditions. However, we also observe that normalisation by the largest grain size causes the predicted localisation width to essentially collapse onto a single curve, regardless of the initial value of B. This indicates that the largest grain size is a better predictor of shear band width than the mean grain size, which varies with B.

If we examine the tendency of the system to favour grain breakage or plastic volumetric straining as a mode of dissipation by changing the material parameter ω, we must once again recalculate the regions of the yield surface which can support bifurcation.

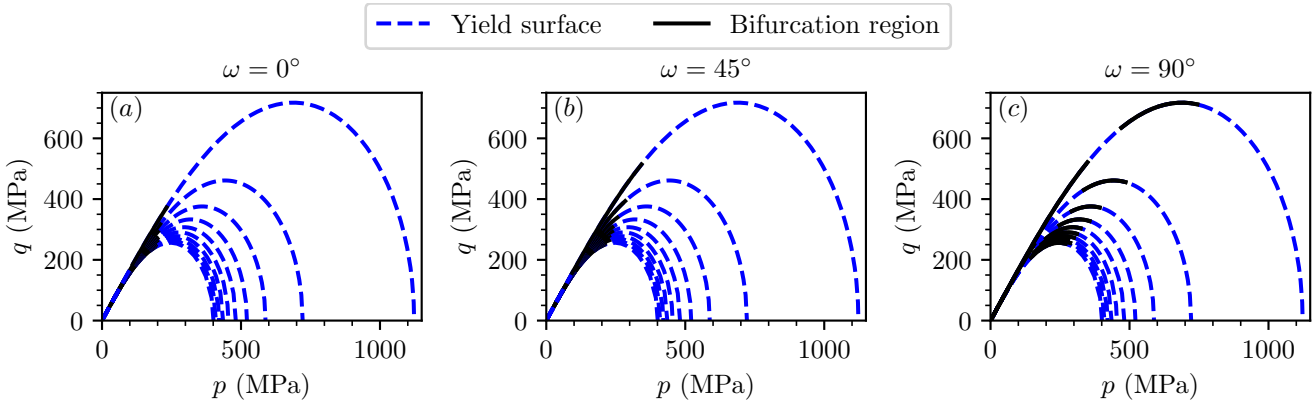

Figure H.6: The regions of the yield surface that can in principle support localisation when sheared under constant confining stress, for (a) $\omega = 0°$, (b) $\omega = 45°$, and (c) $\omega = 90°$. The analysis is once again performed for $B = 0, 0.1, \ldots, 0.9$.

We observe a similar trend to Figure 5.8, in that increasing the value of ω results in larger regions of the yield surface being able to support bifurcation. However, it is important to note than in the case of $\omega = 90°$ (and for similarly high values of ω), the system suffers from a numerical blow up when $0.70 \leq n_1 \leq 0.75$, for certain stress states, which leaves certain regions to appear as if they do not support bifurcation when the favoured bifurcation angle is in this range.

If we follow instead individual load paths, we can observe the tendency of the system as it evolves.

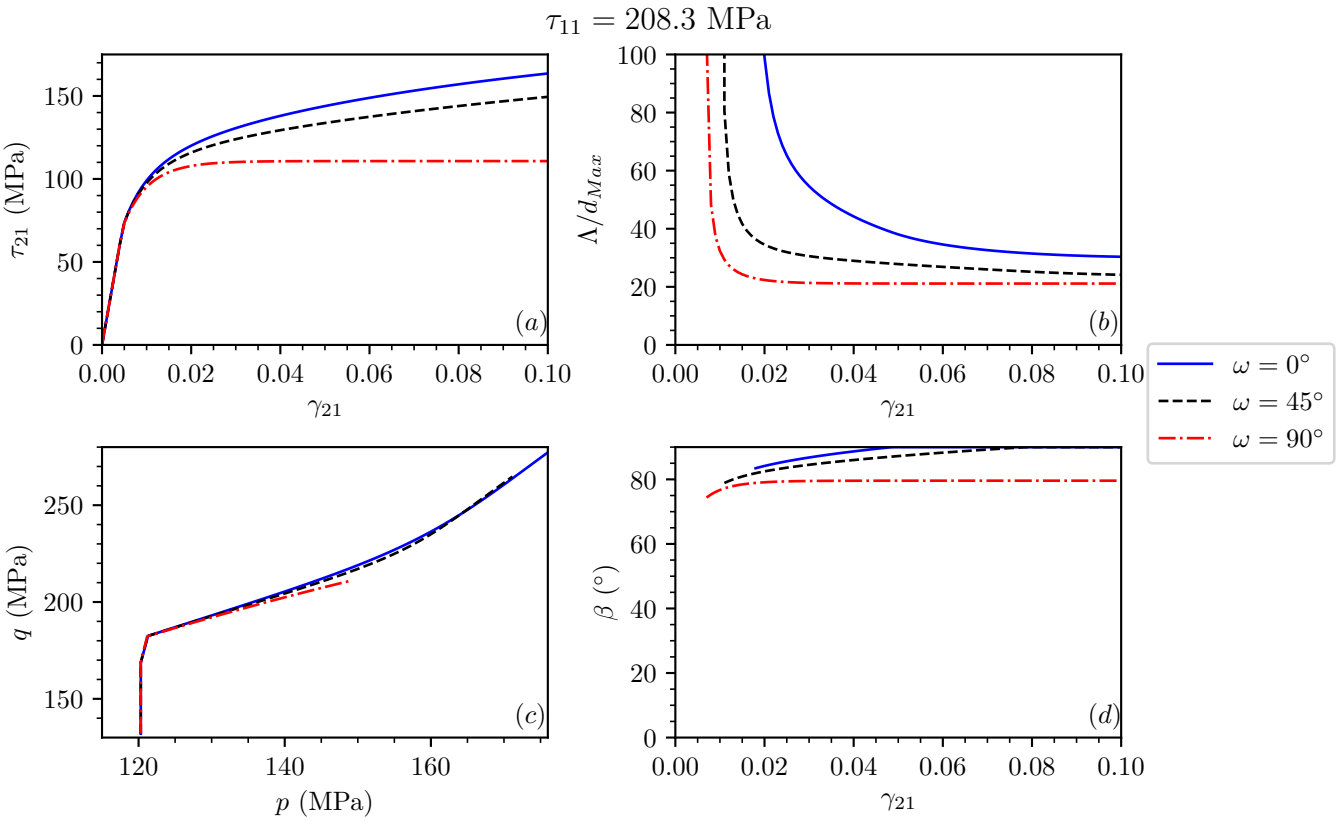

Figure H.7: (a) The shear stress τ_{21} against the total shear strain γ_{21} under constant confining stress $\tau_{11} = 208.3$ MPa, for three different values of ω. (b) The fastest growing wavelength Λ_{max} against the total shear strain γ_{21} for three different initial values of B. The wavelengths have all been normalised by the largest grain size d_{Max}. (c) The deviatoric stress invariant q against the mean stress p. (d) The angle β of the fastest growing wavelength against the total shear strain γ_{21}.

Considering Figure H.7, we can see that changing the value of ω changes the specifics of the behaviour, but not the overall tendencies, with larger ω being more favourable to early localisation and a more slowly growing band angle.

The nature of the bands predicted by these LSAs is different to the principal shear bands we observe in faults, which are typically parallel to the shear plane. These bands are consistently at a high angle to the shear plane, which indicates that they are in fact the antithetic Riedel bands often observed around faults in the field (Davis et al., 2000; Lin and Nishikawa, 2011; Rao et al., 2011). The fact that these are the bands predicted by the model is unexpected, and poses a challenge for finite element analysis, because in constructing our analysis we have assumed the system is invariant in the x_2 direction, so only bands that are parallel to the layer can be modelled. We thus continue our analysis considering other boundary conditions.

Appendix I

Œdometric compression

As detailed in Chapter 2, the cataclastic compaction bands found in æolian sandstones in the field, and which are present in many laboratory tests on a wide range of sandstones, are an object of interest in this thesis. This case is straightforwardly modelled as a unit of material subject to isotropic pre-confinement and then compactive displacement in only one direction.

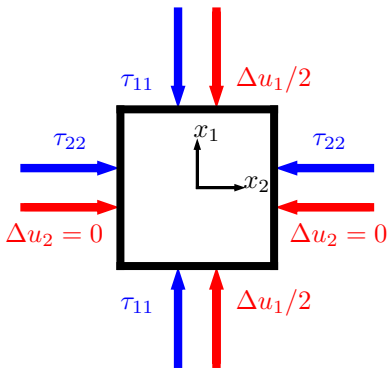

Figure I.1: A schematic of the system that we consider. We first apply an isotropic pre-confinement $p = \tau_{11} = \tau_{22}$, and then start our test by applying a displacement Δu_1 in the x_1 direction, while disallowing displacements in the other two directions. The conditions imposed in the x_3 direction are identical to those imposed in the x_2 directions.

The system that we consider is illustrated in Figure I.1. Applying the appropriate simplifications to (4.1) and (4.5) results in reduced strain and curvature rate tensors:

$$\dot{\gamma}_{ij} = \begin{bmatrix} \frac{\partial \dot{u}_1}{\partial x_1} & \dot{\omega}_3^c & 0 \\ -\dot{\omega}_3^c & 0 & 0 \\ 0 & 0 & 0 \end{bmatrix}, \tag{I.1}$$

and

$$\dot{\kappa}_{ij} = \begin{bmatrix} 0 & 0 & 0 \\ 0 & 0 & 0 \\ \frac{\partial \dot{\omega}_3^c}{\partial x_1} & 0 & 0 \end{bmatrix}. \tag{I.2}$$

I.1 Linear stability analysis

Once again, the first step is using the linear stability analysis to understand the behaviour of the system in a general sense. For the same reasons as previously discussed in §5.5.1 we consider systems with isotropic values of elastic strains. This allows the determination of which parts of the yield surface can *in principle* support bifurcation for our

load conditions.
Thus, the calculation steps are:

1. Fix a value of B (thus determining the yield surface),
2. Set an isotropic value of $\gamma^e_{11/22/33}$ less than or equal to $\gamma^e_{p_{crit}}$, the isotropic elastic strain that corresponds to the critical pressure for that value of B,
3. Calculate the compacting strain γ^e_{11} that places the system on the yield surface,
4. Check whether for a very large wavelength $\Lambda = 10000$ mm there is a value of s with positive real part.

If the condition in step 4 is fulfilled, there is a bifurcation and the system will form a shear band. We check only the horizontal orientation $n_i = 1, 0, 0$ in step 4, as for these load conditions this is the fastest growing orientation.

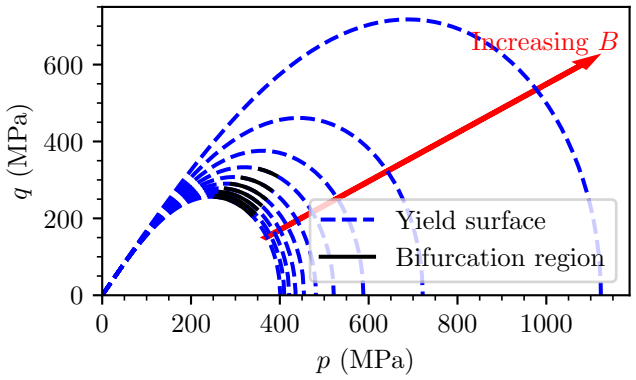

Figure I.2: The regions of the yield surface that can in principle support localisation perpendicular to the compaction direction when compacted under œdometric conditions, using the calibrated values of the material parameters. The analysis is performed for $B = 0, 0.1, \ldots, 0.9$, with the corresponding yield surfaces above.

In Figure I.2 we can observe that the region that supports compaction band formation for the calibrated values occurs on the higher confining pressure side of the yield surfaces, and shrinks as B increases.

If we were to follow an individual load path for œdometric loading, as per §5.5.1, we would find that the fastest growing wavelength in the system is always $\Lambda = 0$ mm. This indicates that the Cosserat continuum does not regularise the case of pure compaction bands, and so we cannot use this model to predict the thickness of compaction bands.

However, we can still use the LSA technique to explore the sensitivity of the system to different material parameters. By changing the material parameter ω we may instead examine the tendency of the system to favour dissipation via plastic volumetric straining over dissipation via grain crushing.

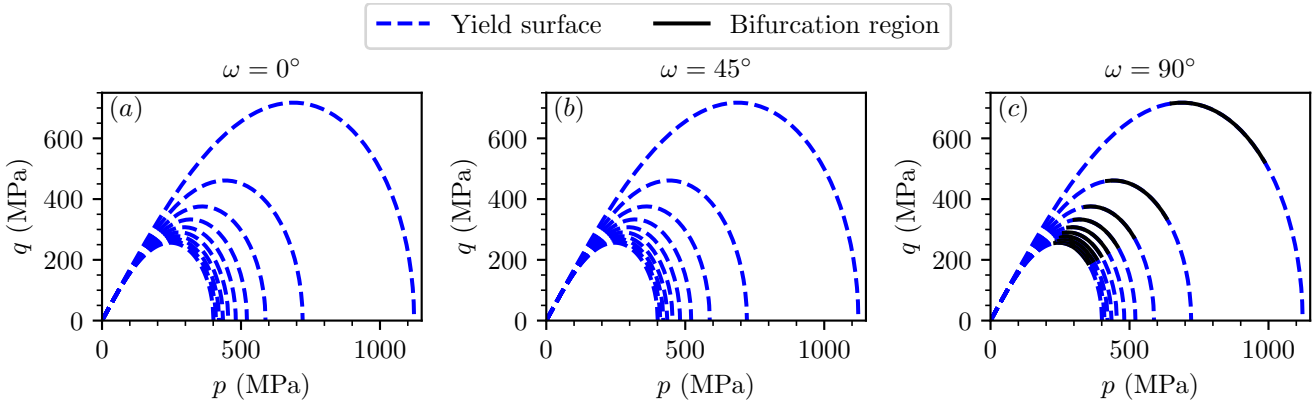

Figure I.3: The regions of the yield surface that can in principle support localisation normal to the compression direction when compacted under œdometric conditions, for (a) $\omega = 0°$, (b) $\omega = 45°$, and (c) $\omega = 90°$. The analysis is once again performed for $B = 0, 0.1, \ldots, 0.9$, with the corresponding yield surfaces above.

In Figure I.3 we can see that changing the value of the parameter ω has a significant effect on the ability of the system to support compaction band formation. In the systems where $\omega = 0°$ and $\omega = 45°$ there is no compaction band formation whatsoever. By contrast, the system where $\omega = 90°$ i.e. where pore collapse is most strongly favoured, supports compaction band formation for any value of B.

We can also change the size of the largest grains present in the system, x_r. Via (4.54), changing this will also have the effect of changing the value of θ_γ, and thus the size of the yield surfaces will also change slightly.

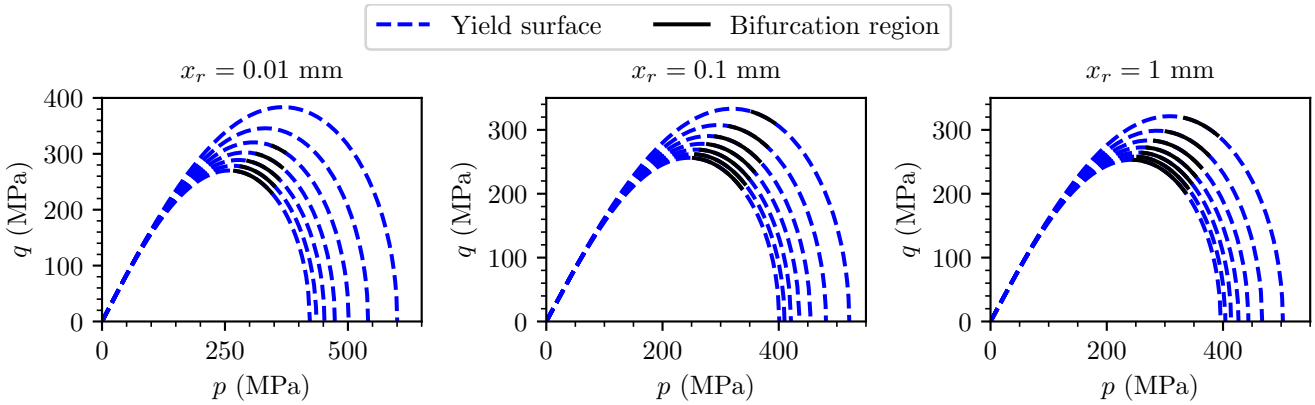

Figure I.4: The regions of the yield surface that can in principle support localisation normal to the compression direction when compacted under œdometric conditions, for (a) $x_r = 0.01$ mm, (b) $x_r = 0.1$ mm, and (c) $x_r = 1$ mm. The analysis is performed for $B = 0, 0.1, \ldots, 0.6$, with the corresponding yield surfaces above.

In Figure I.4 we can see that changing the largest grain size in the system has a substantial effect on both the size of the region that supports compaction band formation, and the behaviour as B grows. For all values of x_r the compaction band region shrinks as B grows, but for $x_r = 0.01$ mm the effect is sufficiently strong that for $B \geq 0.5$ there is no band formation. For both $x_r = 0.1$ mm and $x_r = 1$ mm, there is no band formation for $B \geq 0.7$ (the associated yield surfaces are not shown on the plots for the sake of clarity).

Due to the lack of regularisation offered by the Cosserat continuum in œdometric conditions, if we observe a compaction band formation, it will necessarily be localised entirely in one element, for the reasons that we have previously outlined. Hence, there is no benefit in studying the system using FEM, as we cannot make any valid conclusions under these conditions.

Appendix J

Biaxial compression

We can now move from pseudo-one-dimensional cases to a pseudo-two-dimensional case, that of the biaxial test. In this case, a rectangular specimen is confined between two plates that prevent strains in the x_3 direction. A constant confining stress is applied to the specimen in the x_2 direction, and a compactive displacement is applied in the x_1 direction.

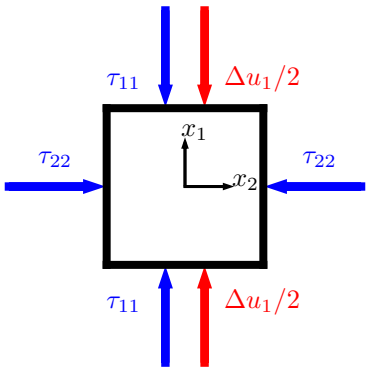

Figure J.1: A schematic of the system that we consider. We apply a pre-confinement of τ_{11} in the x_1 direction and τ_{22} in the x_2 direction, marked in blue, with $\tau_{11} = \tau_{22}$. We then start our test at $t = 0$ by applying a displacement Δu_1 in the x_1 direction, marked in red. We hold the value of τ_{22} constant during the test. The system is invariant in the x_3 direction.

The system that we consider is illustrated in Figure J.1. Biaxial tests typically only apply the pre-confinement in the x_2 direction, but we find it aids the numerical stability of our model to apply it in both the x_1 and x_2 directions.

Applying the appropriate simplifications to (4.1) and (4.5) results in reduced strain and curvature rate tensors:

$$\dot{\gamma}_{ij} = \begin{bmatrix} \frac{\partial \dot{u}_1}{\partial x_1} & \frac{\partial \dot{u}_1}{\partial x_2} + \dot{\omega}_3^c & 0 \\ \frac{\partial \dot{u}_2}{\partial x_1} - \dot{\omega}_3^c & \frac{\partial \dot{u}_2}{\partial x_2} & 0 \\ 0 & 0 & 0 \end{bmatrix}, \tag{J.1}$$

and

$$\dot{\kappa}_{ij} = \begin{bmatrix} 0 & 0 & 0 \\ 0 & 0 & 0 \\ \frac{\partial \dot{\omega}_3^c}{\partial x_1} & \frac{\partial \dot{\omega}_3^c}{\partial x_2} & 0 \end{bmatrix}. \tag{J.2}$$

J.1 Linear stability analysis

In following a single element load path, we confine the system to $p = 0.3p_{crit}$ by applying compression in both the x_1 and x_2 directions. We then start our test by holding τ_{22} constant and apply further compression in the x_1 direction.

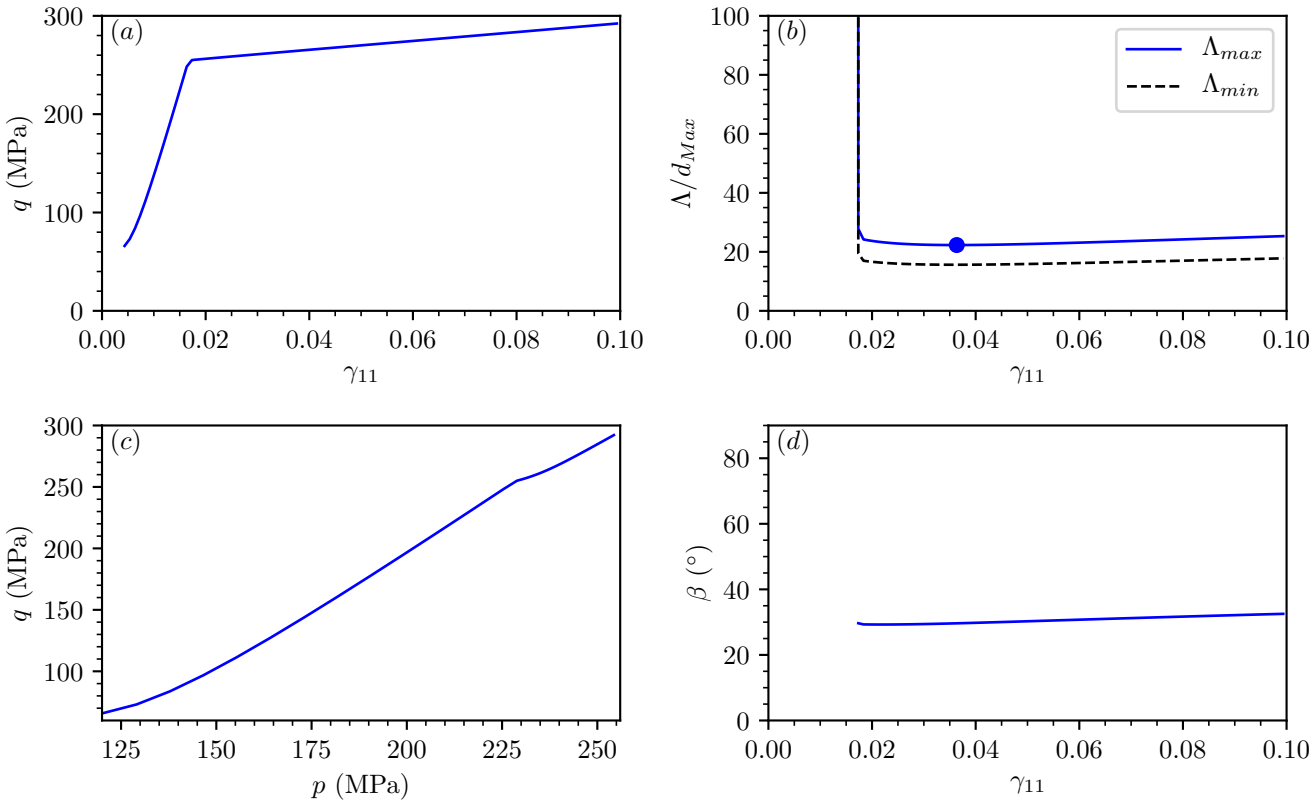

Figure J.2: (a) The deviatoric stress invariant q against the total compressive strain γ_{11} under biaxial conditions. (b) The minimum wavelength for perturbation growth Λ_{min}, and the fastest growing wavelength Λ_{max} against the total compressive strain γ_{11}. Both wavelengths have been normalised by the largest grain size d_{Max}. We place a marker on the minimum value of Λ_{max} for clarity. (c) The system evolution in $p - q$ space. (d) The evolution of the angle of the band relative to the $x_2 - x_3$ plane.

As we can see in Figure J.2, under biaxial loading conditions the system appears to be consistently hardening in the $q - \gamma_{11}$ plot. However, much like under the constant confining stress shear case, in spite of the apparent hardening, the system finds a stable localisation width that changes only very slowly. The band also forms at a relatively shallow angle, which also remains very stable, growing only very slowly under increasing compression.

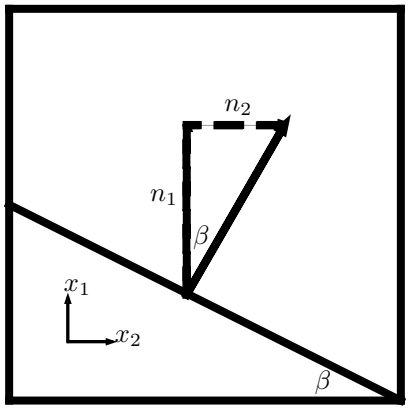

Figure J.3: Illustration of the band geometry with the definition of β.

We illustrate the definition of β in Figure J.3. We can also observe that the initial localisation happens either at or very soon after the system begins yielding plastically.

Once again, we can benefit from considering the sensitivity of the system to different variable and parameter values. Starting by considering different initial values of breakage:

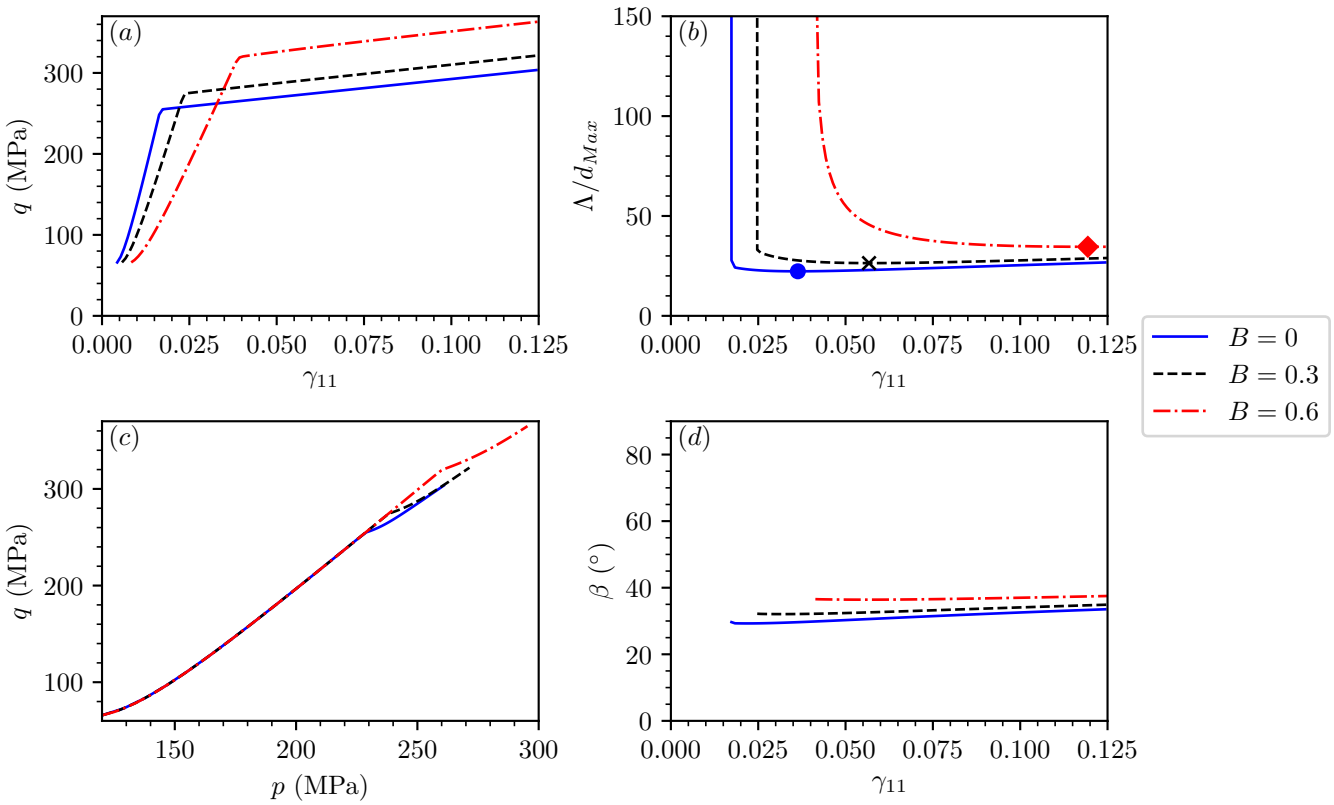

Figure J.4: (a) The deviatoric stress invariant q against the total compressive strain γ_{11} under biaxial conditions. (b) The fastest growing wavelength Λ_{max} against the total compressive strain γ_{11}, normalised by the largest grain size d_{Max}. We place a marker on the minimum value of each curve for clarity. (c) The system evolution in $p-q$ space. (d) The evolution of the angle of the band relative to the $x_2 - x_3$ plane.

We can see in Figure J.4 that changing the value of B does not lead to large qualitative changes in the behaviour of the system, but the quantitative values are somewhat different. We note that all samples are initially compacted to the same stress, which requires slightly more initial strain as B increases. Similarly, as B increases, we can observe on the $q - \gamma_{11}$ plot that it takes more strain for the more broken samples to begin yielding. This behaviour is also demonstrated in very small variations on the $p - q$ plot as less broken samples yield earlier, leading to deviations between the stress paths. Considering the localisation behaviour, we observe that increasing breakage leads to later localisation, as well as a more gradual transition between initial localisation and the minimum value. All three values of B indicate a slowly increasing localisation width as strain increases, and appear to localise at or soon after the point of plastic yielding commencing. Finally, if we consider the angle at which the localisation occurs we see that increasing the initial value of particle breakage slightly increases the angle at which the band forms, but for all three values of B the angle of localisation is relatively stable and only appears to increase gradually.

Once again, we can also consider different values of ω and their effect on the overall system behaviour.

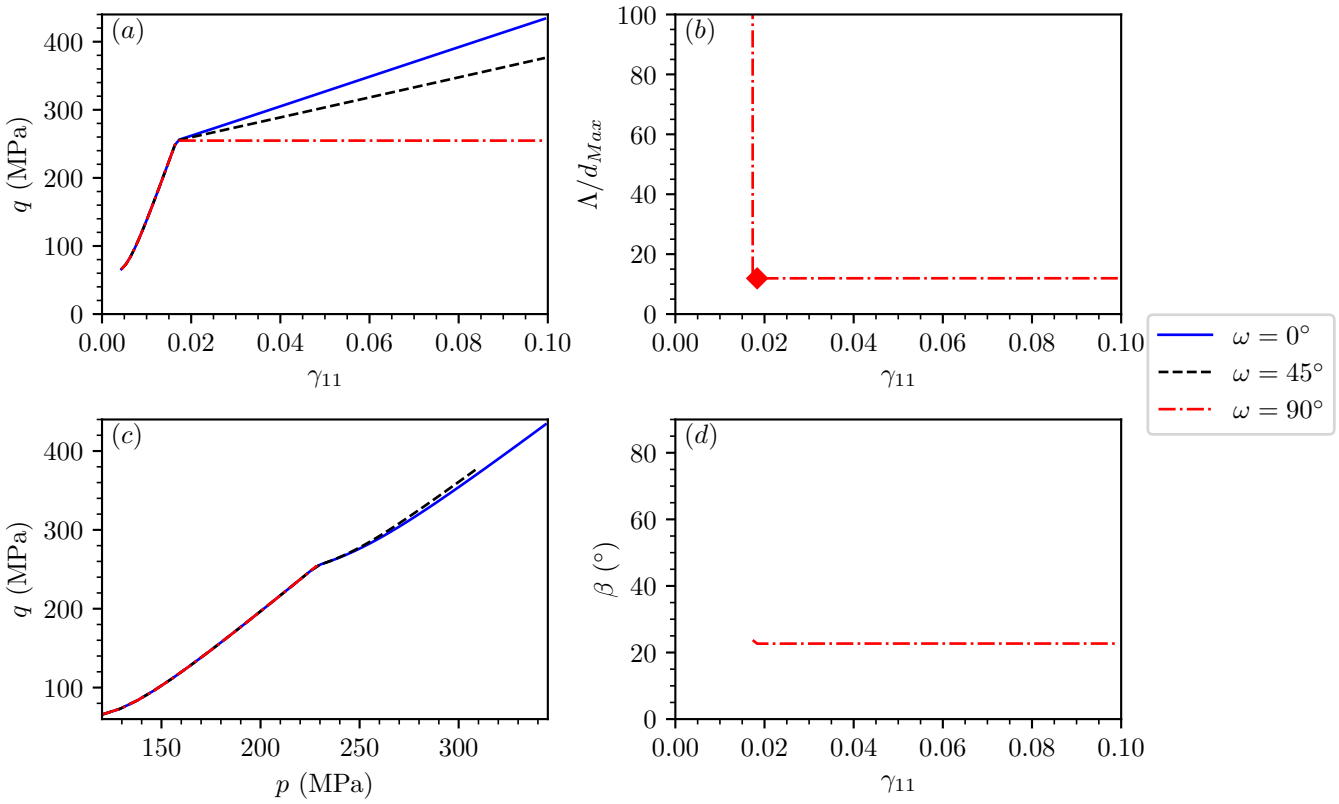

Figure J.5: (a) The deviatoric stress invariant q against the total compressive strain γ_{11} under biaxial conditions. (b) The fastest growing wavelength Λ_{max} against the total compressive strain γ_{11}, normalised by the largest grain size d_{Max}. We place a marker on the minimum value of the curve for clarity. (c) The system evolution in $p-q$ space. (d) The evolution of the angle of the band relative to the $x_2 - x_3$ plane.

In Figure J.5 we can see the different behaviour of the system following a given load path as we change the value of ω. When considering the $q - \gamma_{11}$ plot we can see that the different values of ω correspond to different levels of apparent (and actual) hardening, which can also be observed in the $p - q$ plot. Significantly, when we observe the localisation behaviour, only the system where $\omega = 90°$ predicts any localisation. That system also immediately finds a stable localisation thickness and angle and remains there even as strain increases.